Hydrodeoxygenation of Biomass Pyrolysis Vapor Model Compounds over MoS2 Based Catalysts: A Step in Understanding and Optimizing Fuel Production from Solid Biomass

Dabros, Trine Marie Hartmann

Publication date:
2017

Document Version
Publisher's PDF, also known as Version of record

Hydrodeoxygenation of Biomass Pyrolysis Vapor Model Compounds over MoS_2 Based Catalysts:

A Step in Understanding and Optimizing Fuel Production from Solid Biomass

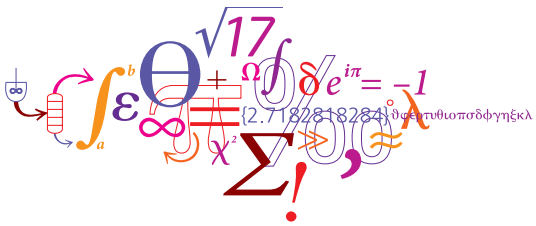

Trine Marie Hartmann Dabros

PhD Thesis

December 2017

DTU Chemical Engineering
Department of Chemical and Biochemical Engineering

Hydrodeoxygenation of Biomass Pyrolysis Vapor Model Compounds over MoS_2 Based Catalysts:

A Step in Understanding and Optimizing Fuel Production from Solid Biomass

PhD Thesis

by

Trine Marie Hartmann Dabros

Formerly: Trine M. H. Arndal

Supervisors:

Anker Degn Jensen, Technical University of Denmark
Martin Høj, Technical University of Denmark
Jan-Dierk Grunwaldt, Karlsruhe Institute of Technology
Jostein Gabrielsen, Haldor Topsøe A/S

Technical University of Denmark
Department of Chemical and Biochemical Engineering
Research Center: CHEC
18th of December 2017

Abstract

This thesis is dedicated to the investigation, development, and optimization of catalysts and operating conditions for catalytic hydropyrolysis and pyrolysis vapor hydrodeoxygenation (HDO) with the aim of producing liquid fuel from solid biomass.

(Ni/Co)-$MoS_2/MgAl_2O_4$ catalysts were prepared and tested for HDO activity in a pressurized fixed bed reactor setup at 380-450 °C, 27 bar H_2, ≤2200 ppm H_2S, and times on stream of up to 220 h. Ethylene glycol (EG) was used in most experiments, representing the most reactive cellulosic fraction of biomass, but acetic acid, phenol, and cyclohexanol were also tested. This work was coupled with density functional theory (DFT) calculations and advanced characterization (e.g. *in-situ* X-ray absorption spectroscopy, XAS) to address the role of promotion and influence of H_2O and H_2S on the catalysts at the atomic level. Several characterization techniques including N_2-physisorption, NH_3-chemisorption, transmission electron microscopy (TEM), X-ray diffraction (XRD), Raman spectroscopy, and elemental analysis were employed to unravel the composition, morphology, and properties of the prepared catalysts.

The $MgAl_2O_4$ support is shown to have a comparable concentration of acid sites as traditionally applied γ-Al_2O_3, and to catalyze dehydration and coupling reactions, while the MoS_2 phases catalyze both cracking (giving C_1 species: CH_4, CO, and CO_2) and HDO (giving C_2 species: ethylene and ethane) with a C_2/C_1 ratio of 1.1-1.5 at 400 °C and 550 ppm H_2S. This ratio could be improved to ∼ 2 with 2200 ppm H_2S, while the presence of a promoter (Ni or Co) increased the activity and stability. DFT calculations indicated that the promoting effect of H_2S is caused by its ability to adsorb as SH groups, which catalyze dehydration and hydrogenation reactions, at the catalyst active edges.

In-situ XAS in terms of extended X-ray absorption fine structure (EXAFS) and X-ray absorption near edge structure (XANES) was additionally used to study the initial catalyst activation ($MoO_x \rightarrow MoS_2$) at 400-450 °C by sulfidation in 10 % H_2S/H_2 and to demonstrate that the resulting active phase, which was anchored to the support, was tolerant towards exposure to water at increasing H_2O/H_2S ratios of 30-300 at 400-450 °C.

The prepared catalysts were shown to have good deoxygenation and hydrogenation activity, which enabled a yield of 40-50 % ethane from ethylene glycol at 400 °C and a co-feed of 550 ppm H_2S. 100 % conversion could be obtained for 172 h on stream at a high ethylene glycol residence time (at a feed of 2 $g_{EG}/g_{cat}/h$), demonstrating the potential of promoted MoS_2 based catalysts in HDO. Catalyst deactivation occurred by carbon deposition, which could be removed in a simple reactivation process (combustion and resulfidation). A kinetic analysis was performed based on experiments with ethylene glycol, cyclohexanol, and phenol, and the results suggested that deoxygenation took place over active sites from the MoS_2 phase as well as over acid sites of the support, and that ethylene glycol strongly inhibited the deoxygenation of cyclohexanol.

This thesis provides new insights into the HDO of reactive biomass derived oxygenates with MoS_2 based catalysts showing high water tolerance and importance of promotion and H_2S level during HDO. These insights allow for further development of catalyst formulations and operating conditions for the production of green fuels from biomass by catalytic fast hydropyrolysis or HDO of pyrolysis vapors.

Resumé

Denne afhandling beskriver undersøgelsen, udviklingen og optimeringen af katalystorer og procesbetingelser til katalytisk hydropyrolyse samt hydrodeoxygenering (HDO) af pyrolysegas med det overordnede formål at producere flydende bændstof fra fast biomasse.

(Ni/Co)-$MoS_2/MgAl_2O_4$ katalysatorer er blevet fremstillet og testet for HDO aktivitet i en tryksat reaktor med et pakket leje ved 380-450 °C, 27 bar H_2, $\leq$2200 ppm H_2S og driftstid på op til 220 timer. Ethylen glykol (EG) er brugt i flest forsøg som repræsentant for den mest reaktive cellulose-afledte del af biomasse, men der er også anvendt eddikesyre, phenol og cyklohexanol. Dette arbejde er samkoblet med tætheds-funktional-teori (DFT) beregninger samt avancerede karakteriseringsmetoder (bl.a. *in-situ* Røntgen absorptions spektroskopi, XAS) for at undersøge indflydelsen af promoter og indvirkningen af H_2O og H_2S på katalysatorerne på atomart niveau. Der er anvendt adskillige karakteriseringsmetoder for at afdække katalysatorernes sammensætning, morfologi og egenskaber; heriblandt N_2-fysisorption, NH_3-kemisorption, transmissions elektron mikroskopi (TEM), Røntgen diffraktion (XRD), Raman spektroskopi og elementar analyse.

Det vises, at $MgAl_2O_4$ bærermaterialet havde en koncentration af sure sites, som var sammenlignelig med en traditional γ-Al_2O_3-bærer. Bærermaterialet katalyserer dehydrering og koblingsreaktioner, mens MoS_2 katalyserer både krakning (hvilket giver C_1 specier: CH_4, CO, and CO_2) og HDO (hvilket giver C_2 specier: ethen and ethan) med et C_2/C_1 forhold på 1.1-1.5 ved 400 °C og 550 ppm H_2S. Dette forhold kunne forbedres til $\sim$ 2 med 2200 ppm H_2S, mens tilstedeværelsen af en promoter (Ni eller Co) øgede aktiviteten og stabiliteten. DFT beregninger indikerede, at den promoterende effekt fra H_2S er dets evne til at adsorbere som SH grupper, der katalyserer dehydrerings- og hydrogeneringsreaktioner, på katalysatorens aktive kanter.

In-situ XAS i form af EXAFS og XANES blev ydermere anvendt for at undersøge den indledningsvise katalysatoraktivering ($MoO_x \rightarrow MoS_2$) ved 400-450 °C ved sulfidering i 10 % H_2S/H_2 og for at demonstrere at den resulterende aktive fase, som var knyttet til bærermaterialet, var modstandsdygtigt over for vand ved stigende H_2O/H_2S forhold på 30-300 ved 400-450 °C.

Det blev vist, at de fremstillede katalysatorer havde god deoxygenerings- og hydrogenerings-aktivitet, som gav et 40-50 % ethan-udbytte fra ethylen glykol ved 400 °C med 550 ppm H_2S i føden. 100 % omsætning kunne opnås i 172 timer ved høj ethylen glykol opholdstid (ved en fødning af 2 g_{EG}/g_{kat}/time), hvilket demostrerede promoterede MoS_2 katalysatorers potentiale i HDO. Kulaflejring gav anledning til katalysator deaktivering, hvoraf det opbyggede kul kunne fjernes i en simpel reaktiveringsproces (afbrænding og gensulfidering). En kinetikanalyse er foretaget på basis af forsøg med ethylen glykol, cyklohexanol samt phenol, og resultaterne indikerede, at deoxygenering foregik over aktive sites fra MoS_2 fasen samt over bærermaterialtets sure sites, og at ethylen glykol stærkt inhiberede deoxygenering af cyklohexanol.

Denne afhandling giver nye indblik i HDO af reaktive biomasse-afledte oxygenater med MoS_2-baserede katalysatorer; modstandsdygtighed over for vand og vigtigheden af promoter samt H_2S niveau under HDO. Disse indblik muliggør videre udvikling af katalysatorformuleringer og procesbetingelser til produktion af grønne brændsler fra biomasse ved katalytisk hydropyrolyse og HDO af pyrolysegas.

Preface and Acknowledgments

This work was conducted at the CHEC research center at The Department of Chemical and Biochemical Engineering (KT) at DTU as part of the H_2CAP project. The H_2CAP project (1377-00025A), is funded by Innovation Fund Denmark, which at the time of funding was called The Danish Council for Strategic Research (The Programme Commission on Sustainable Energy and Environment). It would not have been possible to present the current results without the help of many colleagues, whom I would like to express my sincere gratitude towards.

My supervisors Anker Degn Jensen (DTU), Martin Høj (DTU), Jan-Dierk Grunwaldt (KIT), and Jostein Gabrielsen (Haldor Topsøe) have guided me throughout this work in a dedicated manner, allowing for me to strive towards the development of new knowledge and skills within this field of science. Anker Degn Jensen and Martin Høj have always kept their door open, ready to engage in a scientific discussion. Jan-Dierk Grunwaldt was always ready to provide insights into e.g. advanced characterization techniques, and enabled catalyst characterization at KIT by several techniques. Jostein Gabrielsen contributed with catalyst expertise as well as knowledge on industrial processes and commercial know-how. All of my supervisors contributed to a professional and friendly work environment, and it has been a true pleasure working with all of them.

Hendrik Kramer, Simon Brædder Lindahl, and Mads Lysgaard Andersen, conducted their B.Sc. theses under my supervision and contributed significantly to the experimental work. They all learned that experimental research requires many hours in the lab, and I am thankful for their efforts. Former and current technicians Anders Tiedje and Anders Kjersgaard have assisted the maintenance of the continuous flow reactor setup among many other tasks. The DTU KT workshop has performed various modifications on the experimental flow reactor setup.

Abhijeet Gaur (KIT) and Tim Prüßmann (KIT) took part in a beamtime at the Swiss Light Source (SLS) synchrotron together with Martin Høj, where the catalyst structure was studied with *in-situ* XAS under operating conditions. Abhijeet Gaur also performed the subsequent XAS data treatment (EXAFS, XANES, MES), which significantly aided the understanding of the employed catalyst systems.

Delfina Garcia Pintos (Stanford University) has performed DFT calculations used in this work, allowing for detailed insights into the catalyst structure. Felix Studt (Stanford University and KIT) provided useful insights into the calculations, and aided the discussions during project meetings. Paul Sprenger, Alexey Boubnov, and Dmitry Doronkin (KIT) have aided characterization work performed at KIT. From Haldor Topsøe, Jostein Gabrielsen, Nadia Luciw Ammitzbøll, Lars Frøsig Østergaard, and Lars Kürstein have helped in the analysis of various samples. Thomas Willum Hansen (DTU CEN) conducted transmission electron microscopy (TEM) studies allowing for visualization of prepared and spent catalyst samples.

Finally, I have had so many good, fun, and valuable moments together with my colleagues; both in the lab, on the bowling lane, during lunch, and on the go during casual encounters in the hall-way.

I am thankful that those of my colleagues who worked in the pilot hall tolerated my desire to keep the windows closed, even during humid summer days with >35 °C, in order to avoid process fluctuations.

And just like there is always room for a bottle of beer in the jar of life, there has been time in-between the many hours in the lab to hang out with my friends and family, whom I want to thank for always bearing with me and my urge to do lab work in weekends and to put experiments first on many occasions. My greatest gratitude in this regard goes to my wonderful husband, Mads, who has supported me all the way and has shown great patience during numerous monologues on catalytic hydrogeoxygenation and experimental issues of any kind.

- Thank you -

Publications and Conference Contributions

Articles submitted to peer-reviewed journals

Trine M. H. Dabros, Magnus Z. Stummann, Martin Høj, Peter A. Jensen, Jan-Dierk Grunwaldt, Jostein Gabrielsen, Peter M. Mortensen, Anker D. Jensen, *"Transportation Fuels from Biomass Fast Pyrolysis, Catalytic Hydrodeoxygenation, and Catalytic Fast Hydropyrolysis"*. Submitted to *Progress in Energy and Combustion Science* in September 2017.

Trine M. H. Dabros, Abhijeet Gaur, Delfina G. Pintos, Paul Sprenger, Martin Høj, Thomas W. Hansen, Felix Studt, Jostein Gabrielsen, Jan-Dierk Grunwaldt, Anker D. Jensen, *"Influence of H_2O and H_2S on the Composition, Activity, and Stability of Sulfided Mo, CoMo, and NiMo Supported on $MgAl_2O_4$ for Hydrodeoxygenation of Ethylene Glycol"*. Accepted by *Applied Catalysis A: General* in December 2017.

Articles in preparation

Trine M. H. Dabros, Mads L. Andersen, Simon B. Lindahl, Thomas W. Hansen, Martin Høj, Jostein Gabrielsen, Jan-Dierk Grunwaldt, Anker D. Jensen, *"Hydrodeoxygenation of Pyrolysis Vapor Model Compounds over Sulfided NiMo/$MgAl_2O_4$"*. To be submitted, 2018.

Abhijeet Gaur, Trine M. H. Dabros, Martin Høj, Alexey Boubnov, Tim Prüßmann, Felix Studt, Anker D. Jensen, Jan-Dierk Grunwaldt, *"In-situ XAS Study at Multiple Edges Combined with Modulation Excitation Spectroscopy for Detecting Influences of H_2O and H_2S on HDO Catalysts"*. To be submitted, 2018.

Other documents

Trine M. H. Arndal, *"Safety and operation manual for: SLS in-situ EXAFS setup"*. September 2016. A safety and instruction manual for operation of an experimental capillary reactor setup used for *in-situ* XAS analysis.

Trine M. H. Arndal, *"Creating and using calibration files for GC-FID (Shimadzu GCMS-QP2010 Plus, lab 037/229)"*. February 2017. A software instruction manual for quantification of GC-FID signals.

Conference contributions

presenting author, *corresponding author

Posters

Trine M. H. Arndal, Martin Høj, Peter A. Jensen, Lasse R. Clausen, Jan-Dierk Grunwaldt, Jostein Gabrielsen, Felix Studt, Anker D. Jensen*, *"H_2CAP - Hydrogen Assisted Catalytic Biomass Pyrolysis for Green Fuels"*. Presented at Sustain DTU, 2014, Kgs. Lyngby, Denmark.

Trine M. H. Arndal, Martin Høj, Magnus Z. Stummann, Peter A. Jensen, Lasse R. Clausen, Jan-Dierk Grunwaldt, Jostein Gabrielsen, Delfina Pintos, Felix Studt, Anker D. Jensen*, *"H_2CAP - Hydrogen Assisted Catalytic Biomass Pyrolysis for Green Fuels"*. Presented at Sustain DTU, 2015, Kgs. Lyngby, Denmark. This presentation was awarded with a poster award at Sustain DTU. This poster was also presented at the 2nd ProBioRefine workshop, 2015, Johor Bahru, Malaysia.

Trine M. H. Arndal, Martin Høj , Delfina G. Pintos, Felix Studt, Jan-Dierk Grunwaldt, Jostein Gabrielsen, Anker D. Jensen*, *"Catalytic Hydrodeoxygenation of Biomass Pyrolysis Vapor Model Compounds over Molybdenum Sulfide Catalysts: Influence of Support, H_2S and Water"*. Presented at the 16th International Congress on Catalysis, 2016, Beijing, China.

Orals

Trine M. H. Arndal, Martin Høj, Delfina G. Pintos, Felix Studt, Jan-Dierk Grunwaldt, Jostein Gabrielsen, Anker D. Jensen*, *"Catalytic Hydrodeoxygenation of Biomass Pyrolysis Vapor Model Compounds over Molybdenum Sulfide Catalysts: Influence of Support, H_2S and Water"*. Presented at the 17th Nordic Symposium on Catalysis, 2016, Lund, Sweden.

Trine M. H. Arndal, Martin Høj, Abhijeet Gaur, Tim Prüßmann, Delfina G. Pintos, Felix Studt, Jostein Gabrielsen, Jan-Dierk Grunwaldt, Anker D. Jensen*, *"Influence of Promoter, H_2O and H_2S on the Hydrodeoxygenation of Biomass Pyrolysis Vapor over MoS_2 Catalysts"*. Presented at the 25th North American Catalysis Society Meeting, 2017, Denver, United States of America.

Trine M. H. Arndal, Martin Høj, Abhijeet Gaur, Tim Prüßmann, Delfina G. Pintos, Felix Studt, Jostein Gabrielsen, Jan-Dierk Grunwaldt, Thomas W. Hansen, Anker D. Jensen*, *"Influence of Promoter, H_2O and H_2S on the Hydrodeoxygenation of Biomass Pyrolysis Vapor over MoS_2 Catalysts"*. Presented at the 13th European Congress on Catalysis, 2017, Florence, Italy.

Nomenclature

Abbreviations

ACI	Acid catalyzed reactions
AVG	Average
CAN	Cyclohexane
CEN	Cyclohexene
CN	Coordination number
CRA	Cracking
CUS	Coordinatively unsaturated site
Cyc	Cyclohexanol
db	Dry basis
DCO	Decarboxylation and/or decarbonylation
DDO	Direct deoxygenation
DFT	Density functional theory
DMDS	Dimethyl disulfide
DME	Demethylation
DMO	Demethoxylation
DOD	Degree of deoxygenation
EG	Ethylene glycol
ETA	Ethane
ETY	Ethylene
EXAFS	Extended X-ray absorption fine structure
FCC	Fluid catalytic cracking
FID	Flame ionization detector
FT	Fourier Transform
g	gas
GC	Gas chromatography
GGA	Generalized gradient approximation
GHG	Greenhouse gas
HAADF-STEM	High-angle annular dark-field scanning TEM
HAc	Acetic acid
HCR	Hydrocracking
HDM	Hydrodemetallization
HDN	Hydrodenitrogenation
HDO	Hydrodeoxygenation
HDS	Hydrodesulfurization

HHV	Higher heating value
HYD	Hydrogenation
ICP-OES	Inductively coupled plasma optical spectroscopy
IR	Infrared
LCA	Life cycle assessment
LCF	Linear combination fitting
LHSV	Liquid hourly space velocity
MES	Modulation excitation spectroscopy
MFC	Mass flow controller
MS	Mass spectrometry
MSE	Mean square error
MT	Methyl transfer
NMR	Nuclear Magnetic Resonance
Phe	Phenol
QEXAFS	Quick-EXAFS
s	solid
SA	Surface area
SNG	Synthetic natural gas
SP	Setpoint
SSA	Specific surface area
STM	Scanning tunnelling microscopy
STY	Space time yield
TCD	Thermal conductivity detector
TEM	Transmission electron microscopy
TOF	Turnover frequency
TOS	Time on stream
TPD	Temperature programmed desorption
V	Valve
WGS	Water gas shift
WHSV	Weight hourly space velocity
XAFS	X-ray absorption fine structure
XANES	X-ray absorption near edge structure
XAS	X-ray absorption spectroscopy
XRD	X-ray diffraction

Symbols

ΔE_0	Energy shift
ΔH	Enthalpy of reaction
ΔR	Change in path length (XAS)
A	GC-FID peak area
C_{balance}	Carbon balance
C_i	Concentration of compound i
C_p	Heat capacity
C_{WP}	Weisz-Prater coefficient
D_e	Effective diffusion coefficient

D_K	Knudsen diffusion coefficient
d_p	Particle diameter
D_{AB}	Diffusion coefficient for compound A in B
E_a	Activation energy
F	Molar flow rate
f_{obj}	Objective function
K	Equilibrium constant
k	Rate constant
k'	Lumped rate constant
k_c	Mass transfer coefficient
L	Length
m	Mass
M_w	Molar mass
M_{AB}	Combined molar mass for compounds A and B (for Fuller-Giddings correlation)
P	Total pressure
p	Partial pressure
p_f/l	Pressure drop per length through packed bed
Q_l	Liquid Volumetric flow rate
R	Bond length (XAS) -OR- aliphatic/aromatic group -OR- ideal gas constant
r	Reaction rate
r_p	Particle radius
r_{pore}	Pore radius
$r_{reactor}$	Reactor radius
Re'	Modified Reynolds number
Re_p	Modified Reynolds number for packed bed
S_0^2	Amplitude reduction factor
Sc	Schmidt number
Sh'	Modified Sherwood number
T	Temperature
t	Time
T_b	Boiling point
T_c	Critical temperature
U	Linear gas velocity
v	Volumetric flow rate
W	Catalyst mass in packed bed
X	Conversion
Y	Yield
y	Molar (or volumetric) fraction

Superscript

m	Reaction order
n	Reaction order
o	Reaction order
p	Reaction order

Subscript

A	Reactant/compound
B	Reactant/compound
b	Bulk
C	Carbon
cat	Catalyst
exp	Measured, from experiment
g	Gas
i	Compound or reaction
l	Liquid
$model$	Calculated, from model
out	Outlet
p	Particle
ref	Reference
s	Catalyst surface
0	Initial/feed

Greek

η	Dynamic viscosity
η_{eff}	Effectiveness factor
γ	Shape factor
$\nu_{\text{C,eff},i}$	Effective number of carbon atoms (in GC-FID) in compound i
$\nu_{\text{C,non}}$	Number of non-contributing carbon atoms (in GC-FID) in compound i
$\nu_{\text{C},i}$	Number of carbon atoms in compound i
Φ	Thiele modulus
ϕ	Packed bed void fraction
ϕ_c	Catalyst porosity
ρ	Density
ρ_b	Bulk density of packed bed
ρ_c	Density of catalyst
σ^2	Debye-Waller factor
σ	Constriction factor
$\sum_v$	Sum of atomic diffusion volumes
τ	Tortuosity
Θ_i	Feed flow ratio of compound i

Contents

1 Outline

This thesis is based on original research work with the following structure:

- Chapter 2 gives a comprehensive review of catalytic hydrodeoxygenation (HDO) of fast pyrolysis oil and model compounds and discusses the potential of coupling fast pyrolysis and catalytic HDO for sustainable production of liquid carbon based fuels. This chapter is basically composed by a re-print of all sections of the submitted review article *"Transportation Fuels from Biomass Fast Pyrolysis, Catalytic Hydrodeoxygenation, and Catalytic Fast Hydropyrolysis"* that were written by Trine M. H. Dabros, who was also the main author of this work. Sections written by Magnus Z. Stummann (on fast pyrolysis) and by Martin Høj (on catalytic hydropyrolysis) were omitted or in some cases shortened and modified to target chapter 2 towards HDO. The remaining authors for this article (Peter A. Jensen, Jan-Dierk Grunwaldt, Jostein Gabrielsen, Peter M. Mortensen, Anker D. Jensen) contributed to the discussion and proof reading.

- Chapter 3 describes the experimental equipment and procedures employed at DTU, KIT, PSI-SLS, and in collaboration with Haldor Topsøe A/S. It is an expansion of the "Experimental" section in the accepted article *"Influence of H_2O and H_2S on the Composition, Activity, and Stability of Sulfided Mo, CoMo, and NiMo Supported on $MgAl_2O_4$ for Hydrodeoxygenation of Ethylene Glycol"*. In chapter 3, the description of the experimental setup used for catalytic activity tests may be read in addition to the original description [1].

- Chapter 4 presents the results from catalytic activity tests performed on the pure $MgAl_2O_4$ support and supported Ni-MoS_2 and Co-MoS_2 catalysts with different active phase loadings. Trine M. H. Dabros conducted the experimental work, in most cases assisted by Hendrik Kramer (B.Sc. student). Paul Sprenger conducted Raman spectroscopy on selected catalyst samples and provided important insights to the analysis of Raman spectra. Some of the results presented in chapter 4 are considered for the article, which is prepared based on the results presented in chapter 6.

- Chapter 5 is essentially the "Results and Discussion" section from the accepted article: *"Influence of H_2O and H_2S on the Composition, Activity, and Stability of Sulfided Mo, CoMo, and NiMo Supported on $MgAl_2O_4$ for Hydrodeoxygenation of Ethylene Glycol"* (Accepted by *Applied Catalysis A: General* in December 2017). This chapter presents a study of the activity and stability of prepared Ni-MoS_2, Co-MoS_2, and MoS_2 catalysts under varying water and H_2S concentrations. Trine M. H. Dabros was the main author of this work and conducted the catalyst preparation and catalytic activity tests. The *in-situ* XAS experiments were performed at the PSI-SLS synchrotron by Marin Høj, Abhijeet Gaur, Tim Prüßmann, and Trine M. H. Dabros,

and Abhijeet Gaur subsequently performed the XANES and EXAFS data treatment. Abhijeet Gaur wrote the description of the XAS data treatment process, which can be found in Appendix A. Abhijeet Gaur provided the backbone for the analysis of the *in-situ* XAS results, and the text presented in chapter 5.2.4 is the result of a joint effort from both Abhijeet Gaur and Trine M. H. Dabros. Delfina G. Pintos performed DFT calculations, and wrote the description of the computational procedures (which can be found in Appendix B) together with Felix Studt. Paul Sprenger conducted Raman spectroscopy on selected catalyst samples and provided important insights to the analysis of Raman spectra, and the text presented in chapter 5.2.4.1 is the result of a joint effort from both Paul Sprenger and Trine M. H. Dabros. Thomas W. Hansen took TEM images of selected catalyst samples. The remaining authors for this article (Jostein Gabrielsen, Jan-Dierk Grunwaldt, Anker D. Jensen) contributed to the planning, discussion, and proof reading.

- Chapter 6 is the "Results and Discussion" being prepared for the article in preparation: *"Hydrodeoxygenation of Pyrolysis Vapor Model Compounds over Sulfided NiMo/$MgAl_2O_4$"*. It presents the results from a kinetic study of the HDO of various model compounds in pure and mixed solutions over a Ni-MoS_2/$MgAl_2O_4$ catalyst. Trine M. H. Dabros is the main author of this work and conducted the experimental work, partly assisted by Mads L. Andersen and Simon B. Lindahl (B.Sc. students), who also performed the statistical TEM analysis on images taken by Thomas W. Hansen. The remaining authors for the article in preparation (Martin Høj, Jostein Gabrielsen, Jan-Dierk Grunwaldt, Anker D. Jensen) will contribute to the discussion and proof reading.

- Chapter 7 gives the overall conclusions and outlook based on the result obtained in the preceding chapters.

- The appendices provide additional details to many of the chapters presented in this thesis.

Chapters 2, 5, and 6 have been built up according to their respective article structure. A few small modifications such as reference updates and minor modifications of the content have been performed to fit the scope of this thesis. In chapter 5, the "Introduction" section was shortened to avoid repetition of chapter 2. Chapter 6 is still in the process of being prepared for submission. This means that changes may occur before manuscript submission.

2 | Introduction and Background

Transportation Fuels from Biomass Fast Pyrolysis, Catalytic Hydrodeoxygenation, and Catalytic Fast Hydropyrolysis

Abstract

The modern society is presently based on liquid, carbon containing transportation fuels. With depleting fossil resources and an increasing global energy demand, biomass is the most promising renewable carbon source. Fast pyrolysis of biomass is a well-developed technology, which can produce bio-oil at yields up to $\sim$ 75 %. This bio-oil has a high oxygen content of 35-50 wt% (present as water and biomass derived oxygenates), resulting in a low heating value, approximately half of that of fossil based fuels, and other adverse properties such as high polarity, acidity, and instability upon storage and heating. Raw bio-oil produced by fast pyrolysis can therefore primarily be used for gasification or combustion in boilers, and not as a transportation fuel. It is possible to remove the oxygen by catalytic hydrodeoxygenation (HDO), in which the undesired oxygenates react with hydrogen to produce a stable fuel, with similar heating value as fossil fuels, and water, which is removed by separation. HDO is typically carried out on condensed bio-oil or model compounds in a batch or fixed bed reactor operated at 250-400 °C and up to 200 bar hydrogen. Several catalytic systems have been tested with the most widely studied being commercial hydrotreating catalysts (Co/Ni-MoS_2), oxides (MoO_3, V_2O_5, Fe_2O_3), reduced transition metals (Ni, Pt, Pd, Ru), and phosphides (Ni_2P, WP, MoP). HDO on condensed bio-oil seems very challenging for commercial scale for bio-oil upgrading, as the coking and polymerization, which occurs upon re-heating of the oil, rapidly deactivates the catalyst and plugs the reactor. Instead, a promising technology is catalytic fast hydropyrolysis, which combines fast pyrolysis with catalytic HDO in a fluid bed reactor and produces a stable oil with an oxygen content, an H/C ratio, and a heating value comparable to those of fossil fuels. The process development includes several challenges with the following most urgent three issues: i) operating conditions (temperature, H_2 pressure, and residence time) and catalyst formulation should be optimized to maximize oil yield and minimize cracking, coke formation, and catalyst deactivation, ii) development of a proper process design and reactor configuration to allow for continuous operation including pressurized biomass feeding, fast entrainment and collection of catalytically active char, efficient condensation of the produced oil, and utilization and/or integration of by-products (non-condensable gasses and char), and iii) long-term tests with respect to catalyst stability and possible pathways for regeneration.

2.1 Introduction

Today's production and use of energy is responsible for 60 % of the global greenhouse gas (GHG) emissions (2016 number) [2]. With an increasing world population and the continued industrialization of developing countries the energy consumption will keep increasing in the near future [3–5]. In addition, the depletion of fossil resources and the wide awareness of anthropogenic global warming have intensified the search for renewable and sustainable energy resources that can support our modern way of living [6].

The increase in the anthropogenic CO_2 emissions can be traced back to the industrialization that accelerated through the 20^{th} century [6]. In 2010, CO_2 released from fossil fuels and industrial processes constituted 65 % of anthropogenic GHGs emitted [6]. At this time, the transport sector contributed to 14 % of the total GHG emissions with the energy supply sector covering 34.6 %, industry 21 %, agriculture and forestry 24 % and buildings 6.4 %, respectively [6]. In 2016, 20 % of the human population still lived without access to modern electricity and around 40 % rely on wood, coal, or animal waste for cooking and heating [2]. However, as projected by the U.S. Energy Administration in 2016, the global energy consumption of non-OECD countries will increase significantly from $311{\cdot}10^{15}$ Btu in 2012 to $533{\cdot}10^{15}$ Btu in 2040 (see figure 2.1a) [5].

In 2011 , The World Bank estimated that there were 176 vehicles per 1000 people on average in the world. The number was 55 for low and middle income countries, 620 for high income countries, and 797 in the U.S. alone [7]. Especially for non-OECD countries, the liquid fuel consumption is expected to increase (see figure 2.1b) [5]. In order to accommodate the increasing demand from developing countries it is crucial to develop technologies for a sustainable production of renewable transportation fuels. Fluctuations in the crude oil prices [5, 8], which in 2016 were historically low [8], affect the economy of emerging technologies immensely, which calls for the need of political initiative to ensure a dedicated effort.

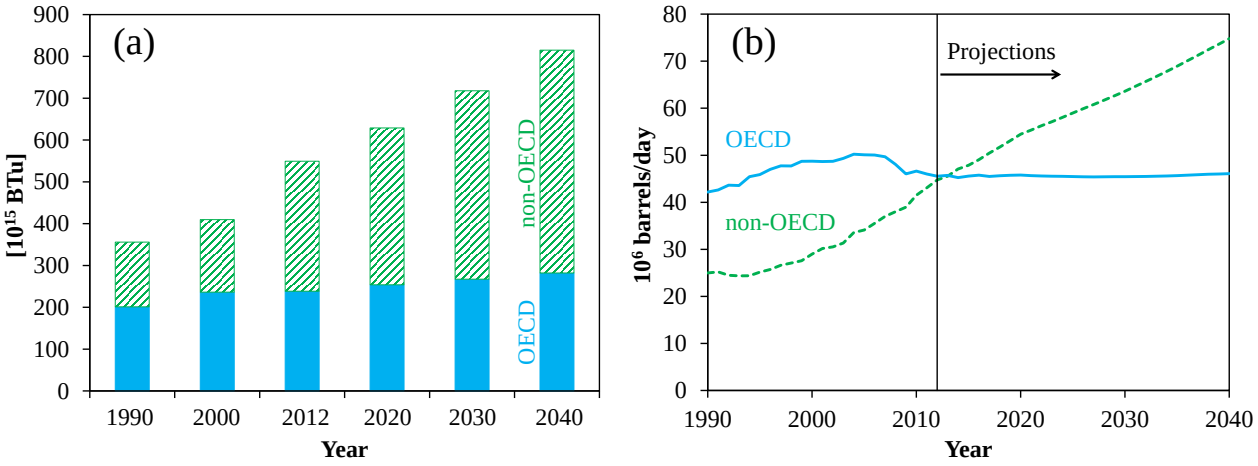

Figure 2.1: *(a) Global energy consumption reported and projected by the U.S. Energy Information Administration in 2016. (b) Petroleum and other liquid fuel consumption by OECD and non-OECD countries. Re-drawn from [5].*

Today, the infrastructure of the modern society is almost solely based on carbon based fuels due to their very high energy density and their availability from the still large oil reserve. At the same time, wind and solar based electricity production is reaching a mature stage. The electrical vehicle industry is, however, facing challenges. An immediate threshold for both fuel-cell and battery driven vehicles is the necessity to build a new fuel infrastructure with charging stations for H_2 and electricity, respectively [9]. Battery driven vehicles also struggle with a low energy density and instability of the currently dominant Lithium batteries [9]. Another challenge lies in the availability of wind and solar based electricity and lack of good storing technologies, e.g. chemical energy storage via hydrogen is not yet economically feasible [10]. Electricity production from photovoltaic cells peaks during the day, whereas power consumption typically peaks in the morning and afternoon, which results in the so-called duck-curve [11]. Consequently, biomass appears as the most promising renewable source of carbon for fuels. Additionally, if we look towards the aviation and shipping industries, it is unlikely that these will be fueled by electricity in the near future.

Biomass can be used as a raw material for the production of fuels with low (potentially zero) carbon footprint [12–14]. First generation biofuel processes such as bio-ethanol (from sugar cane and corn) and bio-diesel (from vegetable oils) convert the biomass into fuels through well-established technologies [15]. However, since the applied biomass types are edible, a political and ethical dilemma arises when the number of undernourished people in the world is more than 10 % (data from 1990-2010); a number which has fortunately been decreasing since 1990 and until today [16]. Additionally, the energy efficiency per unit land is markedly lower for food grade biomass compared to energy crops [14]. Therefore, development of second generation biofuels is based on utilization of non-edible biomasses such as wood, energy crops, algae, and waste material from agriculture, paper production, and municipalities [17,18].

Mortensen et al. [19] reviewed the competitiveness of various routes for biofuel generation. Based on an assessment of the fuel price per mass of oil equivalent, it was concluded that a viable route for renewable liquid fuel production is fast pyrolysis coupled with catalytic hydrodeoxygenation (HDO). While fast pyrolysis is used to increase the biomass energy density by producing a liquid product commonly referred to as bio-oil, which can be transported more easily than solid biomass, catalytic HDO is used to enhance the fuel properties through oxygen removal in an H_2 atmosphere using a suitable catalyst. A promising technology is the coupling of fast pyrolysis and HDO in catalytic fast hydropyrolysis, where the HDO is performed directly in the pyrolysis reactor [20]. Additional H_2 could possibly be provided from the hydrolysis of water powered by wind or solar energy.

This chapter provides an brief introduction to fast pyrolysis (section 2.2), an extensive review of catalytic HDO (section 2.3), and a summary of coupled fast pyrolysis and catalytic HDO in a continuous catalytic fast hydropyrolysis process (section 2.4). The aim of this review is to couple the knowledge from fast pyrolysis and HDO in the evaluation of proposed processes for production of transportation fuels from biomass fast pyrolysis, catalytic HDO, and catalytic fast hydropyrolysis.

2.2 Properties of Fast Pyrolysis Bio-oil

Lignocellulosic biomass can be converted into an oil, typically referred to as bio-oil, by fast pyrolysis, which is a thermochemical degradation obtained by fast heating (700-10,000°C/s) of biomass particles in an inert atmosphere to 400-600 °C with short vapor residence times (<2 s); typically in a fluid bed or cyclone reactor [21]. Fast pyrolysis produces a liquid (bio-oil), solid and gaseous product fraction with the distribution being dependent on the operating conditions, see table 2.1. The typical energy recovery is 45-75 % [22].

Table 2.1: *Typical product yields obtained by different modes of wood pyrolysis, db = dry basis. Adapted from [21].*

		Approximate product yields [wt% db]		
Mode	**Conditions**	**Liquid**	**Solid**	**Gas**
Fast pyrolysis	~ 500°C, short hot vapor residence time <2 s	75	12	13
Intermediate	~ 500°C, hot vapor residence time ~ 10-30 s	50 (two phases)	25	25
Carbonization (slow)	~ 400°C, long solid residence time of hours or days	30	35	35
Torrefaction (slow)	~ 290°C, solid residence time ~ 10-60 min	0-5	80	20

Bio-oil is a dark brown and viscous, but freely flowing, liquid [21,23]. It is a complex mixture, consisting of hundreds of different compounds [24,25]. The chemical composition of bio-oil is similar to that of the parent biomass, but the volumetric energy density is increased, potentially by a factor of >6 [26,27]. The higher heating value (HHV) of bio-oil (16-19 MJ/kg) is however less than half of that of diesel and heavy fuel oil (~ 40 MJ/kg) [21,22,28,29]. This is due to a high content of oxygen (35-50 wt%), which is present as water (15-30 wt%) [21,28,30] and many different oxygenates derived from the cellulosic, hemicellulosic, and lignin part of biomass [24,25]. The properties of bio-oil are compared with those of fossil fuels in table 2.2. It is clear that bio-oil is very different from crude oil.

Bio-oil is unstable upon heating, and the high content of water can therefore not be removed by conventional distillation, as this would cause rapid polymerization resulting in the formation of 30-50 wt% residual solid [30]. Furthermore, the high oxygen content in bio-oil gives it a high polarity which makes it immiscible with conventional petroleum oils [21,23,31]. The density of bio-oil (~ 1.2 kg/L) is significant higher than the density of diesel (0.82-0.85 kg/L) [32,33]. This means that bio-oil has an energy density of 37-44 % compared to that of diesel on mass basis, but 53-65 % on volumetric basis. Depending on the source of biomass, bio-oil typically contains trace amounts of ash, alkali, chlorine, and sulfur [21,34,35]; species that are all potential catalyst poisons.

Table 2.2: *Common properties of wood derived bio-oil and fossil derived oils (data adapted from refs. [21, 22, 28–30, 32, 33, 36, 37]).*

Property	**Unit**	**Bio-oil**	**Diesel**	**Heavy fuel oil**
Water	[wt%]	15-30	0-0.001	0.1-7
Ash	[wt%]	0-0.2	0-0.01	0.03-0.1
Carbon	[wt%]	44-58	86	85
Hydrogen	[wt%]	5.5-7.2	13	11-12
Nitrogen	[wt%]	0-0.2	-	0.6
Oxygen[a]	[wt%]	35-50	0	0-0.1
Sulfur	[ppm]	$<$400	10-500	21,000
Stability	-	Unstable	Stable	Stable
Viscosity (40-50 °C)	[cSt]	13-100	1.9-4.5	140-380
Density (15-40 °C)	[kg/L]	1.1-1.3	0.82-0.85	0.96
Flash point	[°C]	62-95	52-55	65-100
Pour point	[°C]	-19 to -24	-20	15-21
HHV	[MJ/kg]	16-19	43	38-41
pH	-	2.4-3.2	-	-

[a] Includes oxygen from water.

Gas chromatography mass spectrometry (GC-MS) [24, 38] and nuclear magnetic resonance (NMR) spectroscopy [25, 38] analysis of different bio-oils have revealed that the bio-oil contains acids, non-aromatic aldehydes, non-aromatic ketones, furans, pyrans, sugars, benzenes, catechols, lignin derived phenols, guaiacols, and syringols. A list of common molecules found in bio-oil produced from fast pyrolysis of wood is shown in table 2.3. Owing to the nature of these oxygenates, the oil is viscous, acidic, and unstable upon storage and heating; phase separation, coking, or re-polymerization reactions may occur. Thus, the direct application of fast pyrolysis bio-oil as an engine fuel is highly challenged.

Table 2.3: *Common compounds in wood derived bio-oil. Primarily adapted with permission from [39] (copyright 2013, American Chemical Society). Modified and updated based on refs. [21, 23, 24, 28, 30, 40–47].*

Functional group	**Typical compounds**	**Structure**[a]
Simple oxygenates		
Acids	Acetic acid, formic acid, propanoic acid, methyl propanoic acid, butanoic acid, pentanoic acid, glycolic acid, hexanoic acid, ...	
Esters	Methyl acetate, ethyl acetate, methyl formate, ...	
Alcohols	Methanol, 2-propene-1-ol, butanol, ethylene glycol, propylene glycol, 2,3-butandiol, cyclopentanol, cyclohexanol, 1,2-cyclohexanediol, ...	
Ketones	2-butanone, cyclopentanone, methylcyclopentanone, 3-methyl-1,2-cyclopentanedione, 2-petanone, cyclohexanone, ...	
Aldehydes	2-butenal, glyoxal, formaldehyde, benzaldehyde, ...	
Mixed oxygenates	2-hydroxyacetaldehyde	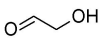
	1-hydroxy-2-propanone	
	Methyl-2-oxopropanoate, 1-hydroxy-2-butanone, ...	
Sugars and derivatives	Levoglucosan	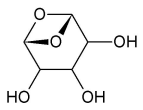
	Xylose, arabinose, glucose, fructose, sorbitol, cellobiosan, ...	
Furans	Furfural	
	Furan, 2-furanone, butyrolactone, methyl-2-furanone, furfuryl alcohol, 2-acetyl furan, 5-methyl furfural, 5-hydroxymethyl furfural, tetrahydrofuran, 2,5-dimethyltetrahydrofuran, ...	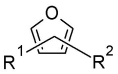
Aromatics		
Oxygen free	Toluene, benzene, xylene, ...	
Phenols	Phenol, methylphenol, dimethylphenol, ethyl phenol, catechol, methylcatechol, ethylcatechol, methoxycatechol, ...	
Guaiacols	Guaiacol	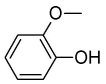
	Methylguaiacol, ethylguaiacol, eugenol, vanillin, ...	
Syringols	Syringol	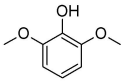
	Methylsyringol, ethylsyringol, 4-propenylsyringol, ...	
Others	Vanilinic acid, sinapaldehyde, syringaldehyde, acetosyringone, ...	
High M_w species[b]	Dimmers, trimmers, oligomers, and cellulose, hemicellulose, and lignin pyrolysis products	

[a] R denotes H, CH_3, or other aromatic/aliphatic groups.
[b] M_w denotes molar mass.

Figure 2.2a shows a typical carbon distribution in the compounds present in oak bio-oil and illustrates that the organics in bio-oil are mainly composed of a lignin-derived fraction as well as a cellulosic/hemicellulosic fraction (C_{5-6}), and short C_2 compounds. In figure 2.2b, the organic content is divided based on compound types and parent biomass component.

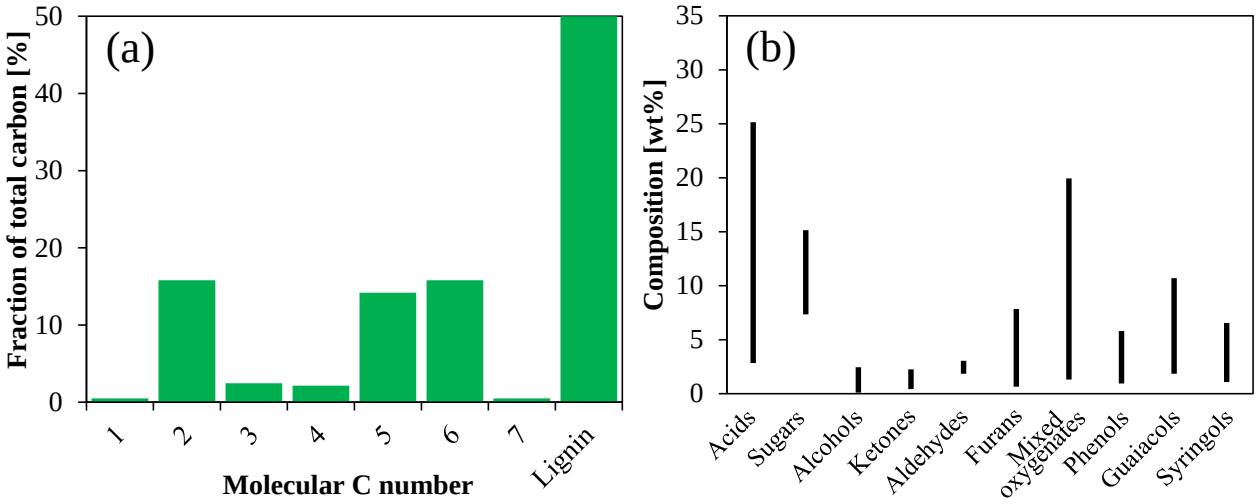

Figure 2.2: *(a) Carbon distribution for compounds present in an oak derived bio-oil. Adapted with permission from [47] (copyright 2017). (b) Composition ranges in wood bio-oil, reproduced from Ruddy et al. [48] (with permission of the Royal Society of Chemistry), who used the data collected by Milne et al. [49].*

Woody bio-oil has a high concentration of hydroxyacetaldehyde and levoglucosan; products from cellulose degradation [24, 50]. The cellulosic and hemicellulosic part of biomass is responsible for the corrosive character (from acids) and instability (from light and reactive oxygenates) of bio-oil.

The lignin part of biomass contributes to the aromatic content in bio-oil. The phenolic content consists of aromatics with a lower O/C content compared to the cellulose and hemicellulose derived compounds. Additionally, these aromatics are stable and do not readily react. In conclusion, the negative influence of aromatic oxygenates on the fuel quality of bio-oil is less significant compared to cellulose and hemicellulose fragments. It is therefore interesting that bio-oil model compounds upgrading studies have mainly focused on oxygen removal from phenolic species. They may be the most difficult compounds to upgrade, but they are also the least problematic compounds with respect to stability upon storage and heating.

2.2.1 Aspects of Bio-oil Utilization

The main challenge in the utilization of raw bio-oil as a transportation fuel is its instability caused by the content of highly reactive oxygenates. Several issues have been reported when using bio-oil in diesel engines: ignition difficulties, fuel injection problems, corrosion of injector needles, and coking of combustion chamber, exhaust valve, and injection nozzles leading to clogging [51–57]. Therefore further upgrading of the bio-oil is necessary, before it can be used as a transportation fuel.

Despite that fast pyrolysis technologies to some extent are commercially available, the market for bio-oil in power plants is challenged. Solid biomass, such as wood chips or pellets, is already used in power plants in Europe with a minimum requirement for pretreatment, which of course challenges the

interest in biomass pyrolysis processes that produce a fuel with limited applicability. Bio-oil can be mixed with the produced char and gasified to form synthesis gas mixture that that can be converted into liquid fuel by use of the dimethyl ether to gasoline process [26,58]. It is also possible to co-process the bio-oil with conventional fuels in a refinery fluid catalytic cracking (FCC) unit [59,60], but co-feeding is highly challenged in hydrotreating units due to the high content of oxygen in bio-oil, which makes it immiscible with fossil feeds and causes severe coking [61]. Additionally, the alkaline metals in the bio-oil can decrease the lifetime of catalysts in both the FCC and hydrotreating processes [59–61]. It should also be mentioned that zeolites, which are used as commercial FCC catalysts [62], typically have a high cracking activity, which limits the oil yield.

2.3 Catalytic Hydrodeoxygenation

Catalytic HDO is known from hydrotreating (also called hydroprocessing) of crude oil, where it is used to remove the <1 % oxygen present in the feed [28, 63]. Hydrotreating covers the removal of sulfur (hydrodesulfurization, HDS), nitrogen (hydrodenitrogenation, HDN), oxygen (HDO), and metals (hydrodemetallization, HDM) from fossil crudes [63]. Since the oxygen content in bio-oil is significantly higher than in fossil feedstocks, the requirements for catalysts for hydrotreating of bio-oil is significantly different from those for hydrotreating a fossil feed.

The literature on bio-oil upgrading by HDO and other techniques has experienced a massive increase within the last decades. Saidi et al. [64] counted the number of bio-oil related HDO papers and found 5, 16, 73, and 131 publications for the years 2006, 2008, 2010, and 2012. A quick view at the literature published after 2012 indicates a near exponential growth. In conclusion, bio-oil upgrading by HDO is a hot topic, which has called many researchers to contribute to the complex task of converting biomass into high quality liquid fuels. The scope of this section is not to give an exhaustive review of the HDO literature, but rather to provide a comprehensive overview of the most important concepts, results, and trends.

In 2007, Elliott [65] reviewed the historical development in hydrotreating of bio-oil produced via different pyrolysis and liquefaction techniques. In 2014, this review was followed up by a critical review including perspectives on industrial process integration and evaluation of techno-economic analyses [66]. Furimsky [67] has provided a comprehensive review on catalytic HDO chemistry in terms of reaction mechanisms and kinetics for both petrochemical and biomass derived model oxygenates with a focus on conventional hydrotreating catalysts. A more general review by Furimsky [68] focuses on hydrotreating of various bio-feeds with vegetable oil, lignocellulosic, algae, and sewage sludge origin over different catalyst classes. A number of recent reviews have a more concentrated focus on catalytic HDO of lignocellulosic bio-oil and model oxygenates including descriptions of the HDO chemistry over different catalytic systems [19,39,48,69].

The majority of studies on catalytic HDO involve the conversion of model compounds chosen to represent selected functionalities present in bio-oil. The results from these studies aid the understanding of individual reaction mechanisms for a given catalyst and set of reaction conditions. Even though these results provide some insight into catalytic HDO, they cannot be used to draw general conclusions for HDO of real bio-oil due to the complexity of its composition and impurities present. The evaluation of catalytic HDO activity should include considerations on catalyst properties such as active phase dispersion (or particle size), surface area, and pore volume as these features will affect the observed HDO activity.

2.3.1 Reactions, Reactivity, and Reaction Mechanisms

The complex structure of biomass results in bio-oil compositions with very high diversity as mentioned in section 2.2 and shown in table 2.3. As a result of the complex composition, catalytic HDO of bio-oil entails a comprehensive reaction network. An overview of reactions that can occur during upgrading of bio-oil is shown in figure 2.3 together with commonly applied acronyms.

Decarboxylation and decarbonylation (DCO) especially occur in upgrading of vegetable oils due to a high content of fatty acids and fatty acid esters [70]. HDO covers the removal of oxygen with H_2 and has the deoxygenated compound and water as products. HDO can occur as direct deoxygenation (DDO) or with saturation of double bonds or aromatic functional groups by hydrogenation (HYD) prior to deoxygenation. It should be noted that HYD has also been used as an acronym for combined hydrogenation and deoxygenation [71–73]. Cracking reactions are dominant in upgrading processes with zeolites and are well-known from the FCC of petrochemical oils [62]. Demethylation (DME), demethoxylation (DMO), and transalkylation reactions such as methyl transfer (MT) are acid catalyzed and are thus observed when using acidic supports such as Al_2O_3 [71,72,74]. Coking and polymerization reactions typically occur as well, and the extent depends largely on the acidity of the catalyst support [75–78], on the temperature [79], and on the oxygenate functionality [65,67].

C-C and C-O bond cleavage is the common route for upgrading of simple oxygenates and furans, while phenols can undergo either DDO or hydrogenation (HYD) prior to deoxygenation [39,74]. The acid catalyzed reactions have previously been assigned the acronym ACI to distinguish these reactions from the HDO pathways [71,72].

Decarbonylation **Decarboxylation**	**DCO**	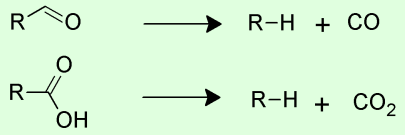
Hydrodeoxygenation	**HDO**	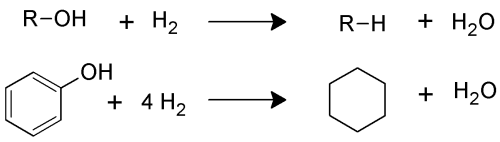
Hydrogenation	**HYD**	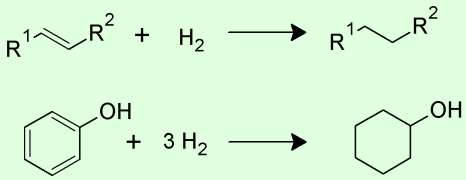
Direct deoxygenation	**DDO**	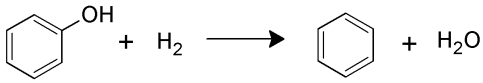
Cracking	**CRA**	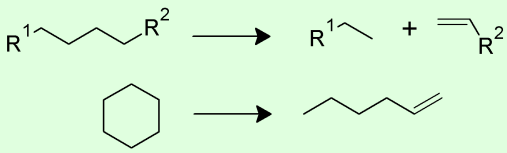
Hydrocracking	**HCR**	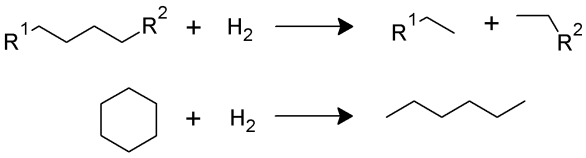
Demethylation	**DME**	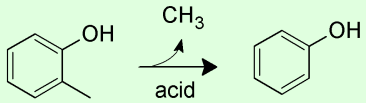
Demethoxylation	**DMO**	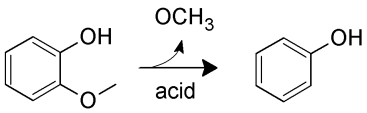
Methyl transfer	**MT**	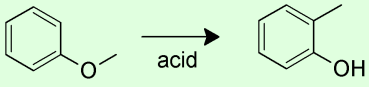

Figure 2.3: *Reactions that may occur during HDO. R denotes H, CH_3, and aromatic/aliphatic groups present in bio-oil. Drawn on the basis of [19, 48, 80].*

Due to the complex nature of the HDO reaction network, the HDO reactivity can be difficult to quantify. In a simple approach, it may be described as inversely related to the oxygen bond dissociation energy, which follows the trend Ar-OH > Ar-OR > R-OH > R-OR' (see table 2.4) [67], with Ar representing aromatic species and R representing aliphatic species.

Table 2.4: *Bond dissociation energies for breakage of C-O bonds between black carbon and red oxygen. Data from [67].*

Bond type	**Dissociation energy [kJ/mol]**
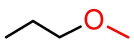	339
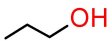	385
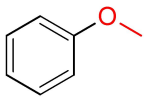	422
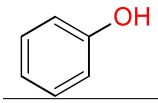	468

A more detailed reactivity scale was presented by Elliott [65](see figure 2.4) and Grange et al. [81] (see table 2.5). Figure 2.4 gives a reactivity ranking, which will depend on the catalyst identity and the thermodynamics. The iso-reactive temperature in table 2.5 is the temperature required for deoxygenation to take place, and as seen from table 2.5 it is much lower for simple oxygenates such as ketones and carboxylic acids (T_{iso} = 203 °C and 283 °C) compared to phenolic species (T_{iso} >300 °C). The activation energy for deoxygenation follows the same trend (see table 2.5).

Phenolic species are very resistant to HDO owing to the strong Ar-O bond and the stabilizing nature of the aromatic ring. Hence, they have received great attention in the bio-oil upgrading literature as will be evident in the following sections. HDO of phenolics may (depending on the choice of catalyst) require hydrogenation of the aromatic ring to facilitate deoxygenation by weakening the C-O bond, which in turn results in a high hydrogen demand. In fact, it has been questioned whether the DDO pathway is even feasible since it requires scission of a strong C-O bond [67,82]. Moreover, presence of other components in the bio-oil may hamper deoxygenation of phenolic compounds [83].

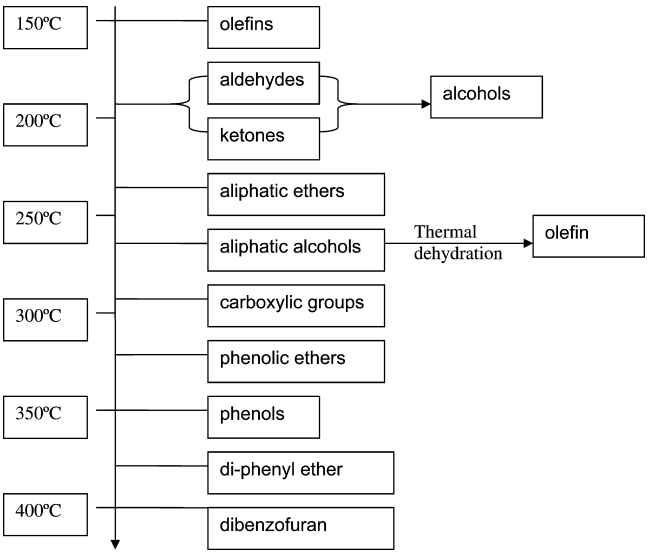

Figure 2.4: *Reactivity of oxygenates under hydrotreating conditions. Reprinted with permission from [65] (copyright 2007, American Chemical Society).*

Simple oxygenates, on the other hand, are very reactive. Aldehydes and ketones readily undergo polymerization and condensation reactions upon storage and heating of bio-oil above around 80 °C may cause undesired coke formation [84–86]. Low temperature and high H_2 pressure is typically required to stabilize such reactive species [39,87]. Simple oxygenates have received little attention in HDO studies, probably due to their high reactivity. This is in spite of their high concentration in bio-oil compared to aromatic species (see figure 2.2) and them being reactive oxygenates responsible for several detrimental properties of bio-oil (e.g. instability and acidity, and coking of catalysts and reactor plugging). Upgrading of simple oxygenates has instead been targeted through other approaches such as liquid phase ketonization and aldol condensation [88]. Cellulosic sugar (polyol) fragments such as levoglucosan and cellobiosan occur as intermediates during pyrolysis [40,89] and are among the most reactive bio-oil species owing to the high polymerization and coking tendency, which directly affects catalyst lifetime and operation stability [87].

Table 2.5: *Activation energy, E_a, iso-reactive temperature, T_{iso}, and H_2 consumption for HDO of different reactants over Co-MoS_2/Al_2O_3. Reprinted from [81] (copyright 1996) with permission from Elsevier.*

Reactant	E_a **[kJ/mol]**	T_{iso} **[°C]**	**Molar H_2 consumption [H_2/reactant]**
Ketone	50	203	2
Carboxylic acid	109	283	3
Methoxyphenol	113	301	≤6
4-methylphenol	141	340	≤4
2-ethylphenol	150	367	≤4
Dibenzofuran	143	417	≤8

Figure 2.5 shows the enthalpy of reaction and equilibrium constant for the HDO and DCO reactions of a range of the most abundant bio-oil compounds (see table 2.3). The HDO reactions (figure 2.5, R1-R4) are highly exothermic, and full conversion of an oxygenate-rich feed is correlated with the risk

of thermal runaway; especially in batch and fixed bed reactor experiments. DCO reactions (figure 2.5, R5 and R6) are less troublesome in terms of heat development and may even be endothermic as in this case for 2-butenal decarbonylation. All reactions in figure 2.5 (except for R1, see below) are spontaneous in the temperature range of 100-700 °C.

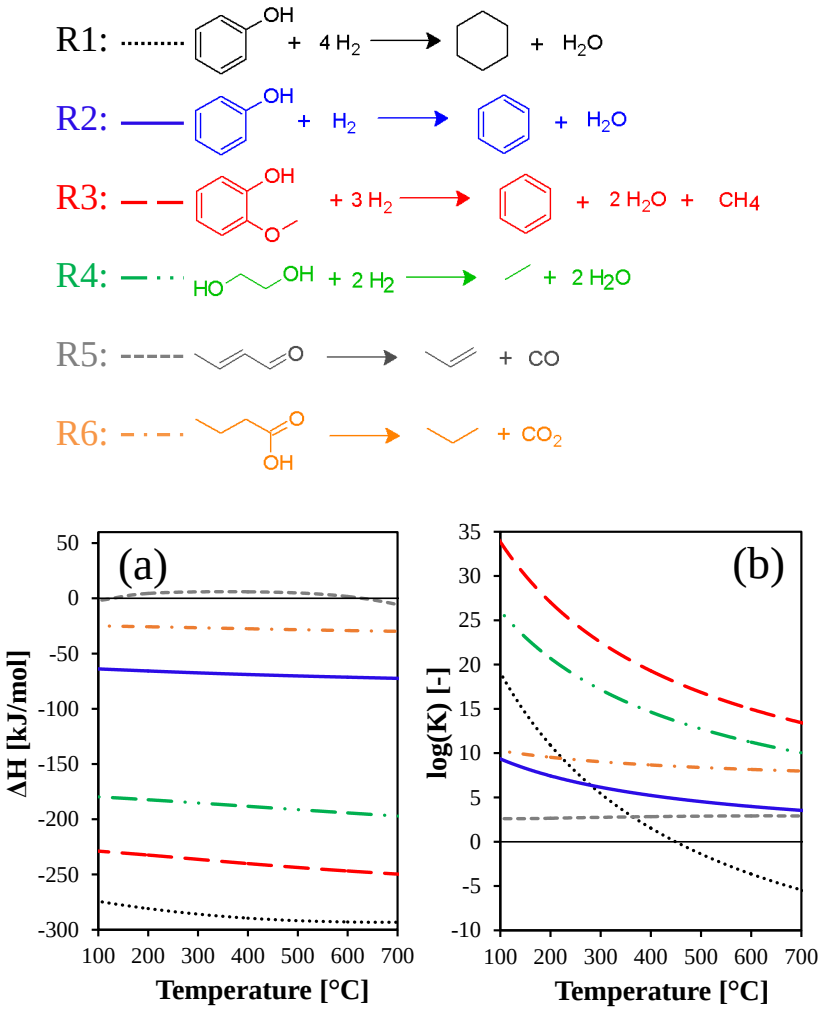

Figure 2.5: *(a) Enthalpy of reaction (per mol oxygenate reacted). (b) Equilibrium constants, K, for model HDO and DCO reactions. Calculated with HSC Chemistry.*

The selectivity towards HYD or DDO products does not only depend on the choice of catalyst but to a high extent also on the reaction thermodynamics. The DDO route for phenol HDO (figure 2.5, R2) becomes more favorable than the HYD route (figure 2.5, R1) at temperatures above $\sim$ 275 °C. At $\sim$ 450 °C, the equilibrium constant for R1 is <1; the Gibbs free energy is >0 kJ/mol, and hydrogenation of the aromatic ring is unfavorable. Similar results were obtained by Edelman et al. [90].

With the thermodynamics in mind, the consumption of hydrogen can be (partly) controlled through the choice of operating temperature and H_2 pressure. A thermodynamic calculation (using HSC chemistry) has shown that the conversion of phenol into cyclohexane (figure 2.5, R1) in H_2 at 25 bar is $\sim$ 100 % at 200-300 °C. At $>$300 °C, the conversion drops reaching 90 % at 475 °C, 60 % at 590 °C, and 40 % at 650 °C. A high temperature ($>$300 °C) and low H_2 pressure (e.g. atmospheric) will

favor the DDO path and a low hydrogen consumption. Note that the DDO path for phenolic species will require a high temperature to activate the strong arylic C-O bond.

Dwiatmoko et al. [91] studied the effect of various carbohydrate derived compounds (sugars, carboxylic acids, furans, furfurals, and aldehydes) on the HDO of guaiacol over ruthenium catalysts in a batch reactor, which was pressurized with 40 bar H_2 and then heated to a reaction temperature of 270-300 °C. Among the tested compounds, only furfural and 5-hydroxymethylfurfural affected the guaiacol conversion. They observed that the conversion of guaiacol dropped from 98 % to 28 % when the molar furfural/guaiacol ratio was increased from 0.47 to 0.96 while the yield of fully deoxygenated products decreased from 50 to 14 % over a Ru/C catalyst at 270 °C. Further increase in the furfural/guaiacol ratio lead to even lower conversion and yields. Full conversion of furfural was obtained in all cases with nearly unchanged product selectivity. The inhibition of guaiacol conversion by furfural was explained by competitive adsorption, which was supported by density functional theory (DFT) calculations of the adsorption energy. A similar observation was made by Ryymin et al. [92] for a Ni-MoS_2/Al_2O_3 catalyst, where methyl heptanoate was reported to suppress phenol conversion without the opposite being observed.

As reviewed by Furimsky [67], numerous mechanistic studies exist for the HDO of bio-oil model compounds and mainly for the conversion of phenolic species. Bui et al. [80] presented a general reaction scheme for guaiacol HDO over transition metal sulfides based on experiments with MoS_2 and Co-MoS_2 (bulk and Al_2O_3-supported) performed in a fixed bed reactor at 300 °C and 40 bar H_2 (see figure 2.6). The Al_2O_3 support was associated with DME and MT reactions, while Co promotion was associated with DDO reactions. A more detailed reaction network was presented by Runnebaum et al. [74] based on a comprehensive experimental study on the conversion of guaiacol, anisole, cyclohexanone and 4-methylanisole in a fixed bed reactor over a Pt/Al_2O_3 catalyst at 300 °C and 1.4 bar (see figure 2.7).

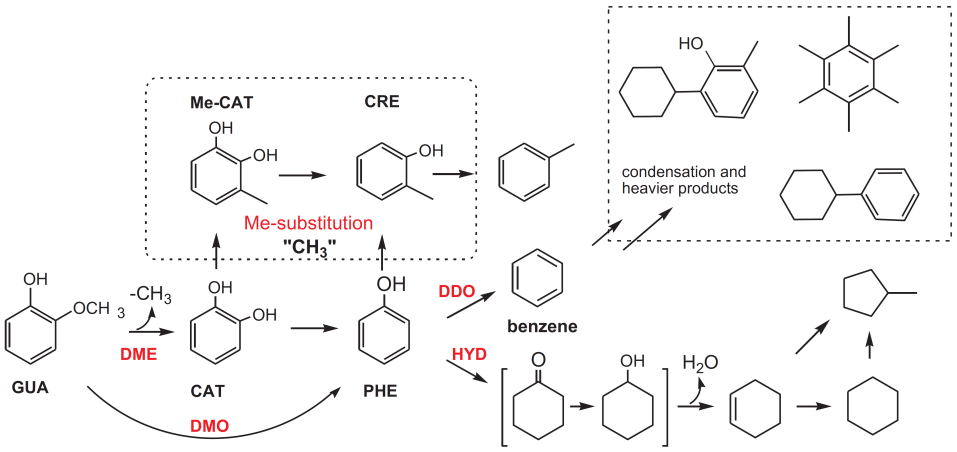

Figure 2.6: *General reaction scheme for guaiacol conversion over transition metal sulfide catalysts under H_2 pressure. Me: methyl. Reprinted from [80] (copyright 2010) with permission from Elsevier.*

As indicated by figure 2.6 and figure 2.7, the reaction mechanism for HDO of even a single bio-oil model compound is rather complex. The specific reaction mechanism will depend on the type of catalyst (incl. active phase particle size, promoters, and support), the operating conditions, and the presence of inhibitors or poisons. Therefore, a complete mechanistic and kinetic understanding of the HDO of real bio-oil will not be obtained in the near future. However, such a detailed understanding may not be necessary in order to develop an industrial scale process. This is the case for conventional hydrotreating, where global, lumped kinetic models are typically applied [63].

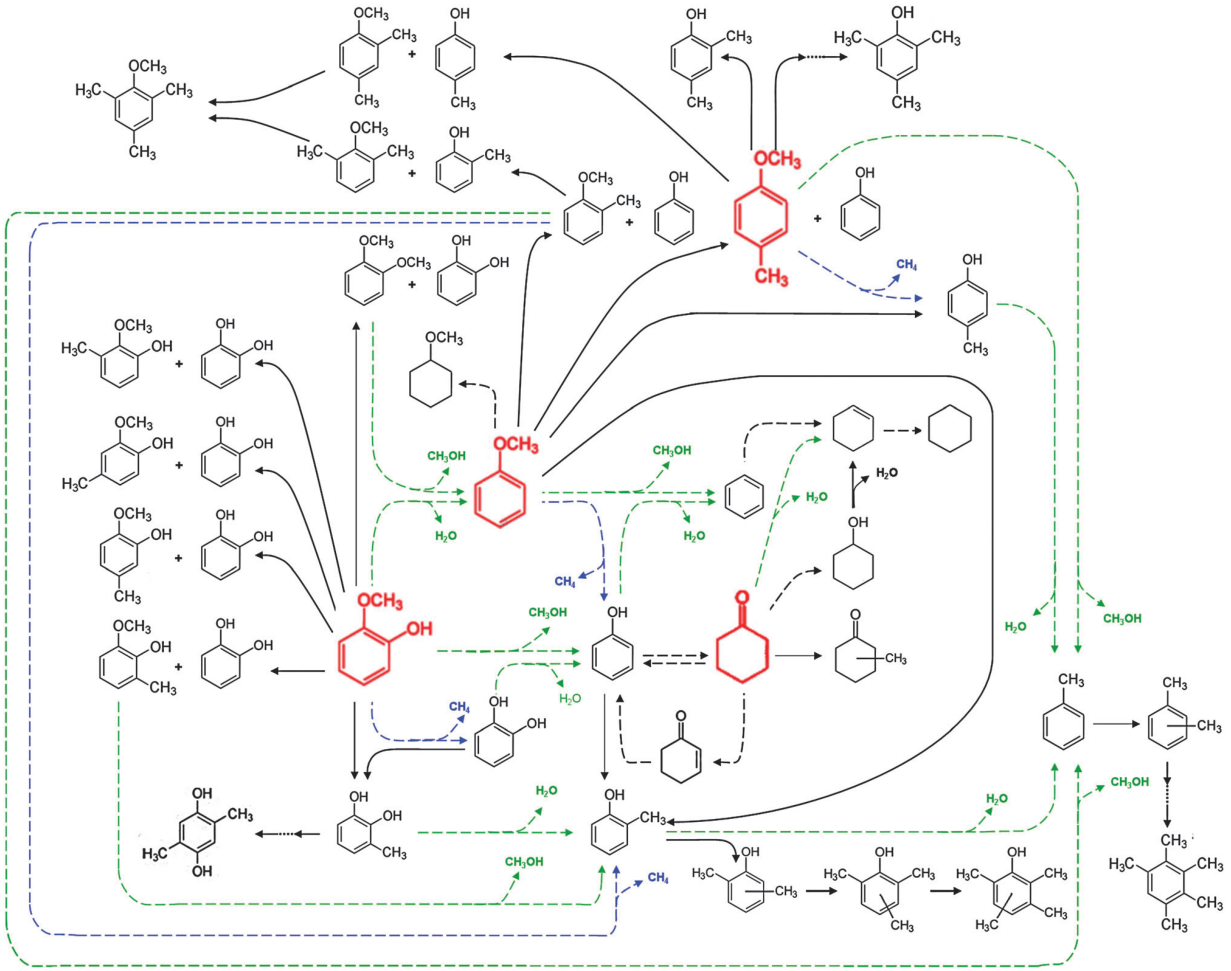

Figure 2.7: *Simplified reaction network for HDO of lignin-derived compounds. Red compounds: Reactants: Black compounds: Intermediates and products. Arrows represent reactions: HDO (dashed green), hydrogenolysis (dashed blue), hydrogenation or dehydrogenation (dashed black), transalkylation (solid black). Reprinted from [74] with permission from the Royal Society of Chemistry.*

2.3.2 Bio-oil Upgrading

An overall simplified reaction for HDO of bio-oil may be written as [21]:

$$CH_{1.33}O_{0.43} + 0.77H_2 \rightarrow CH_2 + 0.43H_2O \tag{2.1}$$

with CH_2 representing the fully deoxygenated hydrocarbon product. The reaction is exothermic with an overall heat of reaction of approximately 2.4 MJ/kg oil [93]. HDO with moderate to high degree of deoxygenation will result in two liquid phases, a low polarity upgraded oil phase and an aqueous phase. Three liquid phases may form if distinct organic phases with higher and lower density than water are formed. This was reported in the case of high degrees of deoxygenation [87, 94]. Complete deoxygenation according to generalized equations, similar to equation 2.1, have been associated with an oil yield of 56-58 wt% [95]. However, this remains a theoretical number due to the complex bio-oil composition and variety of reactions taking place (see figure 2.3). A more realistic reaction was proposed by Venderbosch [87] for a specific experiment (gas phase not included):

$$CH_{1.47}O_{0.56} + 0.386H_2 \rightarrow 0.742CH_{1.47}O_{0.11(\text{oil fraction})} + 0.192CH_{3.02}O_{1.09(\text{water fraction})} + 0.285H_2O \tag{2.2}$$

The product consisted of two phases and the oxygen content in terms of O/C ratio was decreased from 0.56 (feed oil) to 0.11 (product oil fraction). Similarly, the oxygen content in the resulting water fraction was increased compared to that in the feed oil (from 0.56 to 1.09) [87].

The efficiency of bio-oil upgrading processes can be evaluated (and compared) based on the bio-oil yield (Y_{oil}) and degree of deoxygenation (DOD):

$$Y_{oil} = \frac{m_{oil}}{m_{feed}} \cdot 100\% \tag{2.3}$$

$$DOD = 1 - \left(\frac{wt\%_{O,oil}}{wt\%_{O,feed}} \right) \cdot 100\% \tag{2.4}$$

with m being the mass of feed and produced oil, and $wt\%$ covering the fraction of oxygen in the produced oil and feed, respectively. The energy recovery of the upgraded oil compared to the feed is also a very important parameter, which is often overlooked. This is defined as:

$$Y_H = \frac{h_{oil} \cdot m_{oil}}{h_{feed} \cdot m_{feed}} \cdot 100\% \tag{2.5}$$

Here, Y_H is the energy yield, and h is the heat of combustion (MJ/kg) of the produced oil and the feed. Other parameters such as the resulting O/C and H/C ratios provide valuable information on the oil quality. Specifically for catalytic fast hydropyrolysis it has been proposed to evaluate the degree of deoxygenation in the process compared to that of uncatalyzed pyrolysis (thermal deoxygenation) [96]. Full deoxygenation (DOD = 100 %) is not necessarily the ultimate goal in bio-oil upgrading. Methanol, ethanol, and dimethyl ether have high oxygen contents (35 and 50 wt%, respectively) but are regarded as fuels of high value. Additionally, there is an inherent trade-off between the degree of deoxygenation and oil yield, in part due to the removal of oxygen. This can be seen from the representative example on yields of oil, water, and gas at varying degrees of deoxygenation from bio-oil HDO shown in figure 2.8.

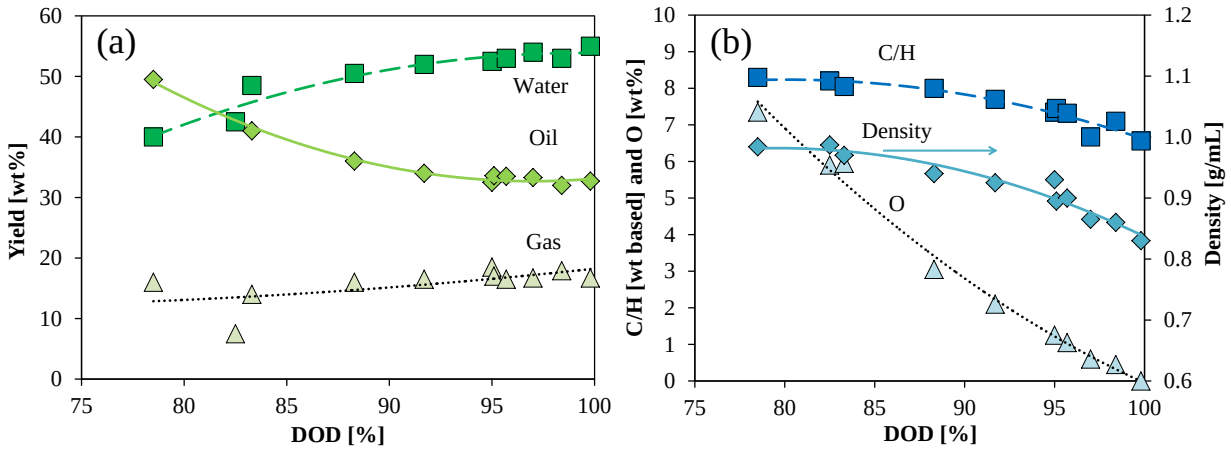

Figure 2.8: *Results from upgrading of eucalyptus bio-oil via thermal hydrotreatment (slurry reactor, DOD <83 %) and catalytic hydrotreatment (fixed bed reactor, commercial Co-MoS_2 and Ni-MoS_2 catalysts, DOD >83 %). (a) Yields of oil, water from feed+reaction, and gas. (b) C/H ratio, O content, and density. Reprinted from Samolada et al. [97] (copyright 1998) with permission from Elsevier.*

As a minimum requirement, deoxygenation should be performed to a degree, which stabilizes the oil. Further deoxygenation and incorporation of hydrogen could be targeted towards increasing the heating value sufficiently to allow for its use of the produced oil directly as a fuel (alternatively as a fuel blend), as a co-feed in petrochemical hydrotreating, or as a means of storing hydrogen in the oil. An overview of different bio-oil upgrading studies is given in table 2.6. More comprehensive reviews of HDO of both bio-oil and model compound studies are available in the literature [19, 48, 67, 68].

Table 2.6: *Updated overview of HDO studies for upgrading of bio-oil. Based on [19] (copyright 2011) with permission from Elsevier.*

Catalyst	Bio-oil source	Setup	Time [h]	P [bar]	T [°C]	DOD [%]	O/C [mol/mol]	H/C [mol/mol]	Y_{oil} [wt%]	Ref.
Co-MoS_2/Al_2O_3	Beech	Batch	4	200	350	82	0.07	1.20	26	[94]
Co-MoS_2/Al_2O_3	Beech	Batch	4	100	250	41	0.27	1.24	28	[94]
Co-MoS_2/Al_2O_3	Maple/oak	Cont.	4	≤300	370	99.9	0.00	1.82	33	[98]
Ni-MoS_2/Al_2O_3	Maple/oak	Cont.	-	≤300	370	97.2	0.00	1.79	34	[98]
Ni-MoS_2/Al_2O_3	Beech	Batch	4	200	350	74	0.10	1.24	28	[94]
Ni-MoS_2/Al_2O_3	Beech	Batch	4	100	250	37	0.31	1.48	31	[94]
Ni-MoS_2/Al_2O_3	Pine	Cont.	-	87	400	28	-	-	84	[99]
Ni-MoS_2/Al_2O_3	Pine	Cont.	168-192[c]	96	330	100	0.00	1.18	-	[100]
Ni-MoS_2/Al_2O_3	-	Cont.	6	100	300	100	-	2.1	-	[1]
Ni/SiO_2	Wheat straw	Batch	4	130-180	250	51	0.25	1.46	15	[38]
Ni/ZrO_2	Wheat straw	Batch	4	130-180	250	41	0.21	1.36	13	[38]
Pd/C	Beech	Batch	4	200	350	85	0.06	1.26	65[a]	[94]
Pd/C	Beech	Batch	4	100	250	56	0.19	1.30	44	[94]
Pd/C	Mixed wood	Cont.	-	138	340	63	0.12	1.49	62	[101]
Pt/Al_2O_3-SiO_2	Pine	Cont.	-	87	400	45	-	-	81	[99]
Pt/C	Beech	Batch	4	200	350	76	0.11	1.36	27[a]	[94]
Pt/C	Beech	Batch	4	100	250	35	0.32	1.60	57	[94]
Pt-Pd/ACP[b]	Black poplar	Cont.	6	≤65	450	-	-	-	21	[102]
Pt-Pd/FCC	Black poplar	Cont.	6	≤65	450	-	-	-	14	[102]
Ru/Al_2O_3	Beech	Batch	4	200	350	78	0.04	1.10	36[a]	[94]
Ru/Al_2O_3	Beech	Batch	4	100	250	37	0.39	1.70	23	[94]
Ru/C	Mixed wood	Cont.	-	230	350-400	70	0.11	1.48	39	[87]
Ru/C	Beech	Batch	4	200	350	86	0.06	1.24	53[a]	[94]
Ru/C	Beech	Batch	4	100	250	44	0.26	1.34	35	[94]
Ru/TiO_2	Beech	Batch	4	200	350	77	0.09	1.32	67[a]	[94]
Ru/TiO_2	Beech	Batch	4	100	250	50	0.23	1.56	37	[94]

[a] A heavy and light oil phase was obtained, results represent an average.
[b] Phosphorous containing activated carbon.
[c] Operating time at the noted conditions. Entire experiment runtime: 240 h.

As seen from table 2.6, several different catalytic systems are active in upgrading of bio-oil with the oil yield and properties depending on the catalyst system and applied operating conditions. The studies in table 2.6 were performed at a high pressure, mostly above 100 bar, and a moderate to high temperature above 250 °C. There is a general trade-off between yield and degree of deoxygenation for the obtained oil as discussed previously. Moreover, a very short operating time (<10 h) was applied in most studies, which makes it difficult to know if the obtained product yield and quality could be obtained in a long-term experiment. In fact, several experiments were terminated due to coking and reactor plugging [98,101,102]. In most of the studies, where reactor plugging was not observed, carbon deposition on the catalyst was mentioned as a main source of deactivation [38, 94, 99, 100, 102]. Sheu et al. [99] were not able to conduct an attempted experiment for HDO of pine bio-oil with a sulfided

NiW/Al_2O_3 catalyst due to rapid reactor plugging. Wang et al. [100] reported 21.4 wt% carbon deposited on a spent Ni-MoS_2/Al_2O_3 used for pine bio-oil HDO; it was however run for more than 200 h at varying operating conditions (280-350 °C and 34-97 bar H_2).

Mortensen [1] reported rapid catalyst deactivation over a commercial Ni-MoS_2/Al_2O_3 catalyst at 300 °C and 100 bar (see figure 2.9). Initially, 100 % deoxygenation could be obtained with the produced oil being clear and colorless with an H/C ratio of 2.1, similar to crude oil. This initial product primarily consisted of naphthenes and linear/branched hydrocarbons. However, rapid catalyst deactivation was observed, and after 11 h the degree of deoxygenation was down to 69 % and the produced oil looked more similar to the feed.

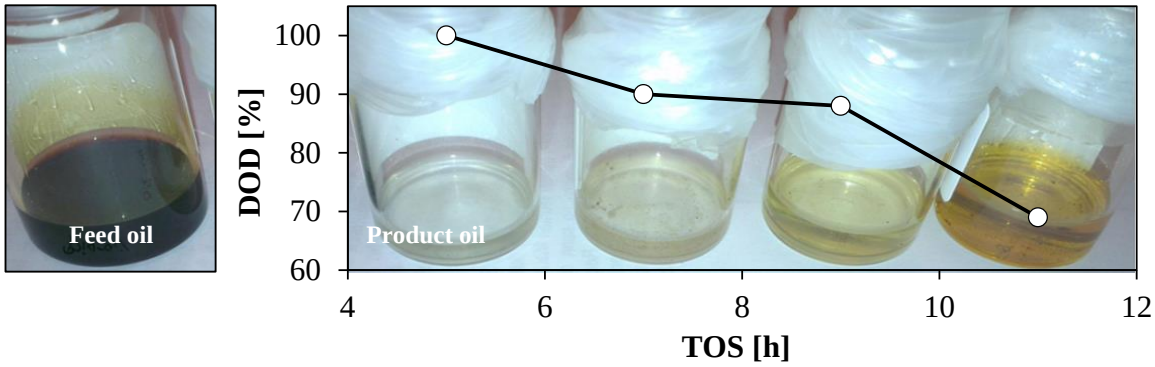

Figure 2.9: *Feed bio-oil (unknown source) and deoxygenated product oil including DOD as a function of time on stream (TOS). HDO performed in a fixed bed reactor using a commercial Ni-MoS_2/Al_2O_3 catalyst at 300 °C and 100 bar. DOD data from [1] is averaged over 2 hours.*

2.3.3 Catalysts

As summarized in table 2.6 several catalytic systems have been applied for the HDO of bio-oil. This section reviews the most widely applied catalysts for HDO, namely sulfides, oxides, reduced transition metals, and phosphides. A brief description of other catalysts is also given.

2.3.3.1 Sulfides

Co- and Ni-MoS_2 catalysts (also referred to as Co-/NiMoS or sulfided Co-/NiMo catalysts) have received significant attention in upgrading of bio-oil by HDO [70, 76, 80, 92, 94, 98–100, 103–116] based on their well-known activity in conventional hydrotreating [63]. Studies also exist on noble metal sulfides such as ReS_2 [117–119] and RuS_2 [120], but their much higher price most likely would prohibit commercial use.

Ni and Co are used as promoters as they significantly enhance the catalytic activity and stability compared to unpromoted MoS_2. Several theories have been proposed for the role of promotion as reviewed by Topsøe et al. [63]. It is now widely accepted that the role of promotion is the formation of highly active CoMoS and NiMoS phases, in which Ni or Co substitutes Mo at the edges of MoS_2 slabs [63, 121, 122]. For Co-MoS_2, it has been shown that Co has a preference for promoting the S-edge of the hexagonal Co-MoS_2 structure, whereas both a hexagonal and a less systematic distorted hexagonal structure has been reported for Ni-MoS_2 [121–123]. The slabs are stacked with the S-edge

in alternating direction as shown in figure 2.10. For NiMoS. The size and shape of the individual particles (composed of mono- and multilayer polygonal slabs) is determined by a complex interplay between catalyst composition (e.g. identity of promoter), and sulfidation conditions [122, 124–127].

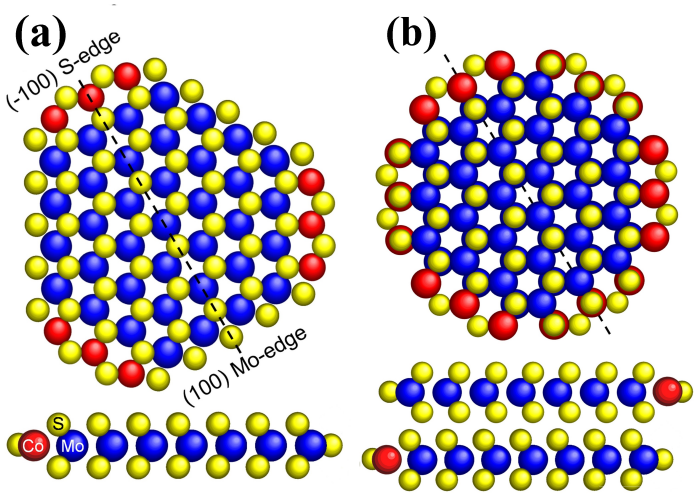

Figure 2.10: *Ball-models for the hexagonal CoMoS structure of Co promoted MoS_2 in top view and side view. Blue: Mo, yellow: S, red: Co. (a) Single slab structure. (b) Double slab structure. Reprinted from [121] (copyright 2015) with permission from Elsevier.*

The active sites for C-O (in HDO) and C-S (in HDS) scission is widely accepted to be coordinatively unsaturated sites (CUS) of sulfur at the promoted (or unpromoted) MoS_2 edge [92,128–130]. CUS can be present either as sulfur vacancies or as unsaturated sites at the sulfur terminated edge, where more sulfur (or oxygen from oxygenates) can adsorb, and this adsorption of a heteroatom may be correlated with a restructuring of the S atoms at the surface.

Romero et al. [71] studied HDO of 2-ethyl phenol over MoS_2 based catalysts and proposed the reaction mechanism shown in figure 2.11. The target oxygen atom chemisorbs to a sulfur vacancy, which has been created at a MoS_2 slab edge by reduction with H_2. SH groups generated from feed H_2 are present at the MoS_2 edges [129, 130]. They enable proton donation from S to the attached molecule, which forms a carbocation that can undergo direct C-O bond cleavage to give the deoxygenated compound [109, 129–131]. The active site is regenerated when the deoxygenated product and water are desorbed. Another mechanism was proposed for HDO of aromatic oxygenates, with initial saturation of the aromatic ring [71]. In this mechanism, two adjacent vacancies are needed in order to facilitate adsorption through a sterically more constrained flat adsorption mode, which facilitates ring hydrogenation (see figure 2.12). As opposed to the mechanism proposed by Romero et al. [71], a DFT study from Moses et al. [128] on HDS of thiophene showed that C-S scission could take place on CUS on a CoMoS edge without formation of sulfur vacancies.

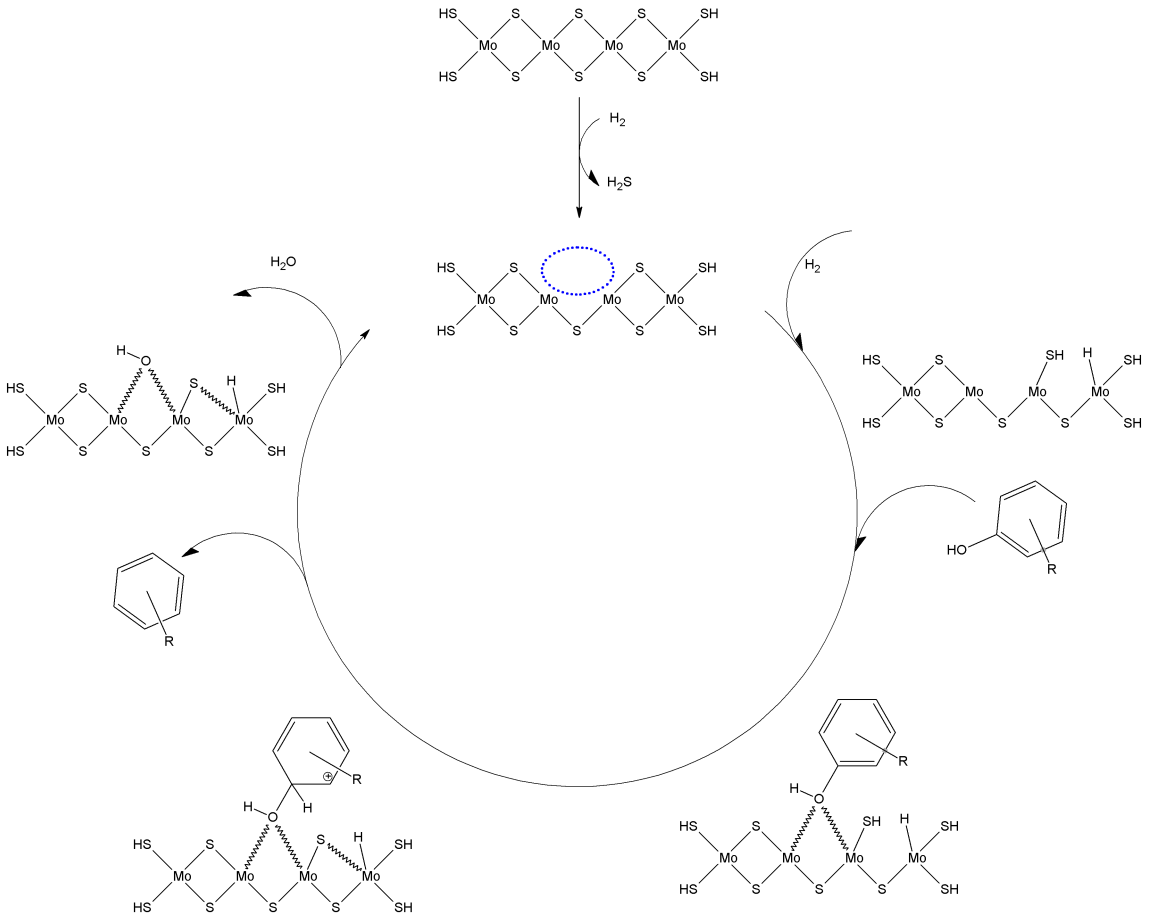

Figure 2.11: *Proposed HDO mechanism of alkyl substituted phenol over MoS_2 on sulfur vacancy active site (R denotes alkyl group). Drawn on the basis of [19] and [71].*

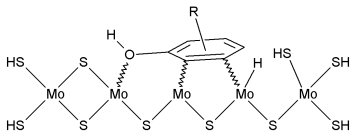

Figure 2.12: *Flat ring adsorption of alkyl substituted phenol onto MoS_2 (R denotes alkyl group). Drawn on the basis of [71].*

Based on DFT and experimental studies with thiophene, Lauritsen et al. [123, 132, 133] found that fully sulfided brim sites at edges of both NiMoS and CoMoS structures exhibit catalytic activity for adsorption and hydrogenation of thiophene. These so-called brim sites have been visualized at atomic resolution as bright brims along the MoS_2 edges using scanning tunneling microscopy (STM) (see figure 2.13). They are located at the edge of the top basal plane of a multi-slab particle and exhibit metallic character due to their electronic properties The mechanisms of HDO and HDS therefore seem to be governed by an interaction of two different active sites controlling the degree of hydrogenation (over brim sites) and desulfurization/deoxygenation (via CUS) [134]. Furthermore, it has been proposed that different types of active sites come into play in the HDO of different oxygenate functional groups [108]. The identity and nature of active sites as well as particle morphology and the exact location of promoter

atoms in Co- and Ni-MoS_2 catalysts is still debated, which can partly be traced back to the high dynamics of the catalyst system.

There are some dissimilarities between HDO and HDS. One example is the comparison between sulfur and oxygen analogues such as thiophene and furan as they interact differently with sulfur vacancies due to steric constraints [135].

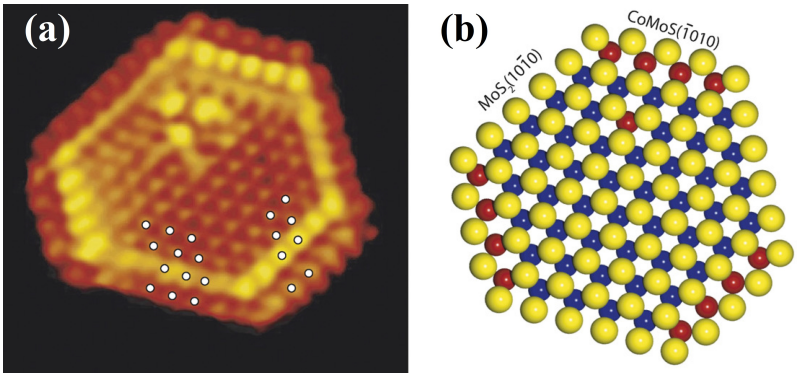

Figure 2.13: *(a) Atom-resolved STM image of a CoMoS slab on an Au(111) surface. (b) Ball-model of the slab. Blue: Mo, yellow: S, red: Co. Reprinted from [123] (copyright 2007) with permission from Elsevier.*

It is necessary to co-feed H_2S in order to the enhance activity [106,136] and avoid oxidation by keeping the sulfide catalyst systems in the active sulfided form during HDO [1,67,106,135]. Gutierrez et al. [112] proposed that H_2S co-fed in the HDO of a broad variety of model compounds is responsible for creating and retaining nucleophilic SH-groups at the sulfided catalyst surface and that these groups can activate oxygenates at the catalyst surface. However, H_2S can also be a reaction inhibitor [107–109], but the inhibiting effect depends on the oxygenate functionality and reaction mechanism [109, 110].

A concern that has been raised is that the use of sulfide catalysts for HDO results in incorporation of sulfur into the product, which contradicts the increasingly strict legislation on sulfur in fuels [37] and contaminates the otherwise sulfur scant bio-oil. It has been shown that sulfur from the catalyst surface - regardless of whether H_2S is fed to the system - can be integrated into the deoxygenated compounds and thereby end up in the product oil [109, 110, 137, 138]. However, sulfide catalysts are used industrially in HDS to remove sulfur from oil down to a few ppm [63]. Mortensen et al. [34] investigated the HDO of phenol in 1-octanol (50 g/L) over a Ni-MoS_2/ZrO_2 catalyst in a fixed bed reactor at 280 °C and 100 bar and found that at sufficient residence time, sulfur incorporation into the product could be avoided. As biomass and bio-oils contain sulfur, it is important to consider a sulfur tolerant catalyst for HDO.

2.3.3.1.1 Role of Promotion MoS_2 is typically promoted with Co or Ni, which weakens the surface metal-sulfur bond energy [139, 140] and facilitates CUS formation. Co or Ni promotion is used to enhance the overall catalyst performance; both in terms of providing better hydrogenation activity [113, 123, 132, 133] and in terms of a better stability towards oxidation [106, 135].

The activities and selectivities of Ni-MoS_2/Al_2O_3 and Co-MoS_2/Al_2O_3 in HDO are comparable according to a study of Laurent and Delmon [108], who investigated the conversion of 4-methylacetophenone, diethyldecanedioate and guaiacol in a batch reactor at 260-300 °C and 10 bar H_2. However, promotion with Ni caused a higher decarboxylation activity as opposed to Co [108]. For phenolic

species, it is commonly accepted that Co promotes DDO routes while Ni promotes HYD routes [80,109, 110,112,113,138,141,142]. In line with this observation, Co-MoS_2/Al_2O_3 seems to have a higher activity for HDO of aromatic species compared to Ni-MoS_2/Al_2O_3, while the opposite is the case for aliphatic species [109,110,136,138]. The choice of Co or Ni promotion could therefore take into consideration the feed composition (aromatic/aliphatic), but also whether the reaction gas contains CO, which has been reported to inhibit Co-MoS_2, but not Ni-MoS_2 [113]. However, the choice of temperature affects this conclusion, as thermodynamics determine whether aromatic ring hydrogenation is favorable or not (see section 2.3.1).

Bouvier et al. [113] studied the HDO of 2-ethylphenol over Al_2O_3 supported MoS_2, Ni-MoS_2, and Co-MoS_2 in a fixed bed reactor at 340 °C and 70 bar with varying H_2S concentration in the feed (0.1-0.5 bar corresponding to ∼ 1430-7145 ppm). Their results are shown in figure 2.14. The HYD and ACI activity for all three catalysts increased with increasing H_2S concentration. At the same time the DDO pathway, which primarily occurred with Co promotion, was strongly inhibited by H_2S. It was proposed that the inhibiting effect observed for Co-MoS_2 was caused by CUS saturation inhibiting oxygenate adsorption.

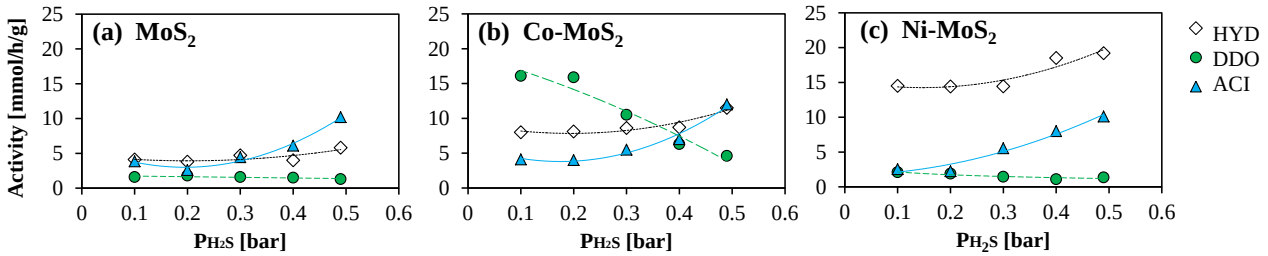

Figure 2.14: *DDO, HYD and ACI activity from HDO of 2-ethylphenol at 340 °C and 70 bar (fixed bed reactor) over promoted and unpromoted MoS_2 catalysts. Drawn on the basis of data from [113].*

The role of Ni promotion in unsupported MoS_2 was investigated by Ruinart de Brimont et al. [70] who found that the selectivity towards DCO of ethyl heptanoate at 250 °C and 15 bar (14.4 bar H_2) increased with increasing degree of Ni promotion, while HDO selectivity followed the opposite trend:

$$\text{DCO selectivity} : Ni_3S_2 > \text{Ni-MoS}_{2(\text{Ni/Mo:0.43})} > \text{Ni-MoS}_{2(\text{Ni/Mo:0.2})} > \text{Ni-MoS}_{2(\text{Ni/Mo:0.1})} > MoS_2$$

In the same study, the HDO reaction rates of heptanal had the following trend with DCO reaction rates being insignificant for all catalysts:

$$\text{Ni-MoS}_{2(\text{Ni/Mo:0.43})} \gg \text{Ni-MoS}_{2(\text{Ni/Mo:0.2})} > \text{Ni-MoS}_{2(\text{Ni/Mo:0.1})} > Ni_3S_2 \sim MoS_2$$

The reactivity was found to be more complex for heptanoic acid and ethyl heptanoate, due to competition between HDO and DCO reactions. Dupont et al. [143] used DFT calculations to study the interaction and HDO pathways of methyl propionate, propionic acid, propanal, and propanol with MoS_2 and Ni-MoS_2. They found that promotion with Ni facilitated a bidentate adsorption of propanal, which lowered the activation energy for the hydrogenation of propanal into propanol. The reaction of propanol to propane was proposed to occur via the formation of an intermediate thiol at the catalyst surface. The rate limiting step in propanal HDO to propane was the C-O cleavage in propanol, for which the activation energy was found to be lower over Ni-MoS_2 compared to MoS_2.

Based on DFT calculations, Badawi et al. [106, 135] found that a H_2S/H_2O partial pressure ratio >0.025 is necessary to avoid S-O exchanges at the S-edge of MoS_2. Promotion by Co was reported to enhance stability towards water with no S-O exchange at 100 % Co promotion at the S-edge in the partial pressure range of H_2S/H_2O of 10^{-5}-10^{2} at 350 °C [106]. This stabilizing effect was supported by transmission electron microscopy (TEM) studies showing that exposure of MoS_2 to water lead to a decrease in slab length and stacking height, which could be explained by S-O exchange. Exposure of Co-MoS_2 to water resulted in insignificant crystallite changes. The conversion of 2-ethylphenol was studied over Co-MoS_2/Al_2O_3 and MoS_2/Al_2O_3 in a fixed bed reactor at 340 °C and 70 bar with a H_2S/H_2O ratio of 0.04-0.12. Deactivation of both catalysts with decreasing H_2S/H_2O ratio by addition of water was seen, but for the Co promoted sample, the deactivation was reversible, as $>$ 90 % of the initial activity could be recovered by returning to the initial water free reaction conditions [106]. Badawi et al. [107] also used DFT calculations to assess the Gibbs free energy of adsorption of known inhibitors at 350 °C for a 50 % promoted Co-MoS_2 edge, which indicated that the inhibition strength followed a trend of $CO > H_2O \sim H_2S$.

Bui et al. [80] investigated the role of Co promotion in bulk and Al_2O_3 supported MoS_2 for the HDO of guaiacol in a fixed bed reactor operated at 40 bar H_2 and 300 °C. They found that promotion with Co enhanced overall reaction rates and the selectivity towards DDO of intermediate phenol into benzene. DME reactions were observed for unpromoted MoS_2 while Co-MoS_2 also exhibited DMO activity.

2.3.3.2 Oxides

Oxides of Mo, Ni, W, V and others have HDO activity [77, 144–148]. It has been proposed that the HDO reaction mechanism for reducible oxide catalysts follows a reverse Mars-van Krevelen mechanism (see figure 2.15) [144, 145], somewhat similar to the mechanism for sulfides proposed by Romero et al. [71] (see figure figure 2.11). This implies that low H_2 pressures are necessary to avoid reduction of the active phase into inactive species [144, 146, 147]. Low H_2 pressures are favored from an economical perspective but may pose difficulties from an upgrading perspective, where higher H_2 pressures can mitigate catalyst deactivation by coking. In this mechanism (see figure 2.15), an O-vacancy (acting as a Lewis acid site) is created by elimination of water (reduction with hydrogen) and facilitates adsorption of an oxygenate at the vacancy. The C-O bond in the oxygenate is cleaved through electron donation from Mo, the deoxygenated product is desorbed and the active site is regenerated by reaction with H_2.

No hydrogenation activity has been detected for MoO_3 [144, 148]. A revised HDO mechanism has been presented for supported MoO_3 suggesting that the support enables dispersion of MoO_x clusters with ZrO_2 and TiO_2 being capable of efficiently stabilizing Mo in the redox active intermediate Mo^{+3} and Mo^{+5} states [148].

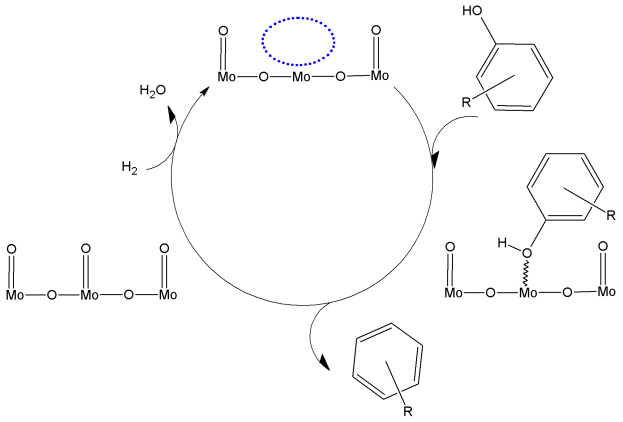

Figure 2.15: *Proposed reverse Mars-van Krevelen mechanism for HDO of alkyl substituted phenol over MoO_3 (R denotes alkyl group). Drawn on the basis of [144, 148].*

The activity of oxides in HDO relies on the presence and strength of acid sites. The Lewis acidity affects the initial chemisorption step, where the oxygen lone pair of the target oxygenate is chemisorbed at a vacancy. Brønsted acidity influences hydrogen availability at the catalyst surface in terms of the presence of hydroxyl groups. Auroux and Gervasini [149] have reported the Lewis acidity, based on NH_3 adsorption, of a broad range of oxides to follow the trends:

$$\text{Concentration of sites} : Cr_2O_3 \gg MoO_3 > ZrO_2 \sim WO_3 > Nb_2O_5 > TiO_2 > Al_2O_3 > V_2O_5$$

$$\text{Strength of sites} : Cr_2O_3 \gg ZrO_2 \sim WO_3 > Nb_2O_5 > TiO_2 > Al_2O_3 > MoO_3 \sim V_2O_5$$

The contribution from Brønsted acid sites was assumed negligible. ZrO_2, TiO_2, and Al_2O_3 are amphoteric and have been reported to have basic character as well [149]. Li and Dixon [150] reported another relative Lewis acid strength scale based on DFT calculations:

$$WO_3 > MoO_3 > Cr_2O_3$$

The Brønsted acid strength in terms of relative hydroxyl acidity was investigated by Busca et al. [151]:

$$WO_3 > MoO_3 > V_2O_5 > Nb_2O_5 > Al_2O_3 > TiO_2 > ZrO_2$$

Furthermore, the metal-oxygen bond strength should be weak enough to facilitate vacancy formation but strong enough to enable oxygenate chemisorption and C-O bond breaking. The catalytic HDO activity of MoO_3 has been ascribed to the formation of oxycarbide and oxycarbohydride phases ($MoO_xC_yH_z$) [146, 147] as well as the formation of hydrogen molybdenum bronzes (H_xMoO_3, x = 0-2) [145].

Prasomsri et al. [144] have reported HDO activity of various oxides tested for acetone conversion in a fixed bed reactor at 400 °C and <1 bar H_2. They reported the acetone consumption rate to follow the trend $MoO_3 > V_2O_5 > Fe_2O_3 > CuO \sim WO_3$ with a selectivity towards deoxygenated hydrocarbon (mainly propene - due to the insignificant hydrogenation activity) above 88 % for all oxides. Reactivation of spent MoO_3 is possible through calcination in O_2 at 400 °C [147,148]. Whiffen

and Smith [146] compared the HDO of 4-methylphenol in a batch autoclave at 41-48 bar and 325-375 °C using MoO_3, MoO_2, MoS_2, and MoP. They reported the turnover frequency (TOF) to decrease in the order MoP > MoS_2 > MoO_2 > MoO_3. MoO_3 was reduced to MoO_2 during the reaction and based on the findings of Prasomsri et al. [144, 147, 148] it can be speculated that the partial pressure of H_2 was too high to retain the MoO_3 in the active phase.

The activity of partially reduced W and Ni-W oxides supported on active carbon was investigated by Echeandia et al. [77] in a fixed bed reactor operated at 150-300 °C and 15 bar. All catalysts were proven active for HDO of phenol with the Ni-W oxide catalysts showing a significantly higher conversion compared to the W oxides. It was shown that W was fully reduced after 6 hours on stream, whereas partial reduction of Ni was achieved.

As described above, the working principle behind oxide and sulfide catalysts is a vacancy or CUS based mechanism, which means that inhibition is possible if continuous regeneration of the active site is not ensured. Water formed during HDO can oxidize the active edge of sulfides [1, 67, 106, 135] and inhibit further reaction (see section 2.3.3.1). The H_2 required for HDO can over-reduce and thereby deactivate oxide catalysts, and sulfur is a potential poison due to its strong adsorption [152, 153]. For both oxide and sulfide catalysts, it thus seems plausible that the identity of the active phase is a dynamic oxysulfide phase, and catalyst preparation and reaction conditions should be chosen to push the active phase towards the desired composition.

2.3.3.3 Reduced Transition Metals

Reduced transition metal catalysts such as Ni, Pt, Pd, Ru, and Rh are active in HYD and HDO reactions [38, 82, 87, 94, 99, 101, 154, 155]. The reaction rate increases with increasing H_2 pressure (as opposed to oxides, see section 2.3.3.2) and these catalysts do not require a feed of H_2S to remain active (as opposed to sulfides, see section 2.3.3.1). As a down-side, most reduced transition metals are highly sensitive to sulfur poisoning, which means that sulfur in bio-oil must be removed upstream of catalytic HDO [34]. This would however require either a sulfur selective adsorbent or hydrotreating over Ni/Co-MoS_2 catalysts which, as discussed above, are also HDO catalysts.

Mortensen et al. [19] proposed that HDO over transition metals relies on a bifunctionality combining the ability of oxygenate activation with hydrogenation activity. It was proposed that oxygenate activation takes place at the metal-support interface, while hydrogen donation is facilitated by the reduced transition metal [19].

A DDO reaction mechanism, in which phenol is converted into benzene by direct C-O scission, is challenged by a high bond dissociation energy (see table 2.4), as shown by DFT calculations for HDO of phenol over Rh [156]. Instead two other mechanisms have been proposed for the DDO mechanism, in which the C-O bond is weakened prior to scission (see figure 2.16). Instead of a direct C-O bond cleavage (mechanism A in figure 2.16), it has been proposed that an initial hydrogenation step at the ortho position weakens the C-O bond and that subsequent acid-catalyzed dehydration then leads to the desired DDO product (mechanism B in figure 2.16) [157, 158]. This mechanism would require a bifunctional catalyst comprising both hydrogenation activity and acid sites.

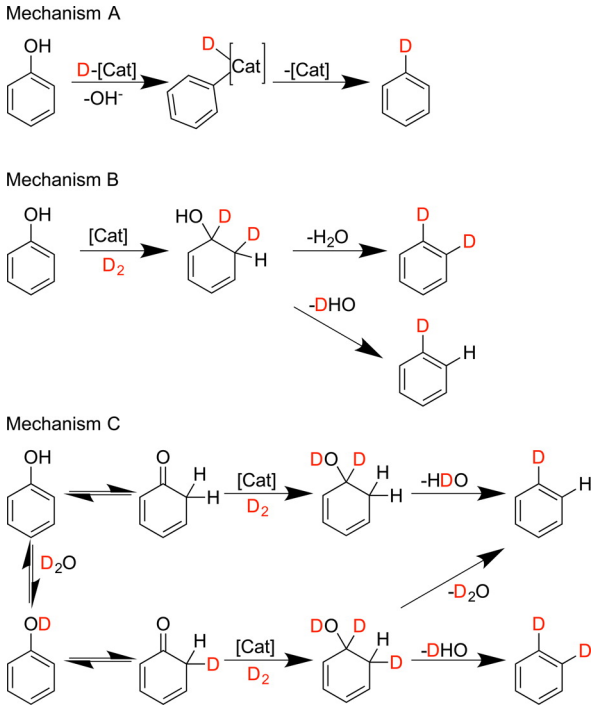

Figure 2.16: *Three proposed reaction mechanisms for DDO of phenol. Isotopic labelling indicates predicted products when using D_2 as reductant. Mechanism A) Based on direct C-O cleavage. Mechanism B) Based on initial hydrogenation followed by dehydrogenation. Mechanism C) Based on initial tautomerization followed by hydrogenation and dehydration. Reprinted with permission from [73] (copyright 2015, American Chemical Society).*

Resasco et. al [82,159–162] have recently presented a mechanism (mechanism C in figure 2.16), which is initialized by a tautomerization step, i.e. the interconversion between the enol and keto form of phenol. This proposed tautomerization step was recently supported by Griffin et al. [163] who compared the conversion of m-cresol over Pt supported on C and TiO_2. Resasco et al. [82, 159–162] have reported that the mechanism depends on the support acidity and oxophilicity. While acid sites catalyze dehydration, oxophilic sites have been proposed to facilitate interaction with the carbonyl (C=O) group present in the tautomer keto form of phenol. This interaction promotes hydrogenation of the C=O bond on metal particles at the metal-support interface. Nelson et al. [73] have recently presented a thorough experimental and theoretical study of the conversion of phenol over Ru/TiO_2, which partly supports the work of Resasco et al. [82, 159–162]. Using isotopic labelling (as indicated in figure 2.16), they confirmed the presence of phenol tautomerization. They were however not able to confirm the subsequent hydrogenation/dehydration steps as proposed by Resasco et al. (see mechanism C in figure 2.16). Instead they proposed that the amphoteric character of the TiO_2 support plays a crucial role in activating H_2O as a co-catalyst with the ability to donate and accept electrons and to lower the C-O scission barrier by donating a proton to the abstraction of the phenolic OH group [73].

As it can be inferred, there is a consensus that the mechanism of HDO over reduced transition metals depends on a bifunctionality based on the interplay between the support and active material. The reaction mechanism is however still under debate. To some extent this may be ascribed to the complexity introduced by the bifunctionality, namely the dependence of choice of catalyst active phase and support. Also, the thermodynamics (see figure 2.5) determine whether ring hydrogenation is favorable or not; an important restriction, which is often left out.

2.3.3.3.1 Noble Metals Noble metals such as Pt [74,94,99,159,164–170], Pd [82,94,101,162,163, 169,171–174], and Ru [87,91,94,159,166,175] have received significant attention in the HDO literature. Oh et al. [166] studied the HDO of *miscanthus sinensis* bio-oil over carbon supported noble metals in a batch reactor filled with H_2 to a pressure of 30 bar (room temperature) and reached a 78.2 % degree of deoxygenation over Pt/C at 350 °C. The HHV of the bio-oil was increased by 61 % during HDO and unstable sugar fragments (acetic acid, furfural, vanillin, and levoglucosan) were reported to be converted into stable compounds.

de Souza et al. [82] converted phenol (in vapor phase) over Pd/SiO_2, Pd/Al_2O_3, and Pd/ZrO_2 at 300 °C and atmospheric pressure in a fixed bed reactor. They reported the density of acid sites (Brønsted and Lewis) to follow the trend: $Pd/Al_2O_3 > Pd/ZrO_2 > Pd/SiO_2$. Compared to the other catalysts, Pd/ZrO_2 was reported to have a two times higher activity (determined as TOF), and a three times higher selectivity towards benzene. A physical mixture of Pd/SiO_2 and ZrO_2 showed similar activity to the Pd/SiO_2 catalyst, and it was therefore proposed that the higher activity of Pd/ZrO_2 was caused by interactions at the metal-support interface , which are governed by the oxophilic nature of ZrO_2. Thee positive support effect from ZrO_2 was confirmed for a Ni/ZrO_2 catalyst [82] in agreement with the work of Mortensen et al. [154]. Another approach is to use bimetallic catalysts, in which an oxophilic metal like Fe is combined with a hydrogenation active metal such as Pd [171,172] or Ni [161].

Different conclusions have been made when comparing the HDO activity of noble metals compared to conventional hydrotreating catalysts. Gutierrez et al. [169] investigated the conversion of guaiacol over various catalysts in a batch reactor at 100 °C and 80 bar. At 100 °C, the guaiacol conversion followed the trend:

$$Rh/ZrO_2 \gg Co\text{-}MoS_2/Al_2O_3 \sim Pd/ZrO_2 > Pt/ZrO_2$$

Gutierrez et al. [169] reported that the activity of the noble metal catalysts was too high for comparison of the tested catalysts at 300 °C. However, HDO was primarily observed in experiments conducted at 300 °C, whereas hydrogenation reactions were dominant at 100 °C [169], which might be explained by 100 °C being too low to facilitate C-O bond breaking.

Results from Wildschut et al. [94] are shown in figure 2.17 (see also table 2.6). They investigated the HDO of beech wood bio-oil in a batch reactor operated at mild (250 °C and 100 bar) and severe (350 °C and 200 bar) conditions over 4 h. Mild conditions only lead to a DOD of 35-56 %, while severe conditions resulted in a degree of deoxygenation of 74-86 %. Especially Ru/C and Pd/C seemed promising with an oil yield of >53 % and a deoxygenation degree >85 %. As it can be seen, the sulfided $Co\text{-}MoS_2$ and $Ni\text{-}MoS_2$ catalysts were among the poorest performing catalysts at both mild and severe conditions with lower oil yields and DOD. However, no sulfiding agent was introduced to the batch reactor to keep these catalysts in their active sulfide form.

Even though noble metals are active in HDO reactions, they are commercially unattractive due to their high price and limited availability [176]. In addition, they are highly sensitive towards sulfur [152], which is present in biomass and bio-oil (see table 2.2).

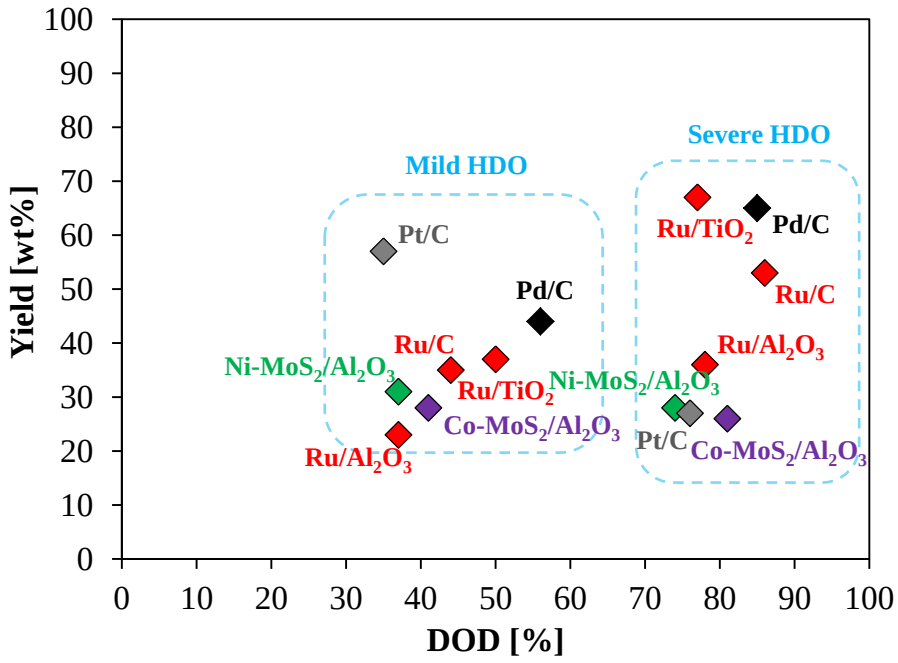

Figure 2.17: *Comparison of DOD and oil yield in HDO of beech wood bio-oil with various catalysts [94]. Experiments were performed in a batch reactor at mild (250 °C and 100 bar) and severe (350 °C and 200 bar) conditions over 4 h. All oil obtained at severe conditions (except for Ni-MoS_2/Al_2O_3 and Co-MoS_2/Al_2O_3) consisted of a heavy and a light oil fraction and hence, this data is represented as an average of both phases.*

2.3.3.3.2 Non-noble Metals A cheaper alternative to noble metals is e.g. Ni, which is the most widely applied non-noble reduced transition metal for HDO [35,38,173,177–181]. Yakovlev et al. have investigated the activity of Ni and bimetallic Ni-Cu catalysts for the HDO of anisole [178,179] and real bio-oil [182]. Selected results from the anisole conversion experiments in a fixed bed reactor operated at 10 bar and 300 °C are given in 2.18, which shows that complete deoxygenation was achieved with Ni-Cu supported on Al_2O_3 and CeO_2. Nie et al. [161] reported that the hydrogenation activity of a Ni/SiO_2 catalyst could be modified by adding oxophilic Fe, which facilitated hydrogenation of the carbonyl group in the tautomerized keto form of phenolic species, which could then be deoxygenated by dehydration.

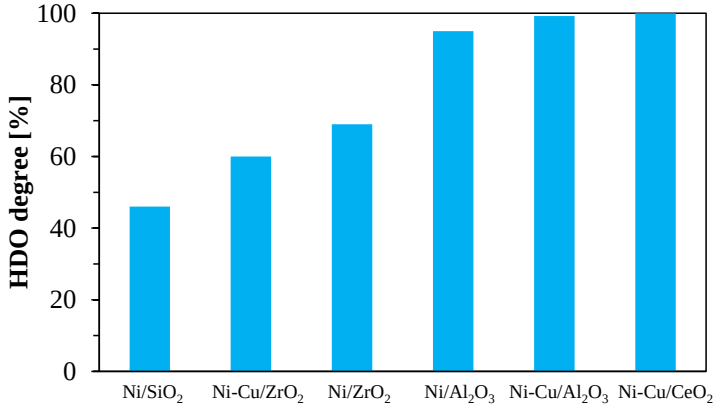

Figure 2.18: *HDO degree (selectivity for deoxygenated products) for anisole conversion over various Ni-based catalysts operated in a fixed bed reactor at 300 °C and 10 bar. Data from [178].*

Mortensen et al. [180] studied the HDO of phenol over Ni/SiO_2 in a batch reactor operated at 275 °C and 100 bar. They reported both hydrogenation and deoxygenation reactions to be dependent on the Ni particle size as shown in figure 2.19 and related the TOF to particle size as well as theoretical distribution of different metal sites (steps, corners, facets). The rate of deoxygenation of cyclohexanol to cyclohexane increased linearly with increasing dispersion (decreasing particle size), and a correlation with the fraction of exposed Ni step sites was proposed. On the other hand, the decreasing rate of hydrogenation of phenol to cyclohexanol with increasing dispersion could not be linked to the exposure of a specific type of site possibly because of the interplay with oxygen vacancies in the support as discussed above.

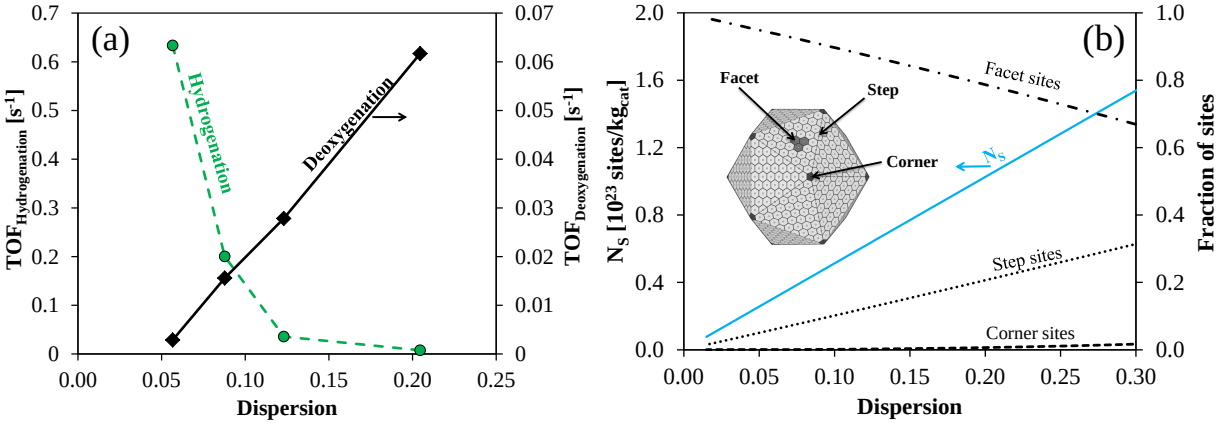

Figure 2.19: *(a) TOF of hydrogenation and deoxygenation of phenol over Ni/SiO_2 in a batch reactor operated at 275 °C and 100 bar. (b) Calculated number of sites (N_S) and fraction of different sites (facet, step, corner) on Ni icosahedron crystal. Adapted from [180] (copyright 2015) with permission from Elsevier.*

Boscagli et al. [38] reported that Ni supported on active carbon and various oxides (Al_2O_3, TiO_2, SiO_2, ZrO_2) had deoxygenation activities comparable to that of a Ru/C benchmark. The experiments were performed in a pressurized batch autoclave (80 bar at room temperature) operated at 250 °C using a wheat straw bio-oil. The O/C ratio was reduced from around 0.6 to less than 0.3 for all catalysts. The Ru/C catalyst possessed better hydrogenation activity resulting in an H/C ratio around 1.7, whereas those from the Ni catalysts were in the range of 1.3-1.5.

2.3.3.4 Phosphides

As discussed in section 2.3.3.2, Whiffen and Smith [146] reported that an unsupported MoP had higher activity for HDO of 4-methylphenol compared to the corresponding sulfides and oxides at the given reaction conditions. Metal phosphides (especially Ni_2P) have shown promising activity and stability in HDO reactions [183–187]. Additionally, there are studies on sulfided [72] and non-sulfided [185] NiMoP systems used for HDO of furans and aromatic oxygenates. Oyama and co-workers investigated the HDO activity of several phosphides (based on Ni, Co, Fe, W, and Mo) supported on SiO_2 [183,188]. For the conversion of 2-methyltetrahydrofuran in a fixed bed reactor at 300 °C and atmospheric pressure [188], MoP and WP showed the highest selectivity towards HDO products while the overall TOF decreased according to:

$$Ni_2P > WP > MoP > CoP > FeP$$

All catalysts were more active than a Pd/Al_2O_3 reference; an improvement compared to previous results [183]. Moon et al. [184] investigated the conversion of guaiacol over Ni_2P/SiO_2 at 1 and 8.1 bar of H_2 in a fixed bed reactor operated at 300 °C during 30 hours on stream. A conversion of ∼ 80 % was achieved at 1 bar while 100 % conversion was achieved at 8.1 bar. Furthermore, the conversion was reported to follow a DDO route at low H_2 pressure and a HYD route at high H_2 pressure. At 1 bar, the main product formed was benzene (∼ 60 % selectivity), while it was cyclohexane (∼ 90 % selectivity) at 8.1 bar. Slight oxidation of the active phase in the spent catalyst exposed to 1 bar was evidenced by X-ray absorption fine structure (XAFS) [184].

2.3.3.5 Alternative Catalysts

A range of other catalysts have also been investigated for the HDO of bio-oil. Transition metal carbides and nitrides (typically based on molybdenum or tungsten) have received increasing attention within the last decade. Their potential lies in their low cost, similar hydrotreating (HDN, HDS) properties as conventional sulfides [189] as well as properties, which bear some similarity to noble metals [190]. Ruddy et al. [48] have presented a detailed overview of model compound HDO studies over a broad range of traditional and alternative catalysts including carbides and nitrides. While studies on nitrides remain scarce it is clear that carbides are less attractive as they are sensitive to water [191,192], which is inevitable in HDO. There are also examples of other reaction conditions and catalyst systems in the HDO literature. These include sub- [193] and super-critical [194] aqueous phase HDO, aqueous phase HDO where a mineral acid is used to promote hydrolysis reactions [158], use of boride catalysts [195], co-feeding a hydrogen donor such as methanol [196], and more.

2.3.4 Role of Support

Investigations of the influence of catalyst support in HDO have been scattered over different catalytic systems and model compounds. The role of the support depends on the catalyst system (e.g. reduced transition metals or sulfides) and on the identity of oxygenates subject to HDO (i.e. reaction mechanism).

In conventional hydrotreating, γ-Al_2O_3 is the prevailing support [63]. In HDO, however, Al_2O_3 has a number of undesired properties. The large concentrations of water present in bio-oil, and formed during HDO, can convert γ-Al_2O_3 into boehmite (AlOOH) [87, 197]. This decreases the activity as the transformation into boehmite can trap crystals of the catalytically active material in the support lattice [197]. Furthermore, the high acidity of Al_2O_3 results in high coke formation propensity. Popov et al. [75] linked the acidity of Al_2O_3 with a high carbon formation affinity through saturation studies using a phenol/argon flow where 2/3 of Al_2O_3 was covered with phenolic species at 400 °C.

The acidity of various supported Ni catalysts was measured by Mortensen et al. [154] by NH_3 chemisorption and was seen to follow a decreasing trend as follows:

$$\begin{aligned} Ni/Al_2O_3 \geq Ni/ZrO_2 \geq Ni/CeO_2 > Ni\text{-}V_2O_5/ZrO_2 > Ni/MgAl_2O_4 > Ni/CeO_2\text{-}ZrO_2 \\ \gg Ni\text{-}V_2O_5/SiO_2 > Ni/SiO_2 > Ni/C \end{aligned}$$

The HDO of phenol at 275 °C and 100 bar H_2 revealed a non-straight forward relation between catalyst acidity and HDO activity. Instead, Mortensen et al. [154] found a correlation between metal-oxygen (M-O) bond strength and catalyst hydrogenation activity (see figure 2.20). This was explained by a weak M-O interaction giving rise to the formation of O-vacancies that in turn act as Lewis acid

sites [198, 199]. The deoxygenation activity (for phenol) was concluded to take place on the Ni metal sites and therefore be independent on O-vacancy formation.

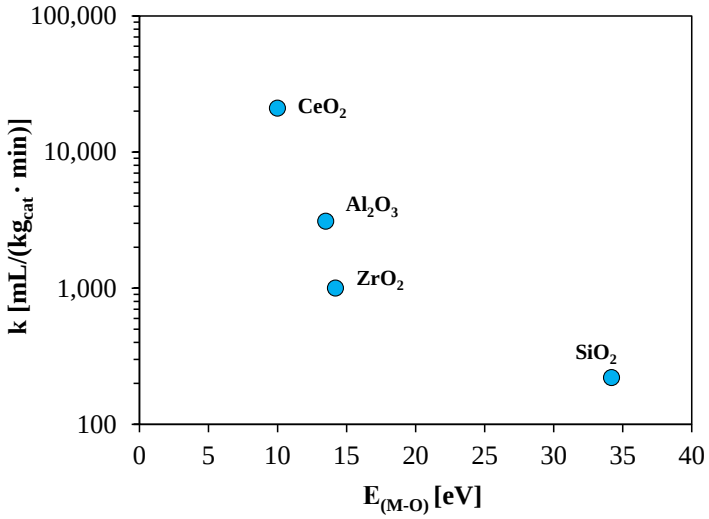

Figure 2.20: *Hydrogenation activity (rate constant, k) of supported Ni catalysts as a function of metal-oxygen bond strength, $E_{(M\text{-}O)}$, of support material. Hydrogenation activity: phenol conversion in autoclave at 275 °C and 100 bar H_2 from [154]. $E_{(M\text{-}O)}$ data from [198]. Adapted with permission from [154] (copyright 2013, American Chemical Society).*

Contrarily, Lee et al. [157] reported that the catalyst acidity and HDO activity for guaiacol conversion in a batch autoclave at 250 °C and >40 bar H_2 followed the same trend for a noble rhodium catalyst, where NAC refers to nitric acid treated carbon black:

$$Rh/SiO_2\text{-}Al_2O_3 > Rh/Al_2O_3 > Rh/NAC > Rh/ZrO_2$$

Carbon has been proposed as a promising support [76–78, 94] due to its low acidity and thereby low coke formation tendency [76–78]. The correlation between low acidity and low coke affinity has also been reported for SiO_2 [183], where Popov et al. [75] showed that the concentration of adsorbed phenol on SiO_2 only was 12 % relative to the concentration on Al_2O_3 at 400 °C. While phenolic species were concluded to only interact with SiO_2 via hydrogen bonds, dissociated species were strongly adsorbed on Al_2O_3 acid sites [75, 200]. Another study concluded that both Ni/Al_2O_3 and Ni/AC caused a lower degree of deoxygenation compared to Ni/SiO_2 due to a respectively too strong and too weak interaction between support and anisole at 180-220 °C and 5-30 bar H_2 [177]. High acidity micro- and mesoporous materials such as hierarchical zeolites and alumina doped silicates have been applied as HDO catalyst support [201–203]. As mentioned, zeolites, which are commercially used in the FCC process [62], typically have a high cracking activity, which may limit the potential oil yield.

ZrO_2, CeO_2, and ZrO_2-CeO_2 mixtures have received attention as promising support materials [82, 111, 154, 162, 165, 169, 178, 186, 204–207]. These oxophilic carriers can potentially activate molecules for HDO on the catalyst surface [82, 178, 207]. CeO_2 is additionally known to be a versatile support with redox sites (oxygen storage and exchange) and acid-base sites [208]. Recent studies on ZrO_2 have proposed that the monoclinic crystal phase (m-ZrO_2) has a higher propensity of forming catalytically active O-vacancies than the tetragonal phase (t-ZrO_2) [209]. It was however pointed out by de Souza

et al. [160] that the reaction rate of the deoxygenation step considered by Foraita et al. [209] was independent on ZrO_2 morphology. In their studies [160], they found that the t-ZrO_2 had more oxophilic sites compared to m-ZrO_2, which promoted deoxygenation.

SiO_2, ZrO_2, and TiO_2 carriers have been shown to promote an HDO reaction route for phenols, which involves a tautomerization step (see section 2.3.3.3) and it has been proposed that the HDO activity can be tuned through the support oxophilicity [73,82,159–161,163]. For MoO_3, which is active in HDO at low H_2 pressures, it was shown that the support plays an important role in stabilizing redox-reactive Mo oxidation states [148] (see section 2.3.3.2).

Wu et al. [186] investigated the conversion of guaiacol in a fixed bed reactor at 300 °C and atmospheric pressure over Ni_2P supported on Al_2O_3, ZrO_2, and SiO_2. The activity declined in the order $Ni_2P/ZrO_2 > Ni_2P/Al_2O_3 > Ni_2P/SiO_2$. The adverse properties of SiO_2 were elaborated by Moon and Lee [187], who performed a combined activity and *in-situ* XAFS study on the HDO of guaiacol over supported Ni_2P. Experiments conducted in a batch reactor at 30 bar and 300 °C showed that while AC and ZrO_2 supported catalysts had a stable conversion over time, Ni_2P/SiO_2 experienced significant deactivation. XAFS studies revealed that SiO_2 was very sensitive to water and via its hydrophilic character facilitated oxidation of the active phase to nickel phosphate [187].

Bui et al. [111] investigated the conversion of guaiacol over MoS_2 and Co-MoS_2 supported on ZrO_2, TiO_2, and Al_2O_3 in a fixed bed reactor operated at 300 °C and 40 bar H_2. Al_2O_3 catalyzed demethylation and methyl substitution reactions at a rate 7 times higher than for the other supports. The HDO activity of Co-MoS_2/ZrO_2 per Mo atom was four times higher than that of Co-MoS_2/TiO_2 and Co-MoS_2/Al_2O_3, while MoS_2 on both ZrO_2 and TiO_2 had an activity two times that of MoS_2/Al_2O_3. Co-MoS_2 on ZrO_2 and TiO_2 was stable for >60 h operation while a constant deactivation was seen for Co-MoS_2/Al_2O_3. The adverse effects of Al_2O_3 were ascribed to its high acidity, which was expected to enhance coke formation on the catalyst surface.

It is crucial to acknowledge that the choice of support material affects the activity and selectivity of HDO catalysts and to include it in the catalyst design. Three aspects are important concerning choice and evaluation of support in HDO catalyst design:

- Propensity of carbon formation. This generally increases with increasing acidity resulting in undesired coke formation.
- The interaction between the support and bio-oil oxygenates. An activation of HDO reactants through oxygen vacancies/oxophilic sites in the support is possible.
- Stability against water and possibility for regeneration, e.g. by burning off coke at high temperatures (>400 °C).

The evaluation of catalytic HDO activity using different supports must include considerations on fundamental properties such as active phase dispersion (or particle size), surface area, and pore volume/size distribution in order to allow proper comparison of different catalysts.

2.3.5 Choice and Influence of Operating Conditions

Reaction conditions for HDO should be chosen to facilitate high catalyst activity over prolonged periods of time with minimum deactivation. In this regard, different requirements will arise depending on the feedstock and catalyst identity.

2.3.5.1 Temperature

HDO is typically carried out in the range of 250-400 °C (see table 2.6), which should favor full HDO from a thermodynamic perspective [19], see also figure 2.5. The process should be operated below ∼ 450 °C, if both deoxygenation and hydrogenation of aromatics is targeted. At higher temperatures, hydrogenation becomes unfavorable, and the exothermic nature of HDO reactions could furthermore limit the choice of temperature in a batch or fixed bed reactor as full deoxygenation could lead to generating hot spots. Additionally, coking increases with temperature, especially above 450 °C [79].

Elliott et al. [101] investigated the influence of temperature in the HDO of wood derived bio-oil over a Pd/C catalyst in a fixed bed reactor operated at 140 bar. Increasing the temperature from 310 °C to 340 °C increased the degree of deoxygenation from 65 % to 70 % but above 340 °C cracking reactions became dominant Overall, increasing the temperature from 310 °C to 360 °C had a negative effect on the oil yield, which decreased from 75 % to 56 %, and on the degree of deoxygenation which decreased from 65 % to 52 %. At the same time, the gas yield increased by a factor of three.

The change in reactivity with temperature is dependent on the bio-oil composition and reactivity of individual species (see section 2.3.1). The catalytic upgrading can be performed in a two stage continuous process to achieve high degrees of deoxygenation with limited formation of gas and coke (e.g. by cracking reactions). In dual stage HDO, a reactor operated at mild conditions below 250-350 °C, aiming at stabilizing the most reactive species, is followed by a reactor operated at higher temperatures, to facilitate complete deoxygenation of refractory phenolic species [39]. A brief review of dual stage studies was presented by Wang et al. [39]. Severe catalyst deactivation as well as coking and reactor plugging has however also been observed in dual stage HDO studies. For example, Routray et al. [47] used Ru/C at 130 °C followed by Pt/ZrP at 300-400 °C to upgrade oak bio-oil in a dual stage setup and reported that reactor plugging occurred after 55-71 h for all their experiments.

2.3.5.2 Residence Time

A fairly low liquid hourly space velocity (LHSV) of 0.1-1.5 h^{-1} (corresponding to a high residence time) is generally applied in HDO processes to obtain high degrees of deoxygenation [23,34,210]. For example, Elliott et al. [101] investigated the HDO of bio-oil over a Pd/C catalyst at 140 bar and 340 °C and observed that the oxygen content in the product oil decreased from 21 to 10 wt% when the LHSV was decreased from 0.70 h^{-1} to 0.25 h^{-1}. For sulfided catalysts, a low LHSV also helps to prevent incorporation of sulfur into the produced oil [34]. There are, however, cases of a slight negative effect of a lower LHSV due to enhanced cracking and coke formation [99].

2.3.5.3 Hydrogen Pressure

A high H_2 pressure of 100-300 bar has traditionally been applied in HDO processing of bio-oil (see table 2.6). It is generally favorable in order to saturate unstable species, suppress coke formation, and ensure a high solubility of hydrogen in the oil leading to an increased availability of hydrogen at the catalyst surface [87,103]. However, recent studies have been concentrated on the HDO of model compounds at near atmospheric pressure [82,144,147,148,184,188].

It has been reported how different reactions (i.e. DDO/DCO or HYD) can be controlled through the H_2 pressure [100,174,184], which is in agreement with the thermodynamics. The thermodynamic restrictions (see figure 2.5) should always be kept in mind, as the equilibrium will determine which reaction pathways are favorable. Mortensen et al. [19] looked into the hydrogen consumption in the

HDO of bio-oil, which was studied by Venderbosch et al. [87] (see figure 2.21). The slope of hydrogen consumption increases as a function of the degree of deoxygenation, which can be related to the difference in reactivity and hydrogen consumption of different oil constituents (see section 2.3.1). For HDO of the least reactive phenolic species, a high hydrogen consumption is required (see table 2.5) as it proceeds through the HYD path, which results in a hydrogen consumption surpassing the stoichiometric demand for oxygen removal at high deoxygenation degrees. The H/C ratio of the produced oil increases when hydrogenation (saturation of double bonds) occurs. As a result, the heating value of the oil increases and it has been reported that the HHV of upgraded oil is proportional to the hydrogen consumption with an increase of 1 MJ/kg for every mol H_2 consumed per kg feed [211].

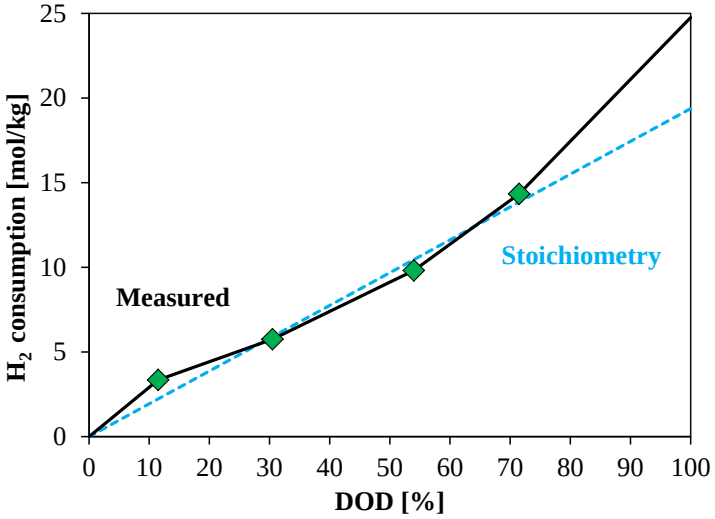

Figure 2.21: *Measured H_2 consumption as a function of degree of deoxygenation for the HDO of forestry residue bio-oil over a Ru/C catalyst operated in a fixed bed reactor at 175-400 °C and 200-250 bar including proposed extrapolation until 100 % DOD [87]. Comparison with stoichiometric requirement re-calculated with 31 wt% organic bound oxygen and a H_2:O requirement of 1 (based on [19]). Adapted from [19] (copyright 2011) with permission from Elsevier.*

2.3.6 Catalyst Deactivation

Catalyst deactivation is a key bottleneck in the development and integration of industrially robust HDO processes. Deactivation generally occurs from exposure to water and due to coking, sintering of the active phase, poisoning by nitrogen, sulfur (except for sulfides) or chlorine species, and metal deposition (especially alkali metals) [1,34,35,83,87,93,212,213]. Catalyst type and operating conditions influence the nature and severity of deactivation, but deactivation from carbon deposition and water is generally dominant in HDO catalysis.

Mortensen et al. [35] studied the influence of sulfur, chlorine, and potassium on a Ni/ZrO_2 catalyst tested for HDO of guaiacol in 1-octanol at 250 °C and 100 bar. The results are shown in figure 2.22. Sulfur (added as 1-octanethiol) caused rapid deactivation of the catalyst due to the sulfidation of Ni particles into NiS_x. Both potassium (added as KNO_3 and KCl) and chlorine (added as chloro-octane) deactivated the catalyst. For chlorine, the deactivation was shown to be reversible, as the activity could be regained after removal of chlorine from the feed. With all tested poisons being strong, it was

concluded that sources of sulfur and alkali metals must be removed from the feed upstream of any HDO unit operating with reduced Ni based catalysts. Alkali metals can potentially be removed with the ash rich char formed during pyrolysis (by filtering the pyrolysis vapors before condensation), but the gaseous sulfur compounds are more difficult to remove. Therefore, sulfur tolerant catalysts, mainly sulfides, show promise as they need sulfur in the gas to stay active.

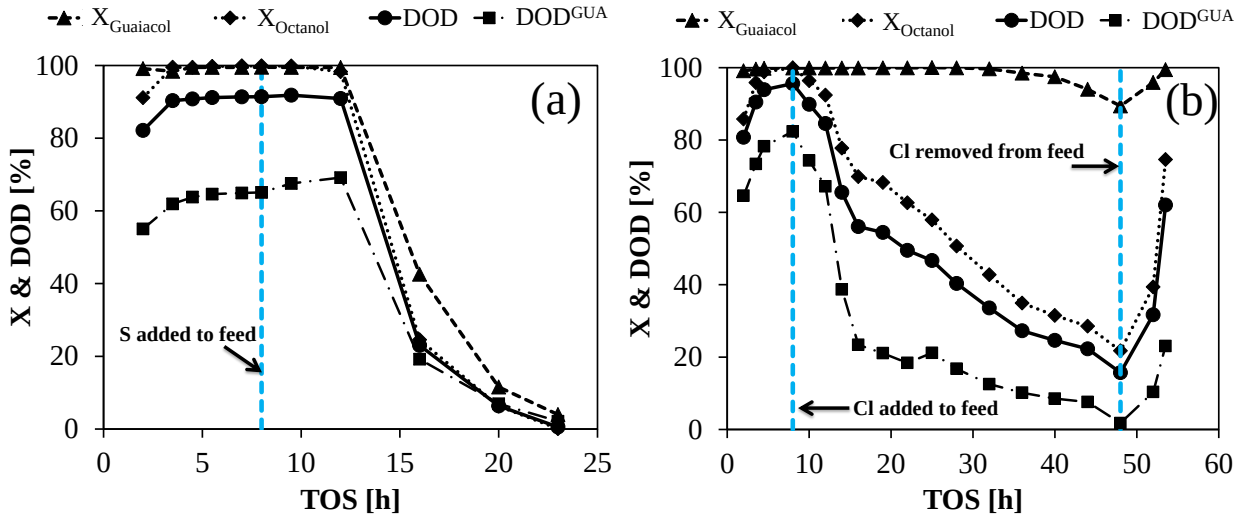

Figure 2.22: *Conversion, X, and DOD of guaiacol (GUA) and 1-octanol over a Ni/ZrO_2 catalyst poisoned with (a) Sulfur (1-octanethiol), and (b) Chlorine (chloro-octane). Tested at 250 °C and 100 bar in a fixed bed reactor. Adapted from [35] with permission from the Royal Society of Chemistry.*

2.3.6.1 Water

Water is a known catalyst poison to many catalyst systems, where it can either interact with the active phase and inhibit the target reactions or degrade the support material, e.g. by accelerating sintering processes and in the case of γ-Al_2O_3 by conversion into boehmite (AlOOH) [87, 197]. Water formed during pyrolysis of biomass is mixed into the bio-oil, and additional water is formed during the subsequent HDO due to the high concentration of oxygen in the feed. It is therefore important to develop water tolerant catalysts; an important aspect, which is often overlooked in HDO research.

For sulfide catalysts, there is a risk that water may saturate active sites (CUS) through chemisorption, which limits oxygenate adsorption and thereby inhibits HDO. As mentioned in section 2.3.3.1, Badawi et al. [106,135] performed DFT calculations showing that a partial pressure ratio of $H_2S/H_2O > 0.025$ is needed to avoid S-O exchanges at the S-edges of MoS_2, while 100 % Co promotion at the S-edge inhibited S-O exchange in the H_2S/H_2O range of 10^{-5}-10^{2} at 350 °C [106]. However, as mentioned by Şenol et al. [136], contradictory conclusions on the effect of water have been presented in the literature. In order to understand the influence of water on HDO, it is important to apply both theoretical and analytical tools (as in [73] and [106]) as well as being able to distinguish between the influence of water from those of other parameters such as operating conditions (e.g. H_2, H_2S, temperature), feed identity and catalyst support.

Looking into the other catalyst classes, phosphides operated at low H_2 pressures are oxidized by water and lose their activity [184]. Carbides have also been reported to deactivate as a function of water

induced oxidation [1]. Oxide catalysts may be subject to active site saturation in a similar manner as sulfides with the difference that oxides cannot be treated with H_2S to remove water from the active phase. For MoO_3, it has been indicated that deactivation by water can be mitigated by controlling the ratio of H_2/H_2O [144,145]. However, this ratio must be carefully controlled, as oxides can only be exposed to a low (near or sub atmospheric) H_2 pressure in order to avoid reduction [146,147].

2.3.6.2 Carbon Deposition

Carbon formation occurs through polymerization condensation reactions at the catalytic surface. The resulting poly-aromatic (potentially also poly-aliphatic) species adsorb strongly to the catalyst surface and block active sites and fill up the pore volume, which in turn reduces reaction rates, especially during initial operation [212]. Fonseca et al. [214,215] reported that carbon occupied about one third of the total pore volume of a Co-MoS_2/Al_2O_3 catalyst used for hydrotreating after an initial deposition stage and that the subsequent carbon deposition was limited.

The reaction rates of carbon formation depend strongly on the feed, but process conditions can be controlled to reduce carbon formation. Unsaturated hydrocarbons such as aromatics and alkenes have a high affinity for carbon formation as they have a significantly stronger interaction with the catalyst surface compared to saturated analogues [212]. For oxygenates, the propensity of coking is increased for compounds with more than one oxygen in its structure [212,216] while carbonyls (i.e. ketones) may polymerize through aldol condensation [217].

Carbon formation increases with increasing catalyst acidity; Lewis acidity is responsible for chemisorbing compounds to the catalyst surface, and Brønsted acidity is responsible for forming polymerization active carbocations through proton donation [212]. For HDO catalysts where the reaction mechanism involves acid sites, coke formation on these sites is critical. Additionally, organic acids (e.g. acetic acid) in the feed can catalyze thermal degradation of bio-oil constituents increasing the affinity for carbon deposition [175].

In terms of mitigating coke formation during HDO, elevated temperatures should be avoided. The rate of dehydration increases at higher temperatures leading to increased carbon formation [212]. Furthermore, H_2 can be used to stabilize reactive coke precursors. For a Co-MoS_2/Al_2O_3 catalyst, H_2 has been shown to effectively decrease carbon formation by saturating adsorbed species such as alkenes [212].

A simple model for the loss of HDS and HDO activity over a Co-MoS_2/Al_2O_3 catalyst due to coking was developed by Yamamoto et al. [218]:

$$k = k_0(1 - \Theta_C) \tag{2.6}$$

Here, k is the apparent rate constant during deactivation, k_0 is the rate constant over the fresh catalyst, and Θ_C is the fraction of active sites covered by coke. The model proposes an apparent proportional correlation between the extent of carbon deposition on the catalytic surface and the resulting degree of catalyst deactivation [212].

Weber et al. [217] proposed that coking during processing of bio-oils is dominated by gelation reactions, forming 2-D and 3-D polymers by thermally induced polymerization and aldol condensation as opposed to linear chain growth. Using gelation kinetics, they successfully modeled the increased pressure drop from carbon deposition in a dual bed setup consisting of a sulfided Ru/C catalyst operated at $\sim$ 180 °C followed by a promoted MoS_2 catalyst operated at $\sim$ 400 °C [217].

2.3.6.3 Regeneration and Activity Control

Only a few studies on regeneration of HDO catalysts have been published. However, the need for catalyst regeneration must be assessed in the development of HDO processes. If a cheap earth abundant catalyst is applied, it may simply be replaced when necessary. Such a catalyst must however be very cheap in order to make disposal, repurchase, and replacement acceptable.

For noble metal catalysts, their cost is so high that any deactivation should be mitigated. Coke deposits can be burned off in an oxidizing atmosphere, but the required temperature could induce sintering of the active metal nanoparticles, which reduces the surface area and thereby the activity. In industrial naphta-reforming, the commonly applied Pt-Re/Al_2O_3 catalyst deactivates over time due to coke deposition, contamination with impurities from the feed and loss of chlorine, which is used as a promoter for the acid function of Al_2O_3 [219]. The regeneration process includes coke burn-off followed by an oxo-chlorination step, which re-introduces chlorine into the catalyst structure and re-disperses the metal phase, which sinters during the coke burn-off [219]. A similar regeneration process may be possible for noble metal based HDO catalysts.

The remaining catalyst classes are cheap to moderately priced, and regeneration should be considered. In FCC units, continuous regeneration is ensured by letting spent catalyst run through a coke-burnoff unit upon recycling into the reactor. This could be favorable for oxide catalysts [147,148]. Prasomsri et al. [147] showed how a bulk MoO_3 catalyst used for the HDO of various phenolic compounds could be regenerated by oxidation in pure O_2 (atmospheric pressure) for 3 h at 400 °C (see figure 2.23). However, even though regeneration is possible, the catalyst lost 50 % of its activity within the 24 h test, which was caused by a combination of reduction of the oxide phase and carbon deposition. Deactivation rates at such scale may require the reaction to take place in a moving bed reactor or to have several parallel reactors in swing operation.

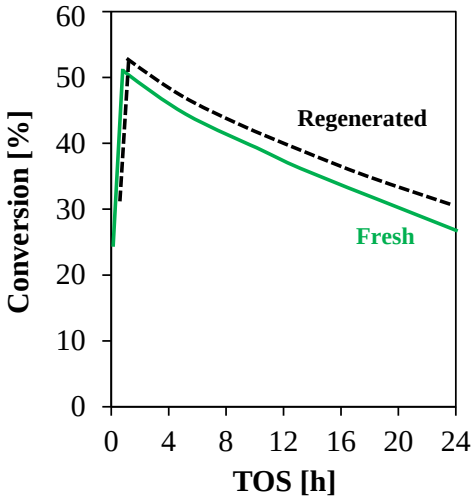

Figure 2.23: *Conversion of m-cresol over bulk MoO_3 in a fixed bed reactor at 320 °C and atmospheric pressure (0.015 bar feed, balance H_2). Regeneration by calcination at 24 h. Data from [147].*

If coke burn-off is used to regenerate sulfides, a separate sulfidation step is needed to reactivate the active phase, which is oxidized during the coke burn-off. A sulfidation step could also be used to regenerate a catalyst deactivated by water, if this is not circumvented by adjustment of the H_2S/H_2O

ratio during operation. Badawi et al. [106] exposed a Co-MoS_2/Al_2O_3 sample to water at 350 °C. This decreased the uptake of CO (a measure for sulfide active sites) measured by infrared (IR) spectroscopy at a frequency of 2072 and 2055 cm^{-1} by 28 %. It was concluded that the catalyst could be regenerated by resulfidation as the CO uptake on the resulfided sample was similar to that of the initial sample.

Industrial hydrotreating catalyst are regenerated by *ex-situ* by combustion to remove coke deposits [220]. Deactivation occurs throughout the entire catalyst lifetime, and thus, the operating conditions are used to control the catalyst activity until *ex-situ* regeneration becomes the last option to regain activity. This deactivation occurs in stages, initially by coking and in the end by pore blockage (see figure 2.24a) [212], and the overall activity can be maintained by increasing the temperature. It is important to do this in steps. If the temperature increase is introduced before sufficient deactivation has occurred, it may result in accelerated coking (see figure 2.24b) [79].

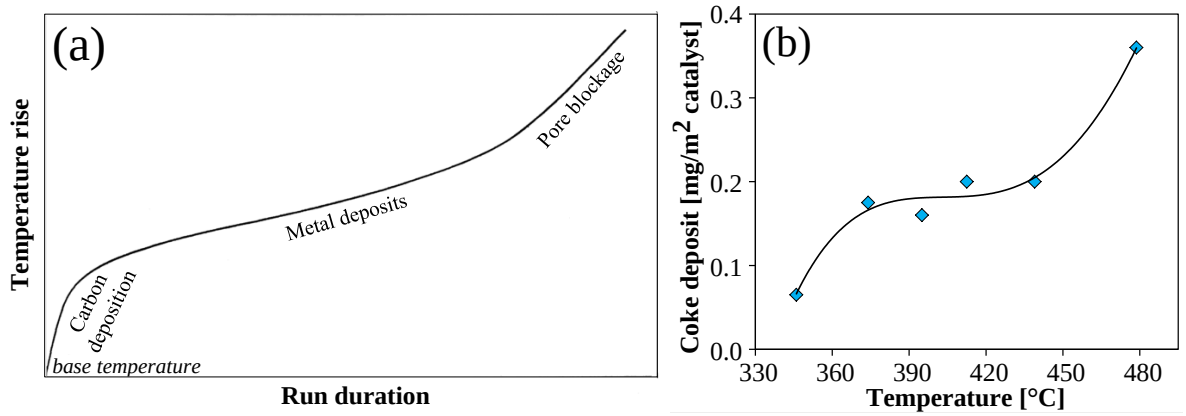

Figure 2.24: *(a) Typical temperature rise in hydrotreater as a function of run time to account for continuous deactivation, based on [212] (copyright 1999) with permission from Elsevier. (b) Temperature dependent carbon deposition on a Co-MoS_2/Al_2O_3 catalyst used for fossil feed hydrotreating, based on [79] (copyright 1979) with permission from Elsevier.*

The stability of sulfides used for HDO of bio-oil is challenged by the large fraction of water present compared to traditional hydrotreating. As described above, adjustment of the H_2S level in the feed gas should be used to keep the catalyst in the active sulfided form, so stable operation can be obtained by increasing the temperature throughout the run. This should be done until catalyst deactivation is so severe that a stable activity cannot be maintained through further temperature increase. At this time, the catalyst should be regenerated or renewed.

2.3.7 Kinetic Models

A comprehensive review on kinetic studies on the HDO of both petrochemical and biomass derived model oxygenates was provided by Furimsky [67]. Several more recent studies also provide kinetic models for the HDO of model compounds, but when it comes to HDO of bio-oil only a few kinetic studies have been performed. In this case, lumped kinetic expressions have been developed due to the complexity of the feed.

Sheu et al. [99] investigated the HDO of pine wood bio-oil over supported Pt/Al_2O_3-SiO_2, Ni-MoS_2/Al_2O_3, and Co-MoS_2/Al_2O_3 in a fixed bed reactor at ∼ 350-400 °C and 45-105 bar with a weight

hourly space velocity (WHSV) of 0.5-3.0 h^{-1}. The kinetics were evaluated based on an expression of the type:

$$-\frac{dw_O}{dZ} = kw_O^m P^n \tag{2.7}$$

Here, w_O is the mass of oxygen in the product relative to that in the feed oil, Z is the axial position in the reactor, k is the rate constant defined by an Arrhenius expression, P is the total pressure (mainly H_2), m is the reaction order for oxygen, and n is the reaction order for the total pressure. Sheu et al. [99] assumed that a first order dependency on oxygen (i.e. $m = 1$) could describe the kinetics for all three catalysts. It was then possible to fit the pressure dependency and activation energy to the data as summarized in table 2.7. With n in the range of 0.3-1.0, increased hydrogen pressure had a positive effect on the rate of deoxygenation as expected. The activation energies were found to be in the range of 45.5 to 71.4 kJ/mol with that for the platinum catalyst being the lowest. The dependency on oxygen mass fractions and axial reactor position limits the model to the specific experimental setup and feed, which makes it difficult to apply the model at a general level.

Table 2.7: *Parameters from the kinetic expression in equation 2.7 for different catalysts. Experiments were performed in a fixed bed reactor at ∼ 350-400 °C, 45-105 bar with pine wood bio-oil as feed [99].*

Catalyst	m	n	E_a
	[-]	**[-]**	**[kJ/mol]**
Pt/Al_2O_3-SiO_2	1.0	1.0	45.5±3.2
Co-MoS_2/Al_2O_3	1.0	0.3	71.4±14.6
Ni-MoS_2/Al_2O_3	1.0	0.5	61.7±7.1

A similar kinetic model was presented by Su-Ping et al. [104] who investigated the HDO of bio-oil (feedstock not stated) using a Co-MoS_2/Al_2O_3 catalyst in a batch reactor operated at 360-390 °C. The resulting kinetic expression was:

$$-\frac{dC_O}{dt} = kC_O^{2.3} \tag{2.8}$$

were C_O is the total concentration of oxygen, k is the reaction rate constant and t is the time (which includes the mass of catalyst in the reactor). A dependency on H_2 partial pressure was omitted due to a low dependency observed in the range of 15-30 bar H_2. The oxygenate reaction order of 2.3 is higher than the assumed first order dependency of Sheu et al. [99]. Su-Ping et al. [104] found an activation energy of 91.4 kJ/mol, which is also higher than the values reported by Sheu et al. [99]. Nevertheless, the complexity and diversity of bio-oil feeds as well as differences in reactor setup, choice of catalyst, and process conditions makes it difficult to compare kinetic models across various studies. For the model presented by Su-Ping et al. [104], the high oxygenate reaction order could be explained by a high initial reaction rate caused by very reactive species. As these react and disappear, a rapid decrease in the rate will be observed.

Massoth et al. [114] developed a Langmuir-Hinshelwood type kinetic model for the HDO of methyl substituted phenols over Co-MoS_2/Al_2O_3 in a fixed bed reactor at 28.5 bar and 300 °C:

$$-\frac{dx}{d\tau} = \frac{k_1 K_A x + k_2 K_A x}{(1 + C_0 K_A x)^2} \tag{2.9}$$

Here, x denotes mole fraction of phenol, whereas C_0 denotes the feed concentration. K_A is the equilibrium constant for the adsorption of phenol onto the catalyst, τ is the space velocity, and k_1 and k_2 are reaction rate constants for DDO and HYD of phenol, respectively. Nie et al. [165] presented a more complex Langmuir-Hinshelwood kinetic model for the HDO of m-cresol over a Pt/SiO_2 catalyst operated at 300 °C and atmospheric pressure in a fixed bed reactor. Their model took into account the partial pressures of m-cresol, 3-methyl-cyclohexanone, 3-methyl-cyclohexanol, toluene, methylcyclohexane, and 3-methyl-1-cyclohexene. Direct deoxygenation of the arylic C-O bond was considered through a tautomerization/secondary hydrogenation pathway as opposed to hydrogenolysis. Mortensen et al. [154] took a simpler approach for the screening of a broad range of catalysts and their activity in the conversion of phenol in a batch reactor at 275 °C and 100 bar. They used a set of global reaction rate expressions of the type:

$$r_i = k_i C_y \tag{2.10}$$

Here, r_i refers to the rate of hydrogenation of phenol to cyclohexanol ($i = 1$) and the deoxygenation of cyclohexanol to cyclohexane ($i = 2$), respectively. k is the rate constant and C_y represents the concentration of phenol ($y = 1$) and cyclohexanol ($y = 2$) in the liquid.

Clearly, working with HDO of model compounds allows for a more detailed investigation of reaction pathways and enables a more comprehensive understanding of the reaction mechanisms and kinetics over different catalysts. Setting up detailed kinetic models for HDO of real bio-oil including all possible reaction pathways is challenging due to the high complexity of the feed.

General applications of kinetic models for HDO of model compounds are obviously limited, but they can be used for screening of catalyst activity as shown by Mortensen et al. [154]. Kinetic expressions developed for the HDO of real bio-oil feeds describe the deoxygenation on an overall level, but are highly dependent on the conditions applied (e.g. feed identity, reactor configuration, and operating conditions). On the other hand, detailed mechanistic expressions developed for model compound HDO are limited to the specific model compound(s) of choice, and expanding this type of model for all bio-oil components is very complex. These compromises on accuracy and applicability of are well-known from conventional hydrotreating, where it has been shown that simple and generalized models (similar to equations 2.7 and 2.8) are useful tools in the development and optimization of catalysts and reaction conditions [63].

2.3.8 Perspectives of HDO as Upgrading Technique for Condensed Bio-oil

In section 2.2.1 it was concluded that bio-oil cannot be used as an engine fuel, partly because of its instability. This exact issue also limits the potential for HDO as a feasible upgrading technique for condensed bio-oil. The reactive oxygenates, which originate from cellulose and hemicellulose [65,67,86] cause severe coking and polymerization resulting in reactor plugging and catalyst deactivation [87], which strongly challenges the development of a continuous process. Instead, it is proposed that HDO should be performed on the pyrolysis vapors before condensation. In this way, reactive intermediates can be stabilized by HDO immediately when formed. Processes combining fast pyrolysis and HDO are reviewed in section 2.4.

Catalytic HDO studies have been focused either on upgrading condensed bio-oil or selected model compounds. Table 2.8 summarizes the advantages and disadvantages of using the one or the other type of feed. Studies on HDO of condensed bio-oil cover the complexity of working with real feeds. They enable application industrially relevant operating conditions and they use a diverse multi-compound

feed, which means that the experiments are subject to adverse phenomena such inhibition and coking, which must also be dealt with at large scale. On the other hand, model compound studies allow for catalyst development at a more fundamental stage, which is necessary in order to understand and optimize the catalyst formulation and operating conditions.

Table 2.8: *Advantages and disadvantages of performing HDO on condensed bio-oil or HDO on model compounds.*

HDO on condensed bio-oil	**HDO on model compounds**
Advantages	
HDO of a real and complex feed is performed. This gives a complex reaction network, which cannot be represented by model compounds.	Detailed reaction mechanism, thermodynamics, kinetics, and catalyst deactivation can be investigated and optimized.
Industrial-type reactor design (e.g. trickle flow) and reactant flow patterns (e.g. reactant vapor pressure) can be applied.	Feed mixture is stable upon heating and severe coking is avoided (long time on stream is possible).
Disadvantages	
Feed is too complex to track individual reactions: only overall deoxygenation kinetics and deactivation trends can be obtained.	The highly simplified feed composition does not represent real feeds. Reactions and interactions investigated are limited to the choice of reactants.
Severe coking results in rapid deactivation and reactor plugging (experiment termination).	Typically operated at other conditions (e.g. lower WHSV and hydrogen pressure) than would be required at industrial scale.

In short, both real feed and model compound studies are needed to develop and optimize industrially relevant processes that combine fast pyrolysis and catalytic HDO, with the latter performed on the pyrolysis vapors before condensation of the oil.

2.4 Combined Biomass Fast Pyrolysis and Catalytic Product Upgrading

As reviewed by Resende [221], it has been considered to perform combined fast pyrolysis and catalytic upgrading as a method for obtaining a stabilized, higher quality bio-oil, either with a catalyst in the pyrolysis reactor and/or with a downstream reactor for upgrading pyrolysis vapors before oil condensation. An overview of the possible reactor configurations is given in figure 2.25. The background for this is the adverse properties of fast pyrolysis bio-oil and the difficulties in upgrading by subsequent HDO as outlined in the preceding sections. Catalytic fast pyrolysis is typically performed in fluid bed reactors, where the bed material acts as both heat transfer material and catalyst. Reactors for downstream vapor upgrading are typically fixed bed reactors.

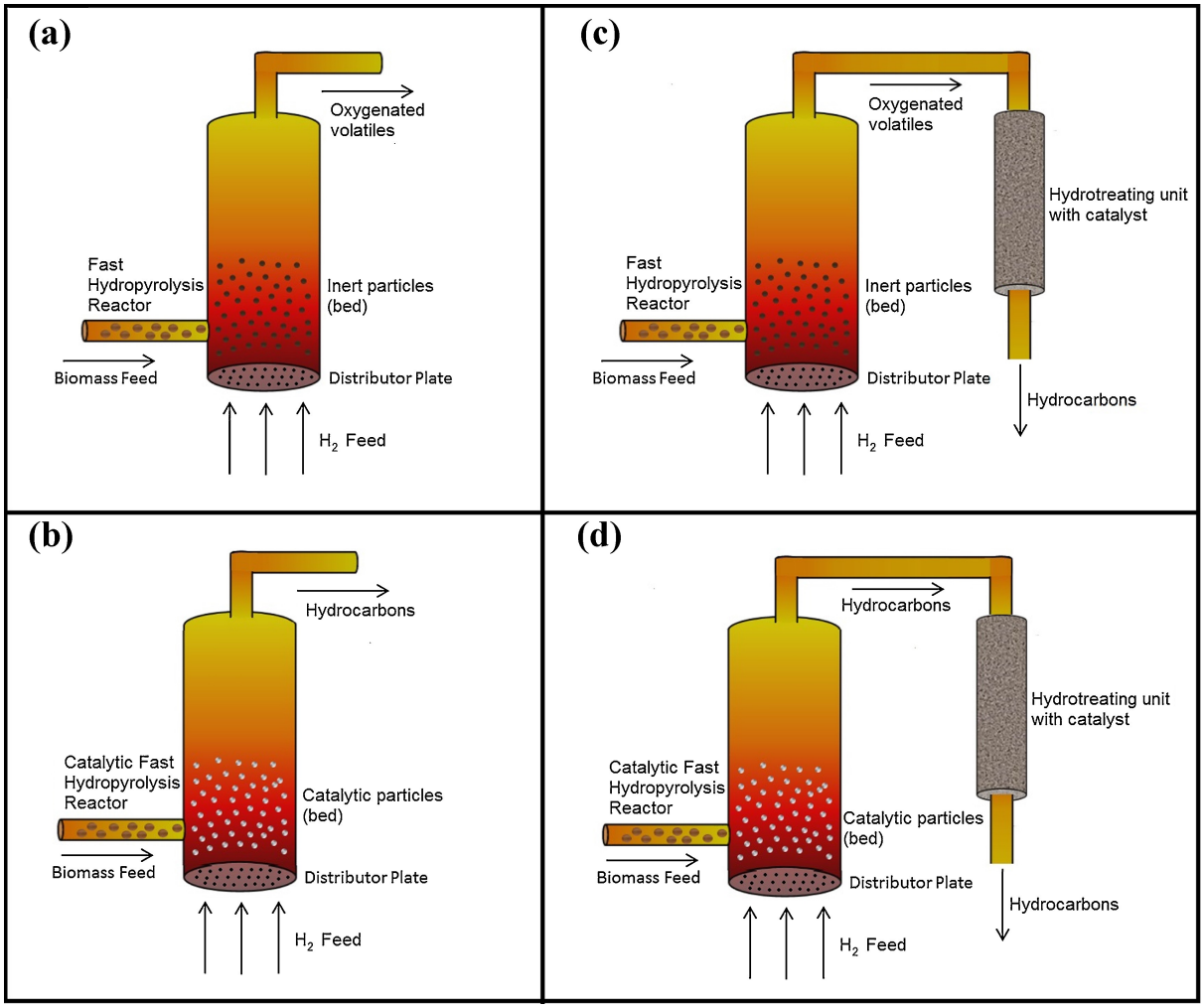

Figure 2.25: *Overview of different reactor configurations for continuous production of bio-oil via fast pyrolysis in a fluid bed reactor: (a) Fast hydropyrolysis, (b) Catalytic fast hydropyrolysis, (c) Fast hydropyrolysis and downstream catalytic HDO (fixed bed) on pyrolysis vapors, (d) Catalytic fast hydropyrolysis and downstream catalytic HDO (fixed bed) on pyrolysis vapors. Reprinted from [221] (copyright 2016) with permission from Elsevier.*

Catalytic fast pyrolysis at atmospheric pressure and without hydrogen addition has been intensively investigated using zeolite catalysts for cracking the bio-oil to achieve lower oxygen content (around 24 wt%) and higher aromatic content compared to standard fast pyrolysis [96]. Such a bio-oil is easier to upgrade by HDO. However, as discussed by Venderbosch [96], the product of catalytic fast pyrolysis is either a low yield of bio-oil and high yield of char, with low energy recovery in the oil, or a bio-oil resembling non-catalytic fast pyrolysis bio-oil.

Another method, which is aimed at achieving both deoxygenation and fast pyrolysis in one step, is fast hydropyrolysis, in which the gas is changed from an inert to H_2 or partial H_2 (scenario *a* in figure 2.25). If an HDO catalyst is present in the reactor it is called catalytic fast hydropyrolysis (scenario *b* in figure 2.25). Catalytic fast hydropyrolysis is often performed at elevated pressure to increase the driving force for HDO. This approach has been more successful in achieving both high energy recovery and bio-oil with low oxygen content [96]. Both non-catalytic and catalytic fast hydropyrolysis can be coupled with downstream HDO, performed in a fixed bed reactor, for vapor phase product upgrading

(scenario *c* and *d* in figure 2.25).

The different concepts in figure 2.25 each have their advantages and disadvantages. An advantage of not having a catalyst in the pyrolysis reactor (scenario *a* and *c*) is that the optimal temperature of $\sim$ 500 °C for fast pyrolysis (see Table 1) [21] can be applied without having to also consider what might be optimal for the catalytic HDO reaction. Note, however, that without the HDO catalyst, the H_2 used in fast hydropyrolysis typically does not enable significant HDO [222–225]. Therefore, the advantage of *in-situ* HDO is not obtained here, and it becomes crucial to have a short residence time before the downstream HDO reactor to avoid secondary reactions. For concepts with a catalyst in the fluid bed (scenario *b* and *d*), the choice of catalyst becomes crucial; a too reactive catalyst may crack all species to light gases, and no oil phase is formed. This was observed by Dayton et al. [226] using a commercial hydrotreating catalyst (pre-reduced). Initially, mostly gaseous products were obtained, but due to catalyst deactivation a liquid product was obtained after $\sim$ 20 hours on stream.

2.4.1 Perspectives of Fast Pyrolysis with *Ex-situ* and *In-situ* Hydrodeoxygenation

Several pilot scale concepts of combined fast pyrolysis and HDO have been investigated [222–224,226–235]. Overall, it appears that to realize biomass to hydrocarbon fuels using a fast pyrolysis based process, fast hydropyrolysis at elevated pressure using a high partial pressure of H_2 is a very promising method. Most likely the pyrolysis step will have to be catalytic and downstream vapor HDO is necessary to achieve a product with low oxygen content. Alternatively, oil condensed after catalytic fast hydropyrolysis may be co-processed in a refinery hydrotreater. There are a number of technical challenges to overcome in the scale-up e.g. feeding solid biomass to a pressurized fluid bed reactor. The catalyst formulation is highly important and questions about poisoning and mechanical degradation in the fluid bed as well as possible regeneration have yet to be answered.

Fast pyrolysis of lignocellulosic biomass produces oil with an increased volumetric heating value compared to its parent biomass. In fact, the bulk energy density can be increased by a factor of >6 through fast pyrolysis [26,27]. There is however limited direct application for this bio-oil due to the high content of oxygen which is responsible for a wide range of detrimental properties. Upgrading of this bio-oil is necessary through catalytic HDO carried out at conditions similar to conventional hydrotreating or even at lower temperatures and pressures. As reviewed in section 2.3, several studies on catalytic HDO show promising results for this technique. However, as the vast amount of research studies have shown, it seems necessary to couple fast pyrolysis and HDO into catalytic fast hydropyrolysis in order to develop a technology which can continuously convert solid biomass into liquid fuel. Otherwise, if HDO is performed on condensed oil in a separate process, coking during heating of the oil will be so severe that catalyst deactivation, low energy recovery of the oil, and plugging make the process infeasible.

It has been proposed that fast pyrolysis of biomass into bio-oil can be implemented at delocalized sites to increase the energy density and make transportation economically feasible [19,27]. Mortensen et al. [19] presented a flow sheet for this process based on the work of Jones et al. [236] (see figure 2.26) where raw bio-oil is produced at delocalized sites and subsequent upgrading is performed at a centralized plant. Here, HDO is used to upgrade the oil with a downstream recovery section similar to that applied in hydrotreating processes [62,63].

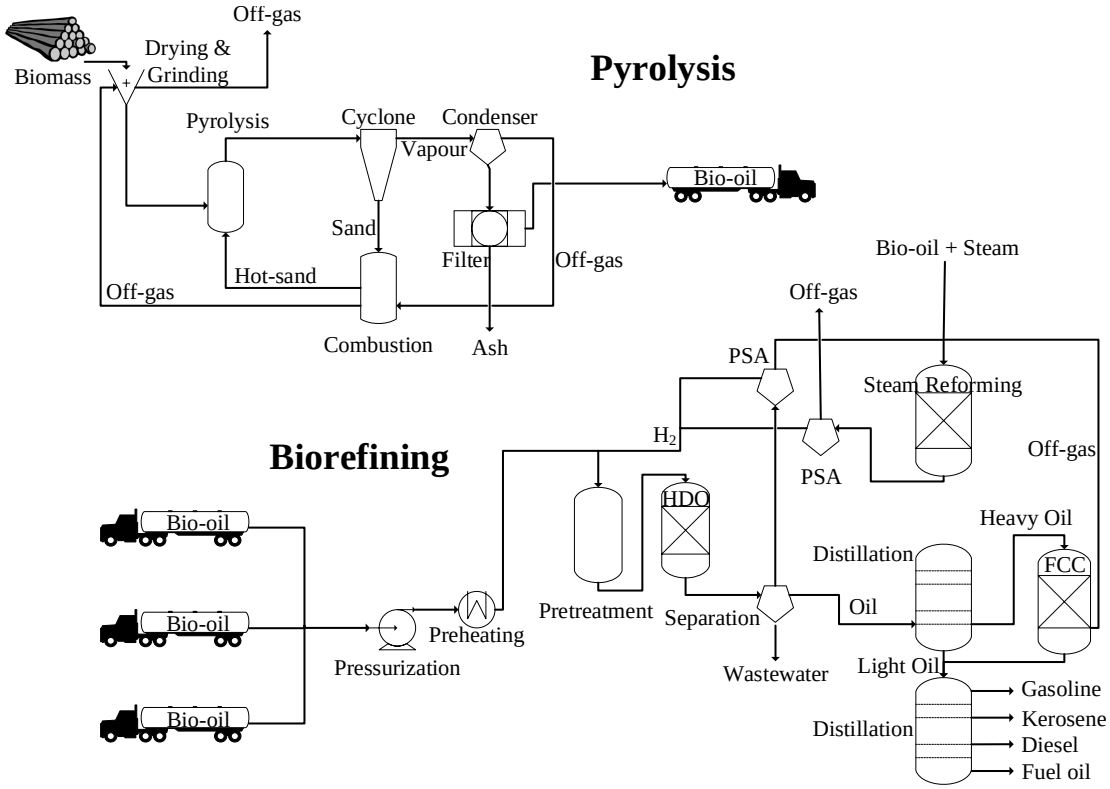

Figure 2.26: *Overall flow sheet for a proposed production of bio-fuels on the basis of catalytic upgrading of bio-oil. PSA = pressure swing adsorption. Reprinted from [19] (copyright 2011) with permission from Elsevier.*

Even with a seemingly promising process economy [236], implementation of delocalized pyrolysis plants is challenged by the instability of bio-oil, which cannot be reheated as required for subsequent HDO without severe coking and polymerization. This challenge can be overcome by performing the pyrolysis as catalytic fast hydropyrolysis followed by transport of the stabilized bio-oil to centralized plants for upgrading to fuel grade oil. This partly upgraded bio-oil could also be transported to already existing oil refineries, where it could be co-processed with fossil feeds. This would eliminate the need for construction and commissioning of new plants.

Centralized plants are more favorable in terms of the H_2 requirement, which is significant for both catalytic fast hydropyrolysis and catalytic HDO, and it becomes clear that there are several challenges to overcome in the development of a commercially attractive process. One option is to use reforming to convert light gasses produced in the fast hydropyrolysis (C_{1-3} hydrocarbons) into CO_2 and H_2 which can then be fed to the pyrolysis reactor. Additional H_2 could potentially be produced sustainably from electrolysis of water using electricity from wind and solar power, but it requires progress in the development of electrolysis cells [10, 237]. H_2 could potentially also be produced from the gasification of char. Another utilization strategy for the light gasses could be conversion into synthetic natural gas (SNG) by methanation.

Techno-economic analyses or life cycle assessments (LCAs) can be used to evaluate whether a process is economically viable and allows for comparison of different processes. Such analyses have been performed for various fast pyrolysis and catalytic upgrading processes, for example stating that transportation of solid biomass is viable within a radius of $<$170 km [26]. As these analyses are based on a complex network of data and assumptions (i.e. agricultural yields, energy prices, process efficiencies,

and yields), it is recommended to interpret the results with caution, especially if an uncertainty and sensitivity analysis is left out.

It must be considered what type of product the combined fast pyrolysis and bio-oil upgrading should produce. Table 2.9 gives an overview of the oil properties achieved by different methods. Even though HDO on condensed bio-oil produces an oil with a low oxygen content and high energy content, the instability of condensed bio-oil is a critical drawback. Instead, catalytic fast hydropyrolysis produces an oil similar to the HDO oil [233] but with the possibility to operate the process continuously for several hundred hours [238]. If the catalytic fast hydropyrolysis is coupled with downstream HDO, the produced oil is further upgraded; the oxygen content is markedly decreased while the contents of carbon and hydrogen are increased.

Table 2.9: *Comparison of bio-oil properties from fast pyrolysis of wood and HDO of condensed fast pyrolysis oil with oils obtained from catalytic hydropyrolysis.*

				Catalytic fast hydropyrolysis oil	
Property	**[Unit]**	**Fast pyrolysis oil**	**HDO oil**[a]	**no HDO**	**downstream HDO**
Scenario (figure 2.25)		-	-	*b*	*d*
Refs.		[21, 22, 28–30, 36]	[87, 94, 98, 101]	[233]	[233]
Carbon	[wt%]	44-58	76-87	77-87	85-88
Hydrogen	[wt%]	5.5-7.2	9.7-13	9.6-12	11-13
Nitrogen	[wt%]	0-0.2	<0.6	0.04-0.1	0.04-0.06
Oxygen	[wt%]	35-50	0.02-14.2	0.5-14	0.7-2.2
Sulfur	[ppm]	<400	<700	300-400	100
Viscosity (40-50 °C)	[cSt]	13-100	1	-	-
Density (15-40 °C)	[kg/L]	1.1-1.3	0.83-0.93	0.82-1.0	0.78-0.86
HHV	[MJ/kg]	16-19	41-46	-	-
H/C	-	1.3-1.9	1.48-1.82	1.40-1.81	1.61-1.76
O/C	-	0.4-0.8	<0.12	<0.14	<0.02

[a] From HDO of condensed bio-oil.

The boiling point of oxygenates is higher than for fuel type hydrocarbons with equivalent carbon numbers [61]. Thus, the oxygen content should preferentially be tuned to fit the target product, which could be a range of boiling point fractions. Fuel compositions are complex [239], and it is necessary to look at the specifications for the target fuel as well as what can be achieved from the biomass and process of choice. A common goal in the literature is to go all the way from solid biomass to a high-quality liquid fuel - preferably in one step. Complete deoxygenation of bio-oil is, however, often only achieved with severe operating conditions (see e.g. figure 2.17 and table 2.6). Furthermore, as discussed above, re-heating of condensed bio-oil causes severe process issues due to coking, polymerization, and reactor plugging. Therefore, catalytic fast hydropyrolysis seems promising as reactive oxygenates can be stabilized *in-situ* when formed. It could perhaps be interesting to target a less deoxygenated product to be used as a fuel additive (similar to ethanol or methanol) or to be co-processed in already functioning hydrotreating plants.

The investigation of catalytic fast hydropyrolysis is still at an early stage and the technology needs to mature before more concrete considerations, for example based on LCAs, can be made regarding the

process economy and sustainability, and application of the product oil. Furthermore, the requirements for (fluid bed) hydropyrolysis catalysts differ from those of commonly applied HDO catalysts. Firstly, they must have a high mechanical strength in order to ensure attrition resistance during fluidization. Secondly, a moderate or even low activity could be preferential in order to avoid extensive cracking or potential generation of hot spots (in fixed bed reactors). As is the case with most other green technologies, subsidies, and political initiatives will be very important in order to facilitate the development of an economically feasible process for the continuous conversion of solid lignocellulosic biomass into transportation fuel grade oil.

2.5 Conclusions and Outlook

The global society is facing challenges with global warming, depleting fossil resources, an increasing population, and a corresponding increase in energy demand. Our lifestyle depends on energy and there is a need for sustainable carbon based fuels. Lignocellulosic biomass such as wood, energy crops, straw, and agricultural waste is a renewable carbon based material that does not compete directly with food; note, however, that considerations on usage of agricultural land must be included. Fast pyrolysis is a simple and efficient way to convert solid biomass into a liquid with an increased volumetric energy density. The significant oxygen content (35-50 wt% compared to $<$0.1 wt% in heavy fuel oil) results in a heating value less than half that of conventional fossil fuels. Furthermore, as much of the oxygen is present as carboxylic acids, ketones, and aldehydes, bio-oil is acidic and unstable upon storage and heating.

Catalytic HDO is a promising technique for upgrading bio-oil, and much research has been devoted to developing and understanding catalyst systems as well as reaction and deactivation mechanisms. Particularly deactivation is a major issue in HDO, where coke deposition and exposure to high water concentrations challenge many catalysts and influence both catalytic performance and selectivity. Due to the thermal instability of bio-oil, catalytic fast hydropyrolysis with immediate product stabilization seems an alternative, promising approach compared to sequential non-catalytic fast pyrolysis and HDO on the condensed oil. However, several challenges remain, such as:

- Catalyst development for both (fluid bed) catalytic fast hydropyrolysis and downstream fixed bed HDO to optimize liquid yields: Investigation and optimization of known formulations as well as novel catalyst materials in combination with advanced experimental and theoretical tools such as DFT, TEM, STM, XAFS, and tomographic techniques.

- Better understanding of the kinetics of HDO occurring during catalytic fast hydropyrolysis including influence of impurities (e.g. alkali metals) on secondary reactions (e.g. cracking), which affect the selectivity towards HDO. Model compound studies using multi compound feeds should be employed in order to investigate how the HDO kinetics of various oxygenates are influenced by the presence of other compounds (e.g. through competitive adsorption).

- Comprehensive investigation of catalyst deactivation (attrition, poisoning, coking, phase change) by poisons abundant in biomass (alkali metals, chlorine, nitrogen, water, and sulfur) of different catalyst types to optimize catalyst performance. Catalyst deactivation should be mitigated and/or efficient regeneration methods should be developed.

- Investigation of catalytic fast hydropyrolysis of solid biomass directed at minimizing coke formation and cracking, and stabilizing reactive oxygenates. Investigation and optimization of operat-

ing conditions for catalytic fast hydropyrolysis (temperature, H_2 partial pressure, space velocity, gas flows, etc.).

- Development of new processes and reactor configurations for the continuous catalytic fast hydropyrolysis and downstream catalytic HDO including feeding of solid biomass into a pressurized reactor, catalyst regeneration and/or replacement, and integrated utilization of by-products (char, light gasses, product water, system heat). Long-term tests should eventually be performed to test the stability and robustness of the process.
- Assessment of target product(s). The operating conditions and catalyst type(s) should be aimed at the desired product composition (e.g. oxygen content in produced bio-oil) and yields (gas vs. bio-oil). The product could e.g. be a moderately oxygenated fuel additive or refinery blend-in, or an oxygen free ready-to-use fuel.

With all the work already performed on fast pyrolysis of biomass and on catalytic HDO of the condensed bio-oil, the task at hand is to combine this knowledge in the further research and development of combined fast pyrolysis and HDO processes such as catalytic fast hydropyrolysis. Combining fast pyrolysis and HDO, e.g. as catalytic hydropyrolysis, is in its industrial infancy, and there are many points to address to obtain optimized, commercially viable processes. An additional point not addressed in this work, is to find suitable sources for H_2, e.g. by solar or wind powered electrolysis of water or by reforming of light pyrolysis gasses. In terms of combining fast pyrolysis and catalytic HDO, several proof of concept studies already exist. Thus, what remains is a directed scientific, commercial, and political effort to ensure the development of an efficient route for renewable liquid fuels from biomass.

3 Experimental Work

This chapter describes the experimental setup used for catalytic activity tests along with methods of catalyst preparation and characterization. Typical operating conditions and calculations employed for activity assessment are included.

3.1 Experimental Setup

Catalytic HDO activity tests were performed using a continuous fixed bed reactor setup capable of operating up to 550 °C and 125 bar. The setup name is the Pyrolysis Oil Converter (POC) (setup 045-28 in the pilot hall at DTU Chemical Engineering). A simplified process diagram is shown in figure 3.1, and a quick overview of main instrument details can be found in table 3.1.

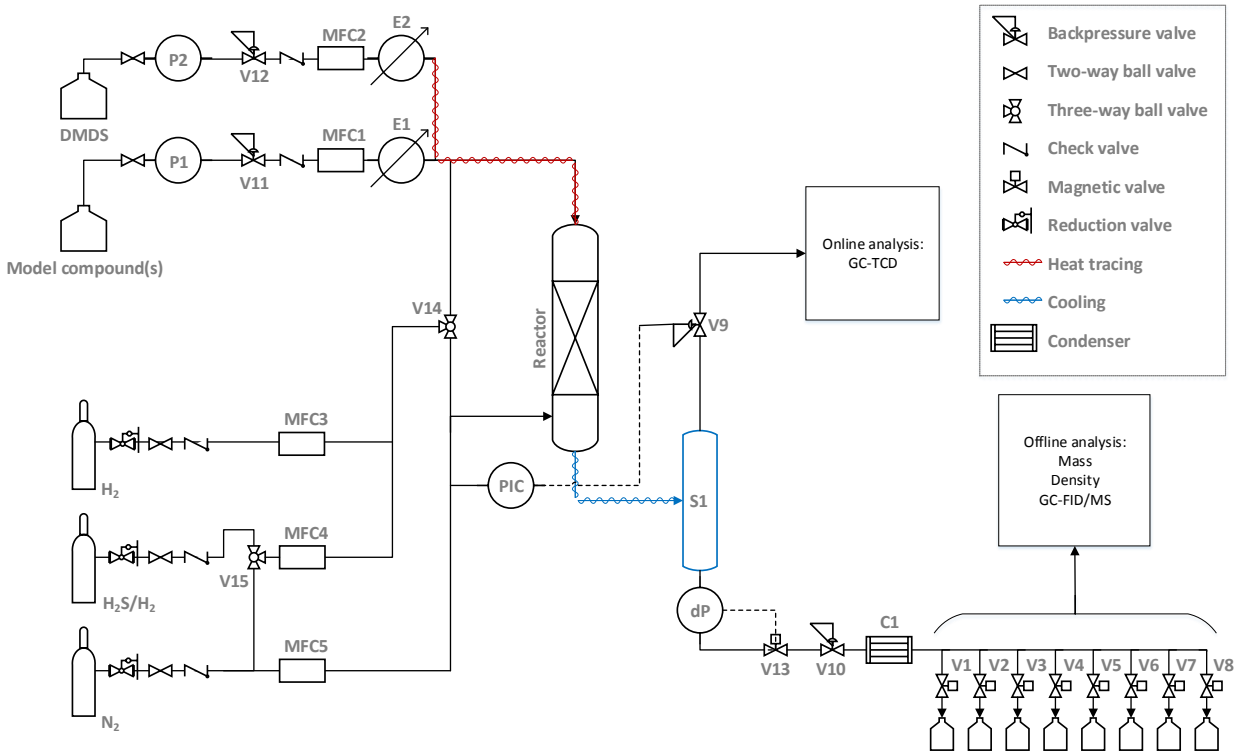

Figure 3.1: *Simplified process diagram for the POC setup. MFC1-5: mass flow controllers, E1-2: evaporators, P1-2: pumps, S1: Separator tube, PIC: pressure indicator and controller, dP: differential pressure cell, C1: condenser, V1-V8: manifold magnetic valves.*

A detailed description of the setup excluding minor modifications can be found elsewhere [1]. The modifications include cooling of the separator tube, S1, possibility for flushing MFC4 with N_2, and other minor alterations. Most of the equipment can be controlled and monitored on a PC via LabView, which enables data logging with a frequency of 1-60 s^{-1} (5 s^{-1} has been used as default). Generally, flows, temperatures, magnetic valve positions, and pressures were logged.

Table 3.1: *Instrumentation details for figure 3.1.*

Instrumentation	Description	Details
P1-2	HPLC pumps	10 or 50 mL pump heads
E1-2	Evaporators	Thermopatron heat cartridges with 6m 1/8" 316L stainless steel tubes
MFC1-2	Liquid mass flow controllers	Used as flow indicators (valves fully open)
MFC3-5	Gas mass flow controllers	Used as flow indicators and controllers
PIC	Pressure indicator and controller	Feedback to backpressure valve V9. Fit for ≤120 bar
V9	Backpressure valve (gas)	Used for automated pressure control (gas effluent). Trim 15 (Cv = 2-250·10^{-6} at 5-100 % opening) installed
V10-12	Backpressure valves (liquid)	Used for build-up of liquid feed pressure and for pressure reduction before C1
dP	Differential pressure cell	Measures liquid column height in S1
V13	Magnetic valve	Feedback to dP for automated liquid collection. Typical open/close level for V13 at dP 45/35 mmH_2O
Heat tracing	Winded electrical heat tracing	80 °C used during catalyst tests
Cooling	Water cooling through winded copper pipes	10-15 °C used during catalytic activity tests
C1	Condenser	6 °C used during catalytic activity tests

3.1.1 Setup Modifications and Material Selection

Some modifications to the original design (see [1]) have been made in order to fit the purposes of this project. The setup has previously been used for the continuous upgrading of wood pyrolysis oil [1]. These experiments resulted in severe coke and tar deposition in the reactor and in downstream pipes and equipment. Coke deposition has most likely been caused by rapid polymerization of highly reactive species, both present in the pyrolysis oil feed and in the product as partly deoxygenated coke precursors. The experimental work performed by the author of this work was thus initiated with extensive cleaning of the setup, and the conclusion was made, that HDO on condensed pyrolysis oil, which is reheated

before upgrading is highly unattractive.

In former experiments, the reactor outlet could be kept warm with heat tracing, and it is possible that polymerization reactions have been further enhanced by this. In order to ensure cooling and stabilization of products leaving the reactor, the heat tracing of the reactor effluent was replaced by water cooling. The setup has additionally been cleaned in a systematic manner prior to start-up of the experimental work presented in the following. Equipment and pipelines have been taken apart and cleaned by scrubbing with deionized water, ethanol, and acetone. Ultrasound cleaning was applied when necessary. Pipelines too small to clean and fully damaged equipment have been exchanged with new equipment.

Figure 3.2a-b illustrates the severity of the coking in the setup. Unfortunately, no pictures were taken of the reactor tube before it was discarded. It had a several mm thick, dark brown/blackish clotted char trace running down the outside of the inlet section, making it resemble an old candle. It indicated that there was a liquid overflow in the last experiment causing the liquid feed to run in reverse direction through the reactor tube. In addition to coking, sealing materials in various components were damaged by the use of pyrolysis oil and the use of acetone during cleaning. Figure 3.2c-d shows a fresh seal from a check valve and a used, swollen one, which poses a risk to the safety of operation.

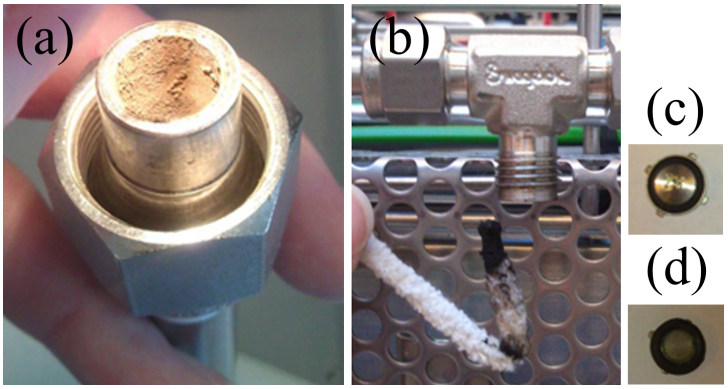

Figure 3.2: *Pictures from initial cleaning of the POC setup after former experiments with real pyrolysis oil. (a) Looking into the separator tube, S1, where a layer of coke (≤0.5 mm) was deposited on the inner surface. (b) A pipe cleaner inserted into a T-piece in the liquid product collection line. (c) A fresh check valve bonnet (kalrez seal). (d) A check valve bonnet (viton seal) exposed to pyrolysis oil and acetone.*

Before starting new experiments, it was ensured that the wetted parts of the setup were compatible with representative pyrolysis oil compounds as well as water, H_2S, H_2, and a few organic solvents which could be relevant for cleaning. Any non-compatible parts were exchanged with compatible materials with only a few exceptions, if the risk of damage was considered low. Fluorinated sealing materials (Kalrez, Kel-F, FFKM, PEEK, PTFE) have frequently been applied in the setup. An overview of the material compatibility between relevant materials and chemical species is provided in table 3.2.

Table 3.2: *Common materials used in the wetted parts of piping and instrumentation in the POC setup, and their compatibility with relevant chemicals [240]. Compatibility: (A) Excellent, (B) Good, (C) Fair, (D) Severe effect, (-) No information. Bu-N: BUNA-N or nitrile, PP: Polypropylene, Sili: Silicone.*

Chemical	VITON	PEEK	PVDF	PTFE	SS316L	EPDM	Bu-N	Kalrez	FKM	FFKM	Kel-F	PP	Sili	PVC
Acetaldehyde	D	A	D	A	A	A	D	A	D	D	A	A	A	D
Acetic acid	B	A	C	A	B	A	C	C	D	-	A	B	C	D
Acetone	D	A	D	A	A	A	D	A	D	A	A	A	D	D
Benzyl alcohol	A	A	A	A	B	B	D	-	A	A	A	A	-	D
Octyl alcohol	B	-	-	-	A	A	B	A	B	A	-	-	B	-
Propyl alcohol	A	A	A	A	A	A	A	A	A	A	-	A	A	A
Benzaldehyde	D	A	A	A	B	A	D	A	D	B	A	D	D	D
Cyclohexane	A	A	A	A	A	D	B	A	A	A	A	D	D	D
Cyclohexanone	D	A	D	A	A	B	D	A	D	B	A	D	D	D
Diesel Fuel	A	A	A	A	A	D	A	A	A	A	A	A	D	A
Diethyl ether	D	A	A	A	B	D	D	A	D	A	C	A	D	D
Diethylene glycol	A	-	A	A	A	A	A	A	A	A	-	A	B	C
Ethanol	A	A	-	A	A	A	C	A	B	A	A	A	B	C
Ether	C	A	B	A	A	C	D	A	D	A	B	D	D	D
Ethylene glycol	A	A	A	A	B	A	A	A	A	A	A	A	A	A
Furan resin	D	-	D	A	A	C	D	A	D	A	A	D	D	A
Furfural	D	-	B	A	B	D	D	A	D	B	D	D	D	D
Glucose	A	-	A	A	A	A	A	A	A	A	-	A	A	A
Hydrogen gas	A	-	A	A	A	A	A	A	A	A	B	A	C	A
H_2S (aqua)	D	A	A	A	A	B	D	A	D	A	A	A	C	B
H_2S (dry)	D	A	A	A	A	B	D	A	D	A	B	A	C	A
Ketones	D	A	C	A	A	A	D	A	D	-	B	C	-	D
Methanol	C	A	A	A	A	A	A	A	C	A	A	A	A	A
Phenol	A	D	A	A	B	B	D	A	A	A	B	B	D	D
Tetrahydrofuran	D	A	B	A	A	D	D	A	D	A	A	C	D	D
Toluene	C	A	A	A	A	D	D	A	A	A	B	C	D	D
Water	A	-	A	A	A	A	A	-	A	D	A	A	-	A

3.1.2 Reactor

A schematic drawing of the in-house designed reactor is shown in figure 3.3. The reactor is constructed from 316L stainless steel, like the piping of the entire setup. The reactor consists of a vertical pressure shell and an internal reactor tube, in which the catalyst bed was placed. The pressure shell consists of a 80 cm straight tube with flanges welded to the top and bottom respectively. The internal reactor (from this point on referred to as the reactor) is a 91.5 cm long straight tube with internal diameter 0.8 cm and outer diameter 1.0 cm. A support pin located 42.15 cm from the outlet of this tube enables fixation of the catalyst bed in the isothermal zone of the furnace using steel wool. A steel reactor was used in all experiments presented here, but it is also possible to use a quartz reactor. Initial experiments using a quarts reactor tube, quarts wool, and glass beads for bed dilution, however showed that all three glass components degraded upon exposure to ethylene glycol, H_2S, and H_2 under reaction conditions (see Appendix C).

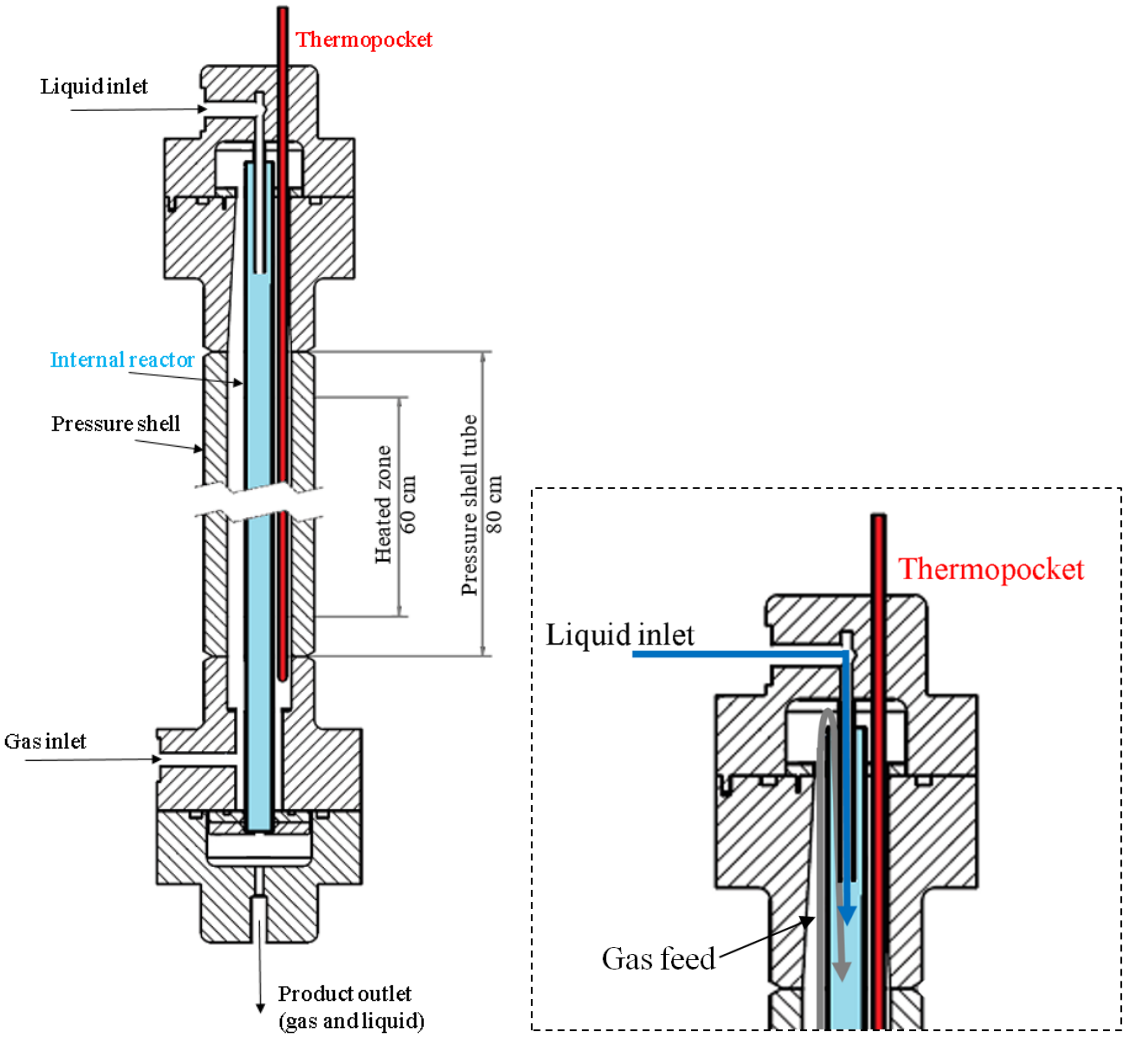

Figure 3.3: *Schematic drawing of the POC reactor. Pressure shell, internal reactor, and thermopocket have been highlighted. The gas and liquid inlets are shown. The insert to the right shows the gas and liquid feed flow paths at the internal reactor tube inlet.*

The gas feed enters the bottom flange and rises through the pressure shell and enters the reactor in the top flange. Some of the gas (MFC3-4) may be fed together with the liquid through the dip tube. The product (gas and liquid) exits the bottom flange. A thermopocket allows for temperature measurements at adjustable locations along the axial direction of the catalyst bed. The liquid feed enters the reactor through a dip tube fitted to the top flange.

The pressure shell and reactor is heated by a Carbolite TVS12/600 furnace which has a 60 cm heated zone. The fixed bed length was <20 cm for all catalyst activity tests, and the catalyst was placed in the isothermal zone of the furnace (see figure 3.4). The temperature profiles in figure 3.4 show that it is more difficult to maintain the isothermal zone at higher temperatures, due to heat loss to the surroundings. The temperature profiles include one profile measured during the HDO of a cyclohexanol/ethylene glycol mixture at 420 °C (see chapter 6). In this experiment, the bed length (including steel wool) was ∼ 6 cm, and the temperature profile revealed endothermal activity in the inlet part of the bed. The exact location of catalyst bed in this experiment is shown in Appendix D. The HDO temperature profile can be compared with that obtained without reaction; in this case, the profile obtained at setpoint 450 °C has been parallel shifted downwards by 31 °C for easy comparison. This comparison shows how the heat of reaction may influence the temperature through the catalyst bed; in this case, endothermal activity was caused by the rapid dehydration of cyclohexanol (see chapter 6).

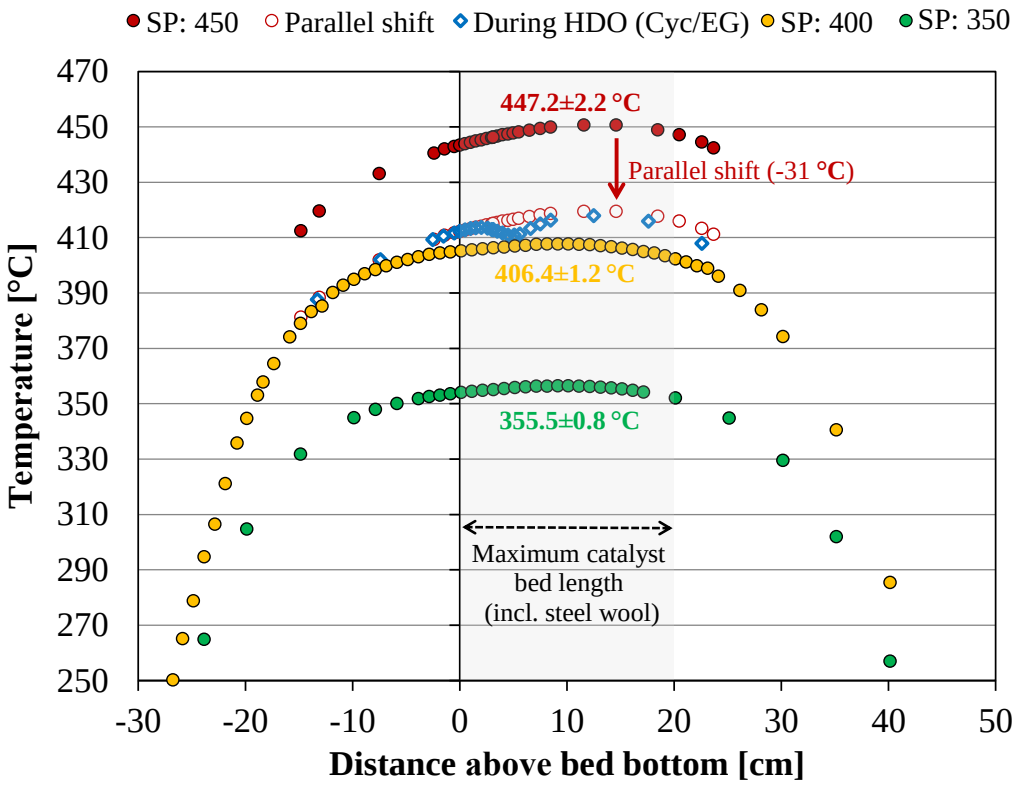

Figure 3.4: *Temperature profiles measured in the POC reactor in the thermopocket at different positions and different setpoints (SP). One temperature profile measured during the HDO of a cyclohexanol/ethylene glycol mixture is shown (at T_{SP} = 420 °C with 3 mol% ethylene glycol and 0.5 mol% cyclohexanol in the feed at total pressure 40 barg (27 bar H_2, 550 ppm H_2S, balance N_2, see chapter 6). Position = 0 is the location of the support pin. The distance relative to 0 corresponds to the distance above the support pin.*

3.1.3 Liquid feed

Two different liquid feeds were pumped from 1 L blue cap bottles into the system via HPLC pumps P1 and P2 (see figure 3.1). During continuous operation, these bottles were refilled when necessary. Line 1 was used for bio-oil model compounds, while line 2 was used for dimethyl disulfide (DMDS). The liquid feed entered the reactor top through a dip tube (see figure 3.3). The pressure in lines 1-2 was built up using backpressure valves V11-12 and the flow was monitored with MFC1-2. Whenever a new liquid was introduced, the respective feed line (1 or 2) was flushed with the new liquid, and it was checked with GC-FID/MS, that the former liquid had been efficiently removed. The corresponding pump and mass flow controller (P1/MFC1 or P2/MFC2) were then calibrated to enable flow rates and logging in the desired feed flow range.

3.1.4 Gas feed

50 L gas cylinders (supplied by AGA) containing N_2 (≥99.95 %), H_2 (≥99.9 %), and 2% H_2S/H_2 (≥99.5 %) were connected to the setup. The gas feed flow was monitored and controlled using MFC3-5 (see figure 3.1). The gas feed feed was consistently sent to the bottom of the reactor pressure shell, where it flowed upward inside the pressure shell along the outer surface of the reactor until it was mixed with the liquid feed in the top and entered the reactor tube in a downflow (see figure 3.3). The H_2 and 2 % H_2S/H_2 feeds could however also have been sent to the reactor top together with the liquid feed depending on the position of three-way valve V13. The setup was flushed with N_2 before and after operation with H_2 to avoid mixture with air.

H_2S a sticky gas and especially MFCs exposed to H_2S may experience deterioration if exposed to air, while H_2S is deposited on inner surfaces. Therefore, a three-way valve, V15, was installed to enable flushing of MFC4 with N_2 to remove air (before experiments were started) and H_2S (after experiments were ended).

The automated pressure control loop consisted of the pressure indicator and controller, PIC, and the backpressure valve V9. The possible pressure range depends on the backpressure valve specifications (i.e. trim dimensions), the temperature (e.g. if heat tracing is employed), and the gas composition. If a nitrogen rich feed is used, the resulting pressure at a given degree of opening of V9 will be higher than that resulting from a hydrogen rich feed, due to the higher density of nitrogen. V9 was equipped with a trim 15 (Cv = 2-250·10^{-6} at 5-100 % opening). The pressure in a typical activity test was maintained at 40 barg with a total feed flow of 1550 NmL/min (31 % N_2, 65 % H_2), and a V9 opening of 70-75 %.

3.1.5 Product Separation, Collection, and Analysis

The reactor effluent was cooled to 10-15 °C and separated by gravity into gas and liquid in the separator tube, S1 (see figure 3.1). The gas flowed upwards from S1 to V9, which reduced the pressure down to near-ambient. Downstream of V9, the gas was analyzed online on a Shimadzu GC-2014 with a thermal conductivity detector (TCD) and a 2 m 0.53 mm ID Shincarbon ST column (N_2, H_2, CO, CO_2, CH_4, C_2H_4, C_2H_6, C_3H_6, C_3H_8 were detected and analyzed). The analysis frequency was typically two GC-TCD measurements per hour.

The differential pressure cell (dP) at the bottom of S1 was connected to the magnetic valve V13, which was controlled to open and close at certain liquid column heights in S1 to keep an approximate steady state liquid level. A note on the development of steady state liquid collection in S1 for a two-

phase liquid product is given in Appendix E. The pressure in the liquid collection line was reduced by backpressure valve V10, and the condenser C1 provided additional cooling of the product. Liquid products were then collected in a valve manifold (V1-V8), typically programmed for a 4-5 h collection period in separate sample bottles. The mass and density (using an Anton Paar DMA 4100 density meter) of liquid samples was measured to get the volumetric flow rate. The liquid composition was analyzed by GC-FID/MS using a Shimadzu 2010 GCMS-QP2010 Ultra fitted with an Equity®-5 30 m x 0.32 mm column with d_{film} 0.5 μ and equipped with a flame ionization detector (FID).

3.2 Catalyst Preparation

Catalysts composed of Mo, NiMo, and CoMo were prepared by sequential incipient wetness impregnation of a $MgAl_2O_4$ spinel support supplied by Sasol as Al_2O_3-MgO precursor pellets (Puralox MG30 5x5, Z600134). This precursor was initially calcined for 3 h at 1000 °C to obtain the $MgAl_2O_4$ structure (verified by X-ray diffraction, XRD). The calcined $MgAl_2O_4$ sample had a pore volume of 0.44 g_{water}/g (90 % of this volume was used for impregnation), and a pore volume determined by N_2-physisorption of 0.28 cm^3/g (see Appendix F for physisorption isotherm and pore size distribution). The mean pore radius was 104.1 Å. The specific surface area, SSA, of the calcined $MgAl_2O_4$ was 60-62 m^2/g with little variation between the different batches calcined.

The support was crushed and sieved into a 300-600 μm fraction that was impregnated with an aqueous solution of $(NH_4)_6Mo_7O_{24}{\cdot}4H_2O$ (Fluka ≥99.0 %). It was then aged (by stirring) for 1 h and dried at 110 °C overnight. For promoted catalysts, a second impregnation was performed similarly with $Co(NO_3)_2{\cdot}6H_2O$ (Fluka ≥98 %) or $Ni(NO_3)_2{\cdot}6H_2O$ (Sigma-Aldrich ≥97 %) followed by aging and drying at 110 °C overnight. Calcination was then performed in a flow of 2.5 NL/min technical air (20 % O_2 in N_2) by heating with a ramp of 5 °C/min to 500 °C and holding for 3 h. The catalysts were fractioned again (300-600 μm) before activity tests to remove any dust or agglomerates formed during the preparation. A catalyst with 14 wt% Ni was prepared as well to test the activity of supported NiS_x.

Catalyst activation was performed *in-situ* in the catalytic activity setup close to atmospheric pressure in a flow of 10-12 % H_2S created from DMDS (Sigma-Aldrich ≥99.0 %) in H_2; resulting in a total flow rate of ∼ 830 NmL/min. Initial heating was performed in ∼ 100 NmL/min N_2 from room temperature to 200 °C. The temperature was then ramped at 5 °C/min from 200 °C to 360 °C and held at 360 °C until unconverted DMDS started to build up in the outlet. The temperature and pressure was then increased to achieve reaction conditions.

Table 3.3 gives an overview of prepared catalysts. The loading of Mo was targeted at a sub monolayer, which is <4 atoms/nm^2 for $MgAl_2O_4$ and thus similar to that of γ-Al_2O_3 [241]. This was done to ensure a high dispersion of small moderately active sulfide particles and thereby prevent the formation of a highly active type II sulfide phase [63, 242]. An estimated loading of 3.0-3.7 Mo atoms/nm^2 was achieved. The promoter loading was fixed at a M/Mo (M = Ni, Co) molar ratio of 0.3 to optimize the activity [63, 243].

Table 3.3: *Composition and properties of as-prepared calcined catalyst precursors (oxide phase).*

Catalyst	Mo [wt%]	Ni [wt%]	Co [wt%]	Ni/Mo [molar]	Co/Mo [molar]	Mo load[a] [atoms/nm^2]	BET SSA [m^2/g]
Mo#1	3.36	-	-	-	-	3.7	64
Mo#2	3.37	-	-	-	-	3.7	62
NiMo#0	0.83	0.17		0.34		0.85	80
NiMo#1	2.83	0.58	-	0.34	-	3.0	97
NiMo#2	3.33	0.66	-	0.33	-	3.7	77
CoMo#0	0.88	-	0.16	-	0.30	0.91	79.4
CoMo#1	3.28	-	0.59	-	0.29	3.5	73
CoMo#2	3.37	-	0.58	-	0.28	3.7	70
Ni#1	-	14.3	-	-	-	-	49
	Mg [wt%]	**Al [wt%]**	**Al/Mg [molar]**				
$MgAl_2O_4$ (support)	17.4	36.1	1.87[b]	-	-	-	60-62

[a] Estimated Mo loading in atoms per nm^2 support surface area available (assuming presence of MoO_3, NiO, and CoO).

[b] A slight excess of MgO, as reported by Sasol, was verified by XRD.

3.3 Catalyst Characterization

Fresh and spent catalysts have been analyzed using various techniques.

3.3.1 Elemental Analysis and Morphology

Inductively coupled plasma optical emission spectroscopy (ICP-OES) was used to determine the concentration of metals (Mo, Co, Ni, Fe, Si, Mg, and Al), and CS analysis by combustion and IR product detection (CO_2 and SO_2) was used to get the content of C and S (in spent catalysts). N_2-physisorption (BET and BJH) was performed at liquid nitrogen temperature, -196 °C, using a QuantaChrome Autosorb iQ_2 or Monosorb MS-21 gas sorption analyzer. The catalysts were outgassed for 2 h at 350 °C under vacuum, prior to N_2 physisorption in the p/p_0 range of 0.01-0.99. TEM was performed on an aberration corrected FEI Titan 80-300 operated at 300 kV. XRD was performed on a Huber G670 diffractometer with monochromatic Cu-Kα1 radiation ($\lambda_{\text{Cu-K}\alpha1}$ = 1.54056 Å) or on a Panalytical X'pert Pro diffractometer using Cu-Kα1, Cu-Kα2, and Cu-Kβ radiation ($\lambda_{\text{Cu-K}\alpha2}$ = 1.54443 Å, $\lambda_{\text{Cu-K}\beta}$ = 1.39225 Å) in the 2θ range of 0-70 °.

3.3.2 Raman Spectroscopy

Raman spectroscopy was performed at KIT using a Renishaw inVia Reflex Spectrometer System equipped with a frequency doubled Nd:YAG laser (532 nm, 100 mW). Data collection was typically performed in the 60-1300 cm^{-1} spectral range with a grating of 2400 lines/mm resolution. For each sample, an area of $\sim$ 384 x 576 μm was scanned in a raster with 5400 points, which were averaged giving a single spectrum. To avoid sample heating, the laser was set to line shape at 10% intensity and the acquisition time was varied between 10 and 60 s per point. No dehydration was performed on the calcined catalysts prior to Raman spectroscopy; the molybdenum oxide precursor species were thus expected to be in their hydrated state [244,245].

3.3.3 NH_3-TPD

Ammonia temperature programmed desorption (NH_3-TPD) was performed in a horizontal fixed bed reactor setup at KIT. The experimental procedure is illustrated in figure 3.5. The samples were first pretreated by heating at 10 °C/min until 550 °C and holding for ∼ 10 min in a flow of 555 NmL/min N_2. The samples were then cooled in a flow of N_2 until 90 °C, and adsorption of NH_3 was performed at 90 °C in a ∼ 580 NmL/min flow of 2550 ppm NH_3/N_2 for ∼ 5 min. Adsorption was followed by flushing out excess NH_3 at 90 °C for 2 h in 555 NmL/min N_2. Desorption was then performed in a flow of 555 NmL/min N_2, while heating at 5 °C/min until 550 °C and holding for ∼ 5 min. The outlet concentration of NH_3 was determined by Fourier transform infrared (FTIR) spectroscopy using an MKS Multigas 2030 analyzer.

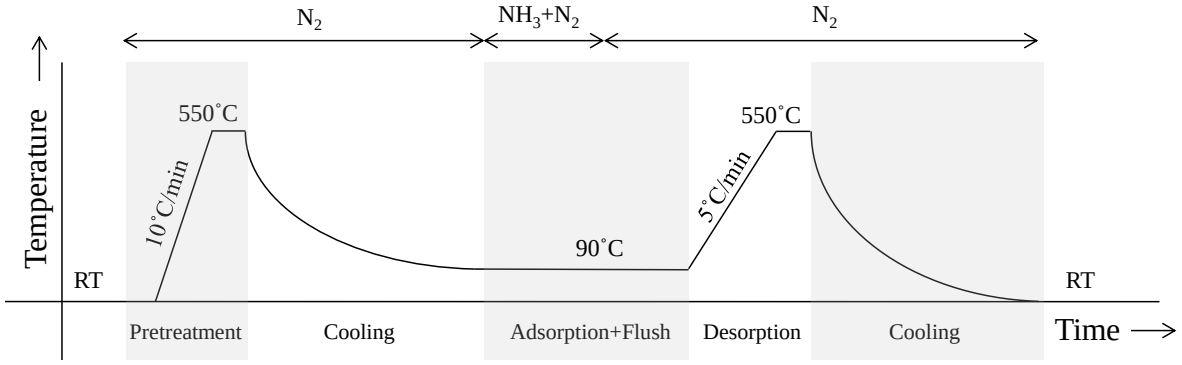

Figure 3.5: *NH_3-TPD experimental procedure.*

3.3.4 XAS

In-situ X-ray absorption spectroscopy (XAS) measurements were performed at the SuperXAS beamline at SLS (2.4 GeV storage ring, 400 mA ring current) [246]. Both X-ray absorption near edge structure (XANES) and extended X-ray absorption fine structure (EXAFS) spectra were collected. Measurements were conducted at the Ni K- (8.333 keV), Co K- (7.709 keV), and Mo K-edge (20 keV) of the prepared Mo, NiMo, and CoMo catalysts.

The catalysts were loaded into a 1 or 1.5 mm quartz capillary microreactor, which was heated by a gas blower [247,248]. The reactor was connected to a H_2S gas feed line and could be switched between 1000 ppm or 10 % H_2S/H_2, and to a H_2 feed line, which could be sent through a water saturater or directly to the reactor. The total flow through the capillary reactor was 40-43 NmL/min. The exhaust was sent through a H_2S absorber (3.5 mol/L NaOH solution) into the exhaust system of the beamline. A N_2 line was installed for flushing. The setup process diagram can be found in Appendix A.

Quick-EXAFS (QEXAFS) spectra were recorded in transmission mode with frequency of 10 Hz using ionization chambers as detectors and using an excentre disk to continuously move the monochromators in an oscillating manner allowing for fast measurements [246]. Reference spectra were recorded for MoS_2, MoO_3, MoO_2, $(NH_4)_6Mo_7O_{24}{\cdot}4H_2O$, $MoO_3{\cdot}H_2O$, CoS, CoO, Co_2O_3, Co_3O_4, Ni_3S_2, and NiO (pressed as BN pellets as received).

The catalysts were first dehydrated in a flow of N_2 while heating at 10 °C/min from room temperature to 200 °C. Sulfidation was then performed by heating until 400 °C at 5 °C/min in a flow of

10% H_2S/H_2 and holding at 400 °C for 1 h. Sulfidation was followed by exposure of the catalyst to increasing ratios of H_2O/H_2S in H_2 with a constant total flow rate of 43 NmL/min at 400-450 °C. In the case, where 450 °C was applied, the sulfidation was immediately followed be heating from 400 °C to 450 °C in 1000 ppm H_2S/H_2 at 5 °C/min, before H_2O was introduced in the gas. The holding time at each H_2O/H_2S ratio was typically 30 minutes. Figure 3.6 schematically illustrates the experimental procedure employed for *in-situ* XAS measurements.

EXAFS spectra were analyzed by using the software package IFEFFIT interfaces, i.e., Athena and Artemis [249]. The model included amplitude reduction factor (S_0^2), coordination number (CN), Debye-Waller factor (σ^2), energy shift for each path (ΔE_0), and change in the path length (ΔR), where R is the bond length. A detailed description of the data treatment can be found in Appendix A.

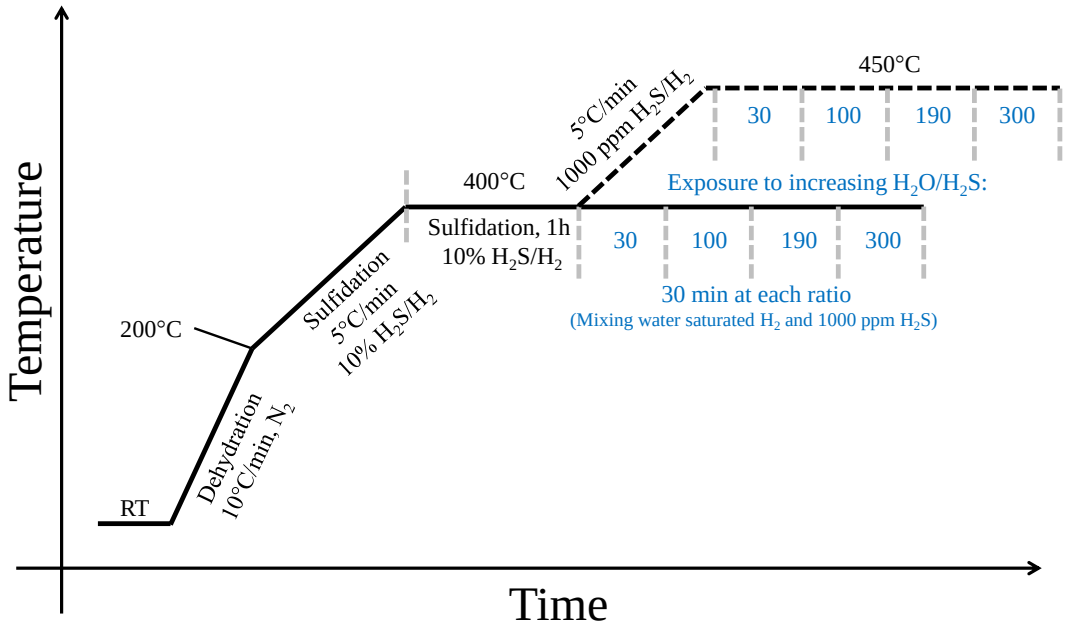

Figure 3.6: *In-situ XAS experimental procedure applied during SLS beamtime.*

3.3.5 DFT

DFT calculations were made to get insights into the structural dependency of molybdenum sulfide catalysts upon promotion and exposure to varying concentrations of H_2O and H_2S. A detailed description of the DFT calculations can be found in Appendix B.

3.4 Catalytic Activity Tests

Ethylene glycol (EG, Sigma-Aldrich, ≥99.8 %), phenol (Phe, Sigma-Aldrich, ≥99 %), cyclohexanol (Cyc, Sigma-Aldrich, ≥99 %), and acetic acid (HAc, Sigma-Aldrich, ≥99.5 %) were used as model compounds. In activity tests, 0.5-4 g catalyst was diluted with 0.5-4 g SiC (150-250 μm) and fixed with steel wool in the reactor tube. The reactor was loaded into the pressure shell and the adjustable thermocouple was placed in the thermopocket in a position corresponding to the middle of the catalyst bed.

In-situ activation was performed as described above. After this sulfidation, the temperature was increased to reaction temperature in N_2. The liquid HDO model compound was pumped around in an internal loop to increase the pressure to a value 10-20 bar higher than the desired reaction pressure (using backpressure valve V11) to ensure flow through the evaporator into the reactor. Once the desired temperature was reached, the gas flow was switched from N_2 to reaction gas and the pressure was increased to reaction pressure. The HDO model compound(s) was added, when the reaction pressure had stabilized, and this point of time is referred to as time on stream (TOS) = 0. The activity tests were typically performed at 380-450 °C, 27 bar H_2, 550-2200 ppm H_2S, 40 barg total (balance N_2), a total gas feed (H_2, N_2, H_2S) of 1550 NmL/min, and a model compound volumetric feed of 0.14-0.16 mL/min. The resulting liquid WHSV was 2.4-21 $g_{model}/(g_{cat} \cdot h)$, depending on the catalyst mass. The model compound concentration in the feed was 0.5-3.5 mol%.

Experiments were terminated by stopping the model compound feed and changing from reaction gas to $\sim$ 500 NmL/min N_2 while reducing the pressure. When ambient pressure was reached, flushing with N_2 was continued at reaction temperature to desorb condensed species from the catalyst pores. After 30 minutes flushing, the furnace was turned off to allow the system to cool to room temperature overnight while continuing the flow of N_2. Unloaded catalysts were separated from SiC and steel wool prior to analysis. No Soxhlet extraction was performed on spent catalysts prior to characterization; thus, any condensed high-molecular weight products formed during reaction could be left in the catalyst pores.

A blank experiment showed negligible HDO activity for the conversion of ethylene glycol at 400 °C with a feed of 3-3.5 mol% ethylene glycol, 27 bar H_2, 550 ppm H_2S, and 40 barg total pressure (balance N_2); ethylene was the main gaseous product formed with a yield <0.7 %.

3.4.1 Calculations

The conversion, X, of model compound A was calculated based on the molar flow in, $F_{A,feed}$, and out, $F_{A,out}$, of the system:

$$X = \frac{F_{A,feed} - F_{A,out}}{F_{A,feed}} \cdot 100\% \tag{3.1}$$

The carbon based yield of product i, Y_i, was calculated as:

$$Y_i = \frac{F_i \cdot \nu_{C,i}}{F_{A,feed} \cdot \nu_{c,A}} \cdot 100\% \tag{3.2}$$

F_i is the molar flow rate of compound i, and $\nu_{C,i}$ is the carbon number in compound i. N_2 was used as an internal standard in GC-TCD measurements so that the molar flow of H_2 and gaseous products could be determined as:

$$F_g = \frac{F_{N_2,feed}}{y_{N_2}} \tag{3.3}$$

$$F_{g,i} = y_i \cdot F_g \tag{3.4}$$

F_g is the total effluent molar gas flow based on the known molar feed flow of N_2, $F_{N_2,feed}$, and the fraction of N_2, y_{N_2}, determined by GC-TCD. $F_{g,i}$ is the resulting molar flow of compound i based on the composition (molar fraction y_i) determined by GC-TCD.

The FID signal from the GC-FID/MS was calibrated for a range of compounds (methanol, ethanol, ethylene glycol, 1-propanol, ethyl acetate, 1-butanol, phenol, cyclohexanol). A broader range of compounds were analyzed and quantified by using the effective carbon method:

$$C_i = \frac{C_{\text{ref}} \cdot \nu_{\text{C,eff,ref}}}{A_{\text{ref}}} \cdot \frac{A_i}{\nu_{\text{C,eff},i}} \tag{3.5}$$

The concentration of compound i, C_i, was calculated based on the area of the corresponding peak, A_i, on the effective carbon number of this compound, $\nu_{\text{C,eff}}$, and on the data from a reference compound (in this case ethanol or phenol). Data on effective carbon numbers for the most abundant products detected can be found in table 3.4.

In experiments with conversion of ethylene glycol and cyclohexanol, cyclohexene was produced, and the GC-FID peak overlapped that of ethylene glycol. In this case, the peak of cyclohexene appeared as a shoulder on the ethylene glycol peak (see figure 3.7). The area of each compound was determined by subtracting the cyclohexene shoulder from the main ethylene glycol peak. This method was verified by analysis of standard mixtures of cyclohexene and ethylene glycol in different concentrations.

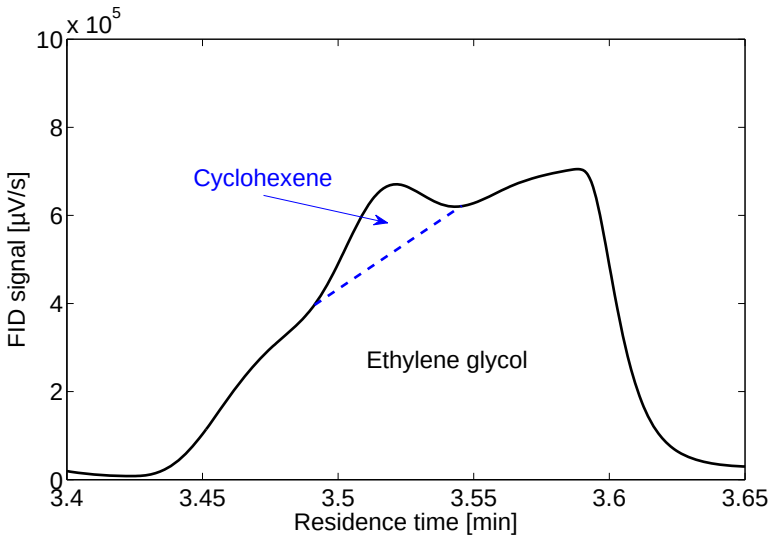

Figure 3.7: *GC-FID spectrum for liquid product collected at TOS 24-29 h for a cyclohexanol/ethylene glycol experiment with a feed of 0.5 mol% cyclohexanol and 3 mol% ethylene glycol, 27 bar H_2, 550 ppm H_2S, and 40 barg total pressure (balance N_2). 87 % conversion of cyclohexanol and 92 % conversion of ethylene glycol. The area of the ethylene glycol peak is determined by subtraction of the shoulder, which is equal to the area of cyclohexene.*

Table 3.4: *Most abundant liquid products from EG, Phe, and Cyc conversion and their corresponding effective carbon number based on [250].*

Compound	**Carbon number** ν_C	**Non-contributing carbon number** $\nu_{C,non}$	**Effective carbon number** $\nu_{C,eff} = \nu_C - \nu_{C,non}$
Oxygenate functionalities			
Primary alcohol	-	0.5	ν_C-0.5
Ketone	-	1	ν_C-1
Carboxylic acid	-	1	ν_C-1
Ether	-	1	ν_C-1
Aldehydes	-	1	ν_C-1
C_{2-6} ester	-	1.1-1.5	ν_C-$\nu_{C,non}$
Most common products detected from EG			
Ethylene glycol	2	1	1
Methanol[a]	1	0.5	0.5
Ethanol (used as ref)	2	0.5	1.5
Acetic acid	2	1	1
Acetone[b]	3	1	2
1-propanol	3	0.5	2.5
Methyl acetate	3	1.5	1.5
1-butanol	4	0.5	3.5
2-butanone	4	1	3
2-methyl-1-propanol	4	1	3
Ethyl acetate	4	1.5	2.5
2-methyl-1,3-dioxolane	4	2	2
Diethylene glycol	4	2	2
4-polyethylene glycol	8	4	4
Most common products detected from Phe (in mixture with EG)			
Phenol (used as ref)	6	0.8	5.2
2-ethylphenol	8	0.5	7.5
Benzofuran	8	1	7
3-methylphenol	7	0.5	6.5
Most common products detected from Cyc (pure or in mixture with EG)			
Cyclohexanol (used as ref)	6	0.5	5.5
Cyclohexane	6	0	6
Cyclohexene	6	0	6
Cyclohexanone	6	1	5
1,4-dioxaspiro[4.5]decane[c]	8	2	6

[a] May also include acetaldehyde, hydroxyacetaldehyde or a mixture of methanol, acetaldehyde, and hydroxyacetaldehyde.

[b] Prior to GC-FID/MS measurement on each sample, the autoinjector flushed the syringe with acetone and then with the sample itself. It was occasionally checked (using a blank sample) that any acetone remaining from the flush was negligible or not detectable.

[c] Structure: 

The molar flow rate of liquid phase compound i, $F_{l,i}$, was then found from the total liquid volumetric flow rate for the specific sample bottle, Q_l, which was determined based on the sample mass, m_l, sample density, ρ_l, and sampling time, t, for the specific bottle analyzed:

$$F_{l,i} = C_i \cdot Q_l \tag{3.6}$$

$$Q_l = \frac{m_l}{\rho_l \cdot t} \tag{3.7}$$

The carbon mass balance was calculated based on the flow of carbon into and out of the system, where n denotes the total number of compounds analyzed in the outlet (gas and liquid) including unconverted model compound A:

$$C_{balance} = \frac{\sum_i^n F_i \cdot \nu_{\mathrm{C},i}}{F_{A,feed} \cdot \nu_{\mathrm{C},A}} \cdot 100\% \tag{3.8}$$

The mass balance closure in the ethylene glycol experiments was challenged by the formation of light oxygenates (methanol, ethanol, acetaldehyde, etc.), which could not be detected by the online GC-TCD analysis. A thorough review of the mass balance closure has been provided in Appendix G.

Space time yields, STY, were calculated for C_1, C_2, and C_3 gas products to compare the catalyst productivity based on the mass of catalyst, m_{cat}, and the molar carbon based product of the compound of interest:

$$STY_i = \frac{F_i \cdot \nu_{\mathrm{C},i}}{m_{cat}} \tag{3.9}$$

In the HDO of ethylene glycol, cracking occurred forming C_1 gasses (CO, CO_2, CH_4). The ratio of fully deoxygenated ethylene glycol products (ethane and ethylene) to C_1 gas products was used to assess the degree of HDO compared to cracking:

$$\frac{\mathrm{C_2}}{\mathrm{C_1}} = \frac{Y_{\mathrm{C_2H_6}} + Y_{\mathrm{C_2H_4}}}{Y_{\mathrm{CO}} + Y_{\mathrm{CO_2}} + Y_{\mathrm{CH_4}}} \tag{3.10}$$

The total carbon based yield of gas products detected, $C_{sum,gas}$, was used to asses the combined yield of C_1 (CO, CO_2, CH_4), C_2 (ethylene and ethane), and C_3 (propylene and propane):

$$\mathrm{C_{sum,gas}} = Y_{\mathrm{C_1}} + Y_{\mathrm{C_2}} + Y_{\mathrm{C_3}} \tag{3.11}$$

3.5 Experimental Results Not Covered by this Thesis

Several conducted experiments did not make their way into this thesis for different reasons. The very first HDO catalytic activity tests were performed using bulk MoO_3 (Sigma-Aldrich, 1-2.5 m^2/g) as catalyst and acetone as model compound, inspired the the work of Prasomsri et al. [144]. These initial experiments were run over shorter periods of time, and were targeted at quickly assessing the activity. The HDO activity tests for acetone conversion were performed at 350-400 °C with $\leq$ 2 bar H_2 and approximately 4 % acetone in the feed. In conclusion, the HDO activity of bulk MoO_3 was negligible, possibly due to reduction of MoO_3 to MoO_2 or coke deposition.

After the initial work with bulk MoO_3, the focus was moved towards molybdenum sulfides, due to their ability to operate at high hydrogen pressures necessary for stabilization of reactive oxygenates and suppression of coke formation in pyrolysis vapor upgrade, and due to their sulfur tolerance. With the aim to study the HDO of the very reactive polyolic sugar fragments in pyrolysis vapor, glycerol was chosen as a model compound. It could be fed as a pure liquid (larger polyolic molecules are typically solid at room temperature) and HDO would produce C_3 gas products that could readily

be determined with the online GC-TCD analysis, enabling high time on stream resolution. These experiments were performed using a commercial hydrotreating catalyst, and it was possible to produce propane at a yield of $\sim$ 50 % at 275 °C at 50 bar H_2 with a co-feed of H_2S and with 1.7 % glycerol in the feed. Glycerol conversion experiments were run for a short period of time (<10 h) showing some deactivation. Experiments with glycerol were challenged by the lack of a proper quantification method for unconverted glycerol, which was necessary for determination of the conversion, and these experiments were thus terminated.

The next model compound of choice was ethylene glycol, which same as glycerol represents a polyolic functionality and produces HDO products that could be detected with the online GC-TCD. At the same time, ethylene glycol could be quantified with instrumentation at hand (GC-FID/MS) allowing for determination of the conversion. The first experiments were conducted at temperatures of 275-420 °C, 40 bar H_2 and a co-feed of approximately 500 ppm H_2S. These experiments provided useful insights into the overall activity, coke deposition, influence of temperature, and influence of promotion. However, it was found that Si from the glassy reactor equipment used was deposited onto the catalysts and thereby induced accelerated deactivation (see Appendix C).

The reactor, bed fixator, and dilution material were then changed to inert materials, and the reaction conditions were furthermore changed to higher temperatures and slightly lower H_2 pressure to fit the properties, that were going to be investigated in another PhD project studying the catalytic (hydro)pyrolysis of solid biomass with downstream HDO of the pyrolysis vapors. The resulting work from these final experiments are presented in this thesis.

4 | Influence of Promotion and Loading

Influence of Promotion and Loading on the Hydrodeoxygenation of Ethylene Glycol over Sulfided NiMo and CoMo Catalysts Supported on $MgAl_2O_4$

Abstract

The hydrodeoxygenation (HDO) of ethylene glycol over $MgAl_2O_4$ supported NiMo and CoMo catalysts with different active phase loadings was studied in a continuous flow reactor setup operated at 27 bar H_2 and 400 °C. A co-feed of H_2S was necessary to avoid accelerated deactivation, and increasing the H_2S concentration was observed to promote both deoxygenation and hydrogenation, which was ascribed to the presence of SH groups at the catalytic active edge of MoS_2. Higher yields of C_{1-3} gas products were obtained with higher loading catalysts. With 2.8-3.3 wt% Mo, a total gas yield of 80-100 % was obtained with an ethane yield of 36-50 % (no ethylene) at up to 118 h on stream. A moderate selectivity towards HDO was obtained, but cracking and HDO were generally catalyzed to the same extent by the active phase. Thus, the ratio of C_2/C_1 products was 1.1-1.5 for catalysts with Mo loadings in the range of 0.8-3.3 wt%. Similar activities were obtained from Ni and Co promoted catalysts, but with a somewhat better hydrogenation activity over NiMo, which for the catalysts with a 0.83-0.88 wt% Mo loading lead to a relatively higher yield of ethane compared to ethylene.

4.1 Introduction

When performing *in-situ* HDO of pyrolysis vapor, the reactive compounds can favourably be upgraded and stabilized before condensation. This could be achieved either via catalytic hydropyrolysis in a fluid bed reactor or by fixed bed HDO on the fast pyrolysis vapors before condensation [20, 221]. For catalytic hydropyrolysis in a fluid bed (at $\sim$ 500 °C), the catalyst must be attrition resistant, and moderate activity is necessary in order to limit cracking of the biomass into light gasses at elevated temperature. For downstream fixed bed HDO of non-catalytic fast pyrolysis vapors (at 250-400 °C) [1, 38, 87, 94, 98–102], a moderate catalyst activity is necessary to limit cracking, but also to avoid hot spots from the exothermic HDO reactions.

Sulfide based catalysts, Ni- and Co-MoS_2/Al_2O_3, which are used commercially as HDS catalysts, are active for HDO of bio-oil and model compounds showing promising activity and stability [70, 76, 80, 92, 94, 98–100, 103–114]. Compared to other catalyst systems such as reduced transition metal catalysts [38, 82, 87, 92, 94, 99, 101, 154], sulfide catalysts are promising due to their moderate price and tolerance against sulfur, which is inevitably present in bio-oil [22, 30]. γ-Al_2O_3, which is a commonly applied support material [63, 67], is however not tolerant against water present in bio-oil and formed during HDO, as it converts into boehmite [87, 197].

In this work, Ni- and Co-promoted MoS_2 catalysts supported on water and attrition resistant $MgAl_2O_4$ have been prepared and tested for HDO activity. Ethylene glycol has been chosen as a model compound as it represents the more reactive polyol functionality present in cellulose [251], which should be upgraded before condensation of pyrolysis vapors to achieve a stable bio-oil. Catalysts with low and higher loading of active phase and with different promoters have been prepared and tested to study the interaction between the active phase and support as well as the influence of promoter. With the aim of developing stable catalysts and optimizing operating conditions, the influence of WHSV was investigated to find reaction conditions where catalyst deactivation could be studied.

The Mo loading in the prepared catalysts was 0.83-0.88 wt% or 2.83-3.28 wt% corresponding to 0.9 or 3.0-3.7 Mo atoms per nm^2 support surface area (see table 3.3). The molar ratio of Ni/Mo and Co/Mo was fixed at 0.3.

4.2 Results and Discussion

4.2.1 XRD

The support material was received as a $MgAl_2O_4$ precursor; an amorphous mixture of MgO and Al_2O_3 (Puralox MG30 5x5, Z600134 from Sasol, see also chapter 3.2). XRD was used to identify that $MgAl_2O_4$ had formed during calcination at 1000 °C, see figure 4.1. While the precursor was amorphous, the calcined support was crystalline $MgAl_2O_4$ with expected peaks at 2θ = 19, 31.2, 36.8, 44.8, 55.6, and 59.4 °. A small peak at 2θ = 42.8 ° indicated the presence of a small amount of MgO in agreement with the excess of Mg compared to Al as revealed by elemental analysis (see table 3.3). As γ-Al_2O_3 (as well as η-Al_2O_3) transforms into θ-Al_2O_3 at $\sim$ 850-1000 °C [252], a comparison with θ-Al_2O_3 was also made (see figure 4.1), which despite some similarity with the $MgAl_2O_4$ diffractogram, did not indicate presence of θ-Al_2O_3 in the sample. Such a comparison was also performed ensuring that there was no presence of α-Al_2O_3 (forms at >1150 °C [252]) or γ-Al_2O_3.

XRD was also performed for the calcined oxide phase precursors of the prepared catalysts with low and higher loading of active phase (see table 3.3 for composition). In all cases, only $MgAl_2O_4$ was

detected suggesting that active phase precursors were present at high dispersion; possibly incorporated into the spinel structure. This was also the case for a sulfided and spent NiMo catalyst, where the diffractogram was also similar to that of the support (see also section 4.2.5).

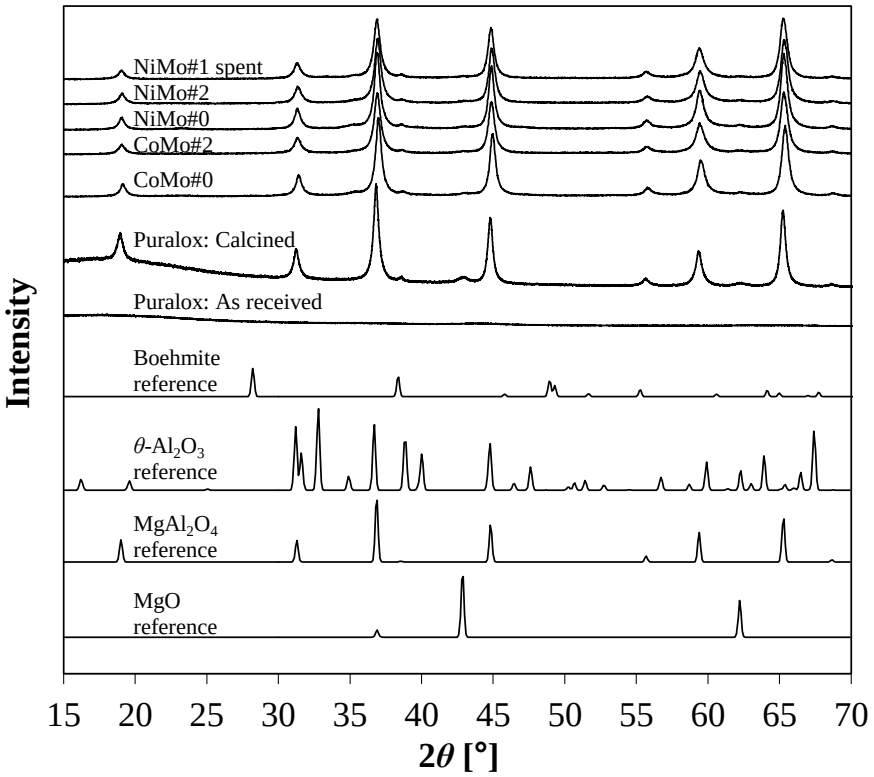

Figure 4.1: *XRD spectra of support material in as-received and calcined state, of oxide phase precursors of prepared catalysts (see table 3.3 for composition), and of a spent NiMo catalyst (see table 4.4 for composition). References for θ-Al_2O_3, $MgAl_2O_4$, MgO, and boehmite (AlOOH) have been inserted (from the ICSD Web Database [253], collection codes 82504, 39161, 9863, and 36340).*

4.2.2 NH_3-TPD

The total number of acid sites was measured by NH_3-TPD for the calcined support (SSA = 60 m^2/g) and compared with that of the precursor (SSA = 266 m^2/g), and a sample of γ-Al_2O_3 (Puralox NWa 155 from Sasol), SSA = 153 m^2/g). The resulting TPD profiles are shown in figure 4.2 with the results summarized in table 4.1. The concentration of acid sites per unit of surface area followed the trend: $MgAl_2O_4$ > γ-Al_2O_3 > Al_2O_3-MgO, but due to the low surface area of $MgAl_2O_4$, the trend based per unit of mass was: Al_2O_3-MgO > γ-Al_2O_3 > $MgAl_2O_4$. In the following, the concentration of acid sites per unit surface area is discussed.

There was no immediate difference in the concentration of acid sites (on the basis of surface area) between $MgAl_2O_4$ used in this work and conventional alumina supports. The spinel precursor showed the lowest concentration of acid sites due to the content of basic MgO, while $MgAl_2O_4$ and γ-Al_2O_3 showed similar concentration of acid sites at $\sim$ 1 μmol/m^2. Slightly higher values of 1.3-1.7 μmol/m^2 have been reported for support material aluminas [254,255], but values of 4-8 or even as high as 34

μmol/m^2 have been reported for aluminas used as dehydration catalysts [256, 257]. The broad peak in the desorption profile for γ-Al_2O_3, which has a shoulder between 30-40 minutes (figure 4.2), could indicate that both weaker and stronger acid sites were present in γ-Al_2O_3, while there was a higher concentration of weaker acid sites in $MgAl_2O_4$. However, even though the applied flow rate was quite large compared to the bed length (the linear gas velocity divided by the bed length was >9 s^{-1}), which should minimize the risk of re-adsorption phenomena during desorption, care should be taken in the interpretation of acid strength [254, 258].

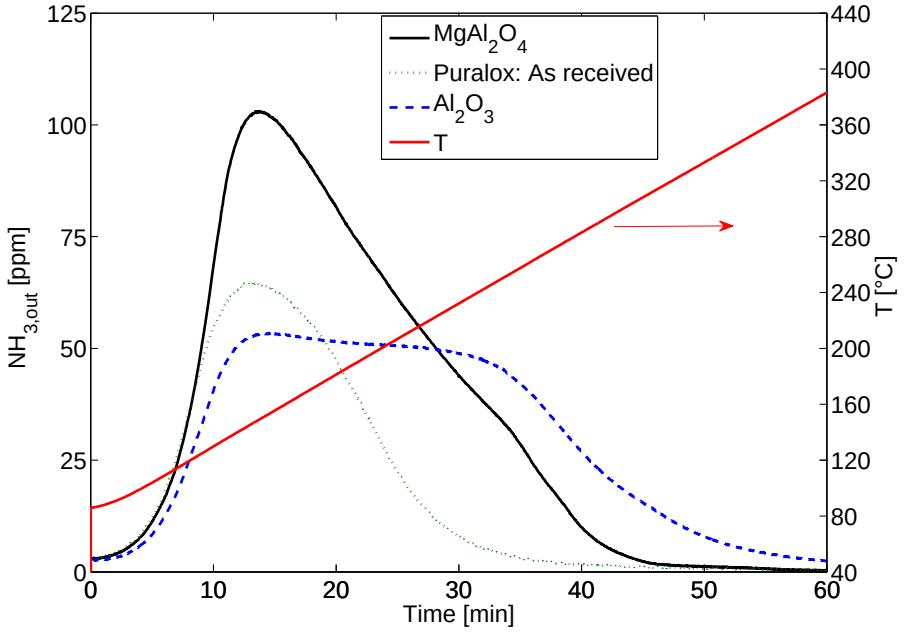

Figure 4.2: *NH_3-TPD profiles for the $MgAl_2O_4$ support material used along with its as-received precursor and a γ-Al_2O_3 sample. The mass of each sample was chosen to achieve a constant total surface area of 45 m^2 (see table 4.1).*

Table 4.1: *Concentration of acid sites (NH_3-TPD) for the support material, its precursor, and a γ-Al_2O_3 sample.*

Property	**$MgAl_2O_4$**	**Puralox: As received (Al_2O_3-MgO)**	**γ-Al_2O_3**
m [mg]	750.2	169.8	294.1
SSA [m^2/g]	60	266	153
SA [m^2]	45.0	45.2	45.0
NH_3 uptake:			
[μmol/m^2]	1.137	0.594	0.993
[mmol/g]	0.068	0.158	0.152

4.2.3 Activity of $MgAl_2O_4$

The activity of the support (without pre-sulfidation) was tested for 52 h on stream at 400 °C, 27 bar H_2, 550 ppm H_2S, and 3.4 mol% ethylene glycol in the feed with a total pressure of 40 barg (balance N_2). The average conversion was 28.3 % and there was negligible cracking and HDO activity over the support, producing a total carbon gas yield of 1.3-2.1 % (≤1.1 % ethylene, ≤0.4 % ethane, ≤0.9 % CO, ≤0.4 % CO_2, no CH_4, and no C_3). There was a more significant yield of 2-methyl-1,3-dioxolane (2.7-5.6 %), diethylene glycol (2.5-4.5 %), and ethanol (2.7-4.4 %). The yield of methanol (0.9-1.4 %) and 4-polyethylene glycol (0.3-0.8 %) along with the remaining liquid products detected, was less significant. The formation of 2-methyl-1,3-dioxolane, diethylene glycol, and 4-polyethylene glycol is proposed to occur via the reaction scheme in figure 4.3. Dehydration of ethylene glycol forms ethenol, which is expected to be shifted to its keto form, acetaldehyde, as the equilibrium constant for this reaction is $\gg 1$ with $\log(K)$ = 3-5 at 300-600 °C (calculated with HSC Chemistry). Acetaldehyde can undergo acetalization with ethylene glycol to form 2-methyl-1,3-dioxolane, while di- and polyethylene glycol can form via alcohol condensation reactions. Mixed magnesium aluminum oxides are known to catalyze both dehydration and alcohol condensation reactions [259,260], and alcohol dehydration has been reported to occur via different reaction mechanisms over Mg-rich and Al-rich $Mg_xAl_yO_z$, with the resulting rate of dehydration being the fastest for the more acidic Al-rich samples [260].

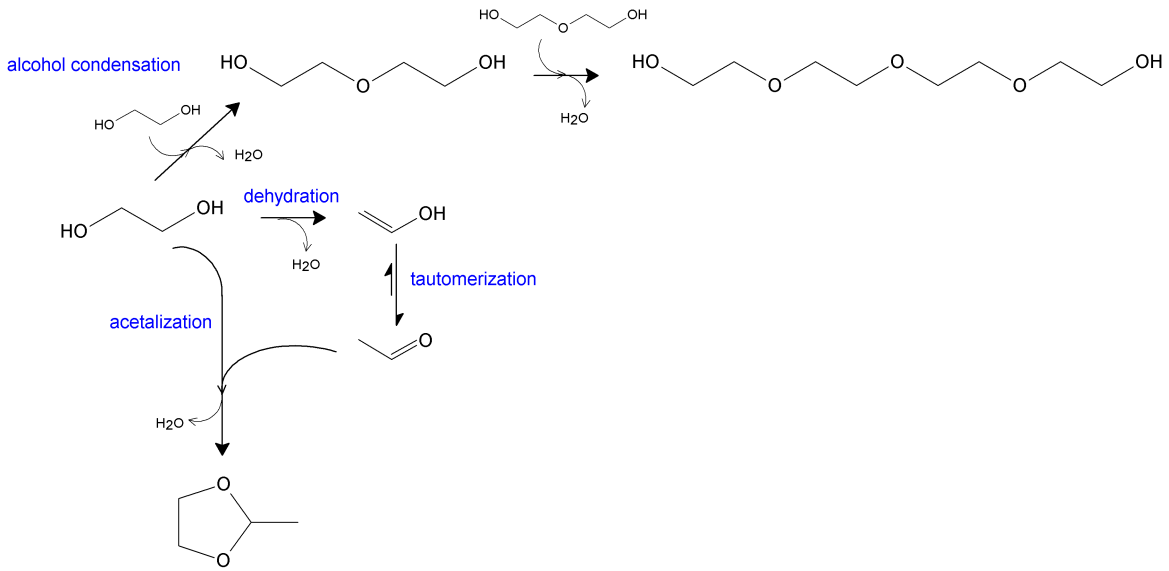

Figure 4.3: *Proposed reaction scheme for formation of common coupling products detected in the conversion of ethylene glycol over* $MgAl_2O_4$.

As shown in figure 4.4, the conversion fluctuated between 13-41 % (average: 28.3 %), while the carbon balance fluctuated between 73-102 % (average: 88.1 %). As it can be seen, these fluctuations were strongly correlated with the flow of liquid product. The fluctuations in the liquid product flow were determined by the performance of the backpressure valve V10 (see figure 3.1). This valve was manually adjusted by turning the range spring to reduce the pressure from 40 barg down to ambient. The degree of opening of the valve gradually decreased during the first day on stream. The valve was heat traced in the attempt to stabilize its temperature. The setpoint of 40 °C was possibly too low to efficiently do so, but on the other hand, a higher temperature could have induced clogging issues in the valve.

Generally, the range spring had to be adjusted during the entire runtime for all experiments to ensure a stable liquid product flow. At a given fixed range spring setting, the degree of opening in the valve was both seen to increase and decrease during experiments, probably due to slight clogging or entrainment of clogged products. In some cases, the degree of opening decreased to a level, which caused the flow through the backpressure valve to stop. The liquid product would then build up in S1, and as a safety function, the liquid feed would automatically stop. In the attempt to avoid these process upsets, which sometimes occurred overnight, the opening degree of the backpressure valve was generally set a little higher than necessary to get a stable flow, which in turn cause the flow to fluctuate more. It should be considered to perform these types of experiments with an automated pressure reduction of the effluent liquid flow, similarly to what was employed for the effluent gas flow.

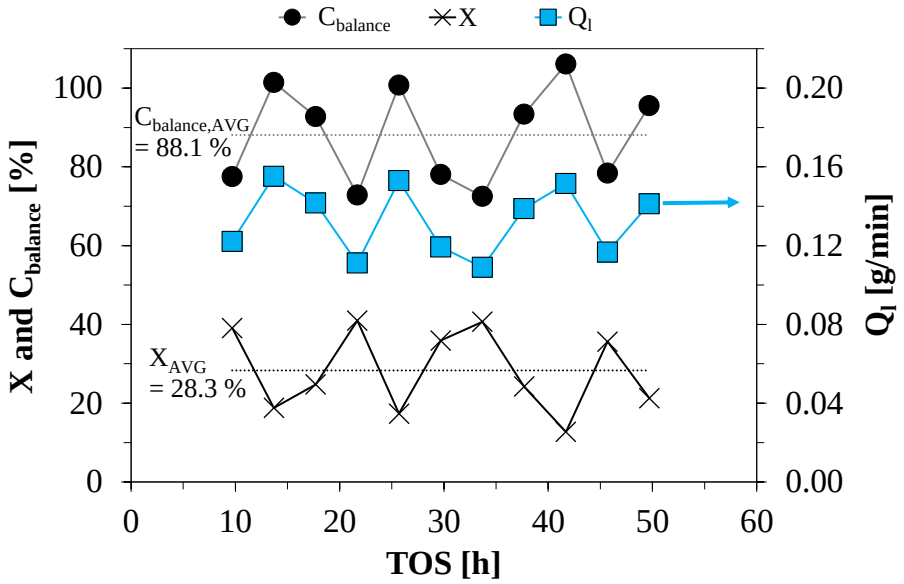

Figure 4.4: *Conversion, X, carbon balance, and liquid product flow, Q_l, from the conversion of ethylene glycol over $MgAl_2O_4$ (1.0 g) at 400 °C, 27 bar H_2, 550 ppm H_2S, and 3.4 mol% ethylene glycol in the feed with a total pressure of 40 barg (balance N_2). The liquid product density was approximately constant at 1.085-1.095 g/mL at 25 °C.*

4.2.4 NiMo and CoMo Activity

4.2.4.1 Influence of Loading and Choice of Promoter

The conversion of ethylene glycol was tested for Ni and Co promoted $MoS_2/MgAl_2O_4$ with an active phase loading corresponding to a slight sub monolayer coverage (NiMo#1 and CoMo#1) and with a four times lower loading (NiMo#0 and CoMo#0), see table 3.3, to study the interaction between the active phase and the support. For $MgAl_2O_4$, monolayer coverage is achieved at a loading of approximately 4 Mo atoms per nm^2 surface area [241], which ensures optimal spreading of oxidic molybdenum species formed during calcination [261] and results in the formation of small and highly dispersed MoS_2 particles during sulfidation. Furthermore, a low loading could be necessary to limit undesired cracking reactions.

Activity tests were performed with 2.2-3.8 mol% ethylene glycol in the feed at 400 °C, 27 bar H_2, 550 ppm H_2S, and a total pressure of 40 barg (balance N_2) using 4.0 g catalyst. The resulting activity in terms of conversion and gaseous product yields are shown in figures 4.5-4.8. The temperature increase upon addition of ethylene glycol was 4-16 °C; being highest for the more active higher loading catalysts. The reaction temperature at TOS >5 h was stable. It was 408-411 °C for NiMo#0, NiMo#1, and CoMo#0, while it was 413-416 °C for CoMo#1. During each activity test, the reaction conditions were changed after initial testing at the mentioned conditions to study the influence of H_2S or H_2O. Time on stream profiles from the initial activity test are shown in figures 4.5-4.8, while the entire time on stream profiles including varying operating conditions are included in sections 4.2.4.2 and 4.2.4.3.

The initial conversion was >90 % for all catalysts, and for the higher loading catalysts, it was close to 100 % (see figure 4.5). Full conversion (NiMo#1 and CoMo#1) resulted in notable fluctuations in the gas yields, which was correlated with fluctuations in the liquid feed. The measured carbon based liquid product yield was ≤4 % for NiMo#1 and CoMo#1, while it was ∼ 30-45 % for NiMo#0 and CoMo#0. Due to incomplete condensation, it should be noted that these yields are expected to have been higher than reported here; especially for the low loading catalysts, which produced low yields of gas products.

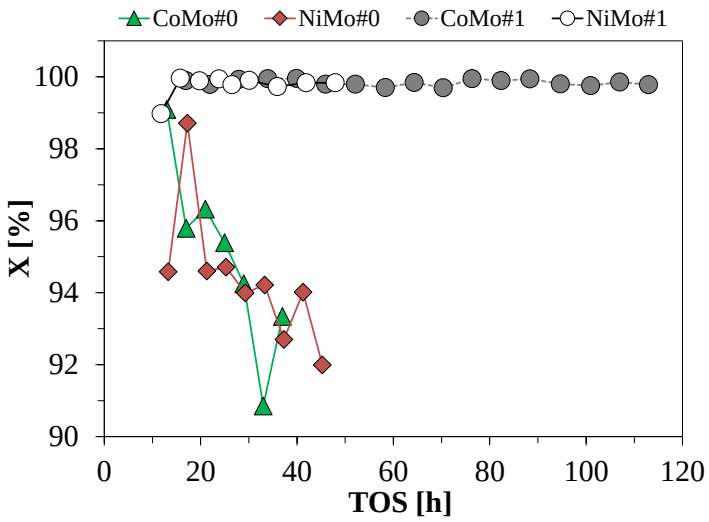

Figure 4.5: *Conversion, X, of ethylene glycol over NiMo#0, NiMo#1, CoMo#0, and CoMo#1 (4.0 g) at 400 °C, 27 bar H_2, 550 ppm H_2S, and 2.2-3.8 mol% ethylene glycol in the feed with a total pressure of 40 barg (balance N_2). For catalyst composition, see table 3.3.*

The TOS at similar reaction conditions was kept around 40-50 h, but for CoMo#1, it was extended to 118 h in order to see, if the catalyst deactivated measurably bringing the conversion below 100 %. Such deactivation in terms of a decrease in the conversion (figure 4.5) or total carbon gas yield (figure 4.6a) was not observed for the higher loading catalysts, but the C_2/C_1 ratio (see figure 4.6b) decreased until 80 h and then stabilized, indicating some deactivation in the HDO activity. The low loading catalysts were subject to deactivation during the first 40-50 h on stream, which could be observed from the conversion as well as all yields presented in figures 4.5-4.8.

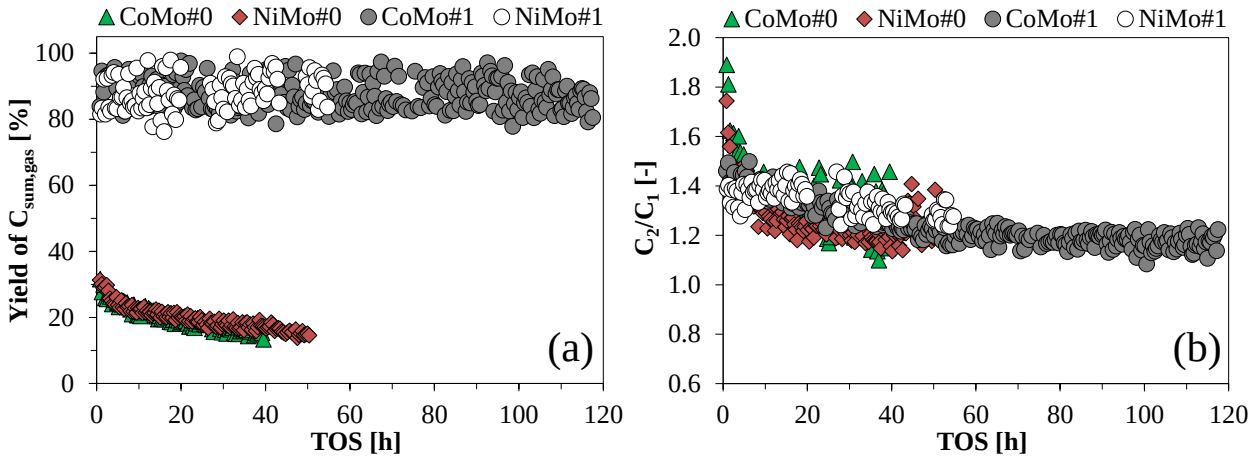

Figure 4.6: *(a) Sum of gas product carbon yields, $C_{sum,gas}$, and (b) C_2/C_1 ratio from the conversion of ethylene glycol over NiMo#0, NiMo#1, CoMo#0, and CoMo#1 (4.0 g) at 400 °C, 27 bar H_2, 550 ppm H_2S, and 2.2-3.8 mol% ethylene glycol in the feed with a total pressure of 40 barg (balance N_2). For catalyst composition, see table 3.3*

The gas product yields were similar for Ni and Co promoted catalysts with the same loading. For the higher loading catalysts, 80-100 % of the carbon feed was converted to gas products (see figure 4.6a). For the low loading catalysts, this number was initially 31 %, and then decreased to 13-15 % at 40-50 h. The ratio of HDO to cracking, the C_2/C_1 ratio, was very similar for all catalysts. It was in the range of 1.1-1.5 with a decreasing trend over time. For the low loading catalysts, the initial C_2/C_1 ratio was 1.7-1.9, but decreased to 1.5 within the first 2-5 h on stream. The independence of this ratio on the loading suggest that both HDO and cracking were equally catalyzed by the active phase without significant influence from the support.

The higher loading catalysts produced hydrogenated HDO products; no ethylene or propylene was detected. Ethane was initially produced at a yield of 40-50 %, see figure 4.7. In the case of NiMo#1, the ethane yield was stable over time, whereas a slight linear decrease was observed for CoMo#1, resulting in the average loss of 3.8 %-points of the ethane yield per hour. The low loading catalysts produced a mixture of ethylene, ethane, propylene, and propane. A slightly higher hydrogenation activity was observed for NiMo#0 compared to CoMo#0. As figure 4.7 shows, the ethane yield was 1.7-12.0 % for NiMo#0 and 1.7-10 % for CoMo#0. Both catalysts experienced an initial rapid decrease down to 4 % within the first 6-12 h on stream. The ethylene yield was 5.9-7.9 % for NiMo#0 and 6.1-10.0 % for CoMo#0. At the same time, the propane yield was $\leq$1.2 % for NiMo#0 and $\leq$0.7 % for CoMo#0, and the propylene yield was $\leq$2.1 % for NiMo#0 $\leq$2.4 % for CoMo#0. Ni promotion is commonly accepted to provide better hydrogenation activity than Co promotion, namely in the conversion of aromatic species [80,109,113,141,142,262]. In this case, however, a rather similar activity was obtained with Ni and Co promotion; especially at higher active phase loadings.

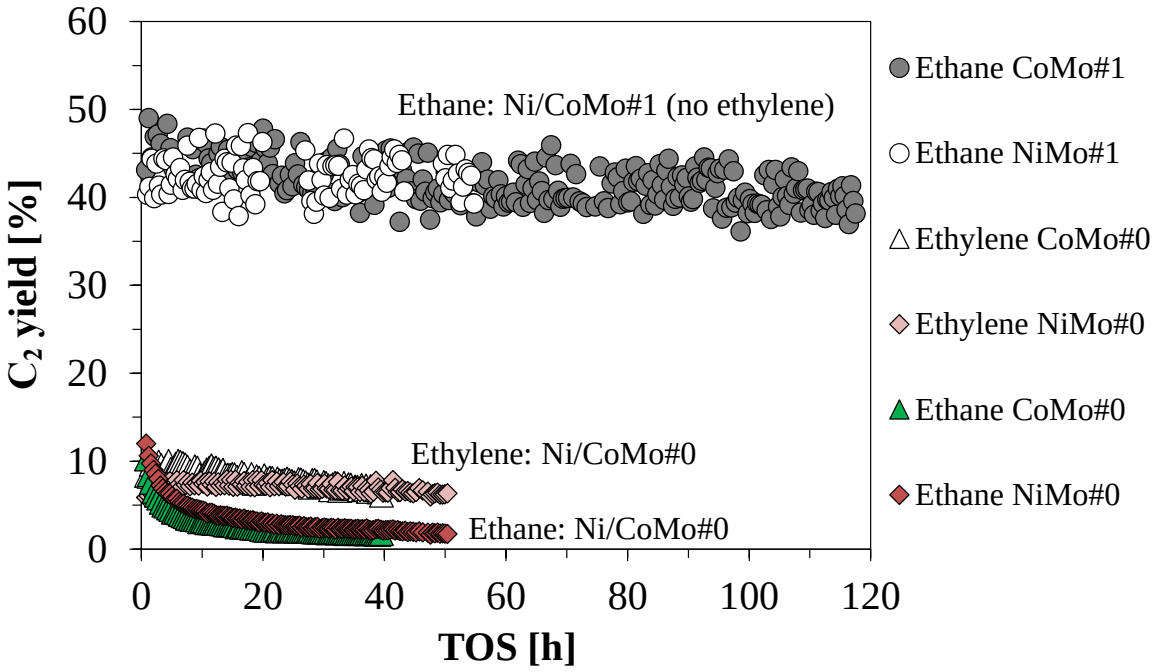

Figure 4.7: *C_2 gas product yields from conversion of ethylene glycol over NiMo#0, NiMo#1, CoMo#0, and CoMo#1 (4.0 g) at 400 °C, 27 bar H_2, 550 ppm H_2S, and 2.2-3.8 mol% ethylene glycol in the feed with a total pressure of 40 barg (balance N_2). For catalyst composition, see table 3.3.*

The cracking activity was practically identical for catalysts having the same loading (see figure 4.8). NiMo#0 and CoMo#0 produced CO, CO_2, and CH_4 at yields of 2.7-4.7 %, 2.5-4.3 %, and 0.6-3.0 %, respectively, with a decreasing trend over time. For the higher loading catalysts, there was no difference between CO, CO, and CH_4, which were all produced at yields of 8-14 %. Cracking is favored at higher temperatures [21], so if HDO is performed *in-situ* during catalytic hydropyrolysis, a catalyst with moderate activity should be employed to avoid gasification of the biomass fed. This was observed during the first $\sim$ 20 h on stream by Dayton et al. [226] who performed catalytic hydropyrolysis of woody biomass using a pre-reduced commercial hydrotreating catalyst at 375 °C and 3 bar H_2. Some cracking will, however, most likely always occur during pyrolysis and potentially also during HDO, so it is important to consider how to utilize these by-products, for example through water gas shift (WGS) and steam reforming to regain H_2 for the reaction or by production of SNG as a valuable by-product by methanation.

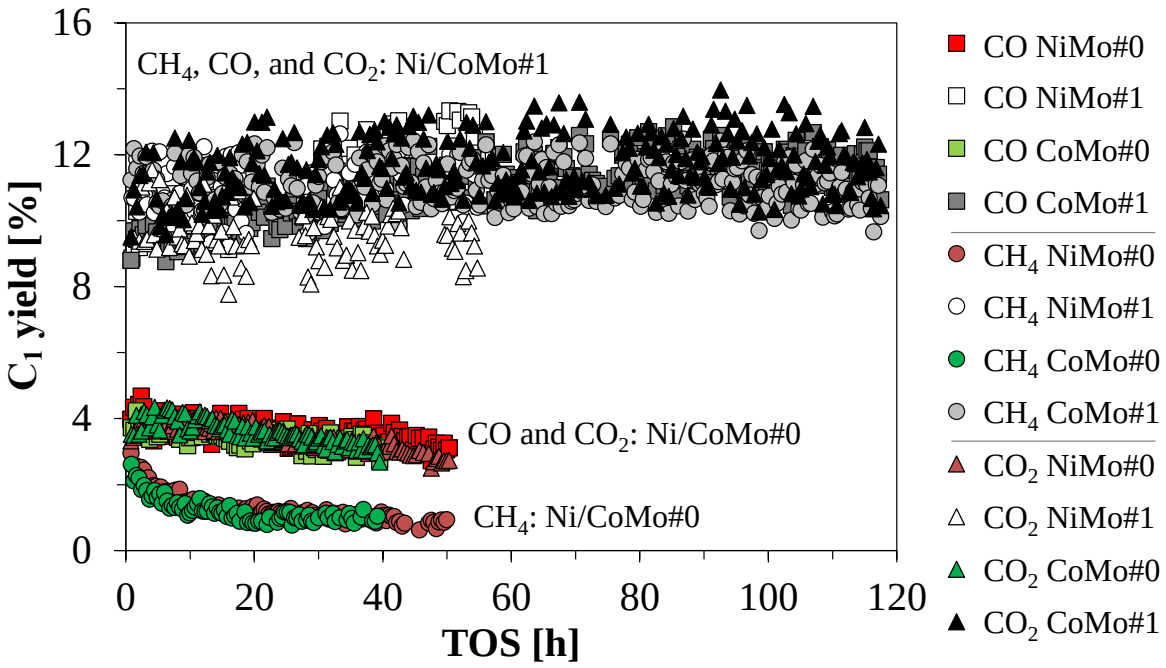

Figure 4.8: *C_1 gas product yields from conversion of ethylene glycol over NiMo#0, NiMo#1, CoMo#0, and CoMo#1 (4.0 g) at 400 °C, 27 bar H_2, 550 ppm H_2S, and 2.2-3.8 mol% ethylene glycol in the feed with a total pressure of 40 barg (balance N_2). For catalyst composition, see table 3.3.*

Comparison of the product yields at the average TOS of 16-17 h (table 4.2) illustrate the trends described above and show how a larger liquid product yield as seen for NiMo#0 and CoMo#0 was correlated with a poorer carbon balance due to incomplete condensation. During the entire time on stream, the liquid collected from NiMo#1 and CoMo#1 was practically pure water with a density of 0.994-0.997 g/mL (25 °C). A four times lower loading of active phase resulted in significant liquid product formation, and as opposed to the activity over pure $MgAl_2O_4$, a higher concentration of partly deoxygenated compounds was formed. Furthermore, the GC-FID/MS spectra revealed a complex composition with low concentrations of many partly deoxygenated and coupled products (polyols, ethers, and ketones) formed over the low loading catalysts, and in several of these compounds, C_2H_xO seemed to be a repeating unit. Only a few of these compounds, such as diethylene glycol and 4-polyethylene glycol, were present in large enough amounts for identification and quantification. With the amount of active phase being insufficient for full deoxygenation, partly deoxygenated ethoxy groups are believed to have been adsorbed on the catalyst, which could then form larger compounds over $MgAl_2O_4$ by acid catalyzed isomerization and coupling reactions [71, 74, 76]

Table 4.2: *Product distribution for conversion of ethylene glycol at 400 °C, 27 bar H_2, 550 ppm H_2S, 40 barg total (balance N_2) and 2.2-3.8 mol% ethylene glycol in the feed. For catalyst composition, see table 3.3.*

Catalyst	**NiMo#0**	**CoMo#0**	**NiMo#1**	**CoMo#1**	**$MgAl_2O_4$**
TOS [h]	15.3-19.3	15.0-19.0	13.8-17.8	14.9-18.9	15.7-19.7
$WHSV_{EG}$ [h^{-1}]	2	2	2	2	9
Conversion [%]	98.7	95.8	100	99.9	24.8
Yields [%]					
Unconverted ethylene glycol	**1.29**	**4.21**	**0.04**	**0.11**	**75.2**
Liquid products	**36.9**	**44.1**	**1.3**	**0.2**	**15.8**
Miscellaneous	12.0	13.0	0.35	<0.1	2.18
Methanol	5.22	6.15	0.23	<0.1	1.20
Ethanol	16.5	21.0	0.57	0.11	3.81
1-propanol	2.96	3.47	0.10	<0.1	0
2-methyl-1,3-dioxolane	0	0	0	0	4.30
Diethylene glycol	0.22	0.35	0	0	3.82
4-polyethylene glycol	<0.1	0.16	0	0	0.49
Gas products	**20.7**	**19.5**	**88.3**	**88.4**	**1.76**
Propane	<0.1	0	14.1	12.36	0
Propylene	1.13	0.75	0	0	0
Ethane	3.36	2.52	43.1	43.7	0.18
Ethylene	7.48	8.18	0	0	0.90
CO	3.82	3.36	10.5	9.87	0.48
CO_2	3.74	3.69	9.61	11.3	0.20
CH_4	1.20	0.98	10.9	11.2	0
Total ($C_{balance}$)	**58.9**	**67.8**	**89.6**	**88.7**	**92.8**

4.2.4.2 Influence of Varying H_2S Feed Concentration

The H_2S concentration was increased by a factor of four from 550 to 2200 ppm after 40-50 h on stream for the low loading catalysts in the attempt to reactivate them (see figure 4.9). At full HDO of the ethylene glycol fed, the water generated would give a molar H_2O/H_2S ratio of $\sim$ 120 at 550 ppm H_2S and $\sim$ 30 at 2200 ppm H_2S. After increasing the H_2S concentration, the conversion was stabilized at 92-95 % for NiMo#0 and partly stabilized, but with some deactivation, for CoMo#0 at 88-95 %. At the higher H_2S concentration the cracking activity and yield of ethylene were stabilized, whereas the yield of ethane was approximately doubled due to a higher degree of both deoxygenation and hydrogenation. The selectivity towards HDO was increased and stabilized at $C_2/C_1 \sim$ 1.4-1.8 for both catalysts. This promoting effect of H_2S in HDO of aliphatic species has been studied by Şenol et al. [109,110] and is further studied here in chapter 5. H_2S adsorbs as SH groups onto the active edges of MoS_2 and thereby provides hydrogen and acidity, which can catalyze dehydration and hydrogenation reactions [109, 129–131].

The difference between Ni and Co promotion was more pronounced when the concentration of H_2S was increased. Ni promotion facilitated a greater ethane yield, which at 2200 ppm H_2S resulted in

a better C_2/C_1 ratio of up to 1.8 compared to the Co promoted catalyst. Thus, both the choice of promoter and feed level of H_2S may affect the HDO activity.

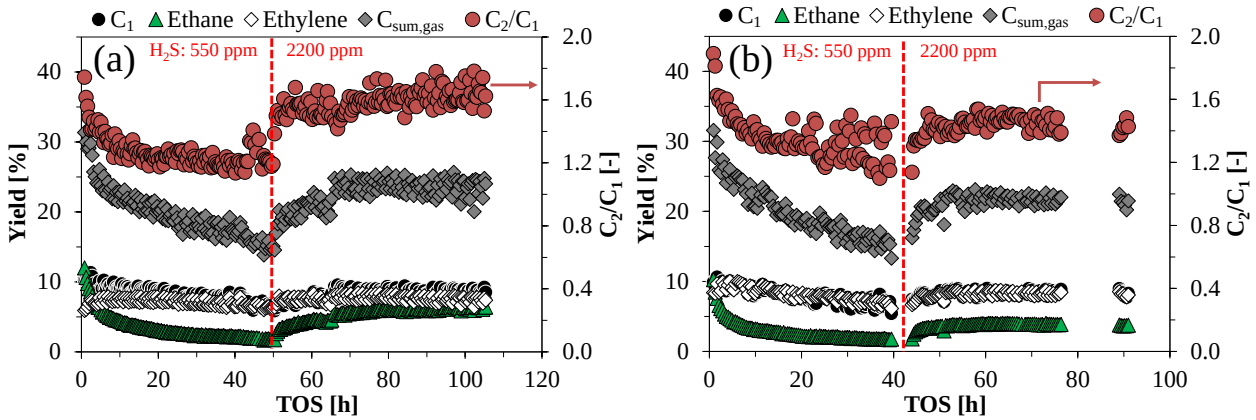

Figure 4.9: *Gas product yields from conversion of ethylene glycol over (a) NiMo#0 and (b) CoMo#0 (4.0 g) at 400 °C, 27 bar H_2, 550-2200 ppm H_2S (noted in figures), and 2.2-3.8 mol% ethylene glycol in the feed with a total pressure of 40 barg (balance N_2). The first 40-50 h on stream are also represented in figures 4.5-4.8. Please note that yields of C_1 and ethylene are almost coinciding. For catalyst composition, see table 3.3.*

The gradual reactivation, which occurred upon increasing the H_2S co-feed was not assumed to be correlated with resulfidation of partially oxidized MoS_2. Addition of water to the feed mixture was not found to oxidize the active phase (see section 4.2.4.3), and furthermore, the work presented in chapter 5 indicates that the promoted MoS_2 active phase in the prepared catalysts was stable upon water exposure, due to a strong interaction with the support.

The importance of co-feeding H_2S at a certain level was also verified from the activity test of the higher loading CoMo#1 catalyst, which was run at 550 ppm H_2S for 118 h (see figures 4.5-4.8) followed by 28 h at 240 ppm, and 26 h with practically no H_2S feed (<5 ppm). The conversion was 100 % throughout the activity test, but the product distribution revealed catalyst deactivation (see table 4.3). Firstly, a higher liquid yield was detected at lower H_2S concentrations, with a correspondingly poorer mass balance from the incomplete condensation. Secondly, the total yield of gasses decreased correspondingly with decreasing H_2S feed. In terms of HDO, both deoxygenation and hydrogenation activity decreased at 240 ppm and at <5 ppm H_2S; i.e. the combined yield of deoxygenated C_{2-3} products decreased and the yield of unsaturated ethylene and propylene increased. The yield of CO increased with decreasing H_2S in the feed, which was partly explained by a lower WGS reaction activity ($CO + H_2O \rightarrow CO_2 + H_2$), as evidenced from the lower yield of CO_2.

Table 4.3: *Product distribution for conversion of ethylene glycol at $WHSV_{EG}$ = 2 h^{-1} 400 °C, 27 bar H_2, 40 barg total (balance N_2), and varying H_2S concentration over CoMo#1. No diethylene glycol, polyethylene glycol, or 2-methyl-1,3-dioxolane was detected. For catalyst composition, see table 3.3.*

H_2S feed [ppm]	**550**	**240**	**<5**
TOS [h]	110-116[a]	140-144[b]	168-172[c]
Conversion [%]	99.8	100	99.8
Yields [%]			
Unconverted EG	**0.22**	**0**	**0.23**
Liquid products	**0.12**	**0.22**	**2.93**
Miscellaneous	<0.1	0.14	1.31
Methanol	<0.1	<0.1	0.59
Ethanol	<0.1	<0.1	0.97
1-propanol	<0.01	<0.01	<0.1
Gas products	**85.8**	**78.3**	**64.5**
Propane	12.2	10.2	4.83
Propylene	0	0.82	3.80
Ethane	39.6	33.3	23.2
Ethylene	0	0	2.98
CO	11.5	13.0	14.0
CO_2	11.7	10.0	5.93
CH_4	10.8	11.0	9.81
Total ($C_{balance}$)	**86.1**	**78.5**	**67.6**

[a] At approximate steady state from 60-118 h (see figures 4.5-4.8).

[b] At approximate steady state from 118-146 h, however with slightly increasing liquid yield over time.

[c] Not at steady state, deactivation was observed over time at 146-172 h.

4.2.4.3 Influence of Water

The sensitivity towards water was tested for NiMo#1 by switching the pure ethylene glycol feed with one containing 30 wt% water at ~ 50 h on stream, while keeping the WHSV of ethylene glycol and the flow of gasses constant (see figure 4.10). This corresponded to a feed partial pressure of 1.1 bar ethylene glycol and 1.6 bar H_2O. At full HDO of ethylene glycol, this would give a total molar H_2O/H_2S ratio of 180, while the pure ethylene glycol feed would give $H_2O/H_2S \sim 120$. Thus, addition of water increased the potential H_2O/H_2S ratio by a factor of ~ 1.5.

No severe effect of water addition was observed. Addition of water only resulted in a slight deactivation over time, but the activity was overall stable, and the conversion was 98.9-100 % during the entire TOS. The S/Mo ratio in the spent catalyst (see table 4.4) furthermore did not suggest oxidation of the active phase, which is a common worry in HDO over MoS_2 based catalysts [1,106,135]. The liquid product yield was low during the entire TOS, and addition of water did not result in a higher observed

liquid product yield, as it was 0.22-3.8 % before water addition and 0.43-0.79 % after water addition. Furthermore, no propylene or ethylene was detected. Thus, there seemed to be a greater sensitivity towards changes in the H_2S feed concentration compared to variation in the H_2O concentration. This could indicate that the promoted catalysts are stable against water induced oxidation, while a co-feed of H_2S is necessary to ensure optimal performance, for example through the adsorption of SH groups at the active edges [109, 129–131].

However, since the experiments were run at 100 % ethylene glycol conversion, it is not possible to determine, if the entire catalyst bed was utilized and therefore, the deactivation induced by water could be more severe than indicated by figure 4.10. Chapter 5 studies the influence of H_2S and H_2O at lower conversions and at the atomic level using *in-situ* XAS.

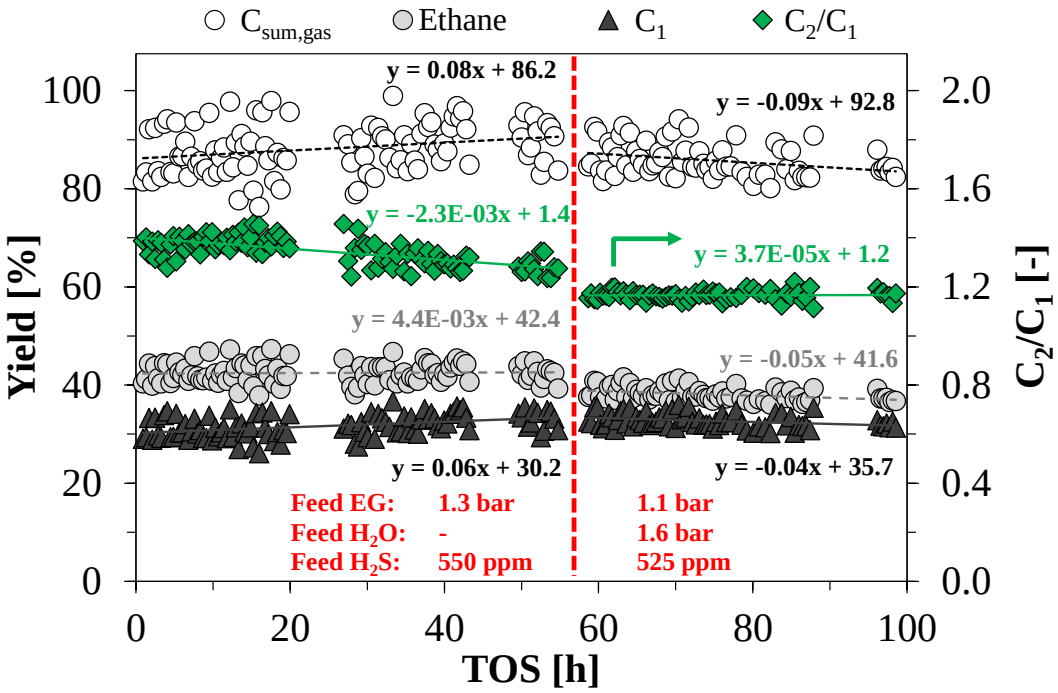

Figure 4.10: *Gas product yields from conversion of ethylene glycol over NiMo#1 (4.0 g) at 400 °C, 27 bar H_2, and 2.2-3.8 mol% ethylene glycol in the feed with a total pressure of 40 barg (balance N_2). The first 50 h on stream are also represented in figures 4.5-4.8. No ethylene or propylene was detected. For catalyst composition, see table 3.3.*

4.2.4.4 Influence of Residence Time

The WHSV of ethylene glycol was increased to lower the fluctuating gas yields and to allow for studying deactivation the behavior at less than 100 % conversion. The activity of NiMo#1 at the initial ethylene glycol WHSV of 2 h^{-1} (figures 4.5-4.8) was compared with the WHSV of 9 and 18 h^{-1}, which was obtained by decreasing the catalyst mass from 4.0 g to 1.0 g and 0.5 g, respectively. As shown in figure 4.11, the conversion was decreased below 90 % at $WHSV_{EG}$ = 18 h^{-1}, which allowed for detection of catalyst deactivation.

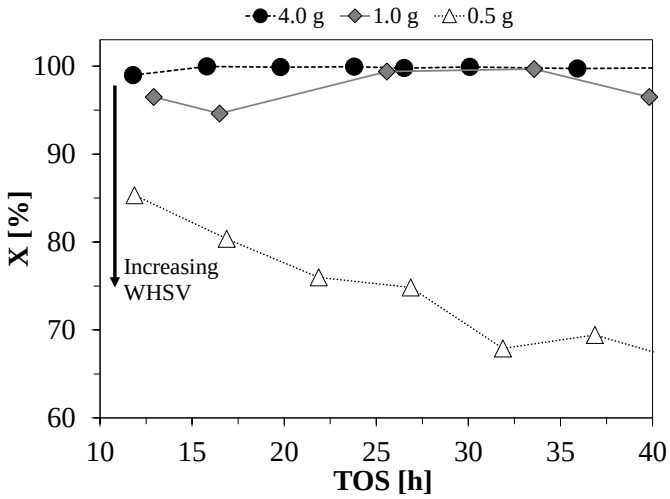

Figure 4.11: *Conversion, X, of ethylene glycol over NiMo#1 at $WHSV_{EG}$ = 2, 9, and 18 h^{-1} using 4.0, 1.0, and 0.5 g of catalyst. At 400 °C, 27 bar H_2, 550 ppm H_2S, and 40 barg total (balance N_2). For catalyst composition, see table 3.3.*

The overall product distribution from NiMo#1 was similar for all three WHSV with the ratio of $C_{sum,gas}/C_1 = 3$ (see figure 4.12). However, the concentration of unsaturated HDO products (ethylene and propylene) increased as the WHSV was increased, indicating insufficient hydrogenation activity, due to a lower amount of active phase and due to deactivation over time, similar to what was observed for the lower loading catalysts. At $WHSV_{EG} = 9\ h^{-1}$, the ratio of ethane to ethylene was 4-5 at TOS > 5.5 h, and that of propane to propylene was 1. At $WHSV_{EG} = 18\ h^{-1}$, the ethane to ethylene ratio was 1.2-1.4, and propylene was the only C_3 gas product detected.

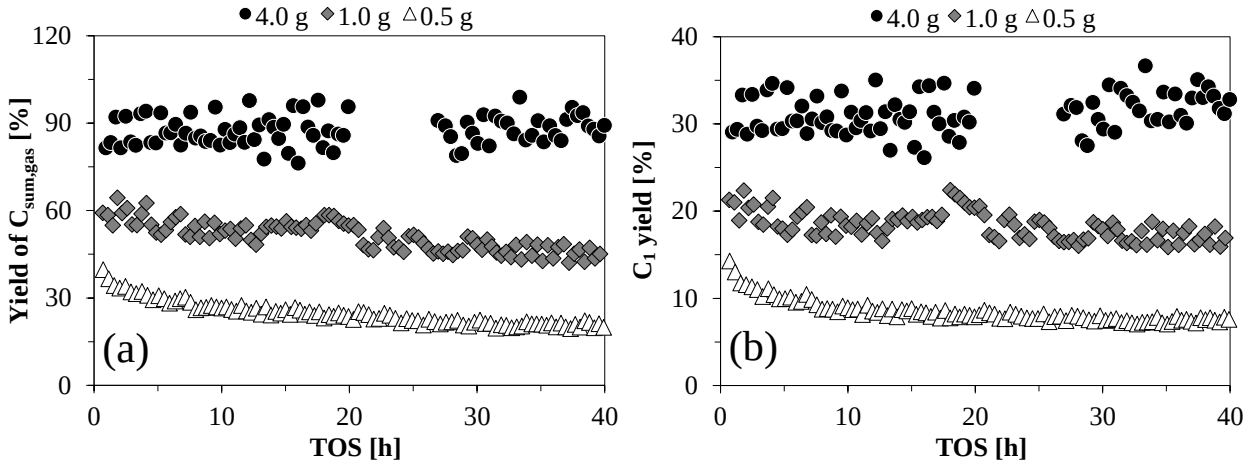

Figure 4.12: *Gas product yields from the conversion of ethylene glycol over NiMo#1 at $WHSV_{EG}$ = 2, 9, and 18 h^{-1} using 4.0, 1.0, and 0.5 g of catalyst. (a) Total gas product yield (C_1+C_2+C_3). (b) C_1 gas product yield (CO+CO_2+CH_4). At 400 °C, 27 bar H_2, 550 ppm H_2S, and 40 barg total (balance N_2). For catalyst composition, see table 3.3.*

4.2.5 Spent Catalyst Characterization

The composition of the spent catalysts (see table 4.4) was approximately the same as the fresh catalysts (table 3.3) in terms of the molar ratio of Ni/Mo, Co/Mo, and Al/Mg. Taking into account the time on stream for each activity test, the carbon deposition was more severe on the lower loading catalysts compared to the higher loading catalysts (see table 4.4). This property was ascribed to the lower hydrogenation activity and greater exposure of the acidic support, when the active phase loading was low.

Table 4.4: *Composition of spent catalysts at 400 °C, 27 bar H_2, varying H_2S concentration, and $WHSV_{EG}$ = 2 h^{-1}. For fresh catalyst composition, see table 3.3.*

Catalyst	**TOS [h]**	**H_2S [ppm]**	**Mo [wt%]**	**Ni [wt%]**	**Ni/Mo [molar]**	**Si [wt%]**	**Fe [molar]**	**S [wt%]**	**C [wt%]**	**S/Mo [molar]**	**C/TOS [wt%/h]**
NiMo#0	106	550, 2200	0.76	0.11	0.24	0.04	0.06	0.73	9.5	2.87	0.09
NiMo#1[a]	99	550, 525	2.91	0.50	0.28	0.06	0.02	2.24	3.5	2.30	0.04
				Co [wt%]	**Co/Mo [molar]**						
CoMo#0	91	550 2200	0.73	0.11	0.25	0.03	0.04	0.70	9.1	2.87	0.10
CoMo#1	172	550, 240, <5	2.56	0.44	0.28	0.05	0.06	1.77	8.8	2.07	0.05
			Mg [wt%]	**Al [wt%]**	**Al/Mg [molar]**						
$MgAl_2O_4$[b]	52	550	16	33	1.86	0.02	0.06	0.06	4.3	-	0.08

[a] Water was added to the feed after 55 h on stream.
[b] $WHSV_{EG}$ = 9 h^{-1}.

Dark-field TEM images of the spent CoMo#1 sample (figure 4.13) show that the active Co-MoS_2 phase was present as small ($\sim$ 5 nm long) slabs, seemingly present in monolayers, and with very high dispersion.

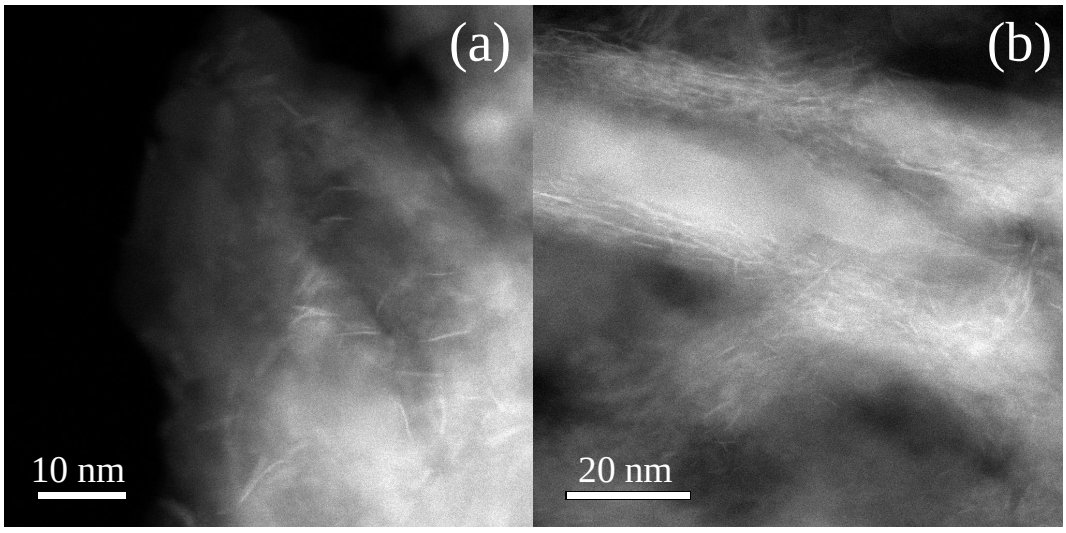

Figure 4.13: *High-angle annular dark-field scanning TEM (HAADF-STEM) images of the spent CoMo#1 sample (see table 4.4). Co-MoS_2 crystallites are visible as bright slabs.*

The spent higher loading catalysts showed similar Raman spectra (figure 4.14) with characteristic MoS_2 Raman bands at 381 and 407 cm^{-1} with a smaller peak at 451 cm^{-1} [263–266]. No peaks were associated with the presence of bulk Ni_3S_2 or Co_9S_8, which was further supported by the identical shape of the spectra obtained from the Ni- and Co-promoted sample. The peaks at 194 and 229 cm^{-1} could possibly be from the presence of MoS_3 [264], but a peak at 530 cm^{-1} was not observed. No peaks were associated with oxide phases of Mo, Ni, or Co as observed in the oxide phase catalyst precursors (see chapter 5.2.4.1). The absence of oxide phases suggests that the prepared catalysts were stable against oxidation at the applied conditions. Additionally, $MgAl_2O_4$ was stable against water, as seen from the XRD spectrum of the spent NiMo#1 sample, which was exposed to water (see figure 4.1). In HDO, this is a clear advantage compared to commonly applied γ-Al_2O_3, which forms boehmite upon water exposure [87,197].

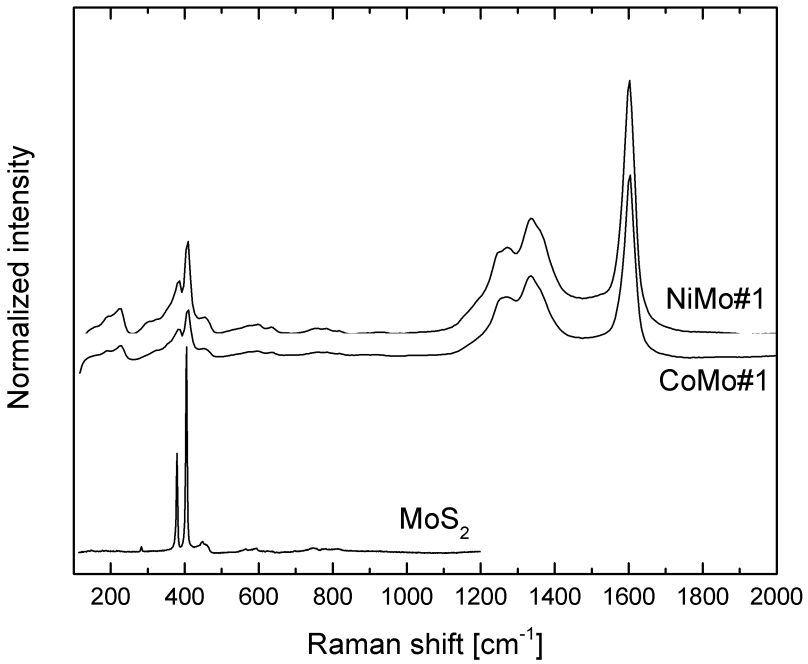

Figure 4.14: *Baseline corrected Raman spectra of spent NiMo#1 and CoMo#1 (see table 4.4) along with a MoS_2 reference (Sigma-Aldrich 99 %).*

Carbon deposition in the spent catalysts was clearly evident from the Raman spectra (figure 4.14). The sharp peak at 1600 cm^{-1} corresponds to crystalline carbon with an ideal graphite lattice (G band), while the broader peaks at 1200-1400 cm^{-1} correspond to a distorted lattice and are typical for more amorphous carbon species [267,268]. Overall, due to the comparatively sharp carbon bands and the strong presence of the G band, the observed carbon species seem crystalline and mostly graphite-like. It is proposed to choose a catalyst with good hydrogenation activity, such as Ni-MoS_2, and operate at moderate to high hydrogen pressure to minimize carbon deposition. As support acidity contributes markedly to the coke formation [75–77], a less acidic support than $MgAl_2O_4$ could be considered.

4.3 Conclusions

Sulfided NiMo and CoMo catalysts were tested for activity in the HDO of ethylene glycol. The Mo loading was targeted at a slight sub monolayer (2.83-3.28 wt%) and at four times lower loading (0.83-0.88 wt%) to study the influence of loading and the interaction with the $MgAl_2O_4$ support. $MgAl_2O_4$ was seen to catalyze dehydration and coupling reactions, which was ascribed to the presence of acid sites, but no significant HDO or cracking was observed.

At an ethylene glycol WHSV of 2 h^{-1}, a conversion >90 % could be obtained for both low and higher loading NiMo and CoMo catalysts. These catalysts produced C_1-C_3 gas products with a moderate selectivity towards HDO relative to cracking in terms of a C_2/C_1 ratio of 1.1-1.5. HDO and cracking reactions were equally catalyzed by the active phase, giving a similar C_2/C_1 ratio independent of catalyst loading. A higher catalyst loading did however enable superior hydrogenation activity, which in turn also resulted in lower carbon deposition on the spent catalysts, possibly masked by the high conversion of 100 % and incomplete usage of the catalyst bed.

Ni and Co promotion gave rise to similar activities and product distributions at the applied conditions, but hydrogenation seemed to be favoured over NiMo. A co-feed of H_2S was necessary to avoid accelerated deactivation. The level of H_2S affected the deoxygenation and hydrogenation activity with a promoting effect with more H_2S. An increase in the ethylene glycol WHSV from 2 to 18 h^{-1} was necessary to achieve a conversion below 90 %, and a high WHSV should be applied in further work, if deactivation and reactivation mechanisms are to be studied further.

5 | Influence of H_2O and H_2S

Influence of H_2O and H_2S on the Composition, Activity, and Stability of Sulfided Mo, CoMo, and NiMo Supported on $MgAl_2O_4$ for Hydrodeoxygenation of Ethylene Glycol

Abstract

In this work, density functional theory (DFT), catalytic activity tests, and *in-situ* X-ray absorption spectroscopy (XAS) was performed to gain detailed insights into the activity and stability of MoS_2, Ni-MoS_2, and Co-MoS_2 catalysts used for hydrodeoxygenation (HDO) of ethylene glycol upon variation of the partial pressures of H_2O and H_2S. The results show high water tolerance of the catalysts and highlight the importance of promotion and H_2S level during HDO.

DFT calculations unraveled that the active edge of MoS_2 could be stabilized against S-O exchanges by increasing the partial pressure of H_2S or by promotion with either Ni or Co. The Mo, NiMo, and CoMo catalysts of the present study were all active and fairly selective for ethylene glycol HDO at 400 °C, 27 bar H_2, and 550-2200 ppm H_2S, and conversions of $\sim$ 50-100 %. The unpromoted $Mo/MgAl_2O_4$ catalyst had a lower stability and activity per gram catalyst than the promoted analogues. The NiMo and CoMo catalysts produced ethane, ethylene, and C_1 cracking products with a C_2/C_1 ratio of 1.5-2.0 at 550 ppm H_2S. This ratio of HDO to cracking could be increased to $\sim$ 2 at 2200 ppm H_2S which also stabilized the activity. Removing H_2S from the feed caused severe catalyst deactivation. Both DFT and catalytic activity tests indicated that increasing the H_2S concentration increased the concentration of SH groups on the catalyst, which correspondingly activated and stabilized the catalytic HDO performance. *In-situ* XAS further supported that the catalysts were tolerant towards water when exposed to increasing water concentration with H_2O/H_2S ratios up to 300 at 400-450 °C.

Raman spectroscopy and XAS showed that MoS_2 was present in the prepared catalysts as small and highly dispersed particles, probably owing to a strong interaction with the support. Linear combination fitting (LCF) analysis of the X-ray absorption near edge structure (XANES) spectra obtained during *in-situ* sulfidation showed that Ni was sulfided faster than Mo and CoMo, and that Mo was sulfided faster when promoted with Ni. Extended X-ray absorption fine structure (EXAFS) results showed the presence of MoS_2 in all sulfided catalysts. Sulfided CoMo was present as a mixture of CoMoS and Co_9S_8, whereas sulfided NiMo was present as NiMoS.

5.1 Introduction

DFT studies have indicated that exposure of MoS_2 to water vapor can lead to exchange of S with O at the active edge of MoS_2 and that promotion can stabilize the catalyst against these exchanges [106,107]. Co-feeding of H_2S is necessary to keep the catalyst in its active sulfide form [1, 67, 106, 135] and to enhance the activity [106,136]. H_2S can however also inhibit the reaction [109,111,113], as it potentially saturates the coordinatively unsaturated sites (CUS), which are commonly accepted as active sites for oxygenate adsorption and deoxygenation [92, 128–130]. Badawi et al. [106] reported that the state of the active edge can be controlled through the H_2O/H_2S ratio to avoid S-O exchanges, but the influence of water on the working catalyst has not been fully understood [136]. In order to optimize sulfide catalysts for HDO, a water tolerant support material should be chosen and the influence of H_2S and H_2O should be investigated experimentally; both in terms of HDO activity and catalyst structure.

In this work, MoS_2, Ni-MoS_2, and Co-MoS_2 clusters have been modeled with DFT to obtain insights into structural changes at the active edges under exposure to varying H_2O/H_2S ratios. MoS_2, Ni-MoS_2, and Co-MoS_2 supported on a water tolerant and attrition resistant $MgAl_2O_4$ spinel support were prepared and tested for the hydroconversion of ethylene glycol. Ethylene glycol was chosen as a simple model sugar fragment; representing the more reactive fraction of pyrolysis vapors. The influence of varying the feed concentration of H_2S was tested in catalyst activity tests with constant ethylene glycol feed. The evolution of the active sulfide phase in the catalysts was studied *in-situ* with XAS in terms of XANES and EXAFS. At first, sulfidation rates were compared for the three catalysts. The influence of varying H_2O/H_2S ratios on the catalyst structure was furthermore investigated experimentally using *in-situ* XAS.

5.2 Results and Discussion

5.2.1 DFT Phase Diagrams

Unpromoted MoS_2 can exhibit a triangular crystal structure exposing only one type of edge, or a hexagonal (truncated triangle) structure depending on the H_2S/H_2 ratio [127]. Promoted MoS_2 exhibits a hexagonal structure with exposure of pure M- and metal doped S-edges [122, 123, 126, 269]. For NiMoS, a less systematic distorted hexagonal structure has also been reported [123]. Figure 5.1 shows the calculated phase diagrams for unpromoted MoS_2 (M-edge), Ni-MoS_2 (S-edge), and Co-MoS_2 (S-edge) at varying H_2O/H_2S partial pressures and 400 °C. Due to the inherent uncertainty associated with generalized gradient approximation (GGA) DFT, it must be noted that the phase diagrams are representative of the trends between the different materials, but do not reflect precise numbers. Thus, the partial pressures of water and H_2S mentioned in the remainder of this section serve the purpose of distinguishing the different edge structures obtained from DFT to clarify the general trends observed in figure 5.1 at varying partial pressures of H_2S and H_2O.

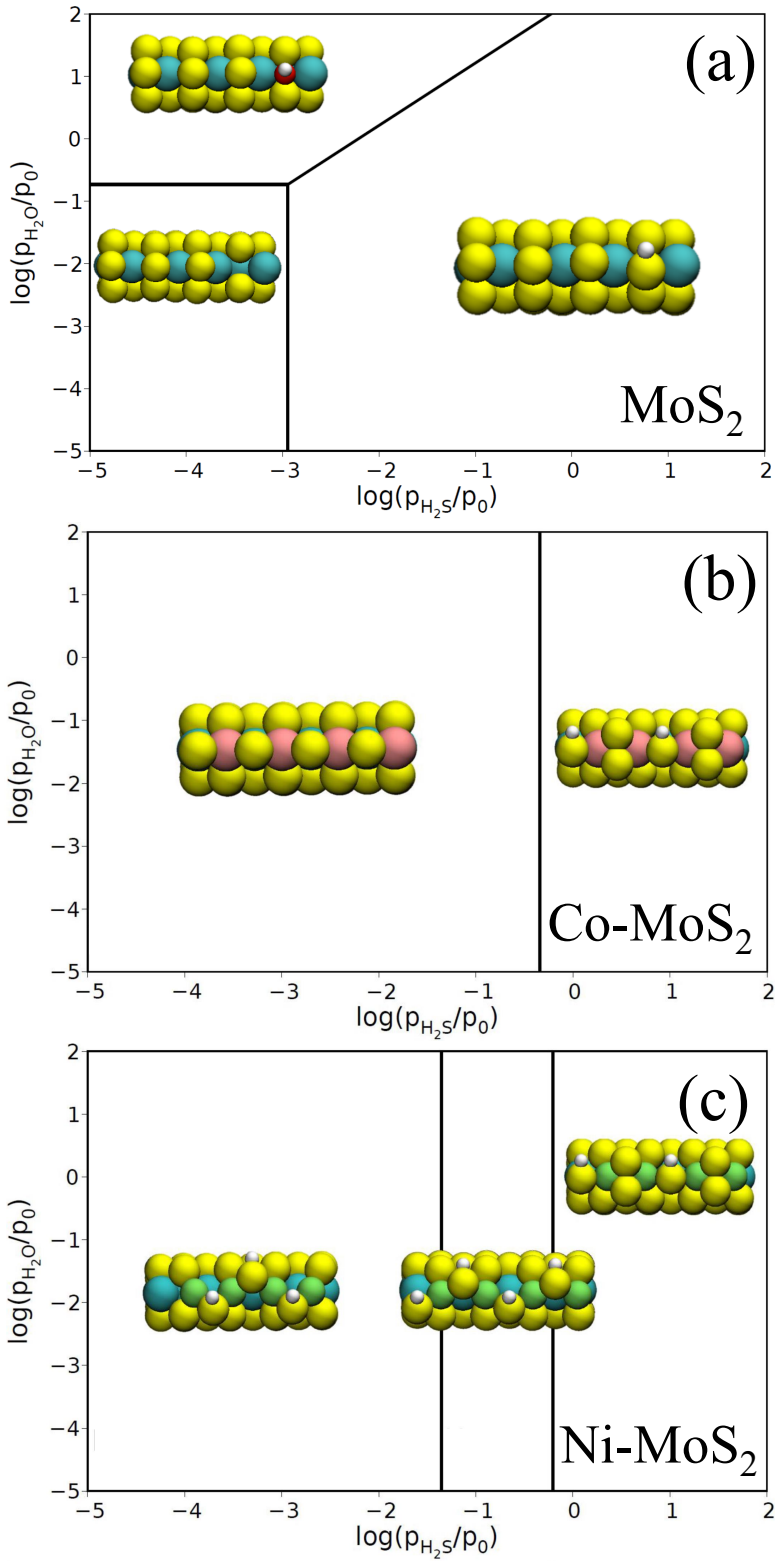

Figure 5.1: *Phase diagrams as function of the partial pressure of water and H_2S for (a) the unpromoted MoS_2 M-edge, and the promoted S-edges of (b) Co-MoS_2, and (c) Ni-MoS_2 as obtained from DFT calculations. Yellow = S, blue = Mo, pink = Co, green = Ni, red = O, white = H. Total pressure 40 bar, 28 bar H_2, 400 °C, p_0 = 1 bar.*

The MoS_2 edge has a single S-vacancy and exhibits a $Mo_{1.00}S_{0.75}$ structure in the range of $\log(p_{H_2O}/p_0)$ = < -0.7 and $\log(p_{H_2S}/p_0)$ < -3 corresponding to ∼ 0.3-5000 ppm H_2O and ∼ 0.3-30 ppm H_2S (see figure 5.1a). An OH group adsorbs on the vacancy site if the H_2O pressure is increased further, resulting in a $Mo_{1.00}S_{0.75}(OH)_{0.25}$ edge structure. If instead the H_2S concentration is increased above 30 ppm, an SH group adsorbs on the vacancy (H_2O concentration <5000 ppm) and the edge structure becomes $Mo_{1.00}S_{1.00}H_{0.25}$. In the concentration range of >5000 ppm H_2O and 30 ppm to 1.5 % H_2S, the H_2O/H_2S ratio should be kept below ∼ 150 to avoid an S-O exchange at the surface. At a H_2S concentration >1.5 %, no S-O exchange is observed no-matter the H_2O pressure. These results indicate that a certain concentration of H_2S should be fed during HDO to avoid oxidation of unpromoted MoS_2 in line with results from other theoretical work [106].

The Co promoted MoS_2 does not exhibit any vacancy formation or S-O exchange in the investigated H_2O/H_2S ranges, which indicates that Co stabilizes the active edge against oxidation (see figure 5.1b). Below $\log(p_{H_2S}/p_0)$ = -0.3, corresponding to ∼ 1 % H_2S, the S-edge is fully decorated with S (edge structure $Co_{1.00}S_{1.00}$), and if the H_2S pressure is increased, two additional S atoms and two H atoms are adsorbed on the surface giving the edge structure $Co_{1.00}S_{1.50}H_{0.50}$. This indicates that the $Co_{1.00}S_{1.00}$ structure has CUS, which could act as active sites for oxygenate adsorption and deoxygenation [128].

Ni promotion also stabilizes the edge; no S-O exchange is observed at the investigated conditions (see figure 5.1c). Three stable phases were obtained with structures that are less ordered compared to the Co promoted analogue; $Ni_{1.00}S_{0.75}H_{0.75}$, $Ni_{1.00}S_{1.00}H_{1.00}$, and $Ni_{1.00}S_{1.50}H_{0.50}$ at low, intermediate, and high H_2S concentration, respectively. H atoms are adsorbed on the surface in the entire H_2S partial pressure range. A single sulfur vacancy is present below ∼ 1000 ppm H_2S ($\log(p_{H_2S}/p_0)$ = -1.35). At ∼ 1000 ppm to 1.5 % H_2S ($\log(p_{H_2S}/p_0)$ = [-1.35;-0.21]), the edge is fully decorated with S exhibiting a $Ni_{1.00}S_{1.00}H_{1.00}$ structure. At higher concentrations, more S is adsorbed indicating presence of CUS at <1.5 % H_2S.

5.2.2 Conversion of Ethylene Glycol over Promoted and Unpromoted $MoS_2/MgAl_2O_4$

Based on the results from the catalytic activity tests, HDO of ethylene glycol is proposed to follow a reaction mechanism involving consecutive dehydration and hydrogenation steps (figure 5.2):

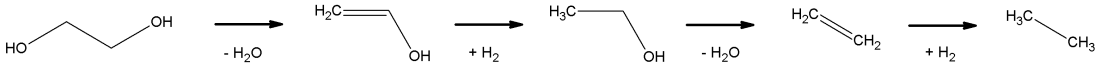

Figure 5.2: *Proposed reaction scheme for HDO of ethylene glycol via consecutive dehydration and hydrogenation reactions.*

5.2.2.1 Overall Activity

The results from the activity tests are shown in figure 5.3 (conversion, STY, and C_2/C_1) in this section and figure 5.4 (yields of ethane, ethylene, and ethanol) in section 5.2.2.4. All gas product yields can be found in Appendix H, figure H.1. The conversion of ethylene glycol was in the range ∼ 50-100 % for the prepared catalysts, and the selectivity towards HDO in terms of the C_2/C_1 ratio followed the trend MoS_2 > Ni-MoS_2 ∼ Co-MoS_2 > NiS_x (see figure 5.3).

A blank experiment (steel reactor packed with steel wool and SiC) showed negligible HDO activity; ethylene was the main gaseous product formed with a yield <0.7 %. In all experiments performed using MoS_2 based catalysts, the yield of ethane and ethylene, respectively, was in the range of ~ 5-45 % depending on the catalyst and level of deactivation. The detected yield of ethanol was 4.5-18 % and accounted for the majority, ~ 35-55 %, of carbon in the liquid products formed (for methanol, this number was 13-18 %). Cracking reactions also occurred, resulting in the formation of CH_4, CO, and CO_2; the latter possibly through the WGS reaction. C-C bond formation also occurred forming small amounts of C_{3+} gas and liquid species, e.g. propane, propylene, 1-propanol, butane, and 1-butanol.

Coupling reactions forming e.g. 2-methyl-1,3-dioxolane and 4-polyethylene glycol were also observed and ascribed to the support acidity, which is known to catalyze coupling reactions such as transalkylation, polymerization, and coking [74–76]. The conversion of ethylene glycol over the pure $MgAl_2O_4$ support (1.0 g) produced an insignificant total gas carbon yield of ≤2 % (C_1, C_2, and no C_3) and a more significant yield of 2-methyl-1,3-dioxolane (≤5.6 %), diethylene glycol (≤4.5 %), and ethanol (≤4.4 %) over 52 h on stream at a conversion of 13-41 % (see chapter 4). Partly deoxygenated and reactive intermediates, such as ethyl or ethoxy groups can readily undergo polymerization if they are not stabilized by hydrogenation into ethane. Ethylene and propylene are furthermore known to be strong coke precursors [270].

Ni-sulfides have shown moderate activity in HDO [70]. The tested Ni catalyst, however, showed poor HDO selectivity at 55-65 % conversion with a C_2/C_1 ratio of ~ 1 at 550 ppm H_2S and low STYs <0.3 mmol/g_{cat}/min (see figure 5.3a). The C_2/C_1 ratio could be increased to ~ 1.5 at 2200 ppm H_2S; mainly by increasing the yield of ethylene, while the yield of ethane remained <1.5 % and the C_2 STY remained low (see figure 5.4a).

The presence of promoter and the feed concentration of H_2S influenced the activity and stability of the Mo, NiMo, and CoMo catalysts as discussed in section 5.2.2.3. During the first ~ 50-70 h of time on stream (TOS), the feed contained 550 ppm H_2S. Then, the H_2S concentration was increased by a factor of four to 2200 ppm. For the NiMo catalyst (see figure 5.3c and figure 5.4c), a subsequent decrease of H_2S down to 1900 ppm was performed from ~ 140-160 h on stream, followed by a stepwise shut-off of H_2S. For the CoMo catalyst, (see figure 5.3d and figure 5.4d), an issue with the ethylene glycol feed arose at TOS ~ 80-90 h. In that period, the feed consisted of reaction gas (N_2, H_2, H_2S) without ethylene glycol.

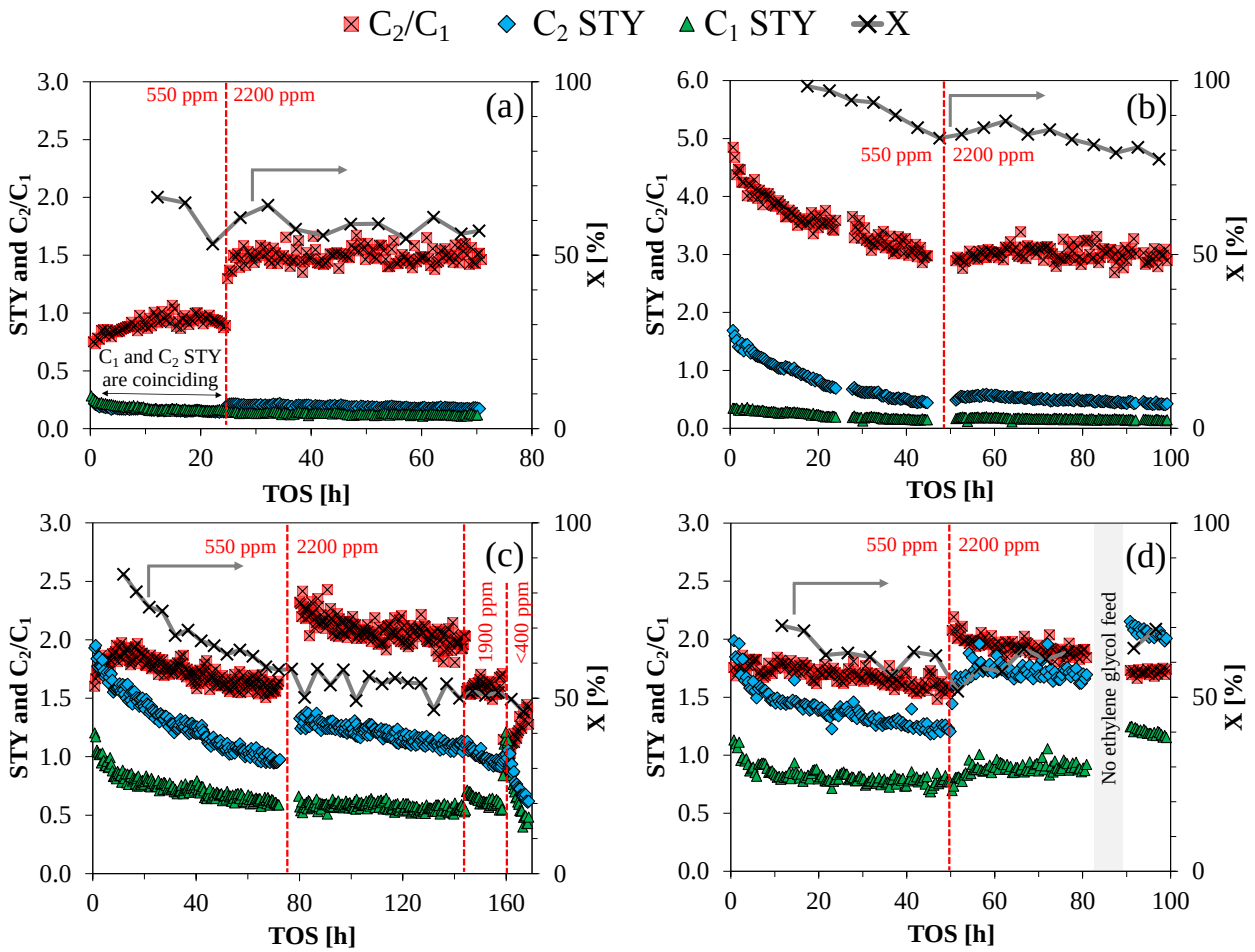

Figure 5.3: *STY [mmol/g_{cat}/min], C_2/C_1 ratio [-], and conversion for ethylene glycol conversion at 400 °C, 27 bar H_2, 550-2200 ppm H_2S (noted in figures), 40 barg total (balance N_2), and 3-3.5 mol% ethylene glycol in the feed for (a) Ni#1(1.5 g), (b) Mo#1 (1.5 g), (c) NiMo#1 (0.5 g), and (d) CoMo#1 (0.5 g) in table 3.3. Cooling on separator tube S1 was not installed in experiments (c) and (d).*

5.2.2.2 Carbon Mass Balance

The carbon mass balance could not be fully closed for the presented experiments; the balance closure at TOS >20 h was 69-83 % for NiS_x (figure 5.3a), 63-76 % for Mo (figure 5.3b), 72-84 % for NiMo (figure 5.3c), and 73-91 % for CoMo (figure 5.3d). The lack of closure in the mass balance was ascribed to the presence of mainly non-condensed oxygenate compounds in the gas phase, which were not detected or quantified. Based on off-line GC-FID and GC-TCD analysis of gas samples from experiments similar to those presented in this work, it was found that the product gas contained non-condensed hydrocarbons (C_{4-6} isomers) and oxygenates (ethanol, acetaldehyde, methanol, 2-propanone, 1- and 2-propanol, 2-butanone, and 2-pentanone), which could not be detected by the online GC analysis. These compounds were present in concentrations, which could account for majority of the missing carbon. As a consequence, the yield of ethanol (figure 5.4) can be assumed to be higher than reported here. In order to improve the carbon balance, it can be considered to perform online analysis of the oxygenates and C_{4+} hydrocarbons present in the gas phase, and to improve cooling further in the liquid product collection and storage.

In an experiment using 4 g NiMo, 100 % conversion into gas and pure water was obtained, and the mass balance could be closed within 87-96 % (no cooling of S1). Also, an >20 h empty tube test conducted at 400 °C and 40 barg, feeding 500 NmL/min N_2 and 0.14 mL/min ethylene glycol had an average carbon balance of 95 % (no cooling of S1). Elemental carbon analysis of four liquid samples from the Mo test (figure 5.3b, 68-83 h) using a Eurovector EA3000 CHNS analyzer was used to confirm that the carbon content determined by GC-FID/MS was precise within a deviation of <10 %. Thus, the gas product results (yields, STY, and C_2/C_1) and the conversion (based on unconverted ethylene glycol) are not affected by the discrepancy in the carbon mass balance. A more detailed review of the carbon mass balance is given in Appendix G.

5.2.2.3 Role of Promotion and H_2S in the C_2/C_1 Selectivity and Stability

Unpromoted Mo showed a very favorable selectivity towards HDO products compared to the promoted catalysts. The ratio of C_2/C_1 was approximately ≥3 for the entire run (see figure 5.3b), while it was <2.5 for the promoted catalysts (see figure 5.3c-d). The mass based productivity was, however, lower for the unpromoted, which initially had a C_2 STY of 1.7 mmol/g_{cat}/min, while it was 1.9-2.0 mmol/g_{cat}/min for the promoted catalysts. Furthermore, the unpromoted catalyst was subject to significant deactivation. After 40 h on stream, the C_2 STY was 0.5 mmol/g_{cat}/min and had thereby decreased by 70 %. In the same period of time, the C_2/C_1 ratio dropped by 30 % from 4.8 to 3.3, showing a decrease in HDO selectivity. In comparison, the promoted catalysts only deactivated with 35 % in terms of the C_2 STY in the same period of time reaching 1.2 mmol/g_{cat}/min at 40 h. The initial decrease in the C_2/C_1 ratio was similar for NiMo and CoMo reaching 1.6 at 40 h. Promotion with Ni or Co was therefore seen to enhance the activity of the catalyst, which is in agreement with other studies on the role of promotion in HDO and HDS over MoS_2 based catalysts [106,113,123,132,133,135]. The selectivity to HDO products was, however, higher for the unpromoted catalyst.

As the H_2S concentration was increased from 550 to 2200 ppm at TOS ∼ 50 h for the unpromoted catalyst, a slight stabilizing effect was obtained, but the activity remained low (see figure 5.3b). For both NiMo and CoMo, the C_2 STY increased when the H_2S concentration was increased to 2200 ppm and a stabilized activity was obtained. For NiMo (see figure 5.3c), the C_2 STY increased from 0.98 to 1.3 mmol/g_{cat}/min (at TOS ∼ 75-80 h) resulting in a C_2/C_1 improvement from 1.6 to 2.3. For CoMo (see figure 5.3d), the C_2 STY increased from 1.2 to 1.7 mmol/g_{cat}/min (at TOS ∼ 50 h), giving a C_2/C_1 from 1.6 to 2.0, since there was also a slight increase in the C_1 STY. The conversion of ethylene glycol did not increase, as the H_2S concentration was changed during each experiment (see figure 5.3), but a slight stabilization of the conversion occurred as the H_2S concentration was increased from 550 to 2200 ppm.

For the NiMo catalyst, it was seen that with a slightly lower H_2S concentration of 1900 ppm (TOS ∼ 140-160 h), deactivation occurred at a faster rate than at 2200 ppm H_2S, and the selectivity towards cracking products increased (see figure 5.3c). A further decrease to <400 ppm H_2S caused severe deactivation. It can be concluded that a feed of H_2S is necessary to keep the catalyst active and that this concentration should be in the order of 2200 ppm at the applied conditions to ensure a higher selectivity towards HDO and a stable activity.

As the ethylene glycol flow was reapplied after feed issues at TOS ∼ 80-90 h (see figure 5.3d) during the CoMo test, the catalyst was more active with a slightly higher conversion (65-70 % at 92-97 h compared to 61-63 % at 72-77 h) and a higher yield of both cracking and HDO products. The activity in terms of yields of ethane (see figure 5.4d) and some C_1 gasses (see also Appendix H,

figure H.1) increased to a level above the initial activity after the period without ethylene glycol in the feed. Based on the DFT findings (see figure 5.1b), it could be speculated that before ethylene glycol is shut off, several CUS were occupied by ethylene glycol and reaction intermediates, while the ethylene glycol free period at the high concentration of H_2S might have either released CUS, increased the concentration of SH at the surface, or both, resulting in a higher HDO activity.

5.2.2.4 Role of H_2S in Primary Alcohol Hydrodeoxygenation

The yield of ethane and ethylene (see figure 5.4) reflected the trends observed in the STYs and C_2/C_1 ratio (see figure 5.3). The Ni catalyst had a poor hydrogenation activity, resulting in a 3-5 times higher yield of ethylene compared to ethane at TOS >5 h (see figure 5.4a).

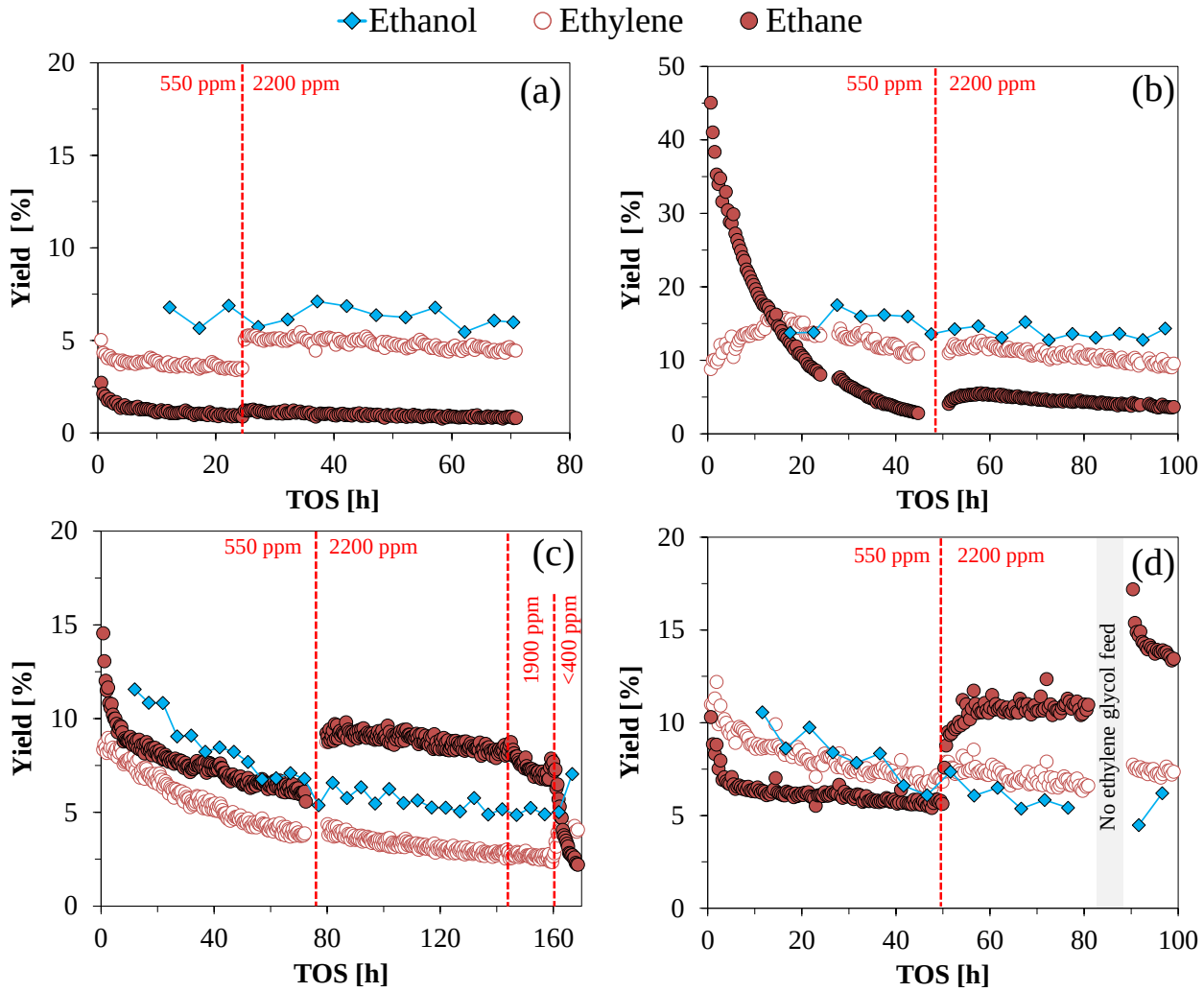

Figure 5.4: *Carbon based yields for ethylene glycol conversion at 400 °C, 27 bar H_2, 550-2200 ppm H_2S (noted in figures), 40 barg total (balance N_2), and 3-3.5 mol% ethylene glycol in the feed for (a) Ni#1(1.5 g), (b) Mo#1 (1.5 g), (c) NiMo#1 (0.5 g), and (d) CoMo#1 (0.5 g) in table 3.3. Cooling on separator tube S1 was not installed in experiments (c) and (d).*

For the unpromoted Mo catalyst (see figure 5.4b), there was an initial fast change in the relative proportions of the yields of ethane and ethylene, caused by deactivation of the hydrogenation activity. The initial ethane yield was 45 % compared to an ethylene yield of 9 %. At 15 h on stream, the ethane yield had dropped and the ethylene yield had increased, both reaching $\sim$ 15 %. After this point in time, the ethane yield continued to decrease, and the ethylene yield also decreased, however, at a slower rate. The lower hydrogenation activity of the unpromoted catalyst compared to the promoted catalysts (see figure 5.4b-d), was ascribed to the ability of Ni and Co promotion to facilitate adsorption of H at the surface as evidenced by DFT calculations (see figure 5.1), thereby providing better hydrogenation activity [113, 123, 132, 133].

For NiMo (see figure 5.4c), the ethane yield was higher than the ethylene yield during the entire TOS, as long as H_2S was added to the feed, which could be explained by the high concentration of H adsorbed at the S-edge (see figure 5.1c). As the H_2S concentration was increased from 500 to 2200 ppm, the ethane yield increased from $\sim$ 6 to 9 %, while the ethylene yield overall remained unchanged. This increase in ethane yield is possibly explained by the change of a $Ni_{1.00}S_{0.75}H_{0.75}$ S-edge structure to $Ni_{1.00}S_{1.00}H_{1.00}$ providing more hydrogen in terms of additional SH groups (see figure 5.1c).

For CoMo (see figure 5.4d), the yield of ethylene was initially higher than that of ethane, until the H_2S concentration was increased from 500 to 2200 ppm, causing the yield of ethane to increase above that of ethylene (from $\sim$ 6 to 10 %), which remained rather unchanged (at 7-8 %). These observations could be explained by the change in the S-edge structure from $Co_{1.00}S_{1.00}$ to $Co_{1.00}S_{1.50}H_{0.50}$, which provides more hydrogen through SH groups (see figure 5.1b).

Since only ethane and not ethylene seemed to be affected by the change in H_2S, this indicates that the hydrogenation of ethylene to ethane in reaction in figure 5.2 is very fast, and that an increased H_2S concentration of 2200 ppm increased both the deoxygenation and hydrogenation activity.

Mortensen [1] saw that even though an increase from 283 to 8172 ppm H_2S (at 280 °C and 100 bar) inhibited the conversion of phenol over a Ni-MoS_2/ZrO_2 catalyst, the conversion of 1-octanol (used as solvent), was increased from 50-75 % to 85-100 % during the 100 h TOS test. In line with this observation, Şenol et al. [109, 110] reported that while H_2S had an inhibiting effect on the HDO of aromatic oxygenates (due to competitive adsorption of H_2S), HDO of aliphatic oxygenates was promoted by increasing H_2S owing to their different reaction mechanisms that depend on acid-catalyzed reactions; e.g. dehydration and hydrogenation. These reactions have been proposed to be governed by the presence of nucleophilic SH groups present at the catalyst surface, which have been suggested to supply hydrogen and provide Brønsted acidity for HDO and HDS reactions [109, 129–131]. Şenol et al. [110] also reported that increasing the H_2S concentration increased the activity and stability of NiMo/Al_2O_3 and CoMo/Al_2O_3 catalysts in the HDO of methyl heptanoate at 250 °C and 15 bar.

Based on the findings in this work, it is therefore proposed that the role of H_2S in the conversion of ethylene glycol is to increase and maintain a high concentration of SH groups at the catalyst surface, which correspondingly aid catalysis of the consecutive dehydration/hydrogenation reactions of ethylene glycol to ethylene and ethane (see figure 5.2). This is supported by the DFT calculations, which showed that the surface concentration S and H generally increased with increasing H_2S pressure (figure 5.1).

5.2.2.4.1 Reproducibility of Stabilizing Effect of H_2S Generally, fast deactivation was seen in the beginning of the catalytic activity tests (figure 5.3 and figure 5.4). Thus, two additional short terms experiments were performed to investigate whether the observed stabilizing effect of H_2S had also been affected by general stabilization of the catalyst activity over time. Two fresh loads of CoMo (CoMo#2 with comparable composition to CoMo#1, see table 3.3) were tested for ethylene glycol

conversion with a H_2S feed concentration of 550 and 2200 ppm, respectively (see figure 5.5). The TOS of 8 h was too short to collect liquid products for calculation of conversion. Instead, the total carbon yield of C_{1-3} gas products indicates the minimum conversion level.

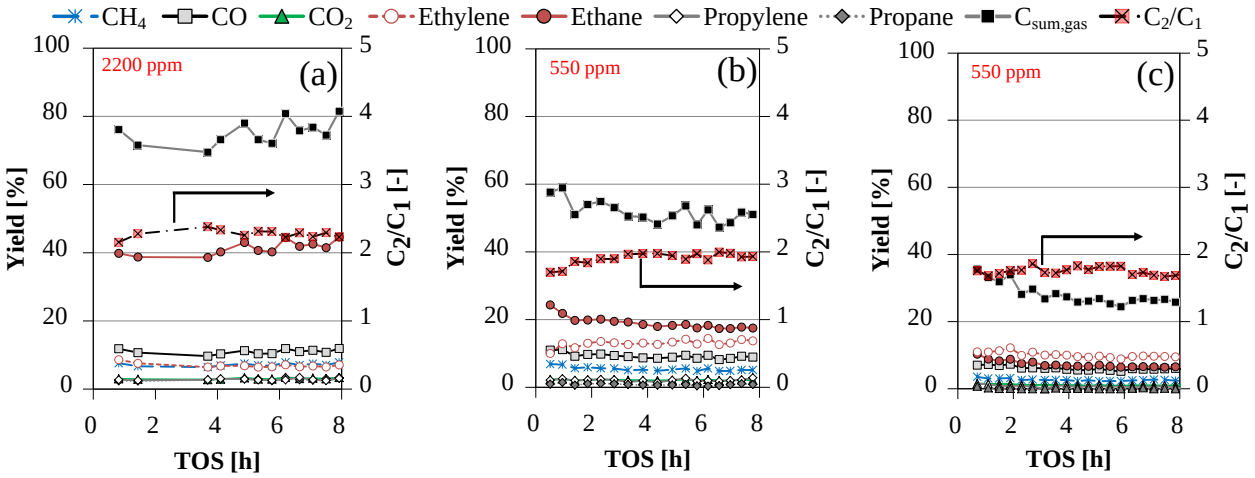

Figure 5.5: *Carbon based yields for ethylene glycol conversion at 400 °C, 27 bar H_2, 550-2200 ppm H_2S (noted in figures), 40 barg total (balance N_2), and 3-3.5 mol% ethylene glycol in the feed with 0.5 g catalyst for (a) CoMo#2 at 2200 ppm H_2S, (b) CoMo#2 at 550 ppm H_2S, and (c) CoMo#1 at 550 ppm H_2S (same experiment as presented in figure 5.3d and figure 5.4d). For catalyst composition, see table 3.3.*

An initial feed concentration of 2200 ppm H_2S (see figure 5.5a) resulted both in a higher activity (total carbon gas yield >70 %) and better HDO selectivity with $C_2/C_1 \sim 2.3$ compared to the lower feed concentration of 550 ppm H_2S, where the total carbon gas yield was ~ 45-60 % and the C_2/C_1 ratio was 1.7-2.0 (see figure 5.5b). For 2200 ppm H_2S, there was a stable (actually slightly increasing) activity over time. For 550 ppm H_2S, similarly as observed previously, deactivation occurred over time, while for 550 ppm H_2S deactivation occurred over time confirming the stabilizing effect of H_2S.

There was some deviation between the activity observed during the first 8 h on stream at 550 ppm H_2S with CoMo#1 (see figure 5.5c) and CoMo#2 (see figure 5.5b), which is essentially an attempted reproduction. A higher activity was obtained for CoMo#2, namely in terms of the ethane yield, but as it can be seen from the long TOS activity tests (see figure 5.4), the initial 10 h period on stream is subject to significant activity changes, and it is recommended to run experiments for long TOS to decouple the initial activity from the long term performance. Also, it should be noted that two different catalyst batches were used for the experiments in figure 5.5a-b (CoMo#2) and c (CoMo#1). As discussed later (see section 5.2.4.3), it is possible that the lower activity obtained in CoMo#1 was caused by formation of Co_9S_8.

Reproducibility was obtained for the NiMo#1 catalyst (see Appendix H, figure H.2), though it was seen that especially the ethane yield, temperature, and conversion were subject to smaller variations. These parameters are correlated, and it is believed that the specific morphology and dispersion of the active phase obtained through the sulfidation could vary slightly and consequently affect the ethane production and thereby also the conversion and temperature. This indicated different sulfidation behavior of the loaded catalysts (even from the same batch), indicating the complex nature of sulfide catalysts [63].

5.2.3 Spent Catalyst Composition

The composition of spent catalysts is given in table 5.1. The deposited carbon (3.4-12 wt%) is approximately linearly correlated with the TOS (see Appendix H, figure H.3) indicating that carbon deposition is a major source of deactivation. This was further evidenced as resulfidation of both spent Mo and NiMo catalysts (tested for ethylene glycol conversion at slightly different conditions), could only reactivate the catalyst for a short period of time. The activity of the reactivated catalysts was lower than the initial activity and the catalysts were subject to rapid deactivation; within <4 h on stream after reactivation, the activity had dropped to the same level as was achieved prior to the resulfidation.

The S/Mo ratio followed the trend NiMo#1 > CoMo#1 > Mo#1 > CoMo#2 (see table 5.1). Ni promotion has been shown to facilitate faster sulfidation of MoO_x into MoS_2 (see figure 5.10in section 5.2.4.2), which might explain the high content of sulfur in the spent NiMo catalyst. The S/Mo ratio of ~ 2 for CoMo#1 indicated that a stoichiometric MoS_2 phase was present in the spent catalyst, but for CoMo#2, including a fresh sulfided sample, this ratio was 1.52-1.70 indicating the complex nature of sulfides and the difficulties in obtaining identical sulfide phases in different experiments. The elemental composition should however be interpreted with caution and more advanced *in-situ* characterization tools are needed to determine the phases present (see section 5.2.4). In this case, the elemental composition does not reveal if there were any presence of segregated Ni or Co sulfides, or if any C or S was present as condensed species in the catalyst pores.

The M/Mo (M = Ni, Co) ratio of the spent catalysts was slightly lower than in the fresh catalysts, but it remained approximately constant at 0.3 indicating that Mo, Ni, and Co are stable against volatilization; potentially induced by e.g. H_2O and CO.

Table 5.1: *Composition and properties of spent catalysts (activity tests presented in figures 5.3-5.5) including TOS and H_2S feed concentrations used.*

Catalyst	**TOS [h]**	**H_2S [ppm]**	**Mo [wt%]**	**Ni [wt%]**	**Ni/Mo [molar]**	**Si [wt%]**	**Fe [wt%]**	**S [wt%]**	**C [wt%]**	**S/Mo [molar]**
Mo#1	99	500, 2200	2.48	-	-	0.05	0.05	1.47	10.4	1.78
NiMo#1	169	500, 2200, 1900, <400	2.52	0.44	0.28	-	0.06	1.90	12.0	2.25
Ni#1	71	500, 2200	-	12.0	-	0.04	0.05	3.54	6.82	0.54 (S/Ni)
				Co [wt%]	**Co/Mo [molar]**					
CoMo#1	90	500, 2200	2.54	0.41	0.26	0.04	0.04	1.72	10.8	2.02
CoMo#2a	8	2200	3.31	0.52	0.26	0.05	<0.02	1.76	3.61	1.56
CoMo#2b	8	500	3.15	0.49	0.25	0.03	<0.02	1.60	3.44	1.52
CoMo#2fresh[a]	0	-	3.11	0.49	0.25	0.02	0.02	1.76	2.83	1.70

[a] Sulfided and subsequently exposed to the same procedure of increasing temperature and pressure as applied in experiments. At the point in time, where ethylene glycol would normally be added, flushing and cooling was performed according to the procedure applied for experiment shut-down.

5.2.4 Characterization of Active Phases

5.2.4.1 Oxide Phase

The calcined catalyst precursors (see table 3.3) were analyzed with Raman spectroscopy to assess the dispersion of Mo, NiMo, and CoMo phases (see figure 5.6). The identification of the various phases present was supported by curve fitting analyses (see Appendix H, figure H.4 and table H.1).

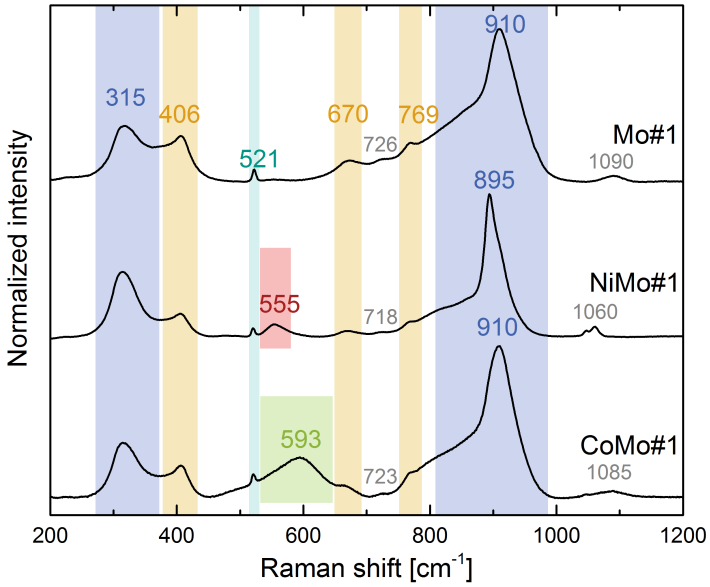

Figure 5.6: *Baseline corrected Raman spectra of Mo#1, NiMo#1, and CoMo#1 in the oxide phase (calcined, not dehydrated, see table 3.3). The Raman bands were assigned to monomolybdate tetrahedral (blue: 315, 895, 910 cm^{-1}), the $MgAl_2O_4$ support (orange: 406, 670, 769 cm^{-1}), supported and dispersed NiO (red: 555 cm^{-1}), supported CoO (green: 593 cm^{-1}), and Si impurities (turquoise: 521 cm^{-1}).*

Broad main signals around 910 and 895 cm^{-1} were found indicating a small crystallite size of tetrahedrally coordinated MoO_4^{2-} species [244,271]. The bands can be assigned to symmetric and asymmetric stretching modes, while broad bands around 315 cm^{-1} are caused by the bending modes of terminal Mo=O [244]. The lack of broad bands at 200-230 cm^{-1} (Mo-O-Mo vibration) and 943-965 cm^{-1} further suggests that the tetrahedral entities are isolated and not present as polymolybdates, which is in agreement with the low catalyst loading that was applied [244,245,271]. For NiMo#1, the main band is slightly shifted to lower wavenumbers, which may represent a lower bond order (higher coordination) or a longer atomic distance of MoO_4^{2-} species. The Raman bands at 406, 670, and 769 cm^{-1} refer to the Eg, F2g, and A1g modes of the support material, $MgAl_2O_4$ [272] and were found for all samples. An additional Raman band at 555 cm^{-1} was found for NiMo#1 and corresponds to supported and dispersed NiO [273]. Similarly, a Raman band at 593 cm^{-1} can be attributed to supported CoO for CoMo#1 [273].

Bulk $NiMoO_4$, $CoMoO_4$, and MoO_3 is unwanted, as crystallites of these phases do not convert into the active NiMoS and CoMoS phases during sulfidation [111]. No sharp Raman bands of crystalline $NiMoO_4$ ($\sim$ 912 and 962 cm^{-1}) or $CoMoO_4$ ($\sim$ 936 (α-$CoMoO_4$) or 935 and 946 cm^{-1} (β-$CoMoO_4$)) [265,274] were observed. For CoMo#1, no bulk Co_3O_4, CoO, or $CoAl_2O_4$ was found ($\sim$ 480, 520, 620, and 690 cm^{-1}) [275,276] and similarly, the lack of a broad peak around 525 cm^{-1} for NiMo#1

indicated that no bulk NiO was present in this catalyst precursor [277]. In general, the presence of bulk MoO_3 (667, 820, and 992 cm^{-1}) [244] could be ruled out for all catalyst precursors. Supported MoO_x may show Raman shifts at higher wavenumbers than 992 cm^{-1} [278]. Nevertheless, this may not explain the observed Raman bands between 1045-1090 cm^{-1} (figure 5.6). Minor Si impurities with a characteristic Raman shift at 521 cm^{-1} were assigned to potential impurities in the support or in the Mo precursor used for the preparation.

The presence of highly dispersed MoO_x was also verified by XAS. Figure 5.7 shows XANES spectra of the dehydrated and sulfided Mo#1 along with references, which exhibit different features depending on the oxidation state and coordination geometry of the central Mo atom. Similar XANES spectra of dehydrated and sulfided NiMo#1 and CoMo#1 at the respective Mo, Ni, and Co K-edges are given in Appendix H, figure H.7. The XANES spectrum of the dehydrated sample exhibits a pre-edge peak at $\sim$ 20,005 eV indicating the presence of Mo^{6+} (see figure 5.7). This pre-edge peak, which was seen for all dehydrated samples, is quite intense, which further indicates tetrahedral geometry around the central Mo atom [279,280].

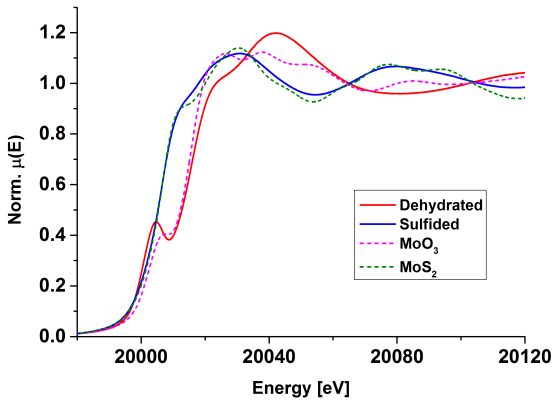

Figure 5.7: *Mo K-edge XANES spectra of the dehydrated and sulfided Mo#1 together with MoO_3 and MoS_2 references.*

The EXAFS fitting results obtained at the Mo K-edge for all dehydrated samples are shown in table 5.2. The corresponding Fourier transformed (FT) spectra with fitted theoretical models are given in the Appendix H, figures H.8-H.9 (Mo K-edge) and figure H.10 (Ni K-edge and Co K-edge). For the dehydrated samples, the CN of Mo-O was found in the range of 4.2-4.6 with an average bond length of 1.75 Å, which is in accordance with the XANES results. Higher metal-metal shells were not observed in the FT spectra of these samples indicating high dispersion as also found by Raman spectroscopy.

Table 5.2: *Mo K-edge EXAFS fitting results for the dehydrated oxide phase precursors. Δ states the uncertainty in the reported values.*

Catalyst	**Mo-O**		
	R **[Å]**	**CN (ΔCN) [-]**	σ^2 **($\Delta\sigma^2$) [Å^{-2}]·10^3**
Mo#1	1.76	4.2(0.4)	4.9(0.7)
NiMo#1	1.73	4.6(0.7)	5.8(1.6)
CoMo#1	1.75	4.3(0.4)	5.1(0.7)

5.2.4.2 Oxide to Sulfide Conversion during Sulfidation

The transition of oxide to sulfide was followed *in-situ* with XANES and EXAFS (see figure 5.8 and figure 5.9). Similarly to what has been obtained in literature [124, 281–283], the oxide precursor underwent transformation into intermediate oxysulfide species prior to conversion into the final sulfide form.

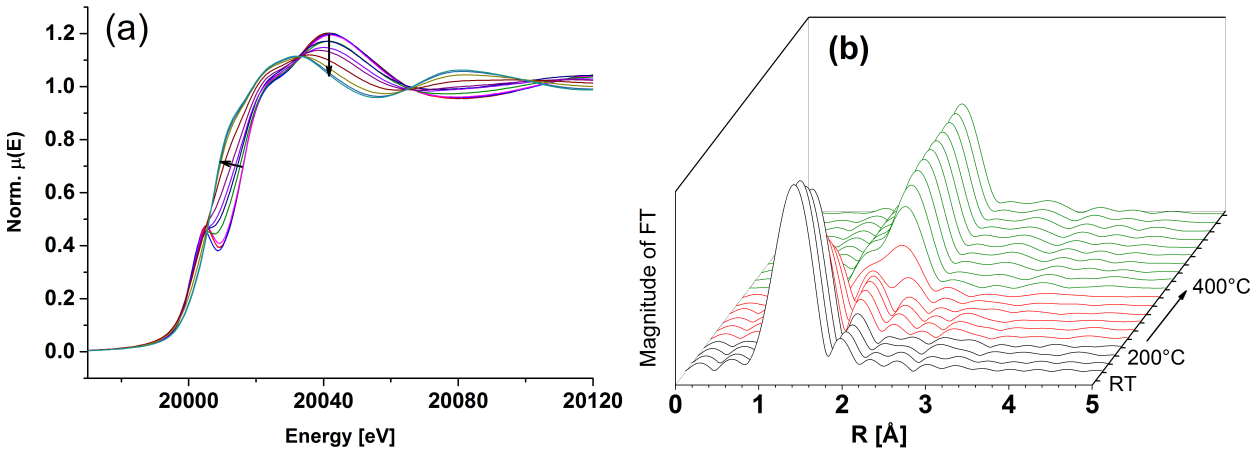

Figure 5.8: *Mo K-edge XAS results as (a) XANES spectra and (b) corresponding magnitude of the FT (fitted k^3-weighted EXAFS spectra) for in-situ sulfidation of Mo#1. (a) Overlaid view; arrows indicate change over time. (b) Averaged magnitude of FT spectra are shown as a function of time indicating presence of oxide (black), intermediate oxysulfide (red), and sulfide (green) phases.*

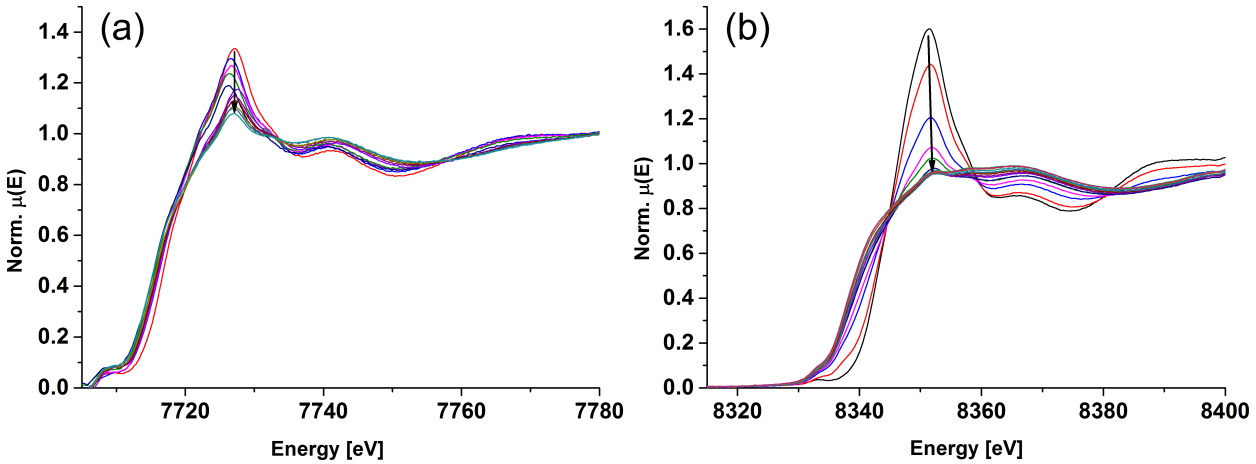

Figure 5.9: *XANES spectra for in-situ sulfidation of (a) CoMo#1 at the Co K-edge and (b) NiMo#1 at the Ni K-edge; arrows indicate change over time.*

A linear combination fitting (LCF) analysis of the XANES spectra obtained during sulfidation of the three catalysts (Mo#1, NiMo#1, CoMo#1) showed that Ni promotion increased the rate of sulfidation (see figure 5.10). Based on the Mo K-edge spectra, 10 % oxide phase remained at $\sim$ 320 °C in Mo, at $\sim$ 335 °C in CoMo, and at $\sim$ 295 °C in NiMo (figure 5.10a-c). Looking at the promoter K-edges, 10 % Co oxide phase remained at $\sim$ 335 °C, whereas 10 % Ni oxide phase remained at $\sim$ 260 °C (figure 5.10d-e). Thus, Ni was sulfided faster than Mo and this aided the sulfidation of Mo, whereas Co had no significant influence on the sulfidation rate of Mo.

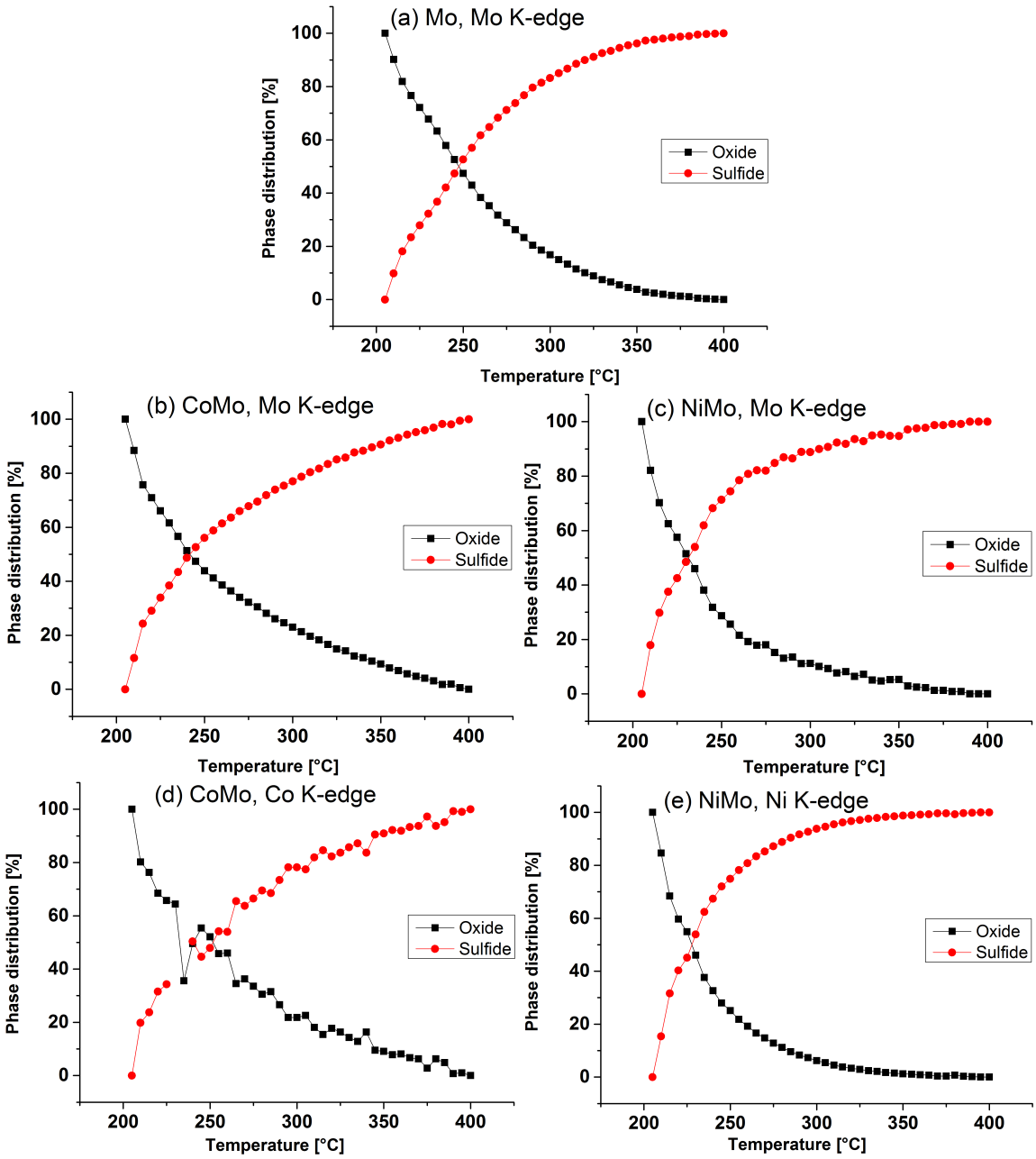

Figure 5.10: *LCF analysis of fitted EXAFS spectra from in-situ sulfidation at the Mo K-edge for (a) Mo#1, (b) CoMo#1, (c) NiMo#1, at the Co K-edge for (d) CoMo#1, and at the Ni K-edge for (e) NiMo#1.*

5.2.4.3 Sulfide Phase

The presence of small and highly dispersed MoS_2 particles was revealed by EXAFS. The structural parameters determined from fitting the Mo K-edge spectra of the sulfided catalysts and the promoter K-edges spectra for the dehydrated and sulfided samples are shown in table 5.3.

Table 5.3: *EXAFS fitting results. Mo K-edge results for all three sulfided catalysts and Ni and Co K-edge results for dehydrated and sulfided NiMo#1 and CoMo#1. Δ states the uncertainty in the reported values.*

K-edge/ catalyst	***R*** **[Å]**	**CN (ΔCN) [-]**	**σ^2 ($\Delta\sigma^2$) [Å^{-2}]·10^3**	***R*** **[Å]**	**CN (ΔCN) [-]**	**σ^2 ($\Delta\sigma^2$) [Å^{-2}]·10^3**	***R*** **[Å]**	**CN (ΔCN) [-]**	**σ^2 ($\Delta\sigma^2$) [Å^{-2}]·10^3**
Mo K-edge/	**Mo-O**			**Mo-S**			**Mo-Mo**		
Mo#1	1.65	0.19(0.07)	4.9(0.7)[a]	2.40	4.1(0.2)	8.4(0.5)	3.16	0.40(0.07)	3.2(0.2)[b]
NiMo#1	1.62	0.32(0.11)	4.9(0.7)[a]	2.40	4.8(0.3)	8.9(0.6)	3.17	0.43(0.10)	3.2(0.2)[b]
CoMo#1	1.64	0.32(0.11)	4.9(0.7)[a]	2.41	4.4(0.4)	9.8(0.9)	3.17	0.26(0.09)	3.2(0.2)[b]
Ni K-edge/	**Ni-O**			**Ni-Ni**			**Ni-Mo**		
Dehydrated	2.04	5.4(0.7)	7.7(1.4)	3.20	3.0(-)[c]	6.7(2.8)	3.20	3.0(-)[c]	6.7(2.8)
	Ni-S			**Ni-Ni**			**Ni-Mo**		
Sulfided	2.22	3.60(0.6)	8.6(1.8)	2.83	1.0(-)[c]	7.8(4.4)	3.30	1.0(-)[c]	5.7(1.4)
Co K-edge/	**Co-O**								
Dehydrated	1.92	4.5(1.1)	3.1(2.0)						
	Co-S			**Co-Co (1st)**			**Co-Mo**		
Sulfided	2.16	2.54(0.55)	6.1(1.8)	2.53	3.0(-)[c]	13.3(1.7)	3.81	2.0(-)[c]	5.7(3.3)
				Co-Co (2nd)					
				3.85	3.0(-)[c]	9.0(0.6)			

[a] $\Delta\sigma^2$ for Mo-O was fixed to the value as determined from the dehydrated Mo#1 sample.
[b] $\Delta\sigma^2$ for Mo-Mo was fixed to the value as determined from a MoS_2 reference.
[c] The parameter was fixed during the fitting.

The Mo K-edge results show that all three sulfided catalysts had a Mo-O contribution at 1.62-1.65 Å with a very low CN of 0.19-0.32 (see table 5.3). This may be explained by an interaction with the support resulting in the formation of highly dispersed, small particles as indicated by Raman. The very low CN observed for the Mo-O coordination, indicates that there is no actual bonding between Mo and O but only a slight interaction. In a recent study, Rochet et al. [281] also reported a very short Mo-O contribution at 1.68 Å with a CN of 1, which was proposed to be due to the presence of molybdenum oxysulfide species. In our case, the Mo-O CN is too low to predict the formation of such phases. Furthermore, Rochet et al. [281] observed a weak pre-edge feature in the XANES spectrum corresponding to the presence of molybdenum oxide species. In the sulfided samples of this work, however, no such peak was observed. Thus, most probably the short Mo-O bond with very low CN was due to interaction with the support.

The Mo-S coordination at 2.40-2.41 Å with a CN of 4.1-4.8 corresponds to the MoS_2 phase and is in agreement with published values [124, 243, 284]. The Mo-Mo coordination at 3.16-3.17 Å also corresponds to literature results [124, 243], but the CN = 0.26-0.43 is too low to obtain a precise estimate of the particle size (e.g. due to high temperature leading to a high Debye-Waller factor and small particle size due to mobility at >300 °C), which is expected to be <2 nm [284]. A TEM analysis was performed (see Appendix H, figures H.5-H.6) giving an average slab length of 4.3±2.8 nm with a mean stacking of 1.2. But with an average Mo-Mo CN <1 from EXAFS, the majority of the particles

were too small (<2 nm) to detect with TEM at the applied resolution. These results are in line with the findings of Seo and Lee [285], who showed that the formation of MoS_2 particles can take place through the initial formation of nanoparticles of ≤1 nm at mild sulfidation conditions. No Mo-Mo backscattering at 3.16 Å was detected for these particles indicating a very low coordination number, but at the same time, a Mo-S signal at 2.4 Å with a CN of 3.6 was reported, and the elemental S/Mo ratio was 1.3 [285]. As the sulfidation temperature was increased, they showed (TEM and EXAFS) that the nanoparticles merged to form the well-known MoS_2 slab structures giving stronger Mo-Mo backscattering. In this work, a low Mo loading (sub monolayer, see table 3.3) and rather mild sulfidation conditions were applied; i.e. moderate temperature and low pressure. Together with a strong support interaction as indicated by the Mo-O contribution at 1.62-1.65 Å, this is proposed to have caused the formation of very small and highly dispersed MoS_2 particles.

Using the EXAFS results (table 5.3), a MoS_2 cluster was constructed from a bulk MoS_2 model by only including the first shell of S and a single Mo atom from the second Mo shell. The central Mo atom thus had a Mo-S CN of 6, similar to bulk MoS_2, and a Mo-Mo CN of 1. The outer Mo atom had a Mo-S CN of 2 and a Mo-Mo CN of 1, which gives an average Mo-S CN of 4, corresponding to the EXAFS results (see table 5.3), and Mo-Mo CN of 1. The structure of this cluster is shown in the Appendix H, figure H.11. FEFF9 simulations were performed with each of the two Mo atoms as the absorber, and the obtained spectra were averaged to get the XANES spectrum shown in figure 5.11. The Debye-Waller factor obtained from the EXAFS fitting was used to introduce the disorder in the model. The spectra were averaged with a 1:1 ratio between the two Mo atoms, which gave a good agreement between modelled and experimental XANES spectra and supported the EXAFS results (see figure 5.11). There are, however, some regions where the shape of the modelled spectrum deviates from the experimental spectrum, possibly due to presence of further contributions from Mo-S and Mo-Mo in the sample not considered in the model.

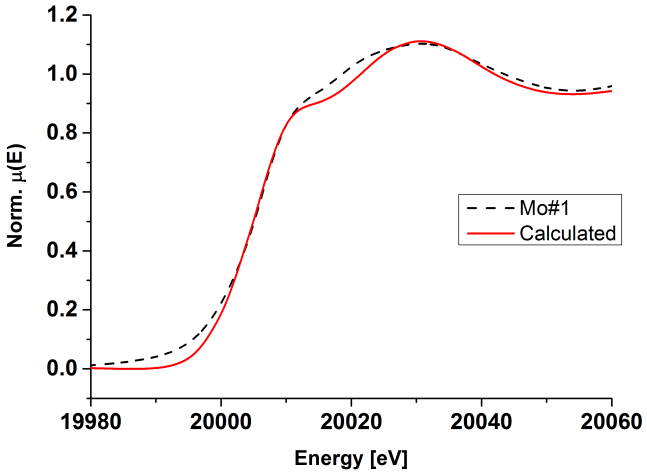

Figure 5.11: *XANES spectrum for sulfided Mo#1 together with the average calculated XANES spectrum (FEFF9) for a MoS_2 cluster consisting of two Mo atoms and with an average Mo-S CN of 4 and an average Mo-Mo CN of 1.*

The EXAFS results obtained at the Co K-edge indicate that a bulk Co_9S_8 phase was present in the sulfided CoMo catalyst (see table 5.3). The Co-S CN of 2.54 with bond length 2.16 Å is similar to

one of the shorter Co-S coordinations present in Co_9S_8 [286], and the low CN of 2.54 indicates the presence of smaller particles on the surface. The presence of a Co-Co shell was observed at a higher distance of 3.85 Å, supporting the presence of a Co_9S_8 phase after sulfidation [286]. Also, a Co-Mo shell was found at about the same distance of 3.81 Å indicating that some Co atoms were replaced by Mo, which points towards the presence of a CoMoS phase. Thus, the sulfided phase in the CoMo catalyst seemed to contain a mixture of Co_9S_8 and CoMoS.

Especially CoMo catalysts have been reported to be sensitive towards bulk Co_9S_8 formation during sulfidation with the propensity to form this undesired phase being dependent on the catalyst preparation method. Co_9S_8 is most likely to form in samples prepared from a stepwise incipient wetness impregnation where the Co precursor has been added prior to the Mo precursor [63]. Co_9S_8 formation can be minimized by application of a chelating agent, such as citric acid, to the impregnation solution, which has been reported to stabilize Co and Mo precursors at the catalyst surface and facilitate a high degree of promotion of Co in the resulting MoS_2 structure [124, 243, 287]. The catalytic activity repeatability test (see section 5.2.2.4.1 and figure 5.5) might thus be improved by altering the catalyst preparation procedure.

For NiMo, the EXAFS results obtained at the Ni K-edge indicated the presence of a NiMoS phase. The Ni-S CN of 3.60 with bond length 2.22 Å is similar to the results obtained by Rochet et al. [288] for a sulfided $NiMo/Al_2O_3$ catalyst, which was prepared with approximately the same metal loading per nm^2 available support surface area as for this work. The Ni K-edge XANES spectrum for the sulfided catalyst (see Appendix H, figure H.7), showed similar features as the NiMoS XANES spectrum reported in literature [289]. Furthermore, a small bump at $\sim$ 8352 eV corresponded to the white line characteristics of $NiAl_2O_4$ indicating some interaction of Ni with the $MgAl_2O_4$ support.

5.2.4.4 Stability against Varying H_2O/H_2S

The stability of promoted and unpromoted MoS_2 against H_2O/H_2S variations was investigated *in-situ* by XAS. After sulfidation, the catalysts were exposed to different molar ratios of H_2O/H_2S (30, 100, 190, and 300) corresponding to 100-500 ppm H_2S and 1.6-3.0 % H_2O. In the performed activity tests (figure 5.3 and figure 5.4), full conversion corresponded to a H_2O/H_2S ratio of $\sim$ 125 and $\sim$ 30 at 550 and 2200 ppm H_2S, respectively.

Figure 5.12 shows the *in-situ* XANES spectra at the Mo K-edge for Mo#1, CoMo#1, and NiMo#1, at the Co K-edge for CoMo#1, and at the Ni K-edge for NiMo#1, respectively, during H_2O/H_2S variations. Any changes induced by adding water to the gas and increasing the H_2O/H_2S ratio were negligible, which indicates that all catalysts were stable against water induced phase change such as oxidation for H_2O/H_2S ratios $\leq$300. Also, the variation in the EXAFS parameters for the catalysts exposed to H_2O were too small to predict any phase transformation and are hence not presented here.

The presence of promoters in the CoMo and NiMo catalysts could stabilize the catalyst against oxidation as indicated by the DFT results (see figure 5.1), which suggested a lower stability of unpromoted MoS_2, but at the same time only provided general trends. Furthermore, the stability of all catalysts could be due to a stabilizing effect from the strong interaction between the small and highly dispersed particles with the support. A possibility for further investigating the influence of H_2O/H_2S variations could be to perform modulation excitation spectroscopy (MES) during *in-situ* experiments, which can potentially enhance the sensitivity of small and fast changes [290]. This is outside the scope of this paper, and it is the topic of further research.

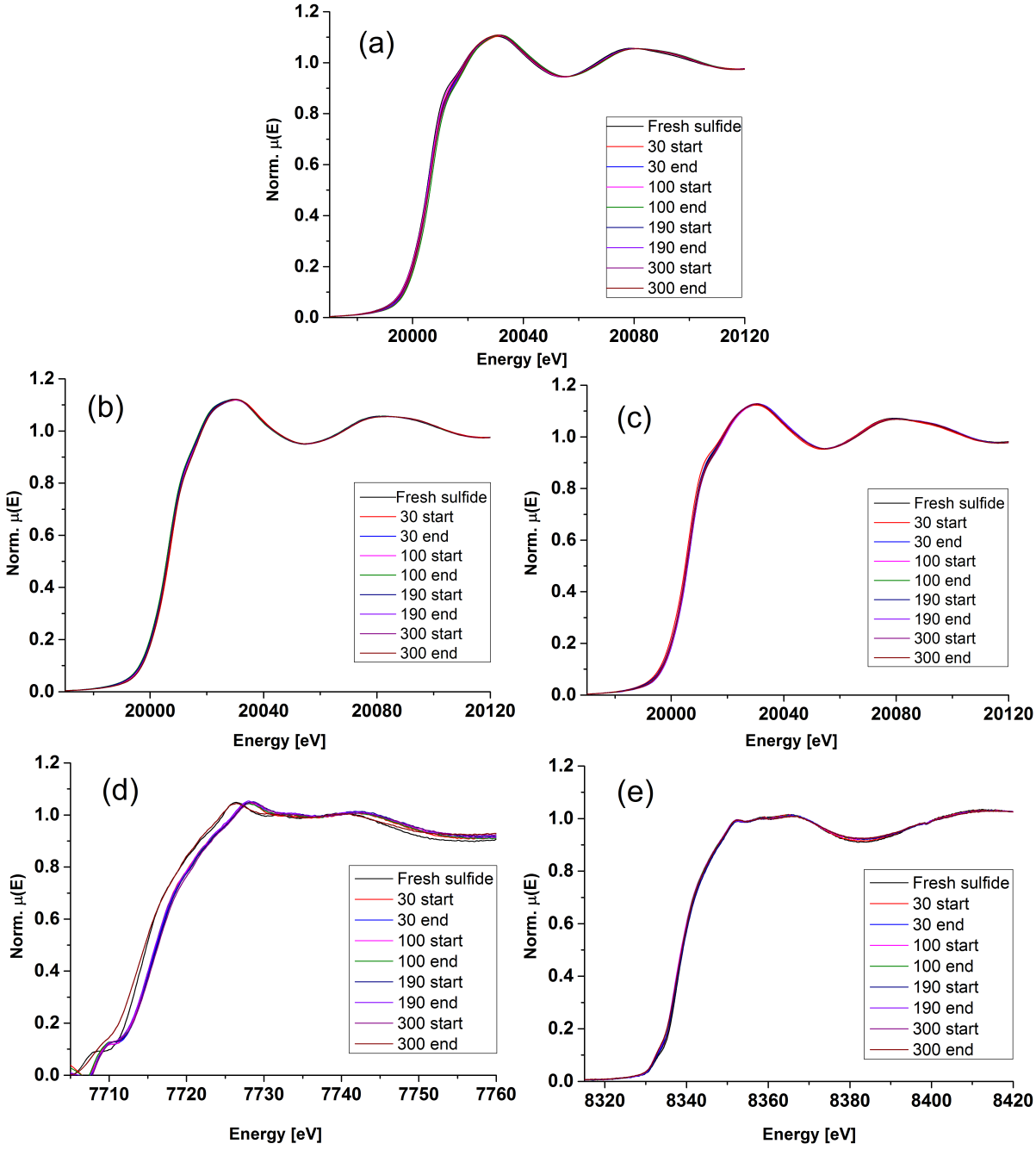

Figure 5.12: *Average XANES spectra from in-situ H_2O/H_2S variations at the Mo K-edge for (a) Mo#1, (b) CoMo#1, (c) NiMo#1, (d) at the Co K-edge for CoMo#1, and (e) at Ni K-edge for NiMo#1. Numbers indicate molar H_2O/H_2S ratios. Start and end denote whether the averaged XANES spectra are from the first or last 5 minutes of the exposure time at the given ratio.*

5.2.5 Target Sulfide Phase for Hydrodeoxygenation at Elevated Temperature

A strong support interaction (commonly through Mo-O-Al linkages) has often been associated with formation of the less active type I sulfide phases [124, 243, 287]. Type I sulfides are smaller particles with higher dispersion than type II sulfides that more resemble bulk MoS_2 [291]. A moderately active

catalyst stabilized through the support interaction of highly dispersed MoS_2 particles was the aim in this work, where a catalyst for *in-situ* HDO of pyrolysis vapors at high temperatures ($\sim$ 500 °C) is targeted. If a too active catalyst (such as type II sulfides) is prepared, extensive cracking can minimize (potentially remove) the oil yield when a real biomass feed is used. Additionally, the strong active phase-support interaction helps in stabilizing the active phase upon water exposure, this could further favor the use of type I sulfides in high temperature HDO of pyrolysis vapor.

A bulk-like MoS_2 structure with a Mo-S CN of $\sim$ 6 can be obtained by lowering the interaction with the support; either by the use of a chelating agent during impregnation on Mo-O-Al anchoring supports such as Al_2O_3 [124,243,287], or by the use of an inert support such as carbon [287]. Sulfidation conditions (temperature, pressure, and sulfur source) can additionally be used to alter the composition of formed sulfides [124, 243, 291, 292]. As mentioned, the loading of Mo also influences the type I/II distribution as a higher loading minimized the support interaction and favors the formation of fully sulfided MoS_2 with Mo-S CN = 6 [63,242].

It has been reported that NiMo catalysts are more active for HDO of aliphatic species, while CoMo catalysts are more active for HDO of aromatic species [109, 110, 136, 138]. In this work, similar activities were seen with the prepared NiMo and CoMo catalysts tested for ethylene glycol conversion. Biomass fast pyrolysis vapor will contain both aliphatic and aromatic oxygenates. It could therefore be interesting to test the activity and stability of the prepared catalysts for HDO of aromatic species. Mixtures of aromatic and aliphatic species should be tested as well to study possible competitive inhibition. However, the aliphatic oxygenates (sugar derived polyols, ketones, acids, and aldehydes) are responsible for the most detrimental properties of bio-oil. These species should be upgraded by HDO immediately when formed during catalytic hydropyrolysis. Further upgrading of more refractory aromatic species could potentially be performed downstream in a fixed bed reactor operating with another catalyst at other operating conditions.

5.3 Conclusions

DFT, catalytic activity tests, and *in-situ* XAS was conducted to provide detailed information on the activity and stability of MoS_2, Ni-MoS_2, and Co-MoS_2 catalysts used for HDO upon variation of the partial pressures of H_2O and H_2S. H_2S was added to the reaction gas to stabilize the sulfide catalyst, while H_2O is a HDO reaction product. DFT calculations showed that the active edge of MoS_2 could be stabilized against S-O exchanges by increasing the partial pressure of H_2S or by promotion with either Ni or Co. HDO activity tests were performed using Mo, NiMo, and CoMo catalysts prepared by incipient wetness impregnation using a $MgAl_2O_4$ support. Ethylene glycol was chosen as a model compound representing the more reactive cellulose derived species formed during pyrolysis of biomass. The prepared MoS_2 based catalysts were all active and fairly selective for ethylene glycol HDO at 400 °C, 27 bar H_2, and 550-2200 ppm H_2S, and produced ethane, ethylene, and C_1 cracking products at C_2/C_1 ratios of 1.5-4.8 and conversions of $\sim$ 50-100 %. Both DFT and catalytic activity tests indicated that increasing the H_2S concentration in the gas increased the concentration of SH groups on the catalyst, which correspondingly activated and stabilized the catalytic HDO performance. *In-situ* XAS showed that the catalysts were tolerant towards water, and that the active phases were present as small and highly dispersed particles.

6 | Kinetics, Deactivation, and Reactivation

Hydrodeoxygenation of Pyrolysis Vapor Model Compounds over Sulfided NiMo/$MgAl_2O_4$

Abstract

Hydrodeoxygenation (HDO) of acetic acid, ethylene glycol, phenol, and cyclohexanol was investigated using a Ni-MoS_2/$MgAl_2O_4$ catalyst. Activity tests were performed in a continuous flow fixed bed reactor operated at 380-450 °C, 27 bar H_2, and 550 ppm H_2S. Acetic acid plugged the reactor inlet within 2 h on stream, illustrating the challenges of performing HDO of reactive oxygenates. Phenol, which was fed together with ethylene glycol, was not converted at the applied conditions, which seemed to be due to a combination of mechanistic and thermodynamic constraints.

For ethylene glycol and cyclohexanol, steady state activity was obtained in the temperature range of 380-415 °C and the kinetics were evaluated in terms of the reactions: ethylene glycol $\xrightarrow{k_1'}$ ethylene $\xrightarrow{k_2'}$ ethane and cyclohexanol $\xrightarrow{k_1}$ cyclohexene $\xrightarrow{k_2'}$ cyclohexane. The hydrogenation of ethylene was the fastest step in the conversion of ethylene glycol with $k_2'/k_1' = 15\text{-}27$, while the initial dehydration was the fastest step during the pure cyclohexanol conversion with $k_2'/k_1 \leq 0.1$. The results could indicate that the conversion of ethylene glycol and cyclohexanol was taking place on different active sites.

There was no significant influence from phenol and cyclohexanol on the rate of HDO of ethylene glycol. But for cyclohexanol, a significant inhibiting effect from ethylene glycol was observed. The rate constant for dehydration of cyclohexanol, k_1, decreased by a factor of 25-51, when ethylene glycol was present. This was explained by competitive adsorption on active sites by ethylene glycol and deactivation by coke from ethylene glycol.

All catalysts deactivated due to carbon deposition with the time on stream of 90-220 h. Catalyst reactivation was possible by oxidation and resulfidation, but the conditions of reactivation should be controlled to limit changes in the active phase.

6.1 Introduction

As discussed in chapter 2.3.8, HDO of a single model compound allows for detailed insights into reaction and deactivation mechanisms, but the complexity of a real feed is neglected. Thus, it is interesting to mix different model compounds to obtain a feed which is slightly closer to representing a real feed. This work studies the reactivity and interaction between acid, polyol, alcohol, and phenol functionalities in HDO over a sulfided $NiMo/MgAl_2O_4$ catalyst.

Ethylene glycol represents the highly reactive polyol functionality, which should be stabilized through HDO immediately when formed during pyrolysis to avoid coking and polymerization. Another important functionality is carboxylic acids, which along with their unwanted corrosiveness also possess a high reactivity (see figure 2.4). Finally, phenolic compounds are interesting in HDO studies due to their refractory properties. The difference in reactivity between alcohols, carboxylic acids, and phenols may challenge single stage HDO. Furthermore, the interaction between oxygenates such as competitive adsorption may limit their HDO [91,92].

6.2 Results and Discussion

6.2.1 Hydrodeoxygenation of Acetic Acid

The HDO of acetic acid was tested in the POC setup at 450 °C and 40 barg with 27 bar H_2 and 550 ppm H_2S using 0.5 g NiMo#2 catalyst (see table 3.3) and a feed of $\sim$ 0.06-0.13 mL/min acetic acid corresponding to 1.0-2.3 mmol/min (experiment: HAc). It was not possible to obtain a stable feed flow. After 2 h on stream, a coke plug developed in the reactor inlet (above the catalyst bed), resulting in a pressure drop of 48 bar. This experiment clearly illustrated the issues of heating reactive oxygenates, which many others also have faced when using condensed bio-oil for HDO studies [98,101,102].

The short TOS with acetic acid over a sulfided NiMo catalyst resulted in the gas product yields summarized in table 6.1, which compares the yields with those from the conversion of pure ethylene glycol at similar conditions. Acetic acid can undergo different reactions such as decarboxylation to form CH_4 and CO_2, decarbonylation (of two acetic acid molecules) to form ethylene, CO, and water, and ketonization (of two acetic acid molecules) to form acetone, CO_2, and water [293]. It is also possible that acetic acid can be converted by HDO to acetaldehyde and water, allowing for similar reactions as for ethylene glycol. The formation of acetone could be the reason for the high yield of propane and propylene formed from acetic acid compared to ethylene glycol, which indicated the higher propensity for carboxylic acids to polymerize. The ratio of ethane/ethylene was higher (at $\sim$ 10) for acetic acid HDO compared to ethylene glycol HDO (at $\sim$ 3), which could either be due to differences in the mechanism for ethylene formation or due to extensive coke formation from the ethylene formed from acetic acid. The higher yield of C_1 and coke from acetic acid HDO also indicated a higher affinity for cracking of acetic acid compared to ethylene glycol, which to some extent, however, was also affected by a higher ($\leq$13 °C) reaction temperature (see figure 6.1).

Table 6.1: *Gas product yields at TOS = 0-2 h for the conversion of ethylene glycol (experiment: EG) and acetic acid (experiment: HAc) at 450 °C, 550 ppm H_2S, 27 bar H_2 and 40 barg total pressure (balance N_2).*

Model compound	**CH_4** [%]	**CO** [%]	**CO_2** [%]	**Ethylene** [%]	**Ethane** [%]	**Propylene** [%]	**Propane** [%]	**$C_{sum,gas}$** [%]
Ethylene glycol	8-9	12-13	4-5	8-11	28-29	4-7	3	67-74
Acetic acid	17-21	17-20	7-8	2	21-24	8-11	9-11	83-93

6.2.2 Hydrodeoxygenation of Ethylene glycol, Phenol, and Cyclohexanol

6.2.2.1 Reaction Conditions

The conversion of ethylene glycol, phenol, and cyclohexanol in pure and mixed solutions was investigated over a sulfided NiMo catalyst (0.5 g NiMo#2, see table 3.3) at 380-450 °C and 40 barg with 27 bar H_2 and 550 ppm H_2S. The conversion of pure ethylene glycol (experiment: EG) was compared with that of an ethylene glycol feed containing either phenol (experiment: Phe/EG) or cyclohexanol (experiment: Cyc/EG). In these experiments, a constant oxygen molar feed flow was targeted (see table 6.2). An experiment with pure cyclohexanol (experiment: Cyc) was performed to see if cyclohexanol was affected by the presence of ethylene glycol. In this experiment, the volumetric feed flow was targeted at a level comparable to the pure ethylene glycol experiment. The catalyst used for HDO of the mixed ethylene glycol and phenol feed was reactivated after the end of the run (see section 6.2.3), and the experiment was then repeated (experiment: Phe/EG-ReGen) to test catalyst regenerability. Catalyst regeneration and activity of the reactivated catalyst is discussed in section 6.2.3.

Table 6.2: *Applied model compound feeds (average values) at 27 bar H_2, 550 ppm H_2S, a total pressure of 40 barg (balance N_2) and temperatures of 280-450 °C.*

Experiment/ parameter	**Unit**	**EG**	**Phe/EG (21 wt% Phe)**	**Cyc/EG (22 wt% Cyc)**	**Cyc**
Total compound flow	[mmol/min]	2.46	2.62	2.57	1.5
EG flow	[mmol/min]	2.46	2.23	2.19	0
Phe	[mmol/min]	0	0.39	0	0
Cyc	[mmol/min]	0	0	0.38	1.5
O	[mmol/min]	4.92	4.85	4.76	1.5
C	[mmol/min]	4.92	6.9	6.7	9.0
Volumetric feed	[mL/min]	0.14	0.16	0.16	0.16
WHSV	[h^{-1}]	EG: 19	EG: 16	EG: 16	-
	[h^{-1}]	-	Phe: 4.4	Cyc: 4.6	Cyc: 18
	[h^{-1}]	Total: 19	Total: 21	Total: 21	Total: 18

Previous activity tests (see chapter 5) showed significant deactivation over time. Steady state activity is crucial for kinetic modelling. Thus, an accelerated deactivation was introduced at 420-450 °C to obtain subsequent steady state activity in the approximate temperature range of 380-400 °C. In most experiments, the initially applied operating temperature of 450 °C was revisited to see if the catalyst had deactivated further during steady state operation.

The temperature programs for the experiments are listed in table 6.3 and the resulting temperature profiles are shown in figures 6.1 and 6.2. Experiments EG and Phe/EG were run in a similar manner, but in the experiment with the reactivated catalyst, a step at 280 °C was introduced to see, if phenol conversion could be obtained at a lower temperature. The experiment Cyc/EG had to be terminated after 90 h on stream due to setup issues. The experiment Cyc was run similarly to Cyc/EG with the addition of a revisit at the initial setpoint of 450 °C at the end of the run.

Table 6.3: *Applied temperature programs in terms of setpoints, T_{SP}, for the experiments listed in table 6.2.*

Experiment	EG		Phe/EG		Phe/EG-ReGen		Cyc/EG		Cyc	
Step	TOS [h]	T_{SP} [°C]	TOS [h]	T_{SP} [°C]	TOS [h]	T_{SP} [°C]	TOS [h]	T_{SP} [°C]	TOS [h]	T_{SP} [°C]
1	0-24	450	0-24	450	0-24	450	0-24	450	0-24	450
2	24-69	420	24-69	420	24-69	420	24-69	420	24-71	420
3	69-105	400	69-105	400	69-105	400	69-90	400	71-91	400
4	105-139	390	105-139	390	105-155	390			91-101	450
5	139-171	380	139-171	380	155-171	380				
6	171-201	410	171-201	410	171-198	280				
7	201-221	450	201-220	450	198-220	450				

Figure 6.1 shows the initial sharp temperature increase of up to 16 °C as the oxygenate feed was added due to the highly exothermic nature of HDO reactions. The subsequent decreasing temperature over time indicated catalyst deactivation, which was also evident from the conversion and product yields.

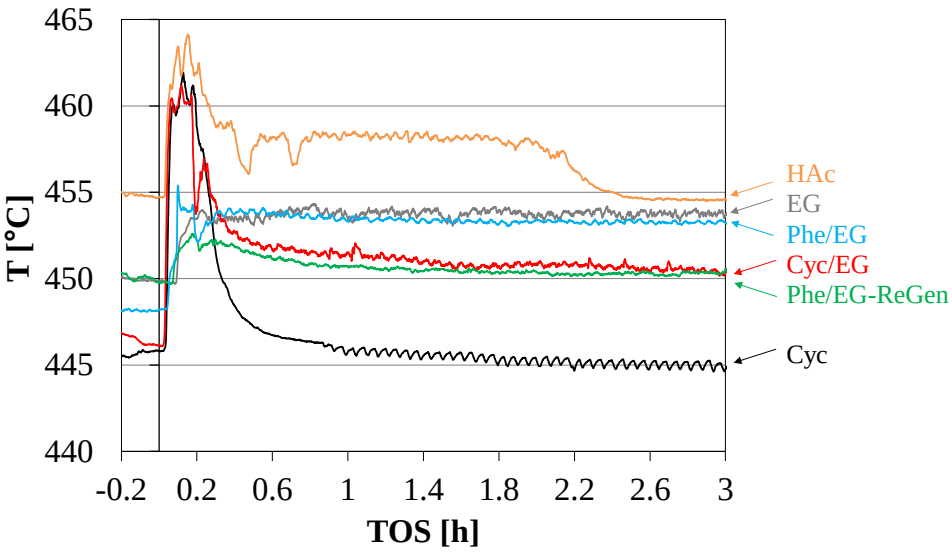

Figure 6.1: *Initial temperature profiles for the experiments listed in table 6.2. In the experiment HAc, the acetic acid feed was stopped at TOS ~ 2.2 h.*

The HPLC pump used to feed cyclohexanol in experiment Cyc broke down at TOS = 63-70 h and no cyclohexanol was fed in this period, which resulted in a slightly higher temperature (~ 2 °C) indicating that the reaction temperature (at T_{SP} = 420 °C) was governed by endothermic reactions (see figure 6.2). During the activity test using the reactivated catalyst (Phe/EG-ReGen) at T_{SP} = 390 °C, the temperature suddenly increased from 385 to 388 °C at TOS = 138 h and stayed at 388 °C. The activity increased correspondingly. Before this temperature increase, there had been a few spikes in temperature and the measured gas product concentrations indicating that the catalyst was somehow changing. At 138 h, this change became permanent leading to a different activity. Apart from an increased activity and a correspondingly higher temperature, no changes in the operational parameters (flows, pressures, etc.) were introduced or detected during this period of time.

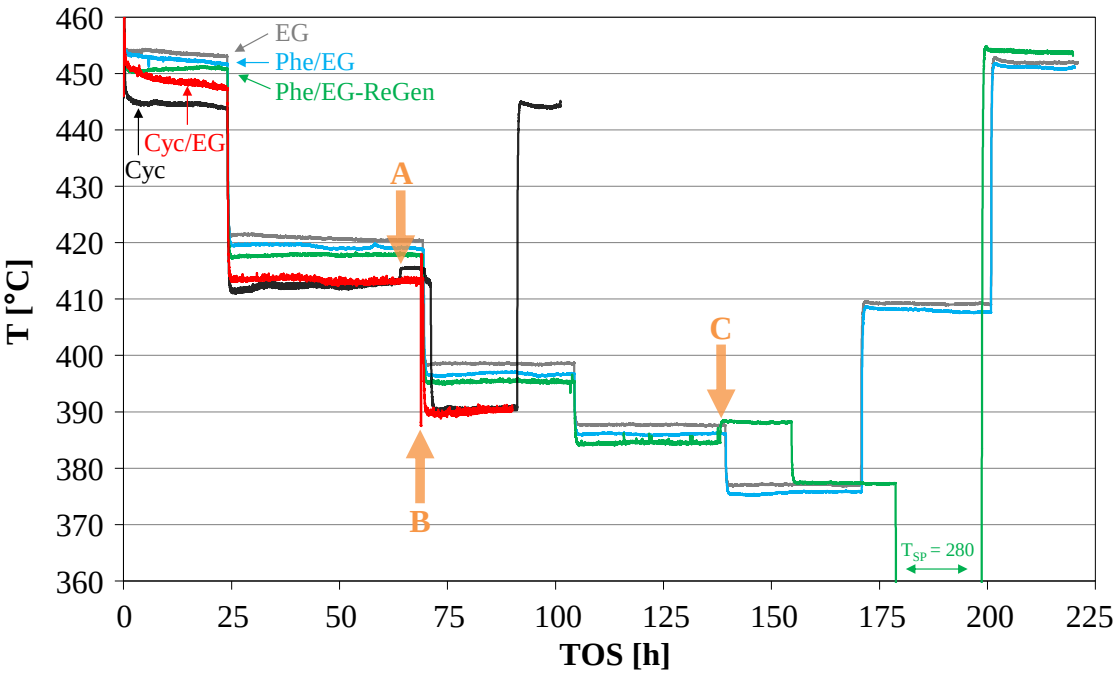

Figure 6.2: *Temperature profiles for the experiments listed in table 6.2 with the temperature programs listed in table 6.3. A) Temperature increase in the Cyc experiment (2 °C) during period without cyclohexanol feed. B) Temperature decrease (25 °C) in the Cyc/EG experiment prior to decreasing the setpoint from 420 °C to 400 °C due to measurement of temperature profile (moving thermocouple out of reaction zone, see Appendix D). C) Unexpected catalyst activation with temperature increase (4 °C).*

6.2.2.2 Conversion of Ethylene Glycol

The conversion of ethylene glycol in the different experiments (EG, Phe/EG, Cyc/EG) is shown in figure 6.3, while figure 6.4 gives the total yield of carbon in the detected C_{1-3} gas products. In all three ethylene glycol experiments, close to complete conversion was obtained initially at ~ 450 °C. Deactivation however occurred, and before the temperature was dropped to ~ 420 °C at TOS = 24 h, the conversion had decreased below 100 %. Steady state activity was obtained at the subsequent temperature setpoints of 400, 390, and 380 °C. This is more evident from the yield profiles (figure 6.4) compared to the conversion profiles (figure 6.3), due to the higher resolution with less fluctuation of the gas data. The initial total carbon yield in the gas (figure 6.4) was ≥20 % at T_{SP} ≥420 °C, while it was 6-14 % at T_{SP} = 380-400 °C.

The ethylene glycol conversion was in the range of 64-96 % at T_{SP} = 420 °C, 46-57 % at T_{SP} = 400 °C, 35-50 % at T_{SP} = 390 °C, and 29-39 % at T_{SP} = 380 °C (see figure 6.3). Increasing the temperature setpoint from 380 °C to 410 °C at TOS = 171 h (experiments EG and Phe/EG), did not allow for steady state operation, and continuous deactivation was observed (see figure 6.4). As the temperature was brought back to the initial setpoint of 450 °C, the conversion increased to 88-95 % and was thus slightly lower than initially obtained, and continued deactivation was evident from the gas yields (see figure 6.4).

The temperature was identical (within <2 °C) for the experiment with pure ethylene glycol and with phenol in the feed. The temperature was however notably lower (up to 10 °C) when cyclohexanol was present in the feed, which affected the conversion and yields accordingly. This lower temperature was explained by the endothermic dehydration of cyclohexanol (see section 6.2.2.6).

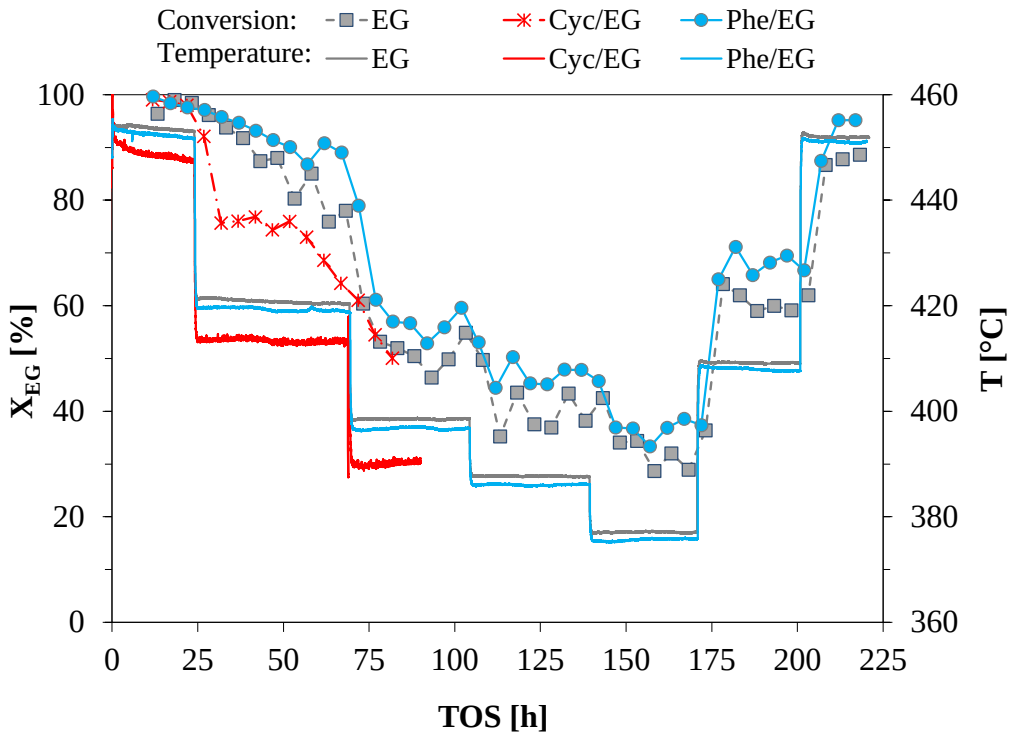

Figure 6.3: *Temperature profiles and ethylene glycol conversion over NiMo#2 (see table 3.3) from experiments with ethylene glycol, phenol, and cyclohexanol in the feed. Based on ethylene glycol. For feed composition, see table 6.2.*

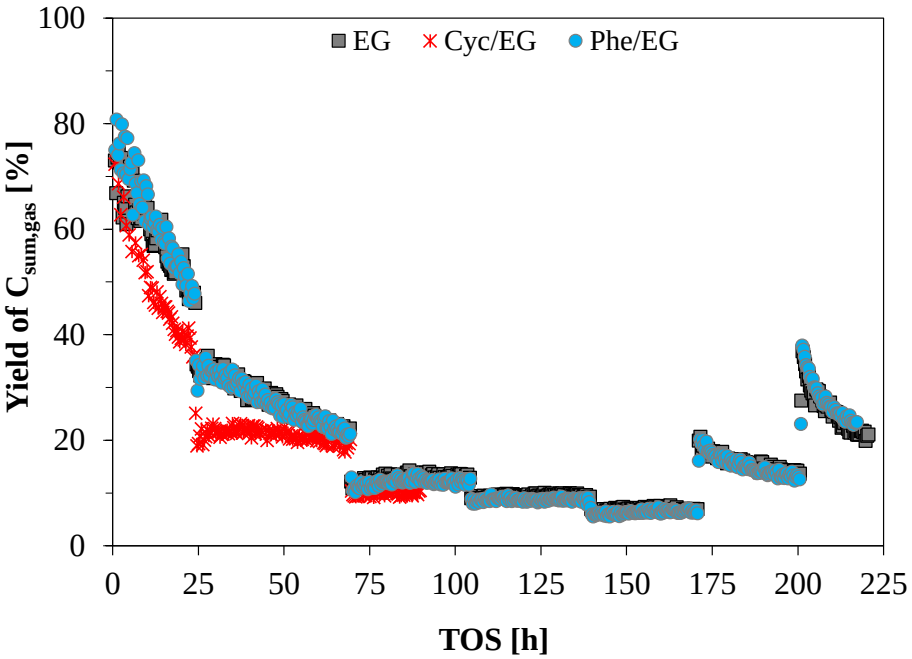

Figure 6.4: *Total carbon yield of gas products from the conversion of ethylene glycol over NiMo#2 (see table 3.3) from experiments with ethylene glycol, phenol, and cyclohexanol in the feed. Based on ethylene glycol. For feed composition, see table 6.2. For temperature profiles, see figure 6.2.*

6.2.2.3 Product yields from Ethylene Glycol Conversion

Based on the product composition and yields from the HDO of pure ethylene glycol and cyclohexanol, and from the mixed ethylene glycol and phenol feed, it was found that C_{1-3} products were formed from ethylene glycol and not from phenol or cyclohexanol. Thus, the yields of these compounds were calculated based on the feed of ethylene glycol. Figure 6.5 shows the yields of C_{1-2} gas products. The yield of CO_2 was $\sim$ 1-5 % during the initial deactivation period and $<$0.5 % at the subsequent steady states.

Looking at the yield of ethylene and ethane for all three experiments (figure 6.5a-b), there was an initial decrease in the yield of ethane and a corresponding increase in ethylene, indicating a deactivation of hydrogenation sites as previously observed (see chapter 5). During steady state operation at T_{SP} = 380-400 °C, the yields of ethane and ethylene, respectively, were below 5 %. The yields obtained immediately after returning to 450 °C at TOS = 198 h was approximately the same as obtained at 24 h in the end of the initial 450 °C operation period, supporting the observation that steady state activity was obtained during 69-171 h on stream with little further deactivation during this period.

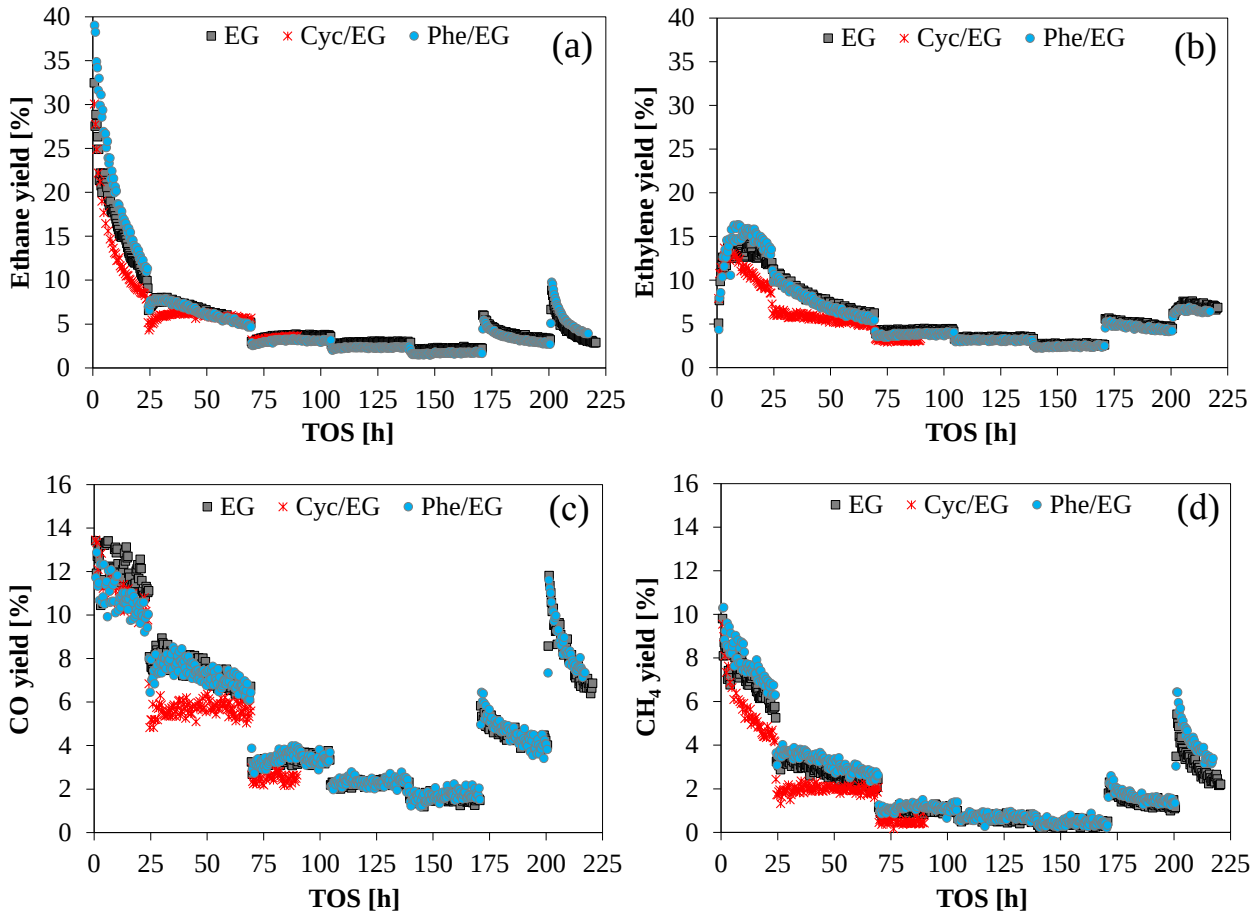

Figure 6.5: *Yields of (a) ethane, (b) ethylene, (c) CO, and (d) CH_4 from the conversion of ethylene glycol over NiMo#2 (see table 3.3) from experiments with ethylene glycol, phenol, and cyclohexanol in the feed. The yield of CO_2 was $<$0.5% during steady state operation. Based on ethylene glycol. For feed composition, see table 6.2. For temperature profiles, see figure 6.2.*

CO was the main cracking product formed (see figure 6.5c-d). The C_2/C_1 ratio obtained in all three experiments (see figure 6.6) increased linearly with decreasing temperature, showing how cracking cannot be avoided at elevated temperature. The higher deviation in the C_2/C_1 ratio at lower temperatures is caused by greater relative fluctuations in the measured concentration of C_1 products.

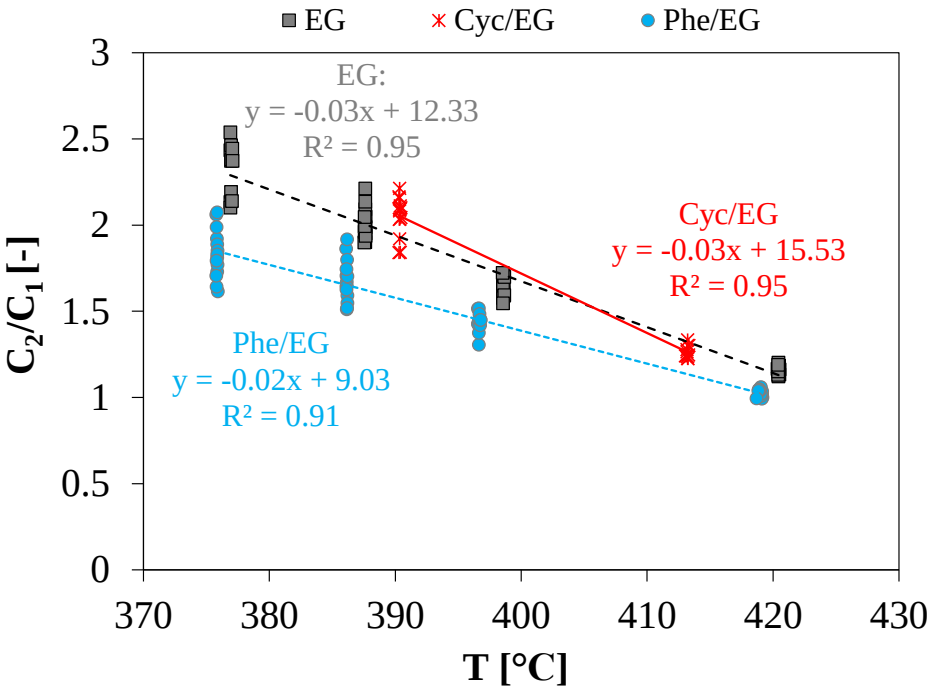

Figure 6.6: *Selectivity towards HDO compared to cracking as a function of temperature from the conversion of ethylene glycol over NiMo#2 (see table 3.3) from experiments with ethylene glycol, phenol, and cyclohexanol in the feed. Data from the final 5 h of each operating temperature. Based on ethylene glycol. For feed composition, see table 6.2. For temperature profiles, see figure 6.2.*

The combined yield of propane and propylene was ≤10 % during the initial deactivation period (TOS ≤69 h). However, at the subsequent steady states (T_{SP} = 380-400 °C), this number was less than 1 %, and it remained low (≤2%) during the remainder of the activity tests, indicating that active sites (potentially acid sites) responsible for carbon-carbon bond formation had been deactivated, probably by coking.

6.2.2.4 Kinetics of Ethylene Glycol Hydrodeoxygenation

The proposed reaction scheme for the conversion of ethylene glycol into C_1, C_2, and C_{3+} products is shown in figure 6.7. Based on the experimental results for conversion of ethylene glycol over sulfided catalysts, the HDO reactions have been assumed to follow a route of consecutive dehydration and hydrogenation reactions (see e.g. figure 5.2). Ethenol, vinyl alcohol, is expected to be shifted via tautomerization towards its keto form, acetaldehyde, which same as ethenol can be hydrogenated to form ethanol. Acetaldehyde was detected in the gas product from ethylene glycol conversion over sulfided catalysts in experiments, where an extended gas analysis was performed (see Appendix G). CO and CH_4 can form from the decarbonylation of acetalaldehyde, but the yields of these products

with Y_{CO}/Y_{CH_4} >1 (see figure 6.5c-d) show that cracking of ethylene glycol also occurred. CO_2 can form from the WGS reaction.

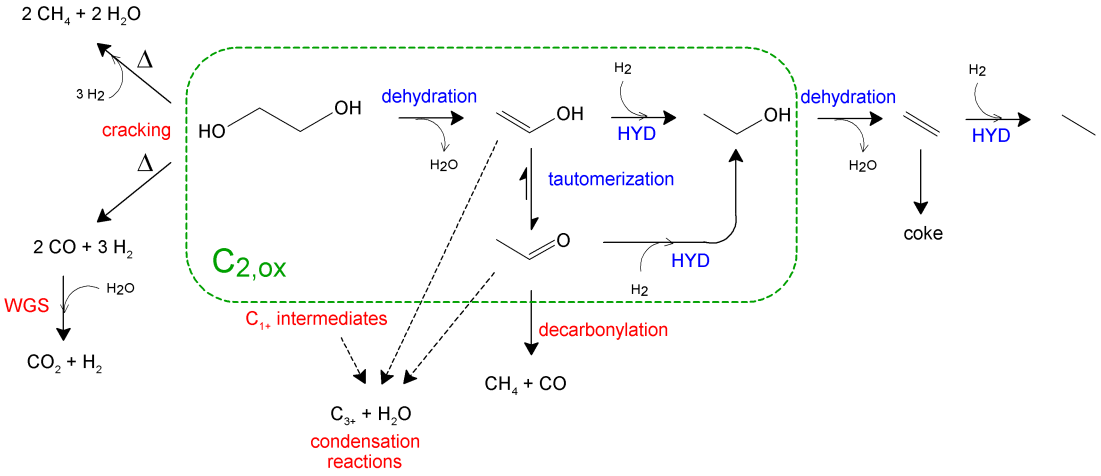

Figure 6.7: *Proposed reaction scheme for the conversion of ethylene glycol into C_1, C_2, and C_{3+} products including target reactions (blue) and side reactions (red).*

Due to incomplete condensation in the separator tube and lack of oxygenate quantification in the product gas, the kinetic model was set up with a lumped $C_{2,ox}$ term covering ethylene glycol, ethenol, acetaldehyde, and ethanol as indicated in figure 6.7. The kinetic model was based on the assumption of a constant and excess hydrogen pressure and first order kinetics for the remaining species (see Appendix I). All species were assumed to be in the gas phase, and the total volumetric flow rate, v, was assumed constant. The reactions included were the joint dehydration and hydrogenation of $C_{2,ox}$ into ethylene, and the subsequent hydrogenation of ethylene into ethane:

$$C_{2,ox} + H_2 \xrightarrow{k_1} C_2H_4 + 2H_2O, \quad \Delta H_{380-400°C} = -47\,\text{kJ/mol}\,,\ C_{2,ox} = \text{EG} \tag{6.1}$$

$$C_2H_4 + H_2 \xrightarrow{k_2} C_2H_6, \quad \Delta H_{380-400°C} = -141\,\text{kJ/mol} \tag{6.2}$$

$$r_1 = k_1' C_{C_{2,ox}} \tag{6.3}$$

$$r_2 = k_2' C_{ETY} \tag{6.4}$$

r_i is the reaction rate for reaction i with the lumped rate constant k_i' and C_y is the concentration of compound y. ETY and ETA denote ethylene, and ethane. The packed bed reactor model was used to set up molar flow balances for ethylene glycol, ethylene, and ethane based on reactions 6.1 and 6.2 and the respective rate expressions in equations 6.3 and 6.4:

$$\frac{dF_{C_{2,ox}}}{dW} = -r_1 = -k_1' C_{C_{2,ox}} \tag{6.5}$$

$$\frac{dF_{ETY}}{dW} = r_1 - r_2 = k_1' C_{C_{2,ox}} - k_2' C_{ETY} \tag{6.6}$$

$$\frac{dF_{ETA}}{dW} = r_2 = k_2' C_{ETY} \tag{6.7}$$

W is the catalyst mass and F_i is the molar flow rate of compound i. The concentration was determined as $C_i = F_i/v$. The rate constants were parametrized according to equation 6.8 in order to decouple the activation energy and the pre-exponential factor:

$$k = k_{\text{ref}} \cdot exp\left(\frac{-E_a}{R}\left(\frac{1}{T} - \frac{1}{T_{\text{ref}}}\right)\right) \tag{6.8}$$

k_{ref} is the reference rate constant at the temperature T_{ref} in K. E_a is the activation energy in kJ/mol and R is the gas constant equal to $8.315{\cdot}10^{-3}$kJ/mol. The inlet molar flows of ethylene glycol ($F_{\text{C}_{2,\text{ox}},0} = F_{\text{EG},0}$), ethylene (zero), and ethane (zero), were used as initial conditions for the system of differential equations presented in 6.5-6.7, which was solved, while values of k_{ref} and E_a were fitted. The conversion in the two reactions was then determined by comparing the calculated outlet flows of ethylene and ethane to the feed flow of ethylene glycol, $F_{\text{EG},0}$:

$$X_1 = \left.\frac{F_{\text{ETY}} + F_{\text{ETA}}}{F_{\text{EG},0}}\right|_{W=0.5\text{g}} \tag{6.9}$$

$$X_2 = \left.\frac{F_{\text{ETA}}}{F_{\text{EG},0}}\right|_{W=0.5\text{g}} \tag{6.10}$$

Only steady state data were used, and for each steady state, the data used were the average from the final 5 hours at the given steady state. The results are summarized in table 6.4 with the Arrhenius plots shown in figure 6.8. Based on the evaluation of the Mears' criterion and the effectiveness factor [294], it was concluded, that the experiments were conducted without significant external or internal diffusion limitations (see Appendix I).

Table 6.4: *Rate constants, conversions, and activation energy for the conversion of ethylene glycol according to the reactions 6.1 and 6.2. T_{ref} = 395 °C.*

Experiment	**TOS**	**T**	$\boldsymbol{k'_1 \cdot 10^3}$	$\boldsymbol{k'_2 \cdot 10^3}$	$\boldsymbol{X_1}$	$\boldsymbol{X_2}$	$\boldsymbol{E_{a,1}}$	$\boldsymbol{E_{a,2}}$	$\boldsymbol{k_{\text{ref},1} \cdot 10^3}$	$\boldsymbol{k_{\text{ref},2} \cdot 10^3}$
	[h]	**[°C]**	**[L/(min·g)]**		**[%]**		**[kJ/mol]**		**[L/(min·g)]**	
	99-104	398.6	16.4	271	8.08	3.76				
EG	134-139	387.6	12.4	264	6.28	2.90	93.3	8.15	15.0	269
	165-170	377.0	9.41	258	4.87	2.23				
	99-104	396.6	14.2	250	7.02	3.10				
Phe/EG	134-139	386.1	10.8	235	5.46	2.33	95.9	22.1	13.6	248
	165-170	375.8	8.15	220	4.23	1.75				
Phe/EG	99-104	395.3	11.5	78.9	5.75	1.03	135	22.2	11.4	78.7
-ReGenA[a]	132-137	384.5	7.71	73.9	3.96	0.679				
Phe/EG	148-153	388.1	12.6	78.4	6.34	1.15	141	32.3	16.4	83.3
-ReGenB[b]	173-178	377.2	8.19	71.1	4.24	0.712				
Cyc/EG	64-69	413.2	22.2	336	10.5	5.52	85.4	2.43	14.8	332
	85-90	390.4	13.3	331	6.65	3.50				

[a] Activity before unexplained change at TOS ∼ 138 h.

[b] Activity after unexplained change at TOS ∼ 138 h.

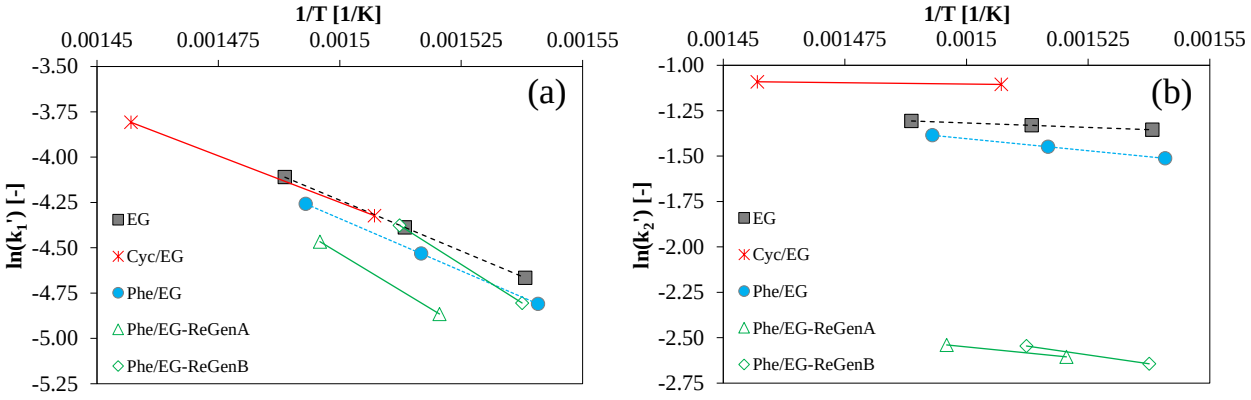

Figure 6.8: *Arrhenius plots for the rate constants presented in table 6.4. (a) k_1': Initial dehydration and hydrogenation of $C_{2,ox}$ into ethylene (reaction 6.1). (b) k_2': Hydrogenation of ethylene into ethane (reaction 6.2).*

The equilibrium of reactions 6.1 and 6.2 are both fully shifted towards the product side with approximately full conversion of ethylene glycol (in reaction 6.1) and ethylene (in reaction 6.2) at the applied operating conditions (calculated with HSC Chemistry). Incomplete conversion of ethylene glycol was however obtained during steady state operation (see table 6.4), and ethylene and ethane were formed at similar yields. Thus, the reactions were run far from equilibrium, and the low activation energy of 2.43-32.2 kJ/mol for the hydrogenation of ethylene therefore indicates that this reaction was restricted by a limited access to hydrogenation active sites. The hydrogenation of ethylene was faster than the rate of the initial dehydration and hydrogenation of ethylene glycol with k_2'/k_1' = 15-27, except in the case for the reactivated catalyst, where this ratio was 6-10.

The Arrhenius plots (see figure 6.8) revealed that the kinetics of ethylene glycol HDO were rather similar for pure ethylene glycol and in the presence of phenol or cyclohexanol, especially in the first dehydration and hydrogenation step with k_1' = 8.15-22.2·10^{-3} L/min/g and $E_{a,1}$ = 85.4-95.9 kJ/mol, suggesting that no immediate inhibition of ethylene glycol HDO from phenol or cyclohexanol occurred (figure 6.8a). The hydrogenation of ethylene was apparently more dependent on whether phenol or cyclohexanol was present in the feed (figure 6.8b). Cyclohexanol seemed to have a slight promoting effect, while phenol seemed to have a slight inhibiting effect. Phenol is expected to adsorb strongly onto the support, which may block the accessibility to active edge sites [75, 200] and thereby limit hydrogenation. Cyclohexanol dehydration was believed to occur over the acid sites of the support, and it is possible that this occupation of acid sites has prevented coke formation, which could block the accessibility to hydrogenation sites. It should however be noted that the hydrogenation activity was generally subject to some variation in reproduced experiments (see Appendix H, figure H.2).

The reactivated catalyst showed a decreased hydrogenation rate (k_2' = 71.1-78.9·10^{-3} L/min/g) and a significantly higher barrier for the initial ethylene glycol dehydration and hydrogenation ($E_{a,1}$ = 135-141 kJ/mol). This was explained by the loss of Mo from the active phase and slight sintering of the active phase (see section 6.2.3.3).

6.2.2.5 Phenol Reactivity in the Presence of Ethylene Glycol

Phenol, which was fed in a mixture with ethylene glycol, was not converted at the applied conditions over the sulfided NiMo catalyst. The only products detected from phenol were small concentrations of alkyl substituted phenols and coupling products (primarily 2-ethylphenol, 3-methylphenol, and benzofuran), which were ascribed to the support acidity. These non-deoxygenated coupled products were mainly formed at TOS <30 h at a total phenol based yield of up to 12 %. At TOS >30 h, this yield was 0.4-3.7 %.

Cyclohexanol on the other hand was converted; both from a pure feed and in a mixture with ethylene glycol (see section 6.2.2.6). This suggested that lack of ring hydrogenation was the reason for the lack of phenol conversion. A NiMo catalyst was chosen over a CoMo catalyst due to its known hydrogenation activity [142, 262]. Ni-MoS_2 has been reported to promote phenol HDO by ring hydrogenation (HYD) prior to breakage of the C-O bond, whereas direct deoxygenation (DDO) can be performed with Co-MoS_2 [80, 109, 113, 141]. Hydrogenation activity is furthermore necessary to stabilize reactive intermediates and limit coke formation [87, 212].

Equilibrium calculations can explain the lack of ring hydrogenation from a thermodynamic perspective, as benzene is the favored HDO product from phenol at the applied temperature and feed composition (see Appendix I.5). At a temperature of $\sim$ 265 °C, thermodynamics prescribe an equimolar mixture of benzene and cyclohexane, whereas a temperature below 210 °C is necessary to thermodynamically favor full hydrogenation of the aromatic ring at the applied feed composition. The temperature was decreased to 280 °C for the reactivated catalyst to test this hypothesis, based on the work of Mortensen et al. [34], who reported $\sim$ 20-55 % phenol conversion over a Ni-MoS_2/ZrO_2 catalyst tested in the same flow reactor setup at TOS $\leq$100 h at 280 °C, 100 bar, $\sim$ 283 ppm H_2S and a WHSV of 4.0 h^{-2} of 50 g/L phenol in 1-octanol. No conversion of either ethylene glycol or phenol was however observed at 280 °C, and another experiment using more catalyst should be performed if the activity at 280 °C is to be assessed. Alternatively, the activity over a Co-promoted catalyst could be tested without changing the temperature to see if DDO is feasible.

The lack of ring hydrogenation can also be explained from a mechanistic perspective as it has been proposed that HDO of phenolic species over Ni-MoS_2 requires a flat ring adsorption onto the slab surface (see figure 2.12) [71, 113], which facilitates ring hydrogenation. If most active sites were occupied by ethylene glycol, its derivatives, or coke, these species could sterically hinder flat ring adsorption of phenol. Ryymin et al. [92] reported a slight suppression of methyl heptanoate HDO in the presence of phenol at 250 °C and 75 bar using a commercial $NiMo/Al_2O_3$ catalyst in a batch reactor at reaction times lower than 50 minutes. At the same time, they reported a notable inhibition of phenol HDO in the presence of methyl heptanoate during the entire reaction time of $\sim$ 4.5-5 h, and they suggested that the inhibiting effect of the ester on phenol was caused by a competition for active sites. An additional possibility, is that the H_2S concentration was too high for phenol conversion in the current experiments [109].

In this work, no hydrogenation or deoxygenation of phenol was observed. Thus, it is speculated that the lack of ring hydrogenation and subsequent deoxygenation might be a combination of thermodynamic and mechanistic constraints. To investigate this further, it could be interesting to study the conversion of phenol at varying temperatures, possibly with a lower H_2S feed and in the absence of other oxygenates, i.e. dissolved in an inert solvent such as an alkane.

6.2.2.6 Conversion and Product Yields from Cyclohexanol Conversion

Cyclohexanol was converted both in the presence and absence of ethylene glycol, see figure 6.9. The conversion and yields were calculated on a cyclohexanol basis. In the case of 1,4-dioxaspiro[4.5]decane ($C_8H_{14}O_2$), the cyclohexanol based yield was calculated from 6/8 of the molar flow of this product to disregard carbon from ethylene glycol.

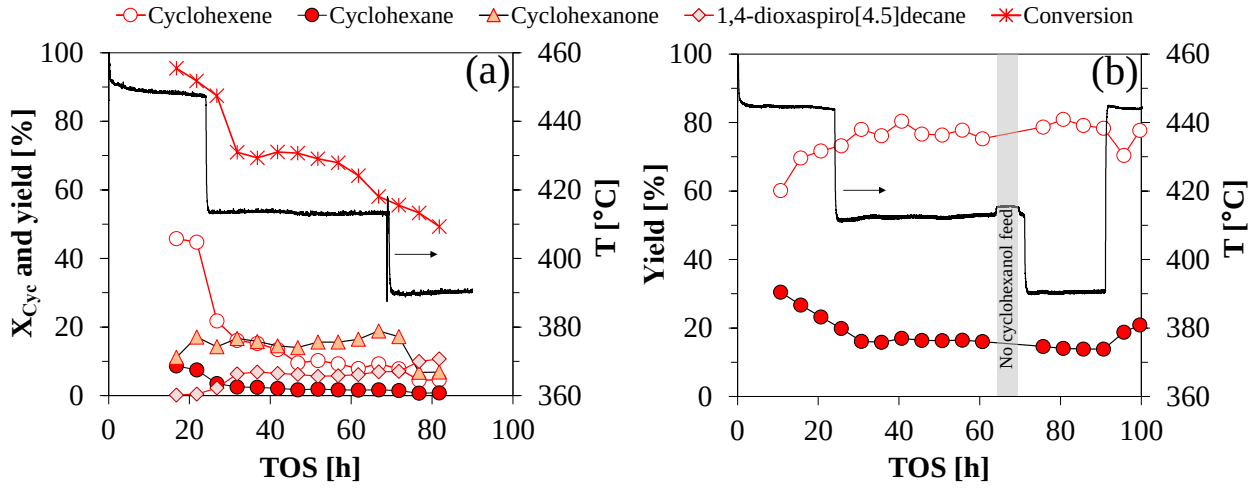

Figure 6.9: *Temperature profile and cyclohexanol based product yields from the conversion of cyclohexanol over NiMo#2 (see table 3.3) in the presence (a) and absence (b) of ethylene glycol. See table 6.2 for feed composition. Based on cyclohexanol. The conversion of cyclohexanol in the absence of ethylene glycol (b) was ≥99.5 % during the entire time on stream.*

In the presence of ethylene glycol, >90 % conversion was initially obtained, decreasing to approximately 70 % at 29-64 h on stream, where an approximate steady state was obtained at 413 °C (figure 6.9a). As the temperature was decreased to the setpoint of 400 °C, the conversion continued to decrease reaching 49 % at 82 h on stream. Shortly after, setup issues (a plug in the backpressure valve for liquid collection), forced termination of the experiment. As steady state was obtained after 8 h upon the temperature change at 24 h, it was assumed that the data points at 77 and 82 h (after the temperature change at 69 h) represented steady state values. The product composition from the feed containing ethylene glycol was comprised of cyclohexene, cyclohexane, cyclohexanone, and 1,4-dioxaspiro[4.5]decane (a ketal coupling product from cyclohexanone and ethylene glycol). The yield of HDO products were 4.5-16 % cyclohexene and 0.7-2.5 % cyclohexane at TOS >30 h. The yields of by-products were significant; 5.7-11 % 1,4-dioxaspiro[4.5]decane, and 6.8-19 % cyclohexanone in the same time period.

Pure cyclohexanol was close to being fully converted (X ≥99.5 %) during the entire duration of the activity test at 390-450 °C and a WHSV of 18 h^{-1} (see figure 6.9b). Cyclohexene and cyclohexane were the dominant products, only trace amounts of cyclohexanone were formed. The yield of cyclohexene was 60-80 % and that of cyclohexane was 14-30 %. There was an initial decrease in the yield of cyclohexane and increase in cyclohexene indicating some deactivation of hydrogenation activity as observed for the conversion of ethylene glycol. As the conversion of pure cyclohexanol was performed at a four times lower cyclohexanol residence time compared to the experiment with ethylene glycol in the feed (see table 6.2), these results show that ethylene glycol inhibited the conversion of cyclohexanol significantly.

The equilibrium conversion for the dehydration of cyclohexanol to cyclohexene at the applied feed composition is 100 % at temperatures above 200 °C (calculated with HSC Chemistry), suggesting that this reaction could be at equilibrium in the activity test using a pure cyclohexanol feed. The equilibrium conversion for hydrogenation of cyclohexene is 100 % at temperatures below 300 °C, and in the range of 390-415 °C, the molar ratio of cyclohexane to cyclohexene is 10-20 at equilibrium. Here, this ratio was 0.2-0-3, which suggested that the hydrogenation reaction was limited. Cyclohexanol dehydration is proposed to mainly take place on the acid sites of the $MgAl_2O_4$ support [259, 260], whereas hydrogenation occurs on the active Ni-MoS_2 phase. It is thus possible that concentration of active sites for hydrogenation, i.e. the loading of Ni-MoS_2, was too low to enable hydrogenation of all the cyclohexene produced, or that the rate of cyclohexene hydrogenation was significantly slower than that of cyclohexanol dehydration.

It was not possible to estimate, if the acidic support provided more active sites for dehydration than the sulfide particles did for hydrogenation. The concentration of acid sites in the $MgAl_2O_4$ support measured by NH_3-TPD (see chapter 4) corresponded to 0.68 acid sites/nm^2 of the support. The Mo loading of the oxide precursor was 3.7 Mo atoms/nm^2 (see table 3.3). A Mo-Mo distance of 3.16 Å [284] and an approximate MoS_2 slab length of 4 nm (see figure 6.17, section 6.2.3.3) corresponds a MoS_2 particle diameter containing 13 Mo atoms. Assuming a perfect hexagonal MoS_2 structure [284], such a particle would have a total of 127 Mo atoms, from which 36 are in active edge positions. Thus, $\sim$ 1.1 Mo atoms/nm^2 (30 % of 3.7) could be expected to be available in active site positions at the edges of hexagonal MoS_2 slabs. If brim sites are necessary for hydrogenation, the availability of these sites could be even lower, as some MoS_2 particles were stacked in two or more layers. An *in-situ* XAS sulfidation study however showed that the majority of the sulfided Mo particles were present as nanoparticles with a low Mo-Mo coordination number, which could be modelled as a MoS_2-derived Mo_2S_6 nanocluster (see chapter 5). If the majority of the sulfide phase in this work was present as such nanoclusters, all 3.7 Mo atoms/nm^2 could potentially be available as edge sites, but their hydrogenation properties compared to brim sites are unknown. Further characterization of the employed NiMo catalyst would be needed to determine the concentration and identity of active sites in this catalyst.

6.2.2.7 Kinetics of Cyclohexanol Hydrodeoxygenation

Based on the results from the activity tests, the conversion of cyclohexanol was assumed to follow a dehydration step forming cyclohexene, which could then be hydrogenated to cyclohexane (figure 6.10). The kinetic model was derived similarly as to that for ethylene glycol (see Appendix I) and steady state data was used to get the results presented in table 6.5.

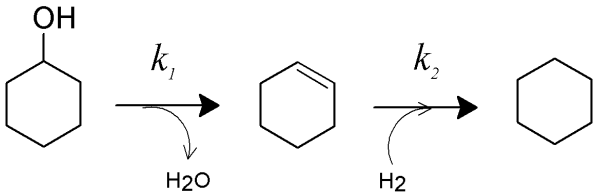

Figure 6.10: *Proposed reactions of cyclohexanol HDO. $\Delta H_{380-400^\circ C}$: 41 kJ/mol (reaction 1) and -124 kJ/mol (reaction 2).*

Table 6.5: *Rate constants, conversions, and activation energy for the conversion of cyclohexanol according to reactions in figure 6.10. T_{ref} = 395 °C.*

Experiment	TOS[a] [h]	T [°C]	$k_1 \cdot 10^3$ [L/(min·g)]	$k_2' \cdot 10^3$ [L/(min·g)]	X_1 [%]	X_2 [%]	$E_{a,1}$ [kJ/mol]	$E_{a,2}$ [kJ/mol]	$k_{\text{ref},1} \cdot 10^3$ [L/(min·g)]	$k_{\text{ref},2} \cdot 10^3$ [L/(min·g)]
Cyc[b]	53-63	412.8	≥524	55.1	93.1	16.5	-	43.3	-	45.2
	78-88	390.5	≥524	43.5	93.7	13.7				
Cyc/EG	54-64	413.0	21.4	74.4	10.2	1.72	121	82.9	12.1	50.3
	74-84	390.0	10.3	44.9	5.2	0.566				

[a] Averages for two sample bottles (TOS of 10 h) collected at steady state operation.

[b] Reaction 1 was assumed at equilibrium, and parameters were not fitted. k_1 represents an average value of the two steady states determined as $k_1 = \frac{v}{W} ln\left(\frac{1}{1-X_1}\right)$.

The results in table 6.5 support the observation that cyclohexanol was readily converted in the absence of ethylene glycol. The first dehydration step was very fast with k_1 ≥524·10^{-3} L/min/g and a conversion above 90 %, and could therefore have been subject to mass transfer limitations. The deviation between the experimentally observed cyclohexanol conversion of close to 100 % and the modelled value of X_1 = 93.1-93.7 % shows that the measured amount of cyclohexene and cyclohexane formed could not account for the full conversion of cyclohexanol.

Ethylene glycol strongly inhibited the dehydration of cyclohexanol. With ethylene glycol present in the feed, the conversion in reaction 1, X_1, dropped by a factor of 9-18, in spite of the higher cyclohexanol residence time in this experiment. The rate constant, k_1, decreased from ≥524 to 10.3-21.4·10^{-3} L/min/g, and there was a notable activation energy of 121 kJ/mol. This detrimental effect was explained by deactivation of acidic active sites by carbon deposition (see also section 6.2.3.1). The hydrogenation of cyclohexene was also affected by the presence of ethylene glycol, which caused the activation energy, $E_{a,2}$, to double, while the rate constant remained more constant. This could be caused by the competition for hydrogenation active sites.

Interestingly, the hydrogenation step was the fastest for ethylene glycol with k_2'/k_1' = 15-27 (disregarding the reactivated catalyst). For pure cyclohexanol, the dehydration was the fastest step with k_2'/k_1 ≤0.1. This further supports that the conversion of ethylene glycol and cyclohexanol was taking place on different active sites. Full deoxygenation of cyclohexanol can occur on acid sites supplied by the support without interaction with the MoS_2 active phase, whereas ethylene glycol HDO depends on MoS_2 for intermediary hydrogenation.

6.2.3 Catalyst Deactivation and Regeneration

Catalyst deactivation occurred in all activity tests performed. For tests performed at 400 °C (see chapter 5), deactivation was evident throughout the tests. In the current tests, where a steady state was obtained at ∼ 380-400 °C, the deactivation was evident at temperatures above 400 °C.

6.2.3.1 Origin of Deactivation

Even though a promoting and stabilizing effect was observed from increasing the H_2S concentration in the feed during ethylene glycol conversion (see chapter 4 and 5), oxidation of the active sulfided phase could not explain the loss of activity over time, as proposed by Badawi et al. [106,107]. This became clear, as resulfidation of deactivated $MoS_2/MgAl_2O_4$ and Ni-$MoS_2/MgAl_2O_4$ catalysts could not regenerate their activity (see figure 6.11). Resulfidation was performed similarly to the initial

catalyst activation. Resulfidation of the unpromoted MoS_2 catalyst after 24.5 h on stream facilitated a brief reactivation (figure 6.11a). During the first 24.5 h, the ethane yield had dropped from 42 to 8 %, while the ratio of C_2/C_1 decreased from 3.1 to 1.8. Resulfidation only partly reactivated the catalyst, giving 18.8 % ethane and $C_2/C_1 = 2.8$. However, the ethane yield rapidly decreased, and within 4 h, it was similar to what was obtained before the resulfidation. The ethylene yield was less affected by deactivation and resulfidation. The same trend was seen for the promoted Ni-MoS_2 catalyst (see figure 6.11b). The activity during 33-106 h on stream is not shown in figure 6.11b, due to uncertainties in the feed flow rate and composition. During this period, the feed bottle with pure ethylene glycol was exchanged back and forth with one containing 30 wt% H_2O in ethylene glycol. The goal was, among others, to vary the H_2O/H_2S ratio while keeping a constant ethylene glycol feed flow. However, the operation time at the different conditions investigated was too low to ensure a stable feed flow of either pure ethylene glycol or 30 wt% H_2O in ethylene glycol. Hence, the yield and conversion could not be calculated without greater uncertainty, and the data has hence been omitted.

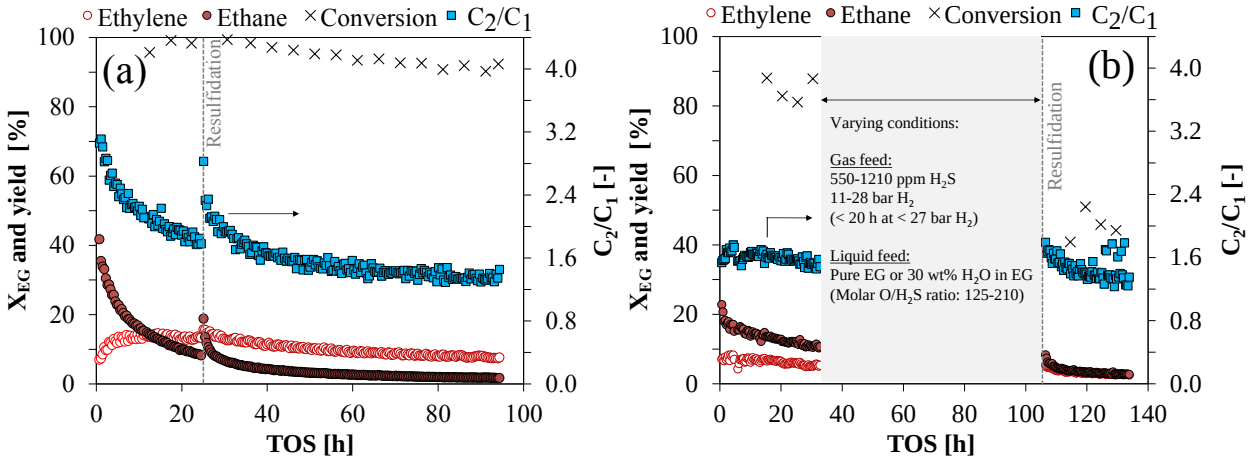

Figure 6.11: *TOS activity for ethylene glycol conversion at 40 barg with 27 bar H_2, 550 ppm H_2S, and 3-3.5 mol% ethylene glycol in the feed. (a) At 450 °C over 1.5 g $MoS_2/MgAl_2O_4$ (Mo#2). (b) At 400 °C over 0.5 g Ni-$MoS_2/MgAl_2O_4$ (NiMo#1), see table 3.3. The activity during TOS = 33-106 h is not shown due to uncertainties in the feed flow, leading to uncertain determination of conversion and yields.*

Carbon deposition was found to be the main source of deactivation rather than oxidation of the sulfide phase. This is in agreement with the findings that the active phase is highly stable towards oxidation (see chapter 5); i.e. exposure to water did not deactivate the catalysts significantly. Figure 6.12 shows how the carbon deposition on spent catalysts followed a linear trend as a function of the activity test run time (summarizing tables 4.4, 5.1, and 6.6). The carbon deposited at TOS = 0 h stems from DMDS residues left in the catalyst pores after sulfidation.

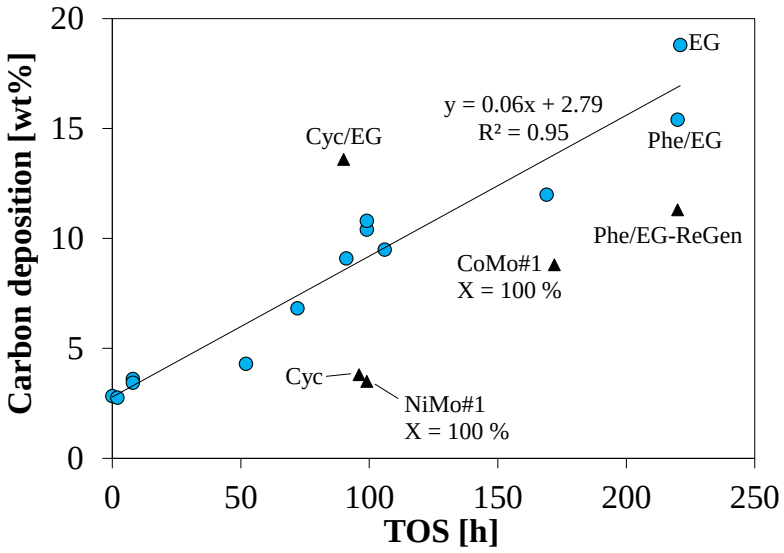

Figure 6.12: *Carbon deposition as a function of run time. From HDO tests performed at 380-450 °C (see tables 4.4, 5.1, and 6.6). Linear trend (circles) for the conversion of ethylene glycol, acetic acid, and phenol in ethylene glycol (1^{st} run) over NiMo and CoMo catalysts (and the $MgAl_2O_4$ support). Outliers (triangles) from experiments with ethylene glycol conversion at 100 % (NiMo and CoMo), for feeds containing cyclohexanol (Cyc and Cyc/EG), and for the reactivated catalyst tested with phenol in ethylene glycol (Phe/EG-ReGen).*

In activity tests with close to 100 % conversion during the entire TOS (see chapter 4), the carbon deposition was lower than expected from the linear trend, indicating that the catalyst bed was not fully utilized and that only a fraction of the catalyst was deactivated by carbon deposition (see figure 6.12). Even though a strong adsorption of phenol onto Al_2O_3 supports has been reported [75, 200], phenol did not seem to prevent carbon deposition by competitive adsorption with ethylene glycol. The carbon deposition from the first Phe/EG run was within the linear trend, whereas the carbon deposition on the reactivated catalyst was lower than expected. This might be explained by the lower activity obtained after reactivation (see table 6.4). The experiments performed with cyclohexanol also deviated from the linear trend. Pure cyclohexanol was seen to have a lower propensity for coke formation than ethylene glycol in agreement with the high propensity for coke formation of polyolic species [87] as well as the fact that ethylene glycol HDO occurs via the formation of strong coke precursors such as ethylene [270]. The carbon deposition from the mixed cyclohexanol and ethylene glycol feed was higher than expected from the linear trend, which was ascribed to the abrupt termination of this experiment (plugging), which did not allow for controlled desorption of condensed species from the catalyst pores.

The proportional deposition of carbon as a function of operating time is known from industrial hydrotreating, where the initial carbon deposition profile similarly follows a linear trend, which is inversely proportional with the catalyst surface area (figure 6.13) [295], as the coke builds up and blocks the catalyst pores [212]. In hydrotreating, this initial carbon deposition is driven by the acidity of the support, and once the acid sites have been saturated, carbon deposition occurs at a slower rate, and the profile levels off at 20-25 wt% coke [212, 295]. Had the activity test TOS been extended beyond 221 h (the maximum TOS used), it is thus possible that the carbon deposition profile shown in figure 6.12 would level off at some point due to saturation of the acid sites.

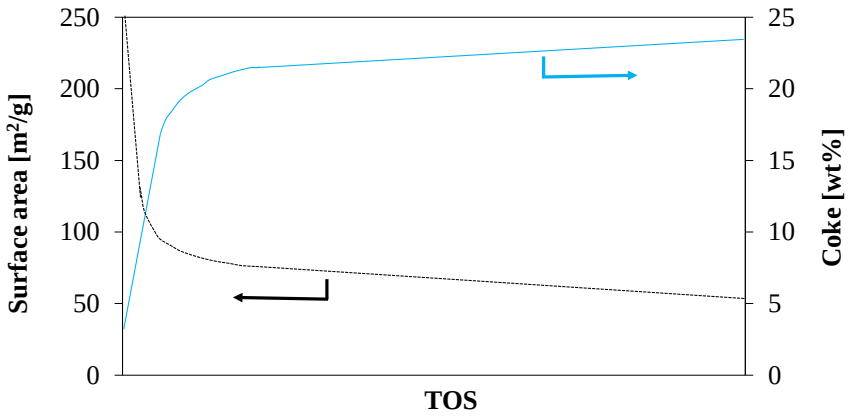

Figure 6.13: *Typical profile for carbon deposition and its influence on specific surface area as a function of TOS for industrial hydrotreating catalysts. Redrawn from [295] with permission from Elsevier.*

Carbon deposition has been reported as a primary cause of catalyst deactivation and process upsets in HDO experiments using real bio-oil [38, 94, 98–102]. As mentioned in chapter 2, this is due to the high content of highly reactive oxygenates that readily polymerize upon heating [86, 212, 217]. When an acidic carrier is used as is the case for these $MgAl_2O_4$ supported catalysts, polymerization and coking reactions are further enhanced [75–77]. The coking propensity also depends highly on the oxygenate identity [76, 217]. This is evident from figure 6.12, which shows that ethylene glycol, a reactive polyol [65, 67] which has ethylene as HDO intermediate, had a high propensity for carbon deposition.

TEM (see figure 6.14), revealed that the deposited carbon was present throughout the spent catalysts, which is in agreement with previous findings [296]. The carbon appeared crystalline in agreement with previous Raman results (see figure 4.14 in chapter 4). The lattice distances were analyzed by performing fast Fourier transforms of several crystalline areas in the TEM images of spent catalysts, which showed the presence of the $MgAl_2O_4$ support, and indicated the presence of carbon as well. Figure 6.14 reveals the consequence of carbon deposition: a $\sim$ 20 nm long, rectangular support particle sticking out of the bulk sample, having a double layer sulfide slab on either side, is covered in carbon. The deposited carbon thus limits the accessibility to the MoS_2 active sites and inhibits HDO as well as other sulfide catalyzed reactions.

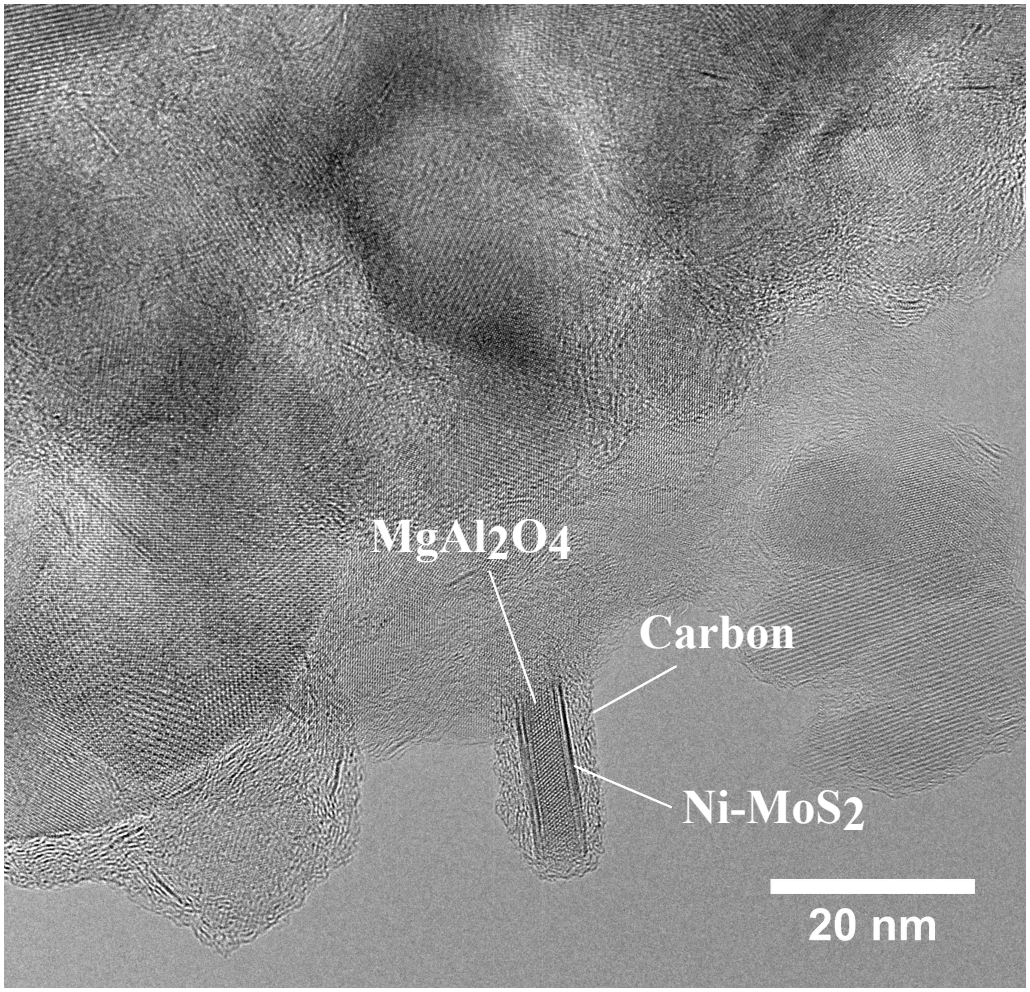

Figure 6.14: *TEM image of spent NiMo#2 from experiment EG (see table 6.2 for feed composition).*

6.2.3.2 Reactivation by Oxidation and Resulfidation

In hydrotreating, the HDS catalyst activity can be maintained for a certain period of time by continuously increasing the reaction temperature [212], and *ex-situ* regeneration can then be performed, once the activity no longer can be maintained by temperature adjustment [220]. When deoxygenation removal occurs during pyrolysis (as catalytic hydropyrolysis), the operation temperature should not be increased markedly, as this would favor gas formation and limit the oil yield [21]. For downstream HDO of pyrolysis vapors, there is however greater flexibility for the choice of temperature, as this step is decoupled from the pyrolysis.

The NiMo catalyst tested for HDO of phenol in ethylene glycol was reactivated. Deposited carbon was burned off in an oxidation step, which left the active sulfide phase in a partially oxidized state requiring a resulfidation step to convert the resulting MoO_xS_y phase back to the active MoS_2 phase. The oxidation step was performed *in-situ* in the POC setup. First, the reactor was heated to 250 °C in a flow of $\sim$ 100 NmL/min N_2. Then the gas was switched to 1 NL/min 7.6 % O_2 (from technical air) in N_2, and slow heating with 1 °C/min was performed until 450 °C. After this point, the temperature was increased in small steps until 545 °C, where it was kept overnight. The concentrations of NO_x (negligible), CO, CO_2, O_2, and SO_2 where monitored using an Emerson NGA 2000 gas analyzer. Upon the change from N_2 to O_2/N_2 at 200 °C, a brief temperature increase of 30 °C was observed, while

concentrations of CO and CO_2 up to 1.8 % and 4.2 %, respectively, were measured. This sudden combustion was explained by the presence of condensed reactant and product residues in the reactor and in the dead volume in the bottom flange of the pressure shell.

The concentration and temperature profiles are shown in figure 6.15 for the period of time, during which the majority of the carbon was burned off. At temperatures above 460 °C, no more carbon was burned off, but continued sulfur removal occurred as a function of temperature. Details on the oxidation can be found in Appendix J.

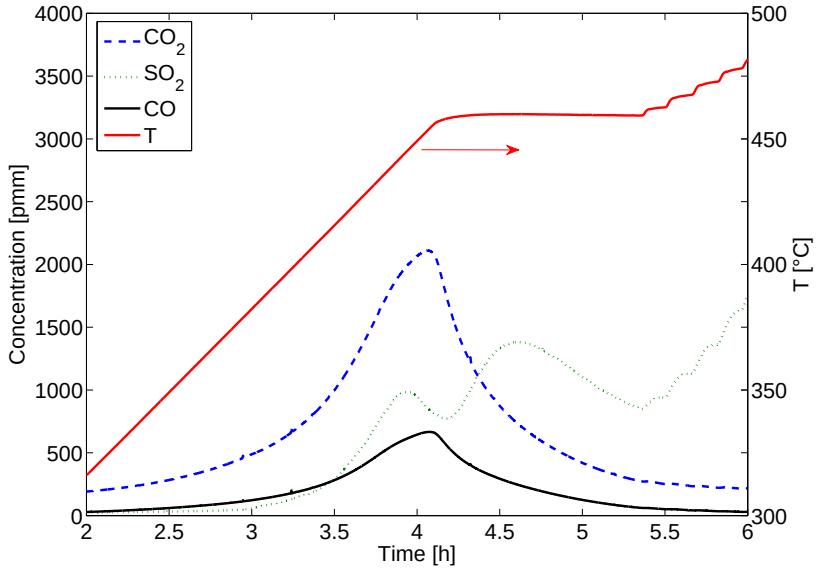

Figure 6.15: *Off-gas concentration profiles and temperature profile from carbon burnoff from NiMo#2 after experiment Phe/EG (before Phe/EG-ReGen). Performed in-situ with 1 NL/min 7.6 %O_2 (from technical air) in N_2. For experimental details, see table 6.2 (feed composition) and figure 6.2 (temperature profiles).*

The following reactions were assumed for the oxidation of deposited carbon and sulfur in MoS_2:

$$C(s) + 0.5O_2(g) \rightarrow CO(g) \tag{6.11}$$

$$C(s) + O_2(g) \rightarrow CO_2(g) \tag{6.12}$$

$$S(s) + O_2(g) \rightarrow SO_2(g) \tag{6.13}$$

The carbon deposition on the catalyst was calculated based on the flow of N_2 and O_2 into the system, and on the concentrations of oxidation products and O_2 measured (see Appendix J) giving a carbon deposition of 15.4 wt%.

The catalyst was then resulfided, and since the catalyst was only converted into a partial oxide phase, MoO_xS_y, by the oxidation step, the resulfidation took shorter time than the initial sulfidation. The catalyst activity was then tested again for the conversion of ethylene glycol and phenol.

6.2.3.3 Activity of Reactivated Catalyst

The 1st run and reactivated catalyst activity is shown in figure 6.16 for TOS $\leq$ 125 h on stream, where the reaction temperatures were comparable (see figure 6.2). During the 1st run, the activity measured

at 450 °C in the end of the run at ≥221 h was significantly lower than the initial activity (see figure 6.3-6.5) with a C_2 yield of 10 % compared to an initial yield above 40 %. After reactivation, the activity in terms of C_2 yield was partly recovered at >35 % and the activity towards cracking had decreased significantly giving a C_2/C_1 ratio >3 (see figure 6.16a-b), which increased with decreasing temperature as expected. The conversion was however lower for the reactivated catalyst, and the kinetic investigation (table 6.4), revealed a poorer activity for ethylene glycol HDO; the activation energy for the initial dehydration/hydrogenation, $E_{a,1}$, had increased from 95.9 to 135-141 kJ/mol, and the rate constant for hydrogenation, k_2', had decreased from 220-250·10^{-3} to 71.1-78.9·10^{-3} L/min/g. The lower hydrogenation activity is evident from figure 6.16c-d; a significant proportion of the ethane yield was lost after reactivation, while the ethylene yield for the reactivated catalyst was greater than observed in the 1st run until TOS ∼ 100 h.

Overall, reactivation of the catalyst was possible, as the yield of deoxygenated C_2 species of the spent catalyst was increased to its initial level with a rate of deactivation for the reactivated catalyst similar to what was initially obtained. However, the reactivated catalyst showed a different activity, namely for hydrogenation and cracking, indicating a change in the catalyst composition or morphology.

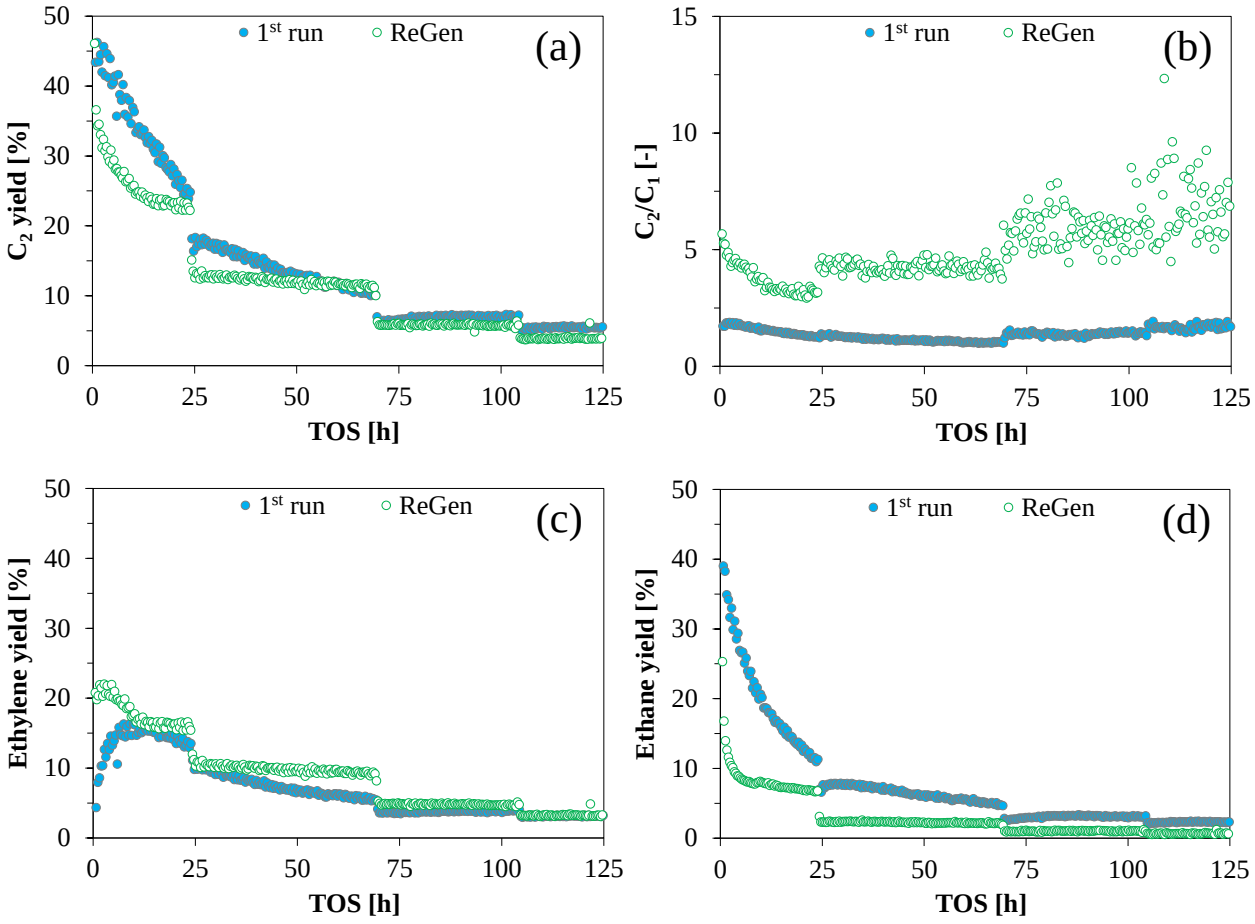

Figure 6.16: *(a) C_2 yield, (b) C_2/C_1 ratio, (c) Ethylene yield, and (d) Ethane yield from 1st run and re-activated catalyst activity in ethylene glycol conversion over NiMo#2 (see table 3.3) from experiment Phe/EG. Based on ethylene glycol. For feed composition, see table 6.2. For temperature profiles, see figure 6.2.*

The spent catalyst compositions (table 6.6), revealed that the reactivated catalyst had lost Mo from its structure, as the Ni/Mo ratio was increased by a factor of 1.7 compared to the remaining catalysts. The

content of Ni and Mo was approximately constant for the other catalysts with a Ni/Mo ratio similar to the fresh catalyst precursor (see table 3.3). There is a risk that Mo present as MoO_3 was volatilized during the oxidation step. The temperature of 545 °C was possibly high enough to facilitate some volatilization of MoO_3 [297], but as it can be seen from figure 6.15 this temperature could be lowered to 460 °C in future work. Water, which is generated from combustion of carbon, may convert MoO_3 into volatile hydroxy molybdenum oxides [220, 297], so the combustion conditions should be optimized to mitigate loss of Mo from H_2O exposure. As the deoxygenation and hydrogenation activity is associated with the MoS_2 and Ni-MoS_2 phases, loss of Mo could explain the change in activity observed for the reactivated catalyst. From table 6.6 it is observed that the spent reactivated sample contained some Si and Fe (0.5-0.6 wt%) indicating insufficient removal of SiC and steel wool from the spent catalyst sample.

Table 6.6: *Composition of spent NiMo#2 (see table 3.3) tested at 380-450 °C in 27 bar H_2, 550 ppm H_2S, and total pressure 40 barg (balance N_2). For experimental details, see table 6.2 (feed composition) and see figure 6.2 (temperature profiles).*

Experiment	TOS [h]	Mo [wt%]	Ni [wt%]	Ni/Mo [molar]	Si [wt%]	Fe [wt%]	S [wt%]	C [wt%]	S/Mo [molar]
EG	221	2.55	0.46	0.29	0.07	0.14	1.71	18.8	2.00
Phe/EG	220(1^{st})	-	-	-	-	-	-	15.4	-
Phe/EG-ReGen	220(2^{nd})	1.45	0.44	0.49	0.51	0.60	2.40	11.3	4.96
Cyc/EG	90	2.63	0.42	0.26	0.05	0.04	1.69	13.6	1.92
Cyc	96	2.96	0.51	0.28	-	0.11	2.18	3.81	2.51
HAc	2	3.09	0.52	0.27	0.02	0.08	2.03	2.76	1.96

The change in activity could furthermore be influenced by a change in the particle size distribution. A TEM analysis was performed for the spent catalysts from the experiment with pure ethylene glycol and with phenol in ethylene glycol (reactivated) with the resulting slab length and slab stacking distributions shown in figure 6.17.

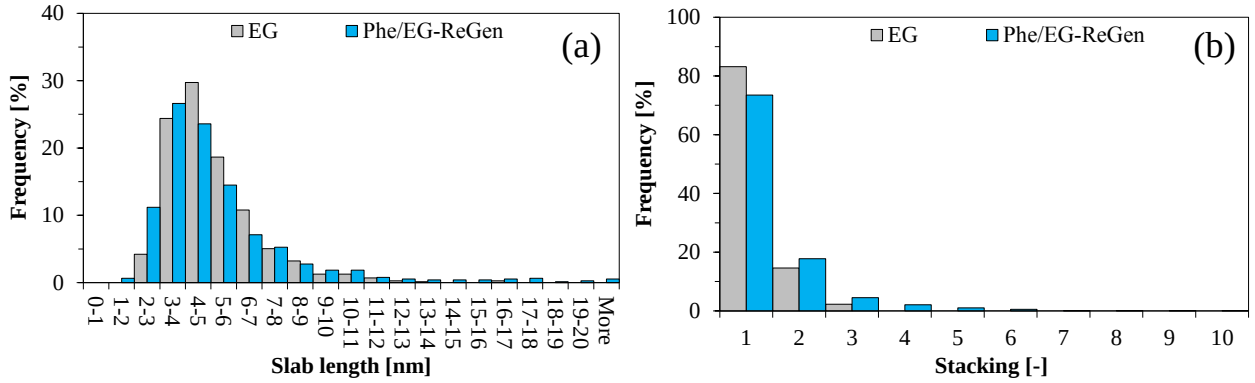

Figure 6.17: *Particle size distribution for spent NiMo#2 catalysts. (a) Slab length. (b) Stacking. Based on > 700 slabs in > 40 images for each sample. For experimental details, see table 6.2 (feed composition) and see figure 6.2 (temperature profiles).*

In line with previous results (see chapter 5), the observed average length and stacking for both spent catalysts were 5.1-5.3 nm and 1.2-1.4. The majority of the observed sulfide particles in the spent catalyst samples were distributed as small monolayer slabs. But while the maximum stacking degree was 3 for the non-reactivated catalyst, several multilayer slabs with stacking degrees of 4-10 were observed in the reactivated sample. These multilayer slabs were also longer than in the non-reactivated sample, as evidenced from the longer tail in figure 6.17. Representative TEM images are given in figure 6.18.

The TEM analysis indicated that some degree of sintering had occurred during the reactivation process, most likely during the high temperature oxidation performed at 545 °C. As a result, the active phase particles present in the reactivated catalyst have had lower concentrations of active edge sites and brim sites (present at the top layer) and a higher concentration of MoS_2 present in inactive bulk and basal plane positions. Especially the loss of brim sites along with the loss of Mo might explain the loss of hydrogenation activity.

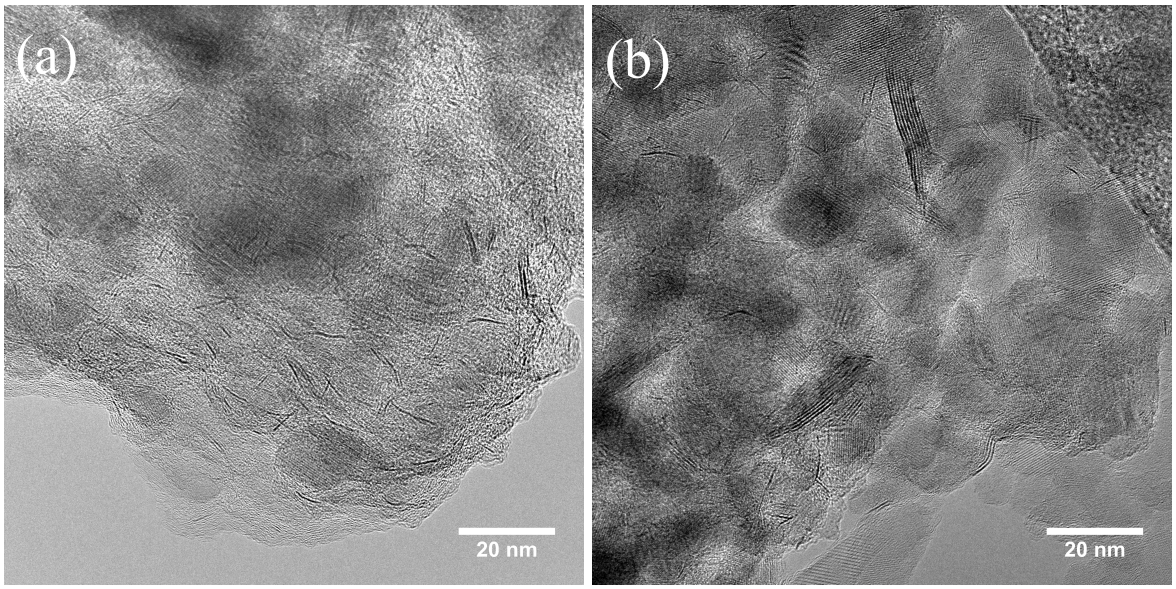

Figure 6.18: *TEM images of spent NiMo#2 catalysts from experiments (a) EG, and (b) Phe/EG-ReGen. For experimental details, see table 6.2 (feed composition) and see figure 6.2 (temperature profiles).*

6.3 Conclusions

The HDO of acetic acid, ethylene glycol, phenol, and cyclohexanol was investigated at 380-450 °C, 27 bar H_2, and 550 ppm H_2S, over Ni-MoS_2/$MgAl_2O_4$. Acetic acid was unstable at the applied conditions, and rapidly coked up the reactor inlet, indicating the necessity of stabilizing reactive pyrolysis vapors immediately when formed, and not through HDO of condensed oil. Prolonged activity tests of 90-220 h were performed for the remaining model compounds. An initial deactivation at 420-450 °C enabled steady state operation in the temperature range of 380-415 °C, but also caused the conversion in the target HDO reactions to be low ($\leq$10.5 %), when ethylene glycol was present in the feed.

No HDO of phenol was detected in the presence of ethylene glycol. This was assigned to a combination of thermodynamic and mechanistic constraints, which prevented hydrogenation of the aromatic

ring. Based on the conversion of cyclohexanol in the presence of ethylene glycol, the lack of phenol conversion at similar operating conditions was ascribed to the lack of aromatic ring hydrogenation.

HDO of ethylene glycol was performed in the presence and absence of cyclohexanol and phenol with a higher rate of ethylene hydrogenation compared to the initial dehydration/hydrogenation step (k_2'/k_1' = 15-27). The thermodynamics prescribe full hydrogenation of ethylene to ethane at the applied conditions, but deactivation of hydrogenation active sites limited this reaction. Phenol and cyclohexanol did not affect the HDO of ethylene glycol significantly.

HDO of pure cyclohexanol readily occurred, and the initial dehydration step occurred at $>$ 90 % conversion, practically at equilibrium, with $k_1 \geq 524 \cdot 10^{-3}$ L/min/g. The subsequent hydrogenation of cyclohexene to cyclohexane was slower and occurred far from equilibrium, indicating that dehydration and hydrogenation reactions could take place on different active sites. Ethylene glycol was seen to inhibit the HDO of cyclohexanol, namely the initial dehydration step, but also the subsequent hydrogenation reaction, which was explained by deactivation of acidic dehydration active sites by competitive adsorption and carbon deposition.

Carbon deposition was the main reason for catalyst deactivation with a linear deposition as a function of TOS. The catalyst could be reactivated by oxidation and resulfidation. The activity for ethylene glycol HDO was however altered by the reactivation, which caused the rate of hydrogenation, k_2' to decrease from 220-250$\cdot 10^{-3}$ to 71.1-78.9$\cdot 10^{-3}$ L/min/g, while the activation energy for the initial dehydration/hydrogenation step increased from 95.9 kJ/mol to 135-141 kJ/mol. This was explained by the loss of Mo from the catalyst structure as well as sintering of MoS_2 slabs, and it is suggested to reconsider the oxidation conditions to prevent volatilization of MoO_3 and sintering of MoS_2.

7 | Conclusions and Outlook

This thesis contributes with new insights to the catalytic hydrodeoxygenation (HDO) of reactive biomass derived oxygenates with (Ni/Co)-$MoS_2/MgAl_2O_4$ catalysts showing high water tolerance of the catalysts and importance of promotion and H_2S level during HDO. These insights allow for further development of catalyst formulations and operating conditions for the production of green fuels from biomass by catalytic fast hydropyrolysis or HDO of pyrolysis vapors.

Processes which couple fast pyrolysis with catalytic HDO prior to condensation of the produced oil show promise, as the reactive oxygenates can be stabilized immediately when formed. Such processes have been presented in the recent literature (within the last <10 years) showing that the technology development for the continuous combined pyrolytic and catalytic conversion of solid biomass to fuels has begun, although still being in its infancy. In most studies on catalyst development for HDO of bio-oil, there is still a focus on condensed oil, which will inevitably coke when heated, and the highly important issues of catalyst deactivation and possible routes for regeneration are often overlooked. Instead, much effort has been put into another important aspect in HDO, which is understanding the chemistry of deoxygenation of the different oxygenate functionalities present in bio-oil. Lignin derived phenolic compounds have been subject to much research. These studies are relevant for downstream HDO of pyrolysis vapor, where the instability and deactivation issues originating from the more reactive cellulosic fraction of biomass have already been dealt with.

In this study, the more reactive oxygenates were targeted with the aim of developing catalysts, understanding deactivation mechanisms, and optimizing operating conditions for the immediate upgrading and stabilization of pyrolysis vapors by HDO. Molybdenum sulfide based catalysts with different loading and promoters (none, Ni, or Co) were supported on a water and attrition resistant $MgAl_2O_4$ support, which is suitable for fluid bed catalytic fast hydropyrolysis. Catalytic activity tests were performed at reaction conditions relevant to catalytic hydropyrolysis (380-450 °C and 27 bar H_2) for different model compounds. Ethylene glycol (EG) was used in most experiments as it represents the reactive polyolic fraction of pyrolysis vapors, which must be upgraded to obtain a stable oil. Several characterization techniques were employed to unravel the composition, morphology, and properties of the prepared catalysts including N_2-physisorption, NH_3-chemisorption, transmission electron microscopy (TEM), X-ray diffraction (XRD), X-ray absorption spectroscopy (XAS), Raman spectroscopy, and elemental analysis.

The conversion of ethylene glycol over the support showed that $MgAl_2O_4$ was responsible for dehydration and coupling reactions forming mainly ethanol, 2-methyl-1,3-dioxolane, and diethylene glycol. Both cracking (giving C_1 species: CH_4, CO, and CO_2) and HDO (giving C_2 species: ethylene and ethane) were catalyzed by the MoS_2 active phase; Ni- and Co-promoted $MoS_2/MgAl_2O_4$ catalysts with different loadings of Mo (0.83-0.88 wt% or 2.83-3.28 wt%) all produced gas yields at the same C_2/C_1 ratio of 1.1-1.5 (at $WHSV_{EG}$ = 2 h^{-1}, 400 °C, and 550 ppm H_2S), but the yields obtained with

the higher loading catalysts were more than four times higher than for the lower loading catalysts. With a co-feed of 550 ppm H_2S, the higher loading catalysts produced ethane at a yield of 40-50 % and thus showed good deoxygenation and hydrogenation activity.

Approximately 100 % conversion was obtained and maintained throughout activity tests of up to 172 h at $WHSV_{EG}$ = 2 h^{-1}, demonstrating the potential of promoted MoS_2 based catalysts. In order to study catalyst deactivation, the WHSV was increased in the subsequent experiments to bring the conversion below 100 % and study loss of activity over time. This allowed for more detailed investigation of the role of promotion, H_2S, and H_2O by coupling activity tests at $\sim$ 50-100 % ethylene glycol conversion with density functional theory (DFT) and *in-situ* XAS. The presence of Ni or Co was confirmed to increase the activity and stability, while H_2S promoted HDO via incorporation of SH groups at the active catalyst edges enabling a better HDO selectivity with $C_2/C_1 \sim 2$ at 2200 ppm H_2S and 400 °C. It was furthermore shown that the prepared catalysts had a good water tolerance, probably owing to a stabilizing interaction with the support.

A significant deposition of mainly crystalline carbon was the main reason for catalyst deactivation and was associated with the support acidity and the reactivity of ethylene glycol. This coking occurred linearly over time, but would be expected to level off at longer time on stream ($>$ 220 h) than investigated in this work. Reactivation of a deactivated Ni-MoS_2 catalyst by oxidation and resulfidation was performed to demonstrate that catalyst regeneration is possible by industrially well-known methods. The high affinity for coke formation from ethylene glycol was shown to inhibit the dehydration of cyclohexanol, and along with a kinetic analysis, this indicated that deoxygenation could take place over active sites from the MoS_2 phase as well as from the support. In this kinetic analysis, it was shown that phenol did not undergo HDO at the applied conditions, indicating that thermodynamic and/or mechanistic constraints hindered the hydrogenation and subsequent deoxygenation of aromatic entities. In a continuous process, HDO of refractory phenolics could potentially be performed downstream of the initial stabilization stage using a different catalyst and different operating conditions.

7.1 Future work

Taking offset in the work presented in this thesis, there are several possible pathways for further research. One could be to investigate the constraints for phenol HDO, where the following experiments could be interesting to conduct:

- Conversion of phenol in ethylene glycol over Ni-$MoS_2/MgAl_2O_4$ at $<$380 °C with more catalyst than currently applied (i.e. WHSV $<$19 h^{-1}) to determine possible thermodynamic constraints.
- Conversion of phenol in ethylene glycol over Ni-$MoS_2/MgAl_2O_4$ with $<$550 ppm H_2S to determine possible inhibition from H_2S.
- Conversion of phenol dissolved in an alkane over Ni-$MoS_2/MgAl_2O_4$ to determine possible inhibition from ethylene glycol.
- Conversion of phenol over Co-$MoS_2/MgAl_2O_4$ to determine possible mechanistic constraints.

Another pathway could be to expand the investigation of catalyst deactivation to include other potential inhibitors/poisons than sulfur, coking, and water, which were covered in this work. Alkali metals, chlorine, ammonia, and carbon monoxide are relevant. Furthermore, the coking affinity of the $MgAl_2O_4$ support could be addressed by increasing the Mg/Al ratio or considering a different support. Yet a

third option could be to perform a more detailed investigation of the reaction mechanism of ethylene glycol HDO with ethanol and acetaldehyde as reactants to determine their role as intermediates in the proposed reaction scheme. This would of course require an expansion of the online gas analysis of the activity setup to include light oxygenates and potentially also require an improvement of the cooling of collected of liquid products.

Looking at it from a more pragmatic approach, the most important issues have been covered by this model compound study: i) Water resistant and sulfur tolerant catalysts have been developed, ii) The developed catalysts are able to operate at high activity with high HDO yields at moderate selectivity (given the inevitable cracking at higher temperature), iii) The main source of deactivation, i.e. carbon deposition, has been identified and a reactivation process has been presented. Given the complexity of solid biomass and the inherent challenges in developing continuous processes for the conversion of such, the next steps should be focused on pilot scale testing of combined pyrolysis and catalytic HDO processes for solid biomass conversion, which can never be fully mimicked with model compounds. With the process development being at an early stage, there are numerous elements to consider. On the short term, issues with continuous operation should be addressed; e.g. feeding of solid biomass to a pressurized system and testing of long time on stream activity, which could be challenged both from catalyst deactivation and from entrainment of catalyst, if a fluid bed reactor is used. On the long term, the process efficiency should be addressed taking into account considerations on sustainable sources for hydrogen and utilization strategies for by-products, namely light gasses from cracking. Overall, the first moves within coupled biomass fast pyrolysis and catalytic HDO seem very promising, and important technological advances are expected in the near future.

Bibliography

[1] P. M. Mortensen, *Catalytic conversion of bio-oil to fuel for transportation.* PhD thesis, Technical University of Denmark, Dept. of Chemical and Biochemical Engineering, 2013.

[2] United Nations, "Sustainable development goals." `http://www.un.org/sustainabledevelopment/energy/`,[Accessed: April 21, 2016], 2016.

[3] United Nations - Department of Economic and Social Affairs Population Division, "Population." `http://www.un.org/en/development/desa/population/`,[Accessed: April 25, 2016], 2015.

[4] Independent Statistics & Analysis - U.S. Energy Information Administration, "Forecasts." `https://www.eia.gov/forecasts/`,[Accessed: April 25, 2016], 2014.

[5] Independent Statistics & Analysis - U.S. Energy Information Administration, "International energy outlook 2016 - DOE/EIA-0484," tech. rep., 2016.

[6] Core Writing Team, R. K. Pachauri, and L. A. Meyers, "Climate change 2014: Synthesis report," tech. rep., IPCC, Geneva, 2014.

[7] The World Bank, "2013 Environment 3.13: World development indicators: Traffic and congestion." `https://web.archive.org/web/20140408034906/http://wdi.worldbank.org/table/3.13`,[Accessed: April 28, 2016], 2013.

[8] Nasdaq, "www.nasdaq.com." `www.nasdaq.com/markets/`,[Accessed: April 28, 2016], 2016.

[9] O. Gröger, H. A. Gasteiger, and J.-P. Suchsland, "Review-Electromobility: Batteries or fuel cells?," *J. Electrochem. Soc.*, vol. 162, pp. A2605–A2622, 2015.

[10] R. Schlögl, *Chemical energy storage.* Göttingen: De Gruyter, 2013.

[11] P. Denholm, M. O'Connell, G. Brinkman, and J. Jorgenson, "Overgeneration from solar energy in California: A field guide to the duck chart. NREL/TP-6A20-65023," tech. rep., NREL, 2015.

[12] M. Balat, "Production of bioethanol from lignocellulosic materials via the biochemical pathway: A review," *Energy Convers. Manag.*, vol. 52, pp. 858–875, 2011.

[13] A. Roedl, "Production and energetic utilization of wood from short rotation coppice-a life cycle assessment," *Int. J. Life Cycle Assess.*, vol. 15, pp. 567–578, 2010.

[14] P. McKendry, "Energy production from biomass (part 1): Overview of biomass," *Bioresour. Technol.*, vol. 83, pp. 37–46, 2002.

[15] A. Demirbas, "Biofuels sources, biofuel policy, biofuel economy and global biofuel projections," *Energy Convers. Manag.*, vol. 49, pp. 2106–2116, 2008.

[16] FAO, IFAD, and WFP, "The state of food insecurity in the world. The multiple dimensions of food security.," tech. rep., Rome, 2013.

[17] P. O'Connor, "Chapter 1: A general introduction to biomass utilization possibilities," in *The role of catalysis for the sustainable production of bio-fuels and bio-chemicals* (K. Triantafyllidis, A. Lappas, and M. Stöcker, eds.), pp. 1–25, Elsevier, 2013.

[18] D. J. Hayes, "Chapter 2: Biomass composition and its relevance to biorefining," in *The role of catalysis for the sustainable production of bio-fuels and bio-chemicals* (K. Triantafyllidis, A. Lappas, and M. Stöcker, eds.), pp. 27–65, Elsevier, 2013.

[19] P. M. Mortensen, J.-D. Grunwaldt, P. A. Jensen, K. G. Knudsen, and A. D. Jensen, "A review of catalytic upgrading of bio-oil to engine fuels," *Appl. Catal. A Gen.*, vol. 407, pp. 1–19, 2011.

[20] M. Linck, L. Felix, T. Marker, and M. Roberts, "Integrated biomass hydropyrolysis and hydrotreating: a brief review," *WIREs Energy Environ.*, vol. 3, pp. 575–581, 2014.

[21] A. V. Bridgwater, "Review of fast pyrolysis of biomass and product upgrading," *Biomass and Bioenergy*, vol. 38, pp. 68–94, 2012.

[22] T. N. Trinh, P. A. Jensen, K. Dam-Johansen, N. O. Knudsen, H. R. Sørensen, and S. Hvilsted, "Comparison of lignin, macroalgae, wood, and straw fast pyrolysis," *Energy & Fuels*, vol. 27, pp. 1399–1409, 2013.

[23] R. H. Venderbosch and W. Prins, "Fast pyrolysis technology development," *Biofuels, Bioprod. Biorefining*, vol. 4, pp. 178–208, 2010.

[24] A. M. Azeez, D. Meier, J. Odermatt, and T. Willner, "Fast pyrolysis of African and European lignocellulosic biomasses using Py-GC/MS and fluidized bed reactor," *Energy & Fuels*, vol. 24, pp. 2078–2085, 2010.

[25] L. Negahdar, A. Gonzalez-Quiroga, D. Otyuskaya, H. E. Toraman, L. Liu, J. T. B. H. Jastrzebski, and et al., "Characterization and comparison of fast pyrolysis bio-oils from pinewood, rapeseed cake, and wheat straw using ^{13}C NMR and comprehensive GC×GC," *ACS Sustain. Chem. Eng.*, vol. 4, pp. 4974–4985, 2016.

[26] K. Raffelt, E. Henrich, A. Koegel, R. Stahl, J. Steinhardt, and F. Weirich, "The BTL2 process of biomass utilization entrained-flow gasification of pyrolyzed biomass slurries," *Appl. Biochem. Biotechnol.*, vol. 129-132, pp. 153–164, 2006.

[27] P. C. Badger and P. Fransham, "Use of mobile fast pyrolysis plants to densify biomass and reduce biomass handling costs-A preliminary assessment," *Biomass and Bioenergy*, vol. 30, pp. 321–325, 2006.

[28] S. Czernik and A. V. Bridgwater, "Overview of applications of biomass fast pyrolysis oil," *Energy & Fuels*, vol. 18, pp. 590–598, 2004.

[29] A. V. Bridgwater, "Renewable fuels and chemicals by thermal processing of biomass," *Chem. Eng. J.*, vol. 91, pp. 87–102, 2003.

[30] A. Oasmaa and S. Czernik, "Fuel oil quality of biomass pyrolysis oils-State of the art for the end users," *Energy & Fuels*, vol. 13, pp. 914–921, 1999.

[31] D. Mohan, C. U. Pittman, and P. H. Steele, "Pyrolysis of wood/biomass for bio-oil : A critical review," *Energy & Fuels*, vol. 20, pp. 848–889, 2006.

[32] Syntek Global Inc., "Technical information: ASTM D975 diesel fuel specification test." `http://emotor-extreme.cl/assets/astm_d975_specification_test.pdf`,[Accessed: August 7, 2017].

[33] Mabanaft, "Sulphur free diesel BS EN 590:2013." `https://www.mabanaft.com/fileadmin/content/global_content/downloads/mabanaft/Mabanaft-Ltd_Prod-Spec_Diesel.pdf`,[Accessed: August 7, 2017], 2015.

[34] P. M. Mortensen, D. Gardini, C. D. Damsgaard, J.-D. Grunwaldt, P. A. Jensen, J. B. Wagner, and A. D. Jensen, "Deactivation of Ni-MoS_2 by bio-oil impurities during hydrodeoxygenation of phenol and octanol," *Appl. Catal. A Gen.*, vol. 523, pp. 159–170, 2016.

[35] P. M. Mortensen, D. Gardini, H. W. P. de Carvalho, C. D. Damsgaard, J.-D. Grunwaldt, P. A. Jensen, J. B. Wagner, and A. D. Jensen, "Stability and resistance of nickel catalysts for hydrodeoxygenation: Carbon deposition and effects of sulfur, potassium, and chlorine in the feed," *Catal. Sci. Technol.*, vol. 4, pp. 3672–3686, 2014.

[36] S. Albertazzi, F. Basile, G. Fornasari, F. Trifirò, and A. Vaccari, "Chapter 7: Thermal biomass conversion," in *Catalysis for renewables: From feedstock to energy production* (G. Centi and R. van Santen, eds.), pp. 147–162, Weinheim: Wiley-VCH Verlag GmbH & Co. KGaA, 2007.

[37] A. Stanislaus, A. Marafi, and M. S. Rana, "Recent advances in the science and technology of ultra low sulfur diesel (ULSD) production," *Catal. Today*, vol. 153, pp. 1–68, 2010.

[38] C. Boscagli, K. Raffelt, T. A. Zevaco, W. Olbrich, T. N. Otto, J. Sauer, and J.-D. Grunwaldt, "Mild hydrotreatment of the light fraction of fast-pyrolysis oil produced from straw over nickel-based catalysts," *Biomass and Bioenergy*, vol. 83, pp. 525–538, 2015.

[39] H. Wang, J. Male, and Y. Wang, "Recent advances in hydrotreating of pyrolysis bio-oil and its oxygen-containing model compounds," *ACS Catal.*, vol. 3, pp. 1047–1070, 2013.

[40] K. Sipilä, E. Kuoppala, L. Fagernäs, and A. Oasmaa, "Characterization of biomass-based flash pyrolysis oils," *Biomass and Bioenergy*, vol. 14, pp. 103–113, 1998.

[41] C. Branca, P. Giudicianni, and C. Di Blasi, "GC/MS characterization of liquids generated from low-temperature pyrolysis of wood," *Ind. Eng. Chem. Res.*, vol. 42, pp. 3190–3202, 2003.

[42] E. M. Hassan, P. H. Steele, and L. Ingram, "Characterization of fast pyrolysis bio-oils produced from pretreated pine wood," *Appl. Biochem. Biotechnol.*, vol. 154, pp. 182–192, 2009.

[43] S. Thangalazhy-Gopakumar, S. Adhikari, and R. B. Gupta, "Catalytic pyrolysis of biomass over H^+ZSM-5 under hydrogen pressure," *Energy & Fuels*, vol. 26, pp. 5300–5306, 2012.

[44] A. Oasmaa, D. C. Elliott, and J. Korhonen, "Acidity of biomass fast pyrolysis bio-oils," *Energy & Fuels*, vol. 24, pp. 6548–6554, 2010.

[45] A. Oasmaa, E. Kuoppala, and Y. Solantausta, "Fast pyrolysis of forestry residue. 2. Physicochemical composition of product liquid," *Energy & Fuels*, vol. 17, pp. 433–443, 2003.

[46] J. Piskorz, D. S. A. G. Radlein, D. S. Scott, and S. Czernik, "Liquid products from the fast pyrolysis of wood and cellulose," in *Research in thermochemical biomass conversion* (A. V. Bridgwater and J. L. Kuester, eds.), pp. 557–571, Elsevier Science Publishing Company Inc., 1988.

[47] K. Routray, K. J. Barnett, and G. W. Huber, "Hydrodeoxygenation of pyrolysis oils," *Energy Technol.*, vol. 5, pp. 80–93, 2017.

[48] D. A. Ruddy, J. A. Schaidle, J. R. Ferrell III, J. Wang, L. Moens, and J. E. Hensley, "Recent advances in heterogeneous catalysts for bio-oil upgrading via "ex situ catalytic fast pyrolysis": catalyst development through the study of model compounds," *Green Chem.*, vol. 16, pp. 454–490, 2014.

[49] T. Milne, F. Agblevor, M. Davis, S. Deutch, and D. Johnson, "A review of the chemical composition of fast-pyrolysis oils from biomass," in *Developments in thermochemical biomass conversion* (A. V. Bridgwater and D. G. B. Boocock, eds.), pp. 409–424, Suffolk: Blackie A & P, an imprint of Chapman & Hall, 1997.

[50] C. A. Mullen and A. A. Boateng, "Chemical composition of bio-oils produced by fast pyrolysis of two energy crops," *Energy & Fuels*, vol. 22, pp. 2104–2109, 2008.

[51] D. Chiaramonti, A. Oasmaa, and Y. Solantausta, "Power generation using fast pyrolysis liquids from biomass," *Renew. Sustain. Energy Rev.*, vol. 11, pp. 1056–1086, 2007.

[52] S. Lee, T. Kim, and K. Kang, "Performance and emission characteristics of a diesel engine operated with wood pyrolysis oil," *Proc. Inst. Mech. Eng. Part D J. Automob. Eng.*, vol. 228, pp. 180–189, 2014.

[53] Y. Solantausta, N.-O. Nylund, M. Westerholm, T. Koljonen, and A. Oasmaa, "Wood-pyrolysis oil as fuel in a diesel-power plant," *Bioresour. Technol.*, vol. 46, pp. 177–188, 1993.

[54] D. Chiaramonti, M. Bonini, E. Fratini, G. Tondi, K. Gartner, A. V. Bridgwater, and et al., "Development of emulsions from biomass pyrolysis liquid and diesel and their use in engines-Part 2: Tests in diesel engines," *Biomass and Bioenergy*, vol. 25, pp. 101–111, 2003.

[55] D. Chiaramonti, M. Bonini, E. Fratini, G. Tondi, K. Gartner, A. V. Bridgwater, and et al., "Development of emulsions from biomass pyrolysis liquid and diesel and their use in engines-Part 1: Emulsion production," *Biomass and Bioenergy*, vol. 25, pp. 85–99, 2003.

[56] A. Shihadeh and S. Hochgreb, "Impact of biomass pyrolysis oil process conditions on ignition delay in compression ignition engines," *Energy & Fuels*, vol. 16, pp. 552–561, 2002.

[57] A. Shihadeh and S. Hochgreb, "Diesel engine combustion of biomass pyrolysis oils," *Energy & Fuels*, vol. 14, pp. 260–274, 2000.

[58] N. Dahmen, E. Henrich, E. Dinjus, and F. Weirich, "The bioliq® bioslurry gasification process for the production of biosynfuels, organic chemicals, and energy," *Energy. Sustain. Soc.*, vol. 2:3, pp. 1–44, 2012.

[59] A. A. Lappas, S. Bezergianni, and I. A. Vasalos, "Production of biofuels via co-processing in conventional refining processes," *Catal. Today*, vol. 145, pp. 55–62, 2009.

[60] A. d. R. Pinho, M. B. B. de Almeida, F. L. Mendes, V. L. Ximenes, and L. C. Casavechia, "Co-processing raw bio-oil and gasoil in an FCC Unit," *Fuel Process. Technol.*, vol. 131, pp. 159–166, 2015.

[61] M. S. Talmadge, R. M. Baldwin, M. J. Biddy, R. L. McCormick, G. T. Beckham, G. A. Ferguson, and et al., "A perspective on oxygenated species in the refinery integration of pyrolysis oil," *Green Chem.*, vol. 16, pp. 407–453, 2014.

[62] G. Alfke, W. W. Irion, and O. S. Neuwirth, "Oil refining," in *Ullmann's Encyclopedia of Industrial Chemistry*, Weinheim: Wiley-VCH Verlag GmbH & Co. KGaA, 2007.

[63] H. Topsøe, B. S. Clausen, and F. E. Massoth, "Hydrotreating catalysis," in *Catalysis - science and technology, vol. 11* (A. J. R and B. Michael, eds.), Springer-Verlag, Berlin Heidelberg, 1996.

[64] M. Saidi, F. Samimi, D. Karimipourfard, T. Nimmanwudipong, B. C. Gates, and M. R. Rahimpour, "Upgrading of lignin-derived bio-oils by catalytic hydrodeoxygenation," *Energy Environ. Sci.*, vol. 7, pp. 103–129, 2014.

[65] D. C. Elliott, "Historical developments in hydroprocessing bio-oils," *Energy & Fuels*, vol. 21, pp. 1792–1815, 2007.

[66] A. H. Zacher, M. V. Olarte, D. M. Santosa, D. C. Elliott, and S. B. Jones, "A review and perspective of recent bio-oil hydrotreating research," *Green Chem.*, vol. 16, pp. 491–515, 2014.

[67] E. Furimsky, "Catalytic hydrodeoxygenation," *Appl. Catal. A Gen.*, vol. 199, pp. 147–190, 2000.

[68] E. Furimsky, "Hydroprocessing challenges in biofuels production," *Catal. Today*, vol. 217, pp. 13–56, 2013.

[69] Z. He and X. Wang, "Hydrodeoxygenation of model compounds and catalytic systems for pyrolysis bio-oils upgrading," *Catal. Sustain. Energy*, vol. 1, pp. 28–52, 2012.

[70] M. R. de Brimont, C. Dupont, A. Daudin, C. Geantet, and P. Raybaud, "Deoxygenation mechanisms on Ni-promoted MoS_2 bulk catalysts: A combined experimental and theoretical study," *J. Catal.*, vol. 286, pp. 153–164, 2012.

[71] Y. Romero, F. Richard, and S. Brunet, "Hydrodeoxygenation of 2-ethylphenol as a model compound of bio-crude over sulfided Mo-based catalysts: Promoting effect and reaction mechanism," *Appl. Catal. B Environ.*, vol. 98, pp. 213–223, 2010.

[72] Y. Romero, F. Richard, Y. Renème, and S. Brunet, "Hydrodeoxygenation of benzofuran and its oxygenated derivatives (2,3-dihydrobenzofuran and 2-ethylphenol) over $NiMoP/Al_2O_3$ catalyst," *Appl. Catal. A Gen.*, vol. 353, pp. 46–53, 2009.

[73] R. C. Nelson, B. Baek, P. Ruiz, B. Goundie, A. Brooks, M. C. Wheeler, and et al., "Experimental and theoretical insights into the hydrogen-efficient direct hydrodeoxygenation mechanism of phenol over Ru/TiO_2," *ACS Catal.*, vol. 5, pp. 6509–6523, 2015.

[74] R. C. Runnebaum, T. Nimmanwudipong, D. E. Block, and B. C. Gates, "Catalytic conversion of compounds representative of lignin-derived bio-oils: A reaction network for guaiacol, anisole, 4-methylanisole, and cyclohexanone conversion catalysed by Pt/γ-Al_2O_3 ," *Catal. Sci. Technol.*, vol. 2, pp. 113–118, 2012.

[75] A. Popov, E. Kondratieva, J. M. Goupil, L. Mariey, P. Bazin, J.-P. Gilson, and et al., "Bio-oils hydrodeoxygenation: Adsorption of phenolic molecules on oxidic catalyst supports," *J. Phys. Chem. C*, vol. 114, pp. 15661–15670, 2010.

[76] A. Centeno, E. Laurent, and B. Delmon, "Influence of the support of CoMo sulfide catalysts and of the addition of potassium and platinum on the catalytic performances for the hydrodeoxygenation of carbonyl, carboxyl, and guaiacol-type molecules," *J. Catal.*, vol. 154, pp. 288–298, 1995.

[77] S. Echeandia, P. L. Arias, V. L. Barrio, B. Pawelec, and J. L. G. Fierro, "Synergy effect in the HDO of phenol over Ni-W catalysts supported on active carbon: Effect of tungsten precursors," *Appl. Catal. B Environ.*, vol. 101, pp. 1–12, 2010.

[78] D. C. Elliott and T. R. Hart, "Catalytic hydroprocessing of chemical models for bio-oil," *Energy & Fuels*, vol. 23, pp. 631–637, 2009.

[79] M. Ternan, E. Furimsky, and B. I. Parsons, "Coke formation on hydrodesulphurization catalysts," *Fuel Process. Technol.*, vol. 2, pp. 45–55, 1979.

[80] V. N. Bui, D. Laurenti, P. Afanasiev, and C. Geantet, "Hydrodeoxygenation of guaiacol with CoMo catalysts. Part I: Promoting effect of cobalt on HDO selectivity and activity," *Appl. Catal. B Environ.*, vol. 101, pp. 239–245, 2011.

[81] P. Grange, E. Laurent, R. Maggi, A. Centeno, and B. Delmon, "Hydrotreatment of pyrolysis oils from biomass: Reactivity of the various categories of oxygenated compounds and preliminary techno-economical study," *Catal. Today*, vol. 29, pp. 297–301, 1996.

[82] P. M. de Souza, R. C. Rabelo-Neto, L. E. P. Borges, G. Jacobs, B. H. Davis, T. Sooknoi, and et al., "Role of keto intermediates in the hydrodeoxygenation of phenol over Pd on oxophilic supports," *ACS Catal.*, vol. 5, pp. 1318–1329, 2015.

[83] C. Boscagli, K. Raffelt, and J.-D. Grunwaldt, "Reactivity of platform molecules in pyrolysis oil and in water during hydrotreatment over nickel and ruthenium catalysts," *Biomass and Bioenergy*, vol. 106, pp. 63–73, 2017.

[84] A. Oasmaa and E. Kuoppala, "Fast pyrolysis of forestry residue. 3. Storage stability of liquid fuel," *Energy & Fuels*, vol. 17, pp. 1075–1084, 2003.

[85] S. Czernik, D. K. Johnson, and S. Black, "Stability of wood fast pyrolysis oil," *Biomass and Bioenergy*, vol. 7, pp. 187–192, 1994.

[86] H. Wang and Y. Wang, "Characterization of deactivated bio-oil hydrotreating catalysts," *Top. Catal.*, vol. 59, pp. 65–72, 2016.

[87] R. H. Venderbosch, A. R. Ardiyanti, J. Wildschut, A. Oasmaa, and H. J. Heeres, "Stabilization of biomass-derived pyrolysis oils," *J. Chem. Technol. Biotechnol.*, vol. 85, pp. 674–686, 2010.

[88] T. N. Pham, D. Shi, and D. E. Resasco, "Evaluating strategies for catalytic upgrading of pyrolysis oil in liquid phase," *Appl. Catal. B Environ.*, vol. 145, pp. 10–23, 2014.

[89] M. R. Hurt, J. C. Degenstein, P. Gawecki, D. J. Borton II, N. R. Vinueza, L. Yang, and et al., "Online mass spectrometric methods for the determination of the primary products of fast pyrolysis of carbohydrates and for their gas-phase manipulation," *Anal. Chem.*, vol. 85, pp. 10927–10934, 2013.

[90] M. C. Edelman, M. K. Maholland, R. M. Baldwin, and S. W. Cowley, "Vapor-phase catalytic hydrodeoxygenation of benzofuran," *J. Catal.*, vol. 111, pp. 243–253, 1988.

[91] A. A. Dwiatmoko, S. Lee, H. C. Ham, J.-W. Choi, D. J. Suh, and J.-M. Ha, "Effects of carbohydrates on the hydrodeoxygenation of lignin-derived phenolic compounds," *ACS Catal.*, vol. 5, pp. 433–437, 2015.

[92] E.-M. Ryymin, M. L. Honkela, T.-R. Viljava, and A. O. I. Krause, "Competitive reactions and mechanisms in the simultaneous HDO of phenol and methyl heptanoate over sulphided NiMo/γ-Al_2O_3 ," *Appl. Catal. A Gen.*, vol. 389, pp. 114–121, 2010.

[93] J. Wildschut, *Pyrolysis oil upgrading to transportation fuels by catalytic hydrotreatment.* PhD thesis, University of Groningen, 2009.

[94] J. Wildschut, F. H. Mahfud, R. H. Venderbosch, and H. J. Heeres, "Hydrotreatment of fast pyrolysis oil using heterogeneous noble-metal catalysts," *Ind. Eng. Chem. Res.*, vol. 48, pp. 10324–10334, 2009.

[95] A. V. Bridgwater, "Production of high grade fuels and chemicals from catalytic pyrolysis of biomass," *Catal. Today*, vol. 29, pp. 285–295, 1996.

[96] R. H. Venderbosch, "A critical view on catalytic pyrolysis of biomass," *ChemSusChem*, vol. 8, pp. 1306–1316, 2015.

[97] M. C. Samolada, W. Baldauf, and I. A. Vasalos, "Production of a bio-gasoline by upgrading biomass flash pyrolysis liquids via hydrogen processing and catalytic cracking," *Fuel*, vol. 77, pp. 1667–1675, 1998.

[98] W. Baldauf, U. Balfanz, and M. Rupp, "Upgrading of flash pyrolysis oil and utilization in refineries," *Biomass and Bioenergy*, vol. 7, pp. 237–244, 1994.

[99] Y.-H. E. Sheu, R. G. Anthony, and E. J. Soltes, "Kinetic studies of upgrading pine pyrolytic oil by hydrotreatment," *Fuel Process. Technol.*, vol. 19, pp. 31–50, 1988.

[100] Y. Wang, H. Lin, and Y. Zheng, "Hydrotreatment of lignocellulosic biomass derived oil using a sulfided NiMo/γ-Al_2O_3 catalyst," *Catal. Sci. Technol.*, vol. 4, pp. 109–119, 2014.

[101] D. C. Elliott, T. R. Hart, G. G. Neuenschwander, L. J. Rotness, and A. H. Zacher, "Catalytic hydroprocessing of biomass fast pyrolysis bio-oil to produce hydrocarbon products," *Environ. Prog. Sustain. Energy*, vol. 28, pp. 441–449, 2009.

[102] T. Cordero-Lanzac, R. Palos, J. M. Arandes, P. Castaño, J. Rodríguez-Mirasol, T. Cordero, and J. Bilbao, "Stability of an acid activated carbon based bifunctional catalyst for the raw bio-oil hydrodeoxygenation," *Appl. Catal. B Environ.*, vol. 203, pp. 389–399, 2017.

[103] K. C. Kwon, H. Mayfield, T. Marolla, B. Nichols, and M. Mashburn, "Catalytic deoxygenation of liquid biomass for hydrocarbon fuels," *Renew. Energy*, vol. 36, pp. 907–915, 2011.

[104] Z. Su-Ping, Y. Yong-Jie, R. Zhengwei, and L. Tingchen, "Study of hydrodeoxygenation of bio-oil from the fast pyrolysis of biomass," *Energy Sources*, vol. 25, pp. 57–65, 2003.

[105] E. Furimsky, J. A. Mikhlin, D. Q. Jones, T. Adley, and H. Baikowitz, "On the mechanism of hydrodeoxygenation of ortho substituted phenols," *Can. J. Chem. Eng.*, vol. 64, pp. 982–985, 1986.

[106] M. Badawi, J.-F. Paul, S. Cristol, E. Payen, Y. Romero, F. Richard, and et al., "Effect of water on the stability of Mo and CoMo hydrodeoxygenation catalysts: A combined experimental and DFT study," *J. Catal.*, vol. 282, pp. 155–164, 2011.

[107] M. Badawi, J.-F. Paul, S. Cristol, and E. Payen, "Guaiacol derivatives and inhibiting species adsorption over MoS_2 and CoMoS catalysts under HDO conditions: A DFT study," *Catal. Commun.*, vol. 12, pp. 901–905, 2011.

[108] E. Laurent and B. Delmon, "Study of the hydrodeoxygenation of carbonyl, carboxylic and guaiacyl groups over sulfided CoMo/γ-Al_2O_3 and NiMo/γ-Al_2O_3 catalyst: II. Influence of water, ammonia and hydrogen sulfide," *Appl. Catal. A Gen.*, vol. 109, pp. 97–115, 1994.

[109] O. İ. Şenol, E.-M. Ryymin, T.-R. Viljava, and A. O. I. Krause, "Effect of hydrogen sulphide on the hydrodeoxygenation of aromatic and aliphatic oxygenates on sulphided catalysts," *J. Mol. Catal. A Chem.*, vol. 277, pp. 107–112, 2007.

[110] O. İ. Şenol, T.-R. Viljava, and A. O. I. Krause, "Effect of sulphiding agents on the hydrodeoxygenation of aliphatic esters on sulphided catalysts," *Appl. Catal. A Gen.*, vol. 326, pp. 236–244, 2007.

[111] V. N. Bui, D. Laurenti, P. Delichère, and C. Geantet, "Hydrodeoxygenation of guaiacol. Part II: Support effect for CoMoS catalysts on HDO activity and selectivity," *Appl. Catal. B Environ.*, vol. 101, pp. 246–255, 2011.

[112] A. Gutierrez, E.-M. Turpeinen, T.-R. Viljava, and O. Krause, "Hydrodeoxygenation of model compounds on sulfided CoMo/γ-Al_2O_3 and NiMo/γ-Al_2O_3 catalysts; Role of sulfur-containing groups in reaction networks," *Catal. Today*, vol. 285, pp. 125–134, 2017.

[113] C. Bouvier, Y. Romero, F. Richard, and S. Brunet, "Effect of H_2S and CO on the transformation of 2-ethylphenol as a model compound of bio-crude over sulfided Mo-based catalysts: Propositions of promoted active sites for deoxygenation pathways based on an experimental study," *Green Chem.*, vol. 13, pp. 2441–2451, 2011.

[114] F. E. Massoth, P. Politzer, M. C. Concha, J. S. Murray, J. Jakowski, and J. Simons, "Catalytic hydrodeoxygenation of methyl-substituted phenols: Correlations of kinetic parameters with molecular properties," *J. Phys. Chemstry B*, vol. 110, pp. 14283–14291, 2006.

[115] G. Liu, A. W. Robertson, M. M.-J. Li, W. C. H. Kuo, M. T. Darby, M. H. Muhieddine, and et al., "MoS_2 monolayer catalyst doped with isolated Co atoms for the hydrodeoxygenation reaction," *Nature Chemistry*, vol. 9, pp. 810–816, 2017.

[116] J. Horáček and D. Kubička, "Bio-oil hydrotreating over conventional CoMo & NiMo catalysts: The role of reaction conditions and additives," *Fuel*, vol. 198, pp. 49–57, 2017.

[117] C. Sepúlveda, R. García, P. Reyes, I. T. Ghampson, J. L. G. Fierro, D. Laurenti, and et al., "Hydrodeoxygenation of guaiacol over ReS_2/activated carbon catalysts. Support and Re loading effect," *Appl. Catal. A Gen.*, vol. 475, pp. 427–437, 2014.

[118] P. E. Ruiz, K. Leiva, R. Garcia, P. Reyes, J. L. G. Fierro, and N. Escalona, "Relevance of sulfiding pretreatment on the performance of Re/ZrO_2 and Re/ZrO_2-sulfated catalysts for the hydrodeoxygenation of guayacol," *Appl. Catal. A Gen.*, vol. 384, pp. 78–83, 2010.

[119] K. Leiva, C. Sepúlveda, R. García, J. L. G. Fierro, and N. Escalona, "Effect of water on the conversions of 2-methoxyphenol and phenol as bio-oil model compounds over ReS_2/SiO_2 catalyst," *Catal. Commun.*, vol. 53, pp. 33–37, 2014.

[120] A. Infantes-Molina, B. Pawelec, J. L. G. Fierro, C. V. Loricera, A. Jiménez-López, and E. Rodríguez-Castellón, "Effect of Ir and Pt addition on the HDO performance of RuS_2/SBA-15 sulfide catalysts," *Top. Catal.*, vol. 58, pp. 247–257, 2015.

[121] Y. Zhu, Q. M. Ramasse, M. Brorson, P. G. Moses, L. P. Hansen, and et al., "Location of Co and Ni promoter atoms in multi-layer MoS_2 nanocrystals for hydrotreating catalysis," *Catal. Today*, vol. 261, pp. 75–81, 2015.

[122] F. Besenbacher, M. Brorson, B. S. Clausen, S. Helveg, B. Hinnemann, J. Kibsgaard, and et al., "Recent STM, DFT and HAADF-STEM studies of sulfide-based hydrotreating catalysts: Insight into mechanistic, structural and particle size effects," *Catal. Today*, vol. 130, pp. 86–96, 2008.

[123] J. V. Lauritsen, J. Kibsgaard, G. H. Olesen, P. G. Moses, B. Hinnemann, S. Helveg, and et al., "Location and coordination of promoter atoms in Co-and Ni-promoted MoS_2-based hydrotreating catalysts," *J. Catal.*, vol. 249, pp. 220–233, 2007.

[124] L. van Haandel, G. M. Bremmer, E. J. M. Hensen, and T. Weber, "Influence of sulfiding agent and pressure on structure and performance of $CoMo/Al_2O_3$ hydrodesulfurization catalysts," *J. Catal.*, vol. 342, pp. 27–39, 2016.

[125] J. Kibsgaard, A. Tuxen, K. G. Knudsen, M. Brorson, H. Topsøe, E. Lægsgaard, and et al., "Comparative atomic-scale analysis of promotional effects by late 3d-transition metals in MoS_2 hydrotreating catalysts," *J. Catal.*, vol. 272, pp. 195–203, 2010.

[126] J. V. Lauritsen, S. Helveg, E. Lægsgaard, I. Stensgaard, B. S. Clausen, H. Topsøe, and F. Besenbacher, "Atomic-scale structure of Co-Mo-S nanoclusters in hydrotreating catalysts," *J. Catal.*, vol. 197, pp. 1–5, 2001.

[127] J. V. Lauritsen, M. V. Bollinger, E. Lægsgaard, K. W. Jacobsen, J. K. Nørskov, B. S. Clausen, and et al., "Atomic-scale insight into structure and morphology changes of MoS_2 nanoclusters in hydrotreating catalysts," *J. Catal.*, vol. 221, pp. 510–522, 2004.

[128] P. G. Moses, B. Hinnemann, H. Topsøe, and J. K. Nørskov, "The effect of Co-promotion on MoS_2 catalysts for hydrodesulfurization of thiophene: A density functional study," *J. Catal.*, vol. 268, pp. 201–208, 2009.

[129] J. V. Lauritsen and F. Besenbacher, "Atom-resolved scanning tunneling microscopy investigations of molecular adsorption on MoS_2 and CoMoS hydrodesulfurization catalysts," *J. Catal.*, vol. 328, pp. 49–58, 2015.

[130] A. Travert, H. Nakamura, R. A. van Santen, S. Cristol, J.-F. Paul, and E. Payen, "Hydrogen activation on Mo-based sulfide catalysts, a periodic DFT study," *J. Am. Chem. Soc.*, vol. 124, pp. 7084–7095, 2002.

[131] N.-Y. Topsøe and H. Topsøe, "FTIR studies of Mo/Al_2O_3-based catalysts. II. Evidence for the presence of SH groups and their role in acidity and activity," *J. Catal.*, vol. 139, pp. 641–651, 1993.

[132] J. V. Lauritsen, M. Nyberg, J. K. Nørskov, B. S. Clausen, H. Topsøe, E. Lægsgaard, and et al., "Hydrodesulfurization reaction pathways on MoS_2 nanoclusters revealed by scanning tunneling microscopy," *J. Catal.*, vol. 224, pp. 94–106, 2004.

[133] J. V. Lauritsen, M. Nyberg, R. T. Vang, M. V. Bollinger, B. S. Clausen, H. Topsøe, and et al., "Chemistry of one-dimensional metallic edge states in MoS_2 nanoclusters," *Nanotechnology*, vol. 14, pp. 385–389, 2003.

[134] A. K. Tuxen, H. G. Füchtbauer, B. Temel, B. Hinnemann, H. Topsøe, K. G. Knudsen, and et al., "Atomic-scale insight into adsorption of sterically hindered dibenzothiophenes on MoS_2 and Co-Mo-S hydrotreating catalysts," *J. Catal.*, vol. 295, pp. 146–154, 2012.

[135] M. Badawi, S. Cristol, J.-F. Paul, and E. Payen, "DFT study of furan adsorption over stable molybdenum sulfide catalyst under HDO conditions," *C.R. Chim.*, vol. 12, pp. 754–761, 2009.

[136] O. İ. Şenol, T.-R. Viljava, and A. O. I. Krause, "Hydrodeoxygenation of aliphatic esters on sulphided $NiMo/\gamma$-Al_2O_3 and $CoMo/\gamma$-Al_2O_3: The effect of water," *Catal. Today*, vol. 106, pp. 186–189, 2005.

[137] E.-M. Ryymin, M. L. Honkela, T.-R. Viljava, and A. O. I. Krause, "Insight to sulfur species in the hydrodeoxygenation of aliphatic esters over sulfided $NiMo/\gamma$-Al_2O_3 catalyst," *Appl. Catal. A Gen.*, vol. 358, pp. 42–48, 2009.

[138] O. İ. Şenol, E.-M. Ryymin, T.-R. Viljava, and A. O. I. Krause, "Reactions of methyl heptanoate hydrodeoxygenation on sulphided catalysts," *J. Mol. Catal. A Chem.*, vol. 268, pp. 1–8, 2007.

[139] P. Raybaud, J. Hafner, G. Kresse, S. Kasztelan, and H. Toulhoat, "Structure, energetics, and electronic properties of the surface of a promoted MoS_2 catalyst: An ab initio local density functional study," *J. Catal.*, vol. 190, pp. 128–143, 2000.

[140] B. R. G. Leliveld, J. A. J. van Dillen, J. W. Geus, D. C. Koningsberger, and M. de Boer, "Structure and nature of the active sites in CoMo hydrotreating catalysts. An EXAFS study of the reaction with selenophene," *J. Phys. Chem. B*, vol. 101, pp. 11160–11171, 1997.

[141] V. O. O. Gonçalves, S. Brunet, and F. Richard, "Hydrodeoxygenation of cresols over Mo/Al_2O_3 and $CoMo/Al_2O_3$ sulfided catalysts," *Catal. Letters*, vol. 146, pp. 1562–1573, 2016.

[142] E. Schachtl, J. S. Yoo, O. Y. Gutiérrez, F. Studt, and J. A. Lercher, "Impact of Ni promotion on the hydrogenation pathways of phenanthrene on MoS_2/γ-Al_2O_3," *J. Catal.*, vol. 352, pp. 171–181, 2017.

[143] C. Dupont, R. Lemeur, A. Daudin, and P. Raybaud, "Hydrodeoxygenation pathways catalyzed by MoS_2 and NiMoS active phases: A DFT study," *J. Catal.*, vol. 279, pp. 276–286, 2011.

[144] T. Prasomsri, T. Nimmanwudipong, and Y. Román-Leshkov, "Effective hydrodeoxygenation of biomass-derived oxygenates into unsaturated hydrocarbons by MoO_3 using low H_2 pressures," *Energy Environ. Sci.*, vol. 6, pp. 1732–1738, 2013.

[145] D. R. Moberg, T. J. Thibodeau, F. G. Amar, and B. G. Frederick, "Mechanism of hydrodeoxygenation of acrolein on a cluster model of MoO_3," *J. Phys. Chem. C*, vol. 114, pp. 13782–13795, 2010.

[146] V. M. L. Whiffen and K. J. Smith, "Hydrodeoxygenation of 4-methylphenol over unsupported MoP, MoS_2, and MoO_x catalysts," *Energy & Fuels*, vol. 24, pp. 4728–4737, 2010.

[147] T. Prasomsri, M. Shetty, K. Murugappan, and Y. Román-Leshkov, "Insights into the catalytic activity and surface modification of MoO_3 during the hydrodeoxygenation of lignin-derived model compounds into aromatic hydrocarbons under low hydrogen pressures," *Energy Environ. Sci.*, vol. 7, pp. 2660–2669, 2014.

[148] M. Shetty, K. Murugappan, T. Prasomsri, W. H. Green, and Y. Román-Leshkov, "Reactivity and stability investigation of supported molybdenum oxide catalysts for the hydrodeoxygenation (HDO) of m-cresol," *J. Catal.*, vol. 331, pp. 86–97, 2015.

[149] A. Auroux and A. Gervasini, "Microcalorimetric study of the acidity and basicity of metal oxide surfaces," *J. Phys. Chem.*, vol. 94, pp. 6371–6379, 1990.

[150] S. Li and D. A. Dixon, "Molecular and electronic structures, Brönsted basicities, and Lewis acidities of group VIB transition metal oxide clusters.," *J. Phys. Chem. A*, vol. 110, pp. 6231–44, 2006.

[151] G. Busca, "Chapter 9: The surface acidity and basicity of solid oxides and zeolites," in *Metal oxides. Chemistry and applications* (J.L.G. Fierro, ed.), pp. 247–318, Boca Raton: CRC Press, Taylor & Francis Group, 2006.

[152] J. A. Rodriguez and J. Hrbek, "Interaction of sulfur with well-defined metal and oxide surfaces: unraveling the mysteries behind catalyst poisoning and desulfurization," *Acc. Chem. Res.*, vol. 32, pp. 719–728, 1999.

[153] I. Chorkendorff and J. Niemantsverdriet, "Chapter 8: Heterogeneous catalysis in practice: Hydrogen," in *Concepts of modern catalysis and kinetics*, pp. 305–352, Darmstadt: Wiley-VCH Verlag GmbH & Co. KGaA, 2nd ed., 2010.

[154] P. M. Mortensen, J.-D. Grunwaldt, P. A. Jensen, and A. D. Jensen, "Screening of catalysts for hydrodeoxygenation of phenol as a model compound for bio-oil," *ACS Catal.*, vol. 3, pp. 1774–1785, 2013.

[155] Q. Tan, G. Wang, A. Long, A. Dinse, C. Buda, J. Shabaker, and D. E. Resasco, "Mechanistic analysis of the role of metal oxophilicity in the hydrodeoxygenation of anisole," *J. Catal.*, vol. 347, pp. 102–115, 2017.

[156] D. Garcia-Pintos, J. Voss, A. D. Jensen, and F. Studt, "Hydrodeoxygenation of phenol to benzene and cyclohexane on Rh(111) and Rh(211) surfaces: Insights from density functional theory," *J. Phys. Chem. C*, vol. 120, pp. 18529–18537, 2016.

[157] C. R. Lee, J. S. Yoon, Y.-W. Suh, J.-W. Choi, J.-M. Ha, D. J. Suh, and Y.-K. Park, "Catalytic roles of metals and supports on hydrodeoxygenation of lignin monomer guaiacol," *Catal. Commun.*, vol. 17, pp. 54–58, 2012.

[158] C. Zhao, Y. Kou, A. A. Lemonidou, X. Li, and J. A. Lercher, "Highly selective catalytic conversion of phenolic bio-oil to alkanes," *Angew. Chemie Int. Ed.*, vol. 48, pp. 3987–3990, 2009.

[159] Q. Tan, G. Wang, L. Nie, A. Dinse, C. Buda, J. Shabaker, and D. E. Resasco, "Different product distributions and mechanistic aspects of the hydrodeoxygenation of m-cresol over platinum and ruthenium catalysts," *ACS Catal.*, vol. 5, pp. 6271–6283, 2015.

[160] P. M. de Souza, R. C. Rabelo-Neto, L. E. P. Borges, G. Jacobs, B. H. Davis, and et al., "Effect of zirconia morphology on hydrodeoxygenation of phenol over Pd/ZrO_2," *ACS Catal.*, vol. 5, pp. 7385–7398, 2015.

[161] L. Nie, P. M. de Souza, F. B. Noronha, W. An, T. Sooknoi, and D. E. Resasco, "Selective conversion of m-cresol to toluene over bimetallic Ni-Fe catalysts," *J. Mol. Catal. A Chem.*, vol. 388-389, pp. 47–55, 2014.

[162] P. M. de Souza, R. C. Rabelo-Neto, L. E. P. Borges, G. Jacobs, B. H. Davis, D. E. Resasco, and F. B. Noronha, "Hydrodeoxygenation of phenol over Pd catalysts. Effect of support on reaction mechanism and catalyst deactivation," *ACS Catal.*, vol. 7, pp. 2058–2073, 2017.

[163] M. B. Griffin, G. A. Ferguson, D. A. Ruddy, M. J. Biddy, G. T. Beckham, and J. A. Schaidle, "Role of the support and reaction conditions on the vapor-phase deoxygenation of m-cresol over Pt/C and Pt/TiO_2 catalysts," *ACS Catal.*, vol. 6, pp. 2715–2727, 2016.

[164] M. Hellinger, H. W. P. Carvalho, S. Baier, D. Wang, W. Kleist, and J.-D. Grunwaldt, "Catalytic hydrodeoxygenation of guaiacol over platinum supported on metal oxides and zeolites," *Appl. Catal. A Gen.*, vol. 490, pp. 181–192, 2015.

[165] L. Nie and D. E. Resasco, "Kinetics and mechanism of m-cresol hydrodeoxygenation on a Pt/SiO_2 catalyst," *J. Catal.*, vol. 317, pp. 22–29, 2014.

[166] S. Oh, H. Hwang, H. S. Choi, and J. W. Choi, "The effects of noble metal catalysts on the bio-oil quality during the hydrodeoxygenative upgrading process," *Fuel*, vol. 153, pp. 535–543, 2015.

[167] M. Saidi, M. R. Rahimpour, and S. Raeissi, "Upgrading process of 4-methylanisole as a lignin-derived bio-oil catalyzed by Pt/γ-Al_2O_3: Kinetic investigation and reaction network development," *Energy & Fuels*, vol. 29, pp. 3335–3344, 2015.

[168] M. Saidi, P. Rostami, M. R. Rahimpour, B. C. Gates, and S. Raeissi, "Upgrading of lignin-derived bio-oil components catalyzed by Pt/γ-Al_2O_3: Kinetics and reaction pathways characterizing conversion of cyclohexanone with H_2," *Energy & Fuels*, vol. 29, pp. 191–199, 2015.

[169] A. Gutierrez, R. K. Kaila, M. L. Honkela, R. Slioor, and A. O. I. Krause, "Hydrodeoxygenation of guaiacol on noble metal catalysts," *Catal. Today*, vol. 147, pp. 239–246, 2009.

[170] S. L. Yohe, H. J. Choudhari, D. D. Mehta, P. J. Dietrich, M. D. Detwiler, C. M. Akatay, and et al., "High-pressure vapor-phase hydrodeoxygenation of lignin-derived oxygenates to hydrocarbons by a PtMo bimetallic catalyst: Product selectivity, reaction pathway, and structural characterization," *J. Catal.*, vol. 344, pp. 535–552, 2016.

[171] A. J. R. Hensley, Y. Wang, and J.-S. McEwen, "Phenol deoxygenation mechanisms on Fe(110) and Pd(111)," *ACS Catal.*, vol. 5, pp. 523–536, 2015.

[172] J. Sun, A. M. Karim, H. Zhang, L. Kovarik, X. S. Li, A. J. Hensley, and et al., "Carbon-supported bimetallic Pd-Fe catalysts for vapor-phase hydrodeoxygenation of guaiacol," *J. Catal.*, vol. 306, pp. 47–57, 2013.

[173] S. Sitthisa and D. E. Resasco, "Hydrodeoxygenation of furfural over supported metal catalysts: A comparative study of Cu, Pd and Ni," *Catal. Letters*, vol. 141, pp. 784–791, 2011.

[174] J. Luo, M. Monai, H. Yun, L. Arroyo-Ramírez, C. Wang, C. B. Murray, and et al., "The H_2 pressure dependence of hydrodeoxygenation selectivities for furfural over Pt/C catalysts," *Catal. Letters*, vol. 146, pp. 711 – 717, 2016.

[175] J. Wildschut, J. Arentz, C. B. Rasrendra, R. H. Venderbosch, and H. J. Heeres, "Catalytic hydrotreatment of fast pyrolysis oil: Model studies on reaction pathways for the carbohydrate fraction," *Environ. Prog. Sustain. Energy*, vol. 28, pp. 440–460, 2009.

[176] P. C. K. Vesborg and T. F. Jaramillo, "Addressing the terawatt challenge: Scalability in the supply of chemical elements for renewable energy," *RSC Adv.*, vol. 2, pp. 7933–7947, 2012.

[177] S. Jin, Z. Xiao, C. Li, X. Chen, L. Wang, J. Xing, and et al., "Catalytic hydrodeoxygenation of anisole as lignin model compound over supported nickel catalysts," *Catal. Today*, vol. 234, pp. 125–132, 2014.

[178] V. A. Yakovlev, S. A. Khromova, O. V. Sherstyuk, V. O. Dundich, D. Y. Ermakov, V. M. Novopashina, and et al., "Development of new catalytic systems for upgraded bio-fuels production from bio-crude-oil and biodiesel," *Catal. Today*, vol. 144, pp. 362–366, 2009.

[179] S. A. Khromova, A. A. Smirnov, O. A. Bulavchenko, A. A. Saraev, V. Kaichev, S. I. Reshetnikov, and V. A. Yakovlev, "Anisole hydrodeoxygenation over Ni-Cu bimetallic catalysts: The effect of Ni/Cu ratio on selectivity," *Appl. Catal. A Gen.*, vol. 470, pp. 261–270, 2014.

[180] P. M. Mortensen, J.-D. Grunwaldt, P. A. Jensen, and A. D. Jensen, "Influence on nickel particle size on the hydrodeoxygenation of phenol over Ni/SiO_2," *Catal. Today*, vol. 259, pp. 277–284, 2016.

[181] X. Zhang, Q. Zhang, T. Wang, L. Ma, Y. Yu, and L. Chen, "Hydrodeoxygenation of lignin-derived phenolic compounds to hydrocarbons over Ni/SiO_2-ZrO_2 catalysts," *Bioresour. Technol.*, vol. 134, pp. 73–80, 2013.

[182] W. Yin, A. Kloekhorst, R. H. Venderbosch, M. V. Bykova, S. A. Khromova, V. A. Yakovlev, and et al., "Catalytic hydrotreatment of fast pyrolysis liquids in batch and continuous set-ups using a bimetallic Ni-Cu catalyst with a high metal content," *Catal. Sci. Technol.*, vol. 6, pp. 5899–5915, 2016.

[183] H. Y. Zhao, D. Li, P. Bui, and S. T. Oyama, "Hydrodeoxygenation of guaiacol as model compound for pyrolysis oil on transition metal phosphide hydroprocessing catalysts," *Appl. Catal. A Gen.*, vol. 391, pp. 305–310, 2011.

[184] J.-S. Moon, E.-G. Kim, and Y.-K. Lee, "Active sites of Ni_2P/SiO_2 catalyst for hydrodeoxygenation of guaiacol: A joint XAFS and DFT study," *J. Catal.*, vol. 311, pp. 144–152, 2014.

[185] K. Li, R. Wang, and J. Chen, "Hydrodeoxygenation of anisole over silica-supported Ni_2P, MoP, and NiMoP catalysts," *Energy & Fuels*, vol. 25, pp. 854–863, 2011.

[186] S.-K. Wu, P.-C. Lai, Y.-C. Lin, H.-P. Wan, H.-T. Lee, and Y.-H. Chang, "Atmospheric hydrodeoxygenation of guaiacol over alumina-, zirconia-, and silica-supported nickel phosphide catalysts," *ACS Sustain. Chem. Eng.*, vol. 1, pp. 349–358, 2013.

[187] J.-S. Moon and Y.-K. Lee, "Support effects of Ni_2P catalysts on the hydrodeoxygenation of guaiacol: In situ XAFS studies," *Top. Catal.*, vol. 58, pp. 211–218, 2015.

[188] P. Bui, J. A. Cecilia, S. T. Oyama, A. Takagaki, A. Infantes-Molina, H. Zhao, and et al., "Studies of the synthesis of transition metal phosphides and their activity in the hydrodeoxygenation of a biofuel model compound," *J. Catal.*, vol. 294, pp. 184–198, 2012.

[189] E. Furimsky, "Metal carbides and nitrides as potential catalysts for hydroprocessing," *Appl. Catal. A Gen.*, vol. 240, pp. 1–28, 2003.

[190] T. G. Kelly and J. G. Chen, "Metal overlayer on metal carbide substrate: Unique bimetallic properties for catalysis and electrocatalysis," *Chem. Soc. Rev.*, vol. 41, pp. 8021–8034, 2012.

[191] P. M. Mortensen, H. W. P. de Carvalho, J.-D. Grunwaldt, P. A. Jensen, and A. D. Jensen, "Activity and stability of Mo_2C/ZrO_2 as catalyst for hydrodeoxygenation of mixtures of phenol and 1-octanol," *J. Catal.*, vol. 328, pp. 208–215, 2015.

[192] J. Engelhardt, P. Lyu, P. Nachtigall, F. Schüth, and Á. M. García, "The influence of water on the performance of molybdenum carbide catalysts in hydrodeoxygenation reactions: A combined theoretical and experimental study," *ChemCatChem*, vol. 9, pp. 1985–1991, 2017.

[193] C. Liu, J. Sun, H. M. Brown, O. G. Marin-Flores, J. T. Bays, A. M. Karim, and Y. Wang, "Aqueous phase hydrodeoxygenation of polyols over Pd/WO_3-ZrO_2: Role of Pd-WO_3 interaction and hydrodeoxygenation pathway," *Catal. Today*, vol. 269, pp. 103–109, 2016.

[194] J. G. Dickinson and P. E. Savage, "Development of NiCu catalysts for aqueous-phase hydrodeoxygenation," *ACS Catal.*, vol. 4, pp. 2605–2615, 2014.

[195] W. Wang, Y. Yang, H. Luo, H. Peng, and F. Wang, "Effect of La on Ni-W-B amorphous catalysts in hydrodeoxygenation of phenol," *Ind. Eng. Chem. Res*, vol. 50, pp. 10936–10942, 2011.

[196] M. Asadieraghi and W. M. A. W. Daud, "In-situ catalytic upgrading of biomass pyrolysis vapor: Co-feeding with methanol in a multi-zone fixed bed reactor," *Energy Convers. Manag.*, vol. 92, pp. 448–458, 2015.

[197] E. Laurent and B. Delmon, "Influence of water in the deactivation of a sulfided NiMo/γ-Al_2O_3 catalyst during hydrodeoxygenation," *J. Catal.*, vol. 146, pp. 281–291, 1994.

[198] H. Idriss and M. A. Barteau, "Active sites on oxides: From single crystals to catalysts," *Adv. Catal.*, vol. 45, pp. 261–331, 2000.

[199] H. H. Kung, "Chapter 4: Surface coordinative unsaturation," in *Studies in surface science and catalysis. Transition metal oxides: Surface chemistry and catalysis*, vol. 45, pp. 53–71, Amsterdam: Elsevier Science Publishing Company Inc., 1st ed., 1989.

[200] A. Popov, E. Kondratieva, L. Mariey, J. M. Goupil, J. El Fallah, J.-P. Gilson, and et al, "Bio-oil hydrodeoxygenation: Adsorption of phenolic compounds on sulfided (Co)Mo catalysts," *J. Catal.*, vol. 297, pp. 176–186, 2013.

[201] T. M. Sankaranarayanan, A. Berenguer, C. Ochoa-Hernández, I. Moreno, P. Jana, J. M. Coronado, and et al, "Hydrodeoxygenation of anisole as bio-oil model compound over supported Ni and Co catalysts: Effect of metal and support properties," *Catal. Today*, vol. 243, pp. 163–172, 2015.

[202] H. Chen, Q. Wang, X. Zhang, and L. Wang, "Effect of support on the NiMo phase and its catalytic hydrodeoxygenation of triglycerides," *Fuel*, vol. 159, pp. 430–435, 2015.

[203] M. Selvaraj, K. Shanthi, R. Maheswari, and A. Ramanathan, "Hydrodeoxygenation of guaiacol over MoO_3-NiO/mesoporous silicates: Effect of incorporated heteroatom," *Energy & Fuels*, vol. 28, pp. 2598–2607, 2014.

[204] V. O. Dundich, S. A. Khromova, D. Y. Ermakov, M. Y. Lebedev, V. M. Novopashina, V. G. Sister, and et al., "Nickel catalysts for the hydrodeoxygenation of biodiesel," *Kinet. Catal.*, vol. 51, pp. 704–709, 2010.

[205] B. M. Q. Phan, Q. L. M. Ha, N. P. Le, P. T. Ngo, T. H. Nguyen, T. T. Dang, and et al., "Influences of various supports, γ-Al_2O_3, CeO_2, and SBA-15 on HDO performance of NiMo catalyst," *Catal. Letters*, vol. 145, pp. 662–667, 2015.

[206] S. M. Schimming, G. S. Foo, O. D. LaMont, A. K. Rogers, M. M. Yung, A. D. D'Amico, and C. Sievers, "Kinetics of hydrogen activation on ceria-zirconia," *J. Catal.*, vol. 329, pp. 335–347, 2015.

[207] S. M. Schimming, O. D. LaMont, M. König, A. K. Rogers, A. D. D'Amico, M. M. Yung, and C. Sievers, "Hydrodeoxygenation of guaiacol over ceria-zirconia catalysts," *ChemSusChem*, vol. 8, pp. 2073–83, 2015.

[208] L. Vivier and D. Duprez, "Ceria-based solid catalysts for organic chemistry," *ChemSusChem*, vol. 3, pp. 654–678, 2010.

[209] S. Foraita, J. L. Fulton, Z. A. Chase, A. Vjunov, P. Xu, E. Baráth, and et al., "Impact of the oxygen defects and the hydrogen concentration on the surface of tetragonal and monoclinic ZrO_2 on the reduction rates of stearic acid on Ni/ZrO_2," *Chem. Eur. J.*, vol. 21, pp. 2423–2434, 2015.

[210] M. J. McCall and T. A. Brandvold, "Fuel and fuel blending components from biomass derived pyrolysis oil US 2009/0253948 A1," 2009.

[211] F. d. M. Mercader, M. J. Groeneveld, S. R. A. Kersten, N. W. J. Way, C. J. Schaverien, and J. A. Hogendoorn, "Production of advanced biofuels: Co-processing of upgraded pyrolysis oil in standard refinery units," *Appl. Catal. B Environ.*, vol. 96, pp. 57–66, 2010.

[212] E. Furimsky and F. E. Massoth, "Deactivation of hydroprocessing catalysts," *Catal. Today*, vol. 52, pp. 381–495, 1999.

[213] C. Boscagli, C. Yang, A. Welle, W. Wang, S. Behrens, K. Raffelt, and J.-D. Grunwaldt, "Effect of pyrolysis oil components on the activity and selectivity of nickel-based catalysts during hydrotreatment," *Appl. Catal. A Gen.*, vol. 544, pp. 161–172, 2017.

[214] A. Fonseca, P. Zeuthen, and J. B. Nagy, "^{13}C n.m.r. quantitative analysis of catalyst carbon deposits," *Fuel*, vol. 75, pp. 1363–1376, 1996.

[215] A. Fonseca, P. Zeuthen, and J. B. Nagy, "Assignment of an average chemical structure to catalyst carbon deposits on the basis of quantitative ^{13}C n.m.r. spectra," *Fuel*, vol. 75, pp. 1413–1423, 1996.

[216] J. Zhang, K. Wang, M. W. Nolte, Y. S. Choi, R. C. Brown, and B. H. Shanks, "Catalytic deoxygenation of bio-oil model compounds over acid-base bifunctional catalysts," *ACS Catal.*, vol. 6, pp. 2608–2621, 2016.

[217] R. S. Weber, M. V. Olarte, and H. Wang, "Modeling the kinetics of deactivation of catalysts during the upgrading of bio-oil," *Energy & Fuels*, vol. 29, pp. 273–277, 2015.

[218] Y. Yamamoto, F. Kumata, and F. E. Massoth, "Hydrotreating catalyst deactivation by coke from SRC-II oil," *Fuel Process. Technol.*, vol. 19, pp. 253–263, 1988.

[219] C. L. Pieck, E. L. Jablonski, and J. M. Parera, "Sintering-redispersion of $Pt\text{-}Re/Al_2O_3$ during regeneration," *Appl. Catal.*, vol. 62, pp. 47–60, 1990.

[220] P. Dufresne, "Hydroprocessing catalysts regeneration and recycling," *Appl. Catal. A Gen.*, vol. 322, pp. 67–75, 2007.

[221] F. L. P. Resende, "Recent advances on fast hydropyrolysis of biomass," *Catal. Today*, vol. 269, pp. 148–155, 2016.

[222] S. Meesuk, J.-P. Cao, K. Sato, Y. Ogawa, and T. Takarada, "Fast pyrolysis of rice husk in a fluidized bed: Effects of the gas atmosphere and catalyst on bio-oil with a relatively low content of oxygen," *Energy & Fuels*, vol. 25, pp. 4113–4121, 2011.

[223] S. Meesuk, J.-P. Cao, K. Sato, Y. Ogawa, and T. Takarada, "Study of catalytic hydropyrolysis of rice husk under nickel-loaded brown coal char," *Energy & Fuels*, vol. 25, pp. 5438–5443, 2011.

[224] S. Meesuk, J.-P. Cao, K. Sato, Y. Ogawa, and T. Takarada, "The effects of temperature on product yields and composition of bio-oils in hydropyrolysis of rice husk using nickel-loaded brown coal char catalyst," *J. Anal. Appl. Pyrolysis*, vol. 94, pp. 238–245, 2012.

[225] H. Zhang, R. Xiao, D. Wang, G. He, S. Shao, J. Zhang, and Z. Zhong, "Biomass fast pyrolysis in a fluidized bed reactor under N_2, CO_2, CO, CH_4 and H_2 atmospheres," *Bioresour. Technol.*, vol. 102, pp. 4258–64, 2011.

[226] D. C. Dayton, J. Carpenter, J. Farmer, B. Turk, and R. Gupta, "Biomass hydropyrolysis in a pressurized fluidized bed reactor," *Energy & Fuels*, vol. 27, pp. 3778–3785, 2013.

[227] D. C. Dayton, J. Hlebak, J. R. Carpenter, K. Wang, O. D. Mante, and J. E. Peters, "Biomass hydropyrolysis in a fluidized bed reactor," *Energy & Fuels*, vol. 30, pp. 4879–4887, 2016.

[228] R. Agrawal and N. R. Singh, "Synergistic routes to liquid fuel for a petroleum-deprived future," *AIChE J.*, vol. 55, pp. 1898–1905, 2009.

[229] N. R. Singh, W. N. Delgass, F. H. Ribeiro, and R. Agrawal, "Estimation of liquid fuel yields from biomass," *Environ. Sci. Technol.*, vol. 44, pp. 5298–5305, 2010.

[230] N. R. Singh, D. S. Mallapragada, R. Agrawal, and W. E. Tyner, "Economic analysis of novel synergistic biofuel (H_2Bioil) processes," *Biomass Convers. Biorefinery*, vol. 2, pp. 141–148, 2012.

[231] V. K. Venkatakrishnan, W. N. Delgass, F. H. Ribeiro, and R. Agrawal, "Oxygen removal from intact biomass to produce liquid fuel range hydrocarbons via fast-hydropyrolysis and vapor-phase catalytic hydrodeoxygenation," *Green Chem.*, vol. 17, pp. 178–183, 2015.

[232] V. K. Venkatakrishnan, J. C. Degenstein, A. D. Smeltz, W. N. Delgass, R. Agrawal, and F. H. Ribeiro, "High-pressure fast-pyrolysis, fast-hydropyrolysis and catalytic hydrodeoxygenation of cellulose: Production of liquid fuel from biomass," *Green Chem.*, vol. 16, pp. 792–802, 2014.

[233] T. L. Marker, L. G. Felix, M. B. Linck, and M. J. Roberts, "Integrated hydropyrolysis and hydroconversion (IH^2) for the direct production of gasoline and diesel fuels or blending components from biomass, Part 1: Proof of principle testing," *Environ. Prog. Sustain. Energy*, vol. 31, pp. 191–199, 2012.

[234] T. L. Marker, L. G. Felix, M. B. Linck, M. J. Roberts, P. Ortiz-Toral, and J. Wangerow, "Integrated hydropyrolysis and hydroconversion (IH^2®) for the direct production of gasoline and diesel fuels or blending components from biomass, Part 2: Continuous testing," *Environ. Prog. Sustain. Energy*, vol. 33, pp. 762–768, 2014.

[235] L. Zhang, K. Gong, J. Lai, and P. Alvey, "Chemical composition and stability of renewable hydrocarbon products generated from a hydropyrolysis vapor upgrading process," *Green Chem.*, vol. 19, pp. 3628–3641, 2017.

[236] S. B. Jones, C. Valkenburg, C. W. Walton, D. C. Elliot, J. E. Holladay, D. J. Stevens, and et al., "Production of gasoline and diesel from biomass via fast pyrolysis, hydrotreating and

hydrocracking: A design case (PNNL-18284). Pacific Northwest National Laboratory," tech. rep., 2009.

[237] J. Rossmeisl, Z.-W. Qu, H. Zhu, G.-J. Kroes, and J. K. Nørskov, "Electrolysis of water on oxide surfaces," *J. Electroanal. Chem.*, vol. 607, pp. 83–89, 2007.

[238] T. Marker, M. Roberts, M. Linck, L. Felix, P. Ortiz-Toral, J. Wangerow, and et al., "Long term processing using integrated hydropyrolysis plus hydroconversion (IH^2) for the production of gasoline and diesel from biomass," tech. rep., GTI, 2013.

[239] P. Dagaut, "On the kinetics of hydrocarbons oxidation from natural gas to kerosene and diesel fuel," *Phys. Chem. Chem. Phys.*, vol. 4, pp. 2079–2094, 2002.

[240] Cole-Parmer, "Chemical-Resistance." `http://www.coleparmer.com/Chemical-Resistance`,[Accessed: November 16, 2017].

[241] S. Houssenbay, E. Payen, S. Kasztelan, and J. Grimblot, "Oxidic precursors of molybdena supported on nickel and magnesium aluminate hydrotreating catalysts," *Catal. Today*, vol. 10, pp. 541–560, 1991.

[242] J. A. R. van Veen, E. Gerkema, A. M. van der Kraan, P. A. J. M. Hendriks, and H. Beens, "A ^{57}Co Mössbauer emission spectrometric study of some supported CoMo hydrodesulfurization catalysts," *J. Catal.*, vol. 133, pp. 112–123, 1992.

[243] L. Medici and R. Prins, "The influence of chelating ligands on the sulfidation of Ni and Mo in $NiMo/SiO_2$ hydrotreating catalysts," *J. Catal.*, vol. 163, pp. 38–49, 1996.

[244] H. Hu, I. E. Wachs, and S. R. Bare, "Surface structures of supported molybdenum oxide catalysts: Characterization by Raman and Mo L_3-edge XANES," *J. Phys. Chem*, vol. 99, pp. 10897–10910, 1995.

[245] J. Strunk, M. A. Bañares, and I. E. Wachs, "Vibrational spectroscopy of oxide surfaces," *Top Catal*, vol. 60, pp. 1–41, 2017.

[246] O. Müller, M. Nachtegaal, J. Just, D. Lützenkirchen-Hecht, and R. Frahm, "Quick-EXAFS setup at the SuperXAS beamline for in situ X-ray absorption spectroscopy with 10 ms time resolution," *J. Synchrotron Rad*, vol. 23, pp. 260–266, 2016.

[247] J.-D. Grunwaldt, M. Caravati, S. Hannemann, and A. Baiker, "X-ray absorption spectroscopy under reaction conditions: Suitability of different reaction cells for combined catalyst characterization and time-resolved studies," *Phys. Chem. Chem Phys.*, vol. 6, pp. 3037–3047, 2004.

[248] B. S. Clausen, G. Steffensen, B. Fabius, J. Villadsen, R. Feidenhans'l, and H. Topsøe, "In situ cell for combined XRD and on-line catalysis tests: Studies of Cu-based water gas shift and methanol catalysts," *J. Catal.*, vol. 132, pp. 524–535, 1991.

[249] B. Ravel and M. Newville, "ATHENA, ARTEMIS, HEPHAESTUS: Data analysis for X-ray absorption spectroscopy using IFEFFIT," *J. Synchrotron Rad.*, vol. 12, pp. 537–541, 2005.

[250] K. Schofield, "The enigmatic mechanism of the flame ionization detector: Its overlooked implications for fossil fuel combustion modeling," *Prog. Energy Combust. Sci.*, vol. 34, pp. 330–350, 2008.

[251] X. Hu, Y. Wang, D. Mourant, R. Gunawan, C. Lievens, W. Chaiwat, and et al., "Polymerization on heating up of bio-oil: A model compound study," *AIChE J.*, vol. 59, pp. 888–900, 2013.

[252] I. Chorkendorff and J. Niemantsverdriet, *Concepts of modern catalysis and kinetics*. Weinheim: Wiley-VCH Verlag GmbH & Co. KGaA, 2 ed., 2007.

[253] FIZ Karlsruhe, "ICSD FIZ Karlsruhe. ICSD Web Database." `https://icsd.fiz-karlsruhe.de/search/basic.xhtml`,[Accessed: November 3, 2017].

[254] F. Arena, R. D. Chio, and G. Trunfio, "An experimental assessment of the ammonia temperature programmed desorption method for probing the surface acidic properties of heterogeneous catalysts," *Appl. Catal. A Gen.*, vol. 503, pp. 227–236, 2015.

[255] A. Stanislaus, M. Absi-Halabi, and K. Al-Doloma, "Effect of phosphorus on the acidity of γ-alumina and on the thermal stability of of γ-alumina supported nickel-molybdenum hydrotreating catalysts," *Appl. Catal.*, vol. 39, pp. 239–253, 1988.

[256] S. Y. Hosseini and M. R. K. Nikou, "Investigation of different precipitating agents effects on performance of γ-Al_2O_3 nanocatalysts for methanol dehydration to dimethyl ether," *J. Ind. Eng. Chem.*, vol. 20, pp. 4421–4428, 2014.

[257] M. Wannaborworn, P. Praserthdam, and B. Jongsomjit, "A comparative study of solvothermal and sol-gel-derived nanocrystalline alumina catalysts for ethanol dehydration," *J. Nanomater.*, vol. 2015, pp. 1–11, Article ID: 519425, 2015.

[258] R. J. Gorte, "Temperature-programmed desorption for the characterization of oxide catalysts," *Catal. Today*, vol. 28, pp. 405–414, 1996.

[259] H. Knözinger and R. Köhne, "The dehydration of alcohols over alumina. I. The reaction scheme," *J. Catal.*, vol. 5, pp. 264–270, 1966.

[260] V. K. Díez, C. R. Apesteguía, and J. I. Di Cosimo, "Effect of the chemical composition on the catalytic performance of Mg_yAlO_x catalysts for alcohol elimination reactions," *J. Catal.*, vol. 215, pp. 220–233, 2003.

[261] S. Braun, L. G. Appel, V. L. Camorim, and M. Schmal, "Thermal spreading of MoO_3 onto silica supports," *J. Phys. Chemstry B*, vol. 104, pp. 6584–6590, 2000.

[262] R. Prins, "Chapter 13.2: Hydrotreating," in *Handbook of Heterogeneous Catalysis*, pp. 2695–2718, Wiley-VCH Verlag GmbH & Co. KGaA, 2008.

[263] P. A. Spevack and N. S. McIntyre, "A Raman and XPS investigation of supported molybdenum oxide thin films. 2. Reactions with hydrogen sulfide," *J. Phys. Chem.*, vol. 97, pp. 11031–11036, 1993.

[264] C. H. Chang and S. S. Chan, "Infrared and Raman studies of amorphous MoS_3 and poorly crystalline MoS_2," *J. Catal.*, vol. 72, pp. 139–148, 1981.

[265] E. Payen, M. C. Dhamelincourt, P. Dhamelincourt, J. Grimblot, and J. P. Bonnelle, "Study of Co(or Ni)-Mo oxide phase transformation and hydrodesulfurization catalysts by Raman microprobe equipped with new cells," *Appl. Spectrosc.*, vol. 36, pp. 30–37, 1982.

[266] G. L. Schrader and C. P. Cheng, "In situ laser Raman spectroscopy of the sulfiding of Mo/γ-Al_2O_3 Catalysts," *J. Catal.*, vol. 80, pp. 369–385, 1983.

[267] J. J. H. B. Sattler, A. M. Beale, and B. M. Weckhuysen, "Operando Raman spectroscopy study on the deactivation of Pt/Al_2O_3 and $Pt\text{-}Sn/Al_2O_3$ propane dehydrogenation catalysts," *Phys. Chem. Chem. Phys.*, vol. 15, pp. 12095–12103, 2013.

[268] A. Sadezky, H. Muckenhuber, H. Grothe, R. Niessner, and U. Pöschl, "Raman microspectroscopy of soot and related carbonaceous materials: Spectral analysis and structural information," *Carbon*, vol. 43, pp. 1731–1742, 2005.

[269] M. Brorson, A. Carlsson, and H. Topsøe, "The morphology of MoS_2, WS_2, Co-Mo-S, Ni-Mo-S and Ni-W-S nanoclusters in hydrodesulfurization catalysts revealed by HAADF-STEM," *Catal. Today*, vol. 123, pp. 31–36, 2007.

[270] J. Towfighi, M. Sadrameli, and A. Niaei, "Coke formation mechanisms and coke inhibiting methods in pyrolysis furnaces," *J. Chem. Eng. Japan*, vol. 35, pp. 923–937, 2002.

[271] J. Medema, C. van Stam, V. H. J. de Beer, A. J. A. Konings, and D. C. Koningsberger, "Raman spectroscopic study of $Co\text{-}Mo/Al_2O_3$ Catalysts," *J. Catal.*, vol. 53, pp. 386–400, 1978.

[272] V. D'Ippolito, G. B. Andreozzi, D. Bersani, and P. P. Lottici, "Raman fingerprint of chromate, aluminate and ferrite spinels," *J. Raman Spectrosc.*, vol. 46, pp. 1255–1264, 2015.

[273] M. A. Vuurman, D. J. Stufkens, A. Oskam, G. Deo, and I. E. Wachs, "Combined Raman and IR study of $MO_x\text{-}V_2O_5/Al_2O_3$ (MO_x = MoO_3, WO_3, NiO, CoO) catalysts under dehydrated conditions," *J. Chem. Soc. Faraday Trans.*, vol. 92, pp. 3259–3265, 1996.

[274] H. M. Abdel-Dayem, "Dynamic phenomena during reduction of α-$NiMoO_4$ in different atmospheres: In-situ thermo-Raman spectroscopy study," *Ind. Eng. Chem. Res.*, vol. 46, pp. 2466–2472, 2007.

[275] H. Ohtsuka, T. Tabata, O. Okada, L. M. F. Sabatino, and G. Bellussi, "A study on selective reduction of NOx by propane on Co-Beta," *Catal. Letters*, vol. 44, pp. 265–270, 1997.

[276] B. Jongsomjit, J. Panpranot, and J. G. Goodwin Jr., "Co-support compound formation in alumina-supported cobalt catalysts," *J. Catal.*, vol. 204, pp. 98–109, 2001.

[277] S. I. Cordoba-Torresi, A. H.-L. Goff, and S. Joiret, "Electrochromic behavior of nickel oxide electrodes: II. Identification of the bleached state by Raman spectroscopy and nuclear reactions," *J. Electrochem. Soc.*, vol. 138, pp. 1554–1559, 1991.

[278] G. Mestl and T. K. K. Srinivasan, "Raman spectroscopy of monolayer-type catalysts: Supported molybdenum oxides," *Catal. Rev.*, vol. 40, pp. 451–570, 1998.

[279] A. M. Beale and G. Sankar, "In situ study of the formation of crystalline bismuth molybdate materials under hydrothermal conditions," *Chem. Mater.*, vol. 15, pp. 146–153, 2003.

[280] A. Tougerti, E. Berrier, A.-S. Mamede, C. La Fontaine, V. Briois, Y. Joly, and et al., "Synergy between XANES spectroscopy and DFT to elucidate the amorphous structure of heterogeneous catalysts: TiO_2-supported molybdenum oxide catalysts," *Angew. Chemie Int. Ed.*, vol. 52, pp. 6440–6444, 2013.

[281] A. Rochet, B. Baubet, V. Moizan, C. Pichon, and V. Briois, "Co-K and Mo-K edges quick-XAS study of the sulphidation properties of Mo/Al_2O_3 and $CoMo/Al_2O_3$ catalysts," *C.R. Chim.*, vol. 19, pp. 1337–1351, 2016.

[282] L. van Haandel, E. J. M. Hensen, and T. Weber, "High pressure flow reactor for in situ X-ray absorption spectroscopy of catalysts in gas-liquid mixtures-A case study on gas and liquid phase activation of a $Co\text{-}Mo/Al_2O_3$ hydrodesulfurization catalyst," *Catal. Today*, vol. 292, pp. 51–57, 2017.

[283] R. Cattaneo, T. Weber, T. Shido, and R. Prins, "A quick EXAFS study of the sulfidation of $NiMo/SiO_2$ hydrotreating catalysts prepared with chelating ligands," *J. Catal.*, vol. 191, pp. 225–236, 2000.

[284] T. Shido and R. Prins, "Why EXAFS underestimated the size of small supported MoS_2 particles," *J. Phys. Chem. B*, vol. 102, pp. 8426–8435, 1998.

[285] H.-R. Seo and Y.-K. Lee, "EXAFS Studies on the formation of MoS_2 nanoparticles," *J. Korean Phys. Soc.*, vol. 59, pp. 730–734, 2011.

[286] S. M. A. M. Bouwens, J. A. R. van Veen, D. C. Koningsberger, V. H. J. de Beer, and R. Prins, "Extended X-ray absorption fine structure determination of the strucutre of cobalt in carbon-supported Co and Co-Mo sulfide hydrodesulfurization catalysts," *J. Phys. Chem.*, vol. 95, pp. 123–134, 1991.

[287] E. J. M. Hensen, V. H. J. de Beer, J. A. R. van Veen, and R. A. van Santen, "A refinement on the notion of type I and II (Co)MoS phases in hydrotreating catalysts," *Catal. Letters*, vol. 84, pp. 59–67, 2002.

[288] A. Rochet, B. Baubet, V. Moizan, E. Devers, A. Hugon, C. Pichon, and et al., "Influence of the preparation conditions of oxidic $NiMo/Al_2O_3$ catalysts on the sulfidation ability: A quick-XAS and Raman spectroscopic study," *J. Phys. Chem. C*, vol. 119, pp. 23928–23942, 2015.

[289] Y. Hamabe, S. Jung, H. Suzuki, N. Koizumi, and M. Yamada, "Quasi in situ Ni K-edge EXAFS investigation of the spent NiMo catalyst from ultra-deep hydrodesulfurization of gas oil in a commercial plant," *J. Synchrotron Rad.*, vol. 17, pp. 530–539, 2010.

[290] A. Urakawa, T. Bürgi, and A. Baiker, "Sensitivity enhancement and dynamic behavior analysis by modulation excitation spectroscopy: Principle and application in heterogeneous catalysis," *Chem. Eng. Sci.*, vol. 63, pp. 4902–4909, 2008.

[291] A. I. Dugulan, J. A. R. van Veen, and E. J. M. Hensen, "On the structure and hydrotreating performance of carbon-supported CoMo- and NiMo-sulfides," *Appl. Catal. B Environ.*, vol. 142-143, pp. 178–186, 2013.

[292] A. I. Dugulan, E. J. M. Hensen, and J. A. R. van Veen, "High-pressure sulfidation of a calcined $CoMo/Al_2O_3$ hydrodesulfurization catalyst," *Catal. Today*, vol. 130, pp. 126–134, 2008.

[293] A. A. Lemonidou, P. Kechagiopoulos, E. Heracleous, and S. Voutetakis, "Chapter 14: Steam reforming of bio-oils to hydrogen," in *The role of catalysis for the sustainable production of bio-fuels and bio-chemicals* (K. Triantafyllidis, A. Lappas, and M. Stöcker, eds.), pp. 467–493, Elsevier, 2013.

[294] S. Fogler, *Elements of Chemical Reaction Engineering*. Westford, Massachusetts: Pearson Education International, Prentice Hall, 4 ed., 2010.

[295] M. Absi-Halabi, A. Stanislaus, and D. L. Trimm, "Coke formation on catalysts during the hydroprocessing of heavy oils," *Appl. Catal.*, vol. 72, pp. 193–215, 1991.

[296] J. van Doorn, J. Moulijn, and G. Djéga-Mariadassou, "High-resolution electron microscopy of spent Ni-Mo/Al_2O_3 hydrotreating Catalysts," *Appl. Catal.*, vol. 63, pp. 77–90, 1990.

[297] G. Smolik, D. Petti, and S. Schuetz, "Idaho National Engineering and Environmental Laboratory, INEEL/EXT-99-01353. Oxidation, volatilization, and redistribution of molybdenum from TZM alloy in air," tech. rep., 2000.

[298] J. J. Rehr, J. J. Kas, F. D. Vila, M. P. Prange, and K. Jorissen, "Parameter-free calculations of X-ray spectra with FEFF9," *Phys. Chem. Chem Phys.*, vol. 12, pp. 5503–5513, 2010.

[299] A. Gaur and B. D. Shrivastava, "Theoretical calculations of X-ray absorption spectra of a copper mixed ligand complex using computer code FEFF9," *J. Phys. Conf. Ser.*, vol. 534, pp. 1–5, 2014.

[300] P. Giannozzi, S. Baroni, N. Bonini, M. Calandra, R. Car, C. Cavazzoni, D. Ceresoli, and et al., "QUANTUM ESPRESSO: a modular and open-source software project for quantum simulations of materials," *J. Phys. Condens. Matter*, vol. 21, pp. 395502:1–19, 2009.

[301] J. Wellendorff, K. T. Lundgaard, A. Møgelhøj, V. Petzold, D. D. Landis, J. K. Nørskov, T. Bligaard, and K. W. Jacobsen, "Density functionals for surface science: Exchange-correlation model development with Bayesian error estimation," *Phys. Rev. B*, vol. 85, pp. 235149:1–23, 2012.

[302] J. B. Varley, Y. Wang, K. Chan, F. Studt, and J. K. Nørskov, "Mechanistic insights into nitrogen fixation by nitrogenase enzymes," *Phys. Chem. Chem. Phys.*, vol. 17, pp. 29541–29547, 2015.

[303] H. J. Monkhorst and J. D. Pack, "Special points for Brillouin-zone integrations," *Phys. Rev. B*, vol. 13, pp. 5188–5192, jun 1976.

[304] M. V. Bollinger, K. W. Jacobsen, and J. K. Nørskov, "Atomic and electronic structure of MoS_2 nanoparticles," *Phys. Rev. B*, vol. 67, pp. 085410:1–17, 2003.

[305] The National Institute of Standards and Technology, "NIST Chemistry WebBook, SRD 69." `http://webbook.nist.gov/chemistry/`,[Accessed: November 7, 2017].

[306] K. H. Clement, P. Fangel, A. D. Jensen, and K. Thomsen, *Kemiske enhedsoperationer*. Lyngby: Polyteknisk Forlag, 5 ed., 2004.

[307] R. H. Perry and D. W. Green, *Perry's chemical engineers' handbook*, vol. 1. McGraw-Hill, 8 ed., 2008.

[308] R. C. Reid, J. M. Prausnitz, and B. E. Poling, *The properties of gases and liquids*. McGraw-Hill, Inc., 4 ed., 1987.

[309] C. N. Satterfield, *Mass transfer in heterogeneous catalysis*. M.I.T. Press, 1970.

[310] K. Eriksen and M. L. N. Andersen, *Find formlen - kemi*. Lyngby: Polyteknisk Forlag, 1 ed., 2006.

Appendices

A | *In-situ* XAS Setup and Data Treatment Details

The process diagram for the constructed setup for *in-situ* XAS investigation is given in figure A.1 below.

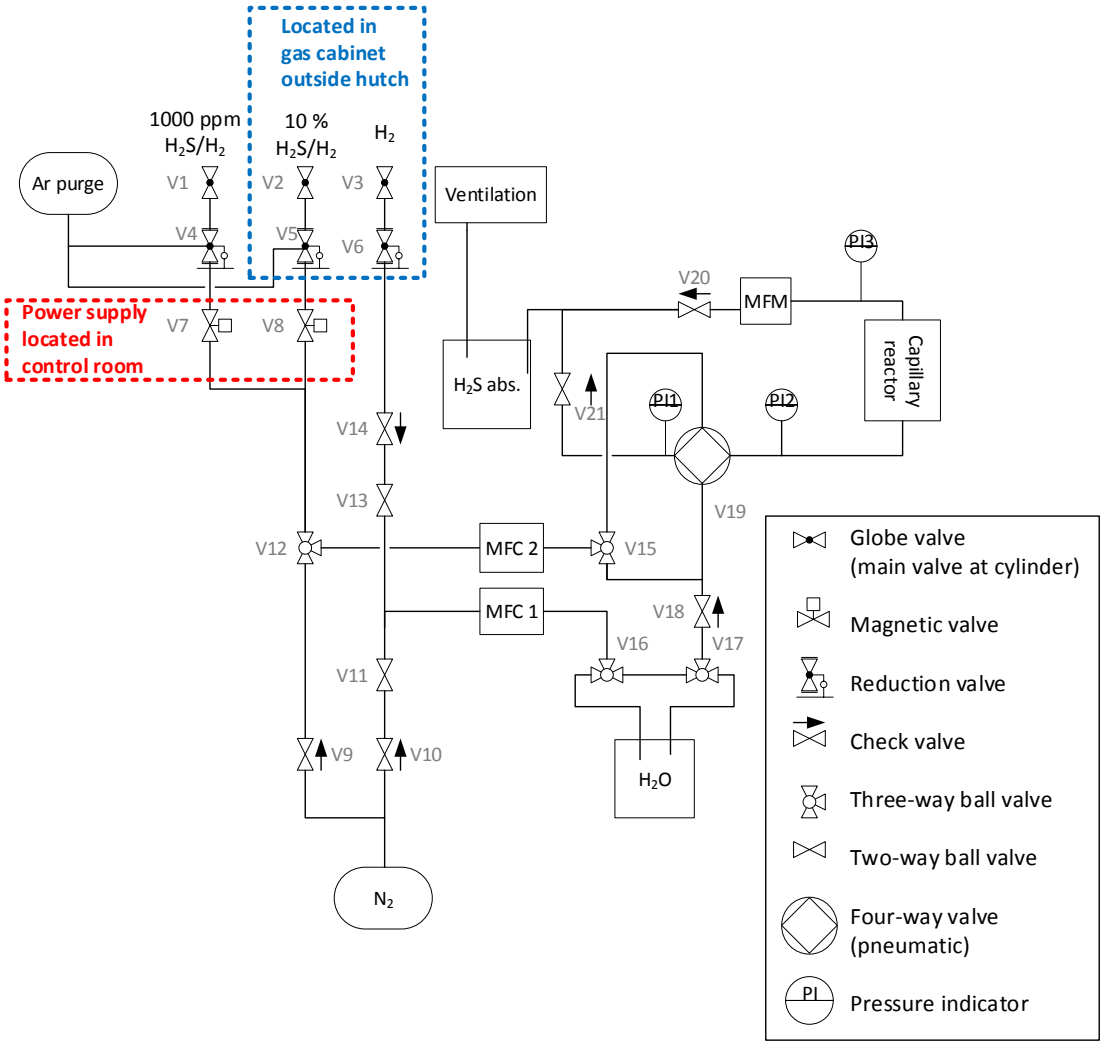

Figure A.1: *In-situ XAS setup constructed for SLS beamtime. MFC = mass flow controller, MFM = mass flow meter, PI = pressure indicator.*

An Ar purge from the SLS gas supply was provided for the reduction valves connected to H_2S gas. 10 % H_2S/H_2 and H_2 cylinders were located outside the hutch, whereas the 1000 ppm H_2S/H_2 cylinder was located inside the hutch. Check-valves V9/V10/V14/V17/V20/V21 ensured flow in the desired direction. Check-valve V21 was an adjustable check-valve which could be used to adjust the pressure read on PI1. MFC2 was used to feed 0-100 NmL/min N_2 or H_2S/H_2 (determined by three-way valve V12). H_2S was fed as 10 % or 1000 ppm (determined by magnetic valves V7/V8). The oulet from MFC2 was sent to one out of two possible positions in the four-way valve V19 (determined by three-way valve V15). MFC1 was used to feed 0-100 NmL/min N_2 or H_2 (determined by two-way valves V11/V13). The gas flow was sent through or bypassed a water saturater (determined by three-way valves V16/V17). The four-way valve V19 connected the reaction gas (from MFC1/2) to the capillary reactor and the MFM or directly to the ventilation. All effluent gas (through V21/V20) was sent through a H_2S scrubber before being sent to the ventilation. Three pressure indicators enabled pressure readings at the outlet of V19 (PI1/PI2) and at the in/outlet of the capillary reactor (PI2/PI3). Capillary heating was performed with the use of a gas blower. The magnetic valves V7/V8 were controlled from the PC in the control room. They were placed as close to the gas cylinders as possible (in the hutch and gas cabinet, respectively). The power supply for these valves was placed in the control room.

The calculations were performed according to the following procedure:

EXAFS spectra were analyzed by using the software package IFEFFIT interfaces, i.e., Athena and Artemis [249]. Athena was first employed to process the raw data, which included removal of smooth background from the measured absorption coefficient, normalization of the X-ray absorption coefficient, and Fourier transform of the resulting spectra from k-space to R-space. Artemis was used for fitting a theoretical model to the experimental data in the R-space to obtain the structural parameters. The model included amplitude reduction factor (S_0^2), coordination number (CN), Debye-Waller factor (σ^2), energy shift for each path (ΔE_0), and change in the path length (ΔR), where R is the bond length.

The FEFF9 code was used to perform ab initio XANES calculations. In FEFF9 [298] [299], the ab initio self-consistent real-space Green's function (RSGF) approach was used including inelastic losses, core-hole effects, vibrational amplitudes, etc. The polarization dependence, core-hole effects, and local field corrections were based on self-consistent, spherical muffin-tin scattering potentials. In the present ab-initio calculations, the Hedin-Lundqvist potential was chosen and XANES, Absolute, SCF (self-consistent field), and FMS (full multiple scattering) cards were used. The self-consistent potential (SCF) parameters were as follows: rfms = 5.2, lfms1 = 0, nscmt = 100, ca = 0.2, nmix = 1. The XANES parameters were as follows: xkmax = 4, xkstep = 0.07, vixan = 0. The LDOS card was added for density of states calculation with an energy range of -20 to 30 eV with a Lorentzian broadening with half-width of 0.1 eV.

Mo K-edge EXAFS spectra were fitted in R space in the range of R = 1.0-3.6 Å and k = 2.1-12.5 $Å^{-1}$. The amplitude reduction factor (S_0^2) as determined from a Mo foil was fixed at 1.0, and one energy shift parameter (E_0) was defined for all scattering paths. For the dehydrated samples, the parameters CN, ΔR, and σ^2 were fitted for the Mo-O path. In case of the sulfided samples, the parameters CN, ΔR, and σ^2 were fitted for each scattering path, i.e. Mo-O, Mo-S and Mo-Mo. For Mo-O, σ^2 was fixed to the value determined from the dehydrated Mo#1 sample. For Mo-Mo, σ^2 was fixed to the value determined from a MoS_2 reference.

Co K-edge EXAFS spectra were fitted in the range of R = 1.0-4.0 Å and k = 2.8-11.9 $Å^{-1}$. S_0^2 as determined from a Co foil was fixed at 0.72, and one value of E_0 was defined for all scattering paths. For the dehydrated sample, parameters CN, ΔR, and σ^2 were fitted for the Co-O path. For

the sulfided sample, the parameters CN, ΔR, and σ^2 were fitted for each scattering path, i.e. Co-S, Co-Co (1^{st}), Co-Co (2^{nd}), and Co-Mo.

Ni K-edge EXAFS spectra were fitted in the range of R = 1.0-3.6 Åand k = 2.1-12.0 $Å^{-1}$. S_0^2 as determined from a Ni foil was fixed at 0.85, and one value of E_0 was defined for all scattering paths. For the dehydrated sample, the parameters CN, ΔR, and σ^2 were fitted for Ni-O, Ni-Ni, and Ni-Mo. In case of the sulfided sample, the parameters CN, ΔR, and σ^2 were fitted for each scattering paths, i.e. Ni-S, Ni-Ni, and Ni-Mo.

B | DFT: Computational Details

Plane-wave DFT calculations were performed using the Quantum Espresso [300] code in combination with the BEEF-vdW [301] exchange correlation functional, as this functional has been shown to yield a reliable description of heats of formation of metal sulfide compounds [302]. The Brillouin zone was sampled using a 2x1x1 Monkhorst-Pack k-points set [303]. A kinetic energy cutoff of 500 Rydberg and a density cutoff of 5000 Rydberg were employed. Ultrasoft pseudopotentials were used to represent the ionic cores. The occupation of the Kohn-Sham states was smeared according to a Fermi-Dirac distribution with a Fermi temperature of $k_BT = 0.1$ eV, and energies were extrapolated to zero electronic temperature. Spin-polarization was considered for all calculations. The MoS_2, Ni-MoS_2, and Co-MoS_2 systems were studied using an infinite stripe model exposing both the M-edge and the S-edge [304]. The unit cell consisted of 4 metal atoms in both x and y direction. The slabs were separated by 8.6 and 14.8 Å in the y and z direction, respectively. Investigations of unpromoted MoS_2 were focused on the M-edge whereas the S-edge was considered for Ni and Co promoted MoS_2, with Ni and Co fully decorating the edge in each case. The phase diagram of the M-edge was constructed considering different coverages of S and H while keeping the S-edge unchanged. Likewise, phase diagrams of Ni and Co promoted S-edges where constructed while keeping the M-edge unchanged.

C | Silica Degradation in Experiments with Ethylene Glycol, H_2, and H_2S

It was found that the silica present in the quartz reactor, in the glass beads used for bed dilution, and in the quartz wool used for bed fixation was degraded during activity tests with the applied feed mixture of ethylene glycol, H_2, and H_2S at 400 °C and 40 barg total pressure. This degradation was most evident from the blank experiments, where glassy deposits were observed in the cold zone of the reactor outlet (see figure C.1). Also, the inner surface of the reactor tube in the packed bed zone had a white erosion pattern after blank and catalytic activity tests (see figure C.2). It was thus concluded that the feed mixture volatilized the silica in the hot zone of the reactor, and that the glassy deposits in the cold outlet were condensed Si compounds. Glassy deposits were most pronounced in blank experiments and catalytic activity tests with low conversion.

Figure C.1: *Glassy deposits on the inner surface of the cold outlet of the reactor tube (quartz) after blank activity test at 400 °C with a feed of 3-3.5 mol% ethylene glycol, 27 bar H_2, 550 ppm H_2S, and 40 barg total pressure (balance N_2).*

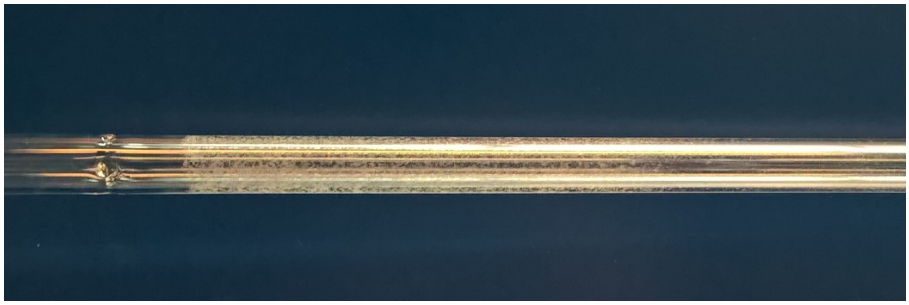

Figure C.2: *Degraded inner surface (white erosion pattern) of the bed zone of the reactor tube (quartz) after taking out the catalyst and cleaning the reactor; especially observed after blank activity tests at 400 °C with a feed of 3-3.5 mol% ethylene glycol, 27 bar H_2, 550 ppm H_2S, and 40 barg total pressure (balance N_2).*

Blank experiments were performed with no catalyst present in the quartz reactor with the bed consisting of either i) quartz wool and glass beads, ii) quartz wool and SiC particles, or iii) steel wool and SiC particles. In all three cases, glassy deposits (see figure C.1) were observed in the reactor outlet, and both quartz wool, glass beads, and the quartz reactor looked partially degraded upon unloading. In conclusion, all quartz and glass components were intolerant towards the applied reaction conditions and were thus exchanged with non-quartz alternatives: a steel reactor, steel wool for bed fixation, and SiC particles for bed dilution.

Degradation of the quartz components led to deposition of Si on the catalyst resulting in deactivation. In figure C.3, the activity obtained for ethylene glycol conversion over a Ni-$MoS_2/MgAl_2O_4$ catalyst is shown for a selected period of time on stream for two experiments run at similar conditions, with and without use of glassy components. It can be seen that accelerated deactivation was observed, when glassy components were used. This deactivation was explained by Si deposition. The spent catalysts contained 3.31 wt% Si when glassy components were used and no Si (0.06 wt%) when the glassy components were substituted. When the pure support was tested at the same conditions for a total TOS of 52 h, the resulting Si deposition was 7.45 wt% indicating that the degradation of SiO_2 formed alkaline species that interacted strongly with acid sites.

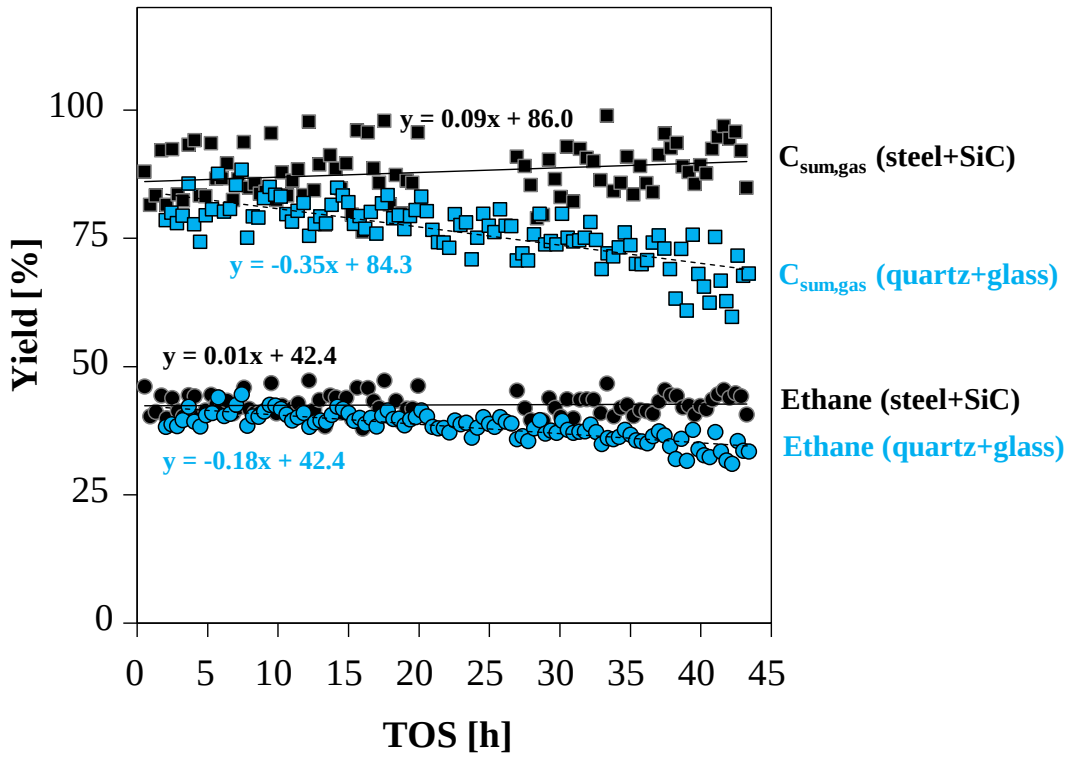

Figure C.3: *Comparison of activity (selected yields) for ethylene glycol HDO at 100 % conversion over 4.0 g Ni-$MoS_2/MgAl_2O_4$ (NiMo#1, see table 3.3). Tested at at 400 °C with a feed of 3-3.5 mol% ethylene glycol, 27 bar H_2, 550 ppm H_2S, and 40 barg total pressure (balance N_2). Steel + SiC: Steel reactor, steel wool, and SiC used. Quartz + glass: Quartz reactor, quartz wool, and glass beads used. After 50-55 h on stream, the liquid feed was changed to a mixture of ethylene glycol and water. Total TOS ∼ 100 h.*

D | Temperature Profile during HDO

Figure D.1 shows the loading profile and measured temperature profile from the HDO of a cyclohexanol/ethylene glycol mixture at at setpoint of 420 °C (see chapter 6). This temperature profile is compared with the corresponding temperature profile without reaction (see also figure 3.4 in chapter 3). The temperature profile from the Cyc/EG experiment clearly shows that endothermal reaction(s) took place in the reactor top; caused by the rapid dehydration of cyclohexanol.

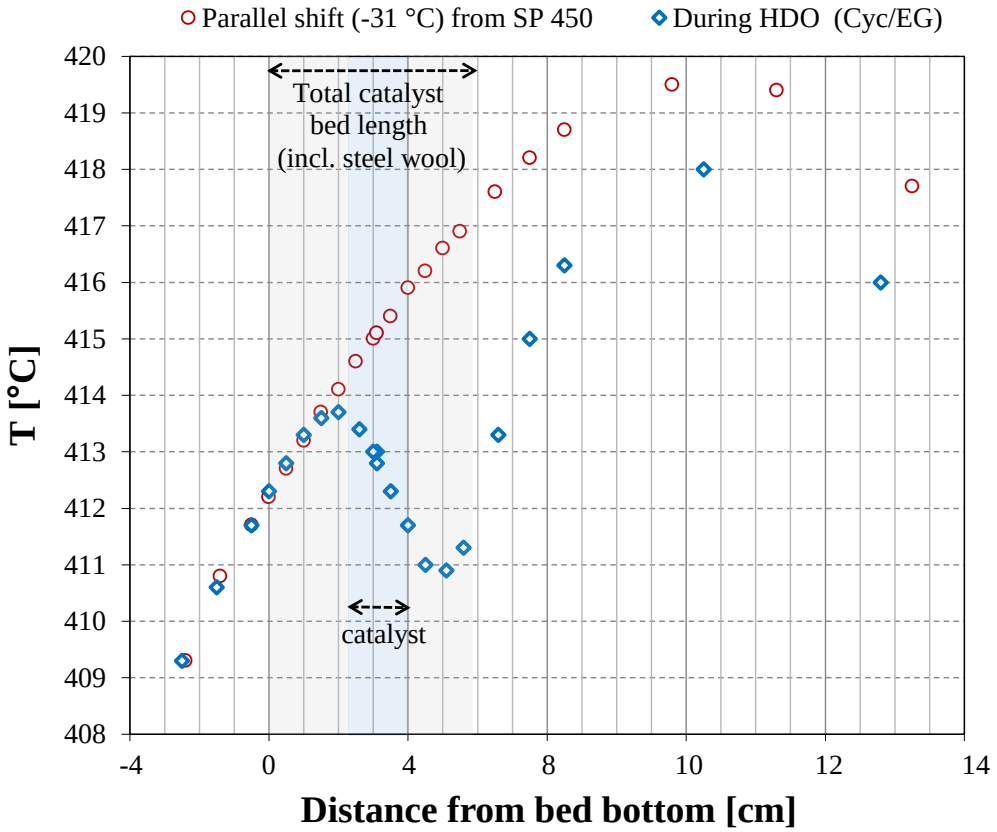

Figure D.1: *Loading profile and temperature profile from the cyclohexanol/ethylene glycol experiment presented in chapter 6, at $T_{SP} = 420\,°C$ with 3 mol% ethylene glycol and 0.5 mol% cyclohexanol in the feed at total pressure 40 barg (27 bar H_2, 550 ppm H_2S, balance N_2). The corresponding temperature profile without reaction (parallel shift (- 31 °C) from SP 450) is shown for comparison. The distance relative to 0 corresponds to the distance above the support pin.*

E Phase Distribution in S1 and Liquid Collection

At high conversions, the product from experiments with phenol and cyclohexanol in the feed consisted of two phases due to the formation of sufficient water to facilitate phase separation. The distribution of liquid phases in the separator tube, S1, was unknown during non-steady state operation, but during steady state operation, it can be assumed that a steady phase distribution developed over time resulting in a steady state liquid product collection. This steady state occurred when the product sample released from S1 via magnetic valve V13 was representative of the phase distribution in the continuous product flow entering S1. See figure 3.1 for an equipment overview.

The development such a steady state depends on the liquid product phase distribution entering S1 and on liquid collection parameters affecting the quantity of liquid released through V13 as well as the rate at which it is released; i.e. the opening and closing level of V13 (via the dP reading) and degree of opening of the backpressure valve, V10, which reduced the pressure from 40 barg to ambient. Figure E.1 illustrates this steady state development in S1 in an example, where the steady state product liquid consists of 1/3 light phase and 2/3 heavy phase.

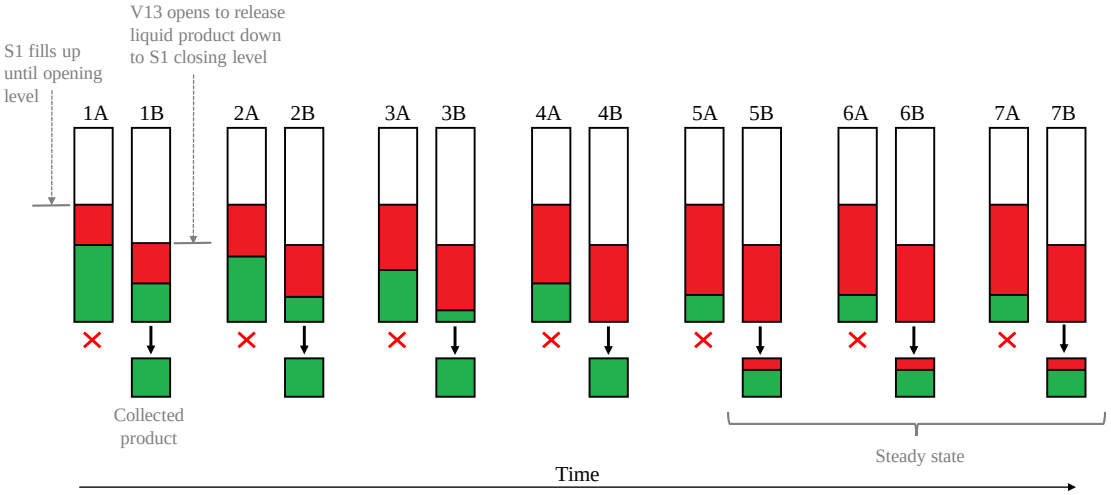

Figure E.1: *Schematic illustration of development of steady state liquid collection of two-phase liquid product in separator tube, S1, over time with 1/3 light phase (red) and 2/3 heavy phase (green) in the liquid product. 1-7: Liquid level before and after product release. A: Just before product release (V13 is closed: X). B: Product release (V13 is open: ↓).*

3-5 h (depending on the conversion) after the model compound feed was added in an experiment, liquid product would start to build up in S1. First, the liquid product filled up S1 until the opening limit for V13 (scenario 1A in figure E.1). Then, V13 opened to release the liquid product (scenario 1B), which was collected downstream in a valve manifold. In this example, 1/3 of the liquid built up in S1 is released when V13 opens ("collected product" in figure E.1). As a result, the first sample of collected product consists of heavy phase only. As product is released through the bottom of S1, the phase boundary moves downwards accordingly giving a 1/1 ratio between the heavy and light phase left in S1 (scenario 1B). Once V13 closes, liquid starts building up again. As the opening level of V13 is reached (scenario 2A), the liquid in S1 consists of the previously accumulated product with a 1/1 heavy/light ratio (from scenario 1B) and the freshly produced product, which consists of 1/3 light phase and 2/3 heavy phase. Assuming equilibrium between the phases, the phase boundary moves up, when the freshly produced liquid enters S1 (scenario 2A compared to 1B). As the opening level is reached, V13 opens again to release the second sample of collected product (scenario 2B). Again, it consists of heavy phase only, and the phase boundary moves to a lower level (scenario 2B compared to 2A). In the given example, this process of liquid build-up and release is repeated four times before steady state is achieved in scenario 5-7, when the released product sample has the same composition (1/3 light and 2/3 heavy) as the product entering S1.

Figure E.2 shows steady state liquid collection in four sample bottles collected over time during an experiment with a pure cyclohexanol feed and a two-phase liquid product. The time it takes before steady state liquid collection is achieved depends on the heavy/light phase ratio and on the liquid collection parameters. If more heavy phase is produced and a smaller quantity of product is released through V13, it will take more time before steady state is achieved. An important note is that the light phase is subject to back mixing to a greater extent than the heavy phase due to the inherent difference in retention times of each phase.

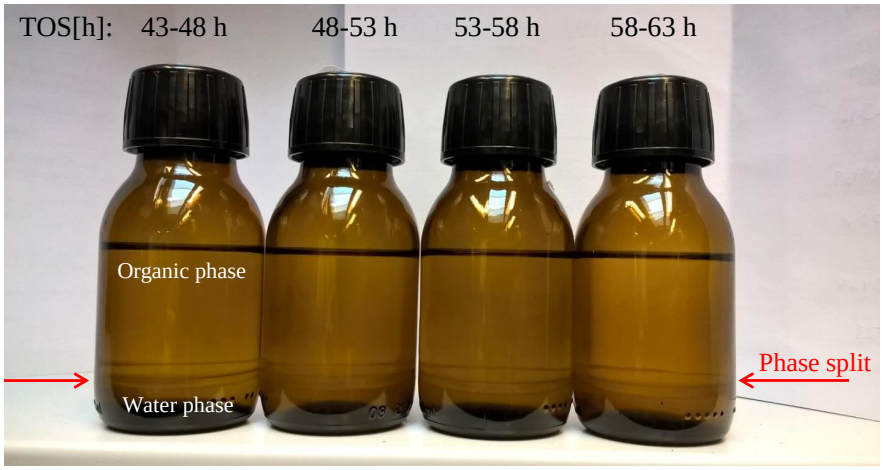

Figure E.2: *Two-phase liquid product obtained at TOS = 43-63 h during conversion of pure cyclohexanol over Ni-$MoS_2/MgAl_2O_4$ (NiMo#2, see table 3.3) at T_{SP} = 420 °C with 2.1 mol% cyclohexanol in the feed at total pressure 40 barg (27 bar H_2, 550 ppm H_2S, balance N_2).*

The development of steady states in the liquid collection could be followed from the liquid product density and flow rates. This is shown for two experiments in figure E.3 (see chapter 6 for activity data). In the experiment Cyc (figure E.3a), full conversion of cyclohexanol was achieved in the entire TOS

range giving a stable flow of a two-phase liquid product. The density of the heavy and light phases were similar to that of water (0.997 g/mL) and cyclohexane/cyclohexene (0.779-0.811 g/mL). In the Phe/EG experiment (figure E.3b), there was initially a high conversion of ethylene glycol leading to the formation of a separate water phase at TOS <40 h. At TOS >40 h, the HDO of ethylene glycol had decreased to a level, where the amount of water formed was low enough to enable it to mix with unconverted ethylene glycol and phenol. As it can be seen from figure E.3b, especially by looking at the product density, the temperature influenced the liquid collection; at ≥420 °C (TOS <69 h), no steady state was obtained, but steady state operation at different temperatures was possible at TOS >69 h.

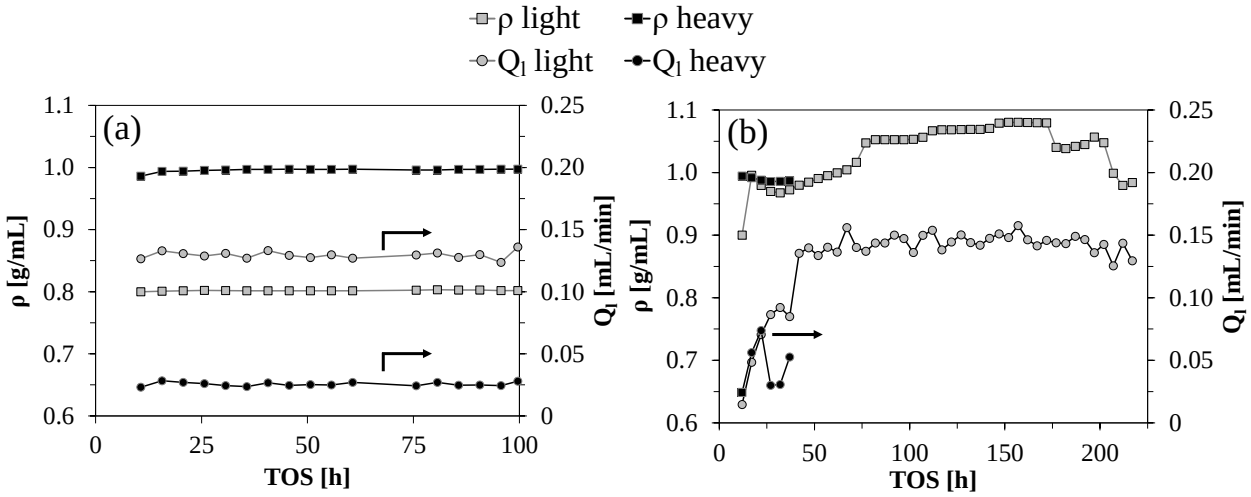

Figure E.3: *Liquid product flow rate, Q_l, and density, ρ (at 25 °C), from oxygenate conversion over Ni-$MoS_2/MgAl_2O_4$ (NiMo#2, see table 3.3) at different operating temperatures at total pressure 40 barg (27 bar H_2, 550 ppm H_2S, balance N_2). (a) Experiment: Cyc, with 2.1 mol% cyclohexanol in the feed. (b) Experiment: Phe/EG, with 3.1 mol % ethylene glycol and 0.55 mol % phenol in the feed. For experimental details, see chapter 6, and table 6.2 (feed composition), and figure 6.2 (temperature profiles).*

F | N_2-Physisorption of $MgAl_2O_4$

Results from N_2-physisorption of $MgAl_2O_4$ are shown in figure F.1 and figure F.2 below.

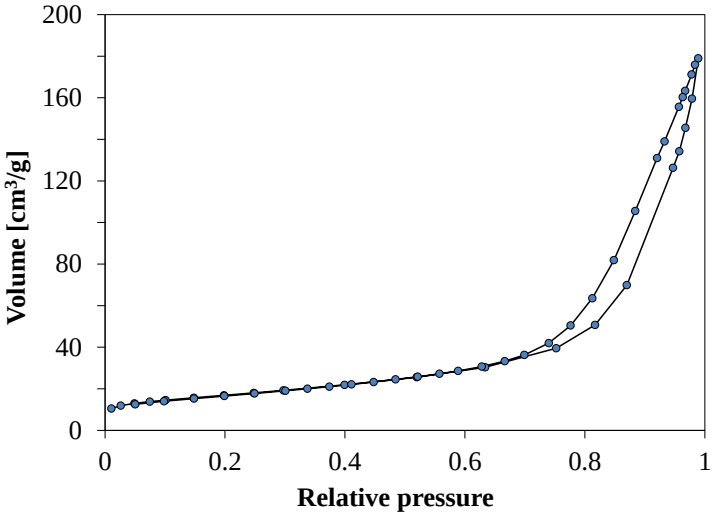

Figure F.1: *Adsorption-desorption isotherms for the $MgAl_2O_4$ support, from N_2-physisorption.*

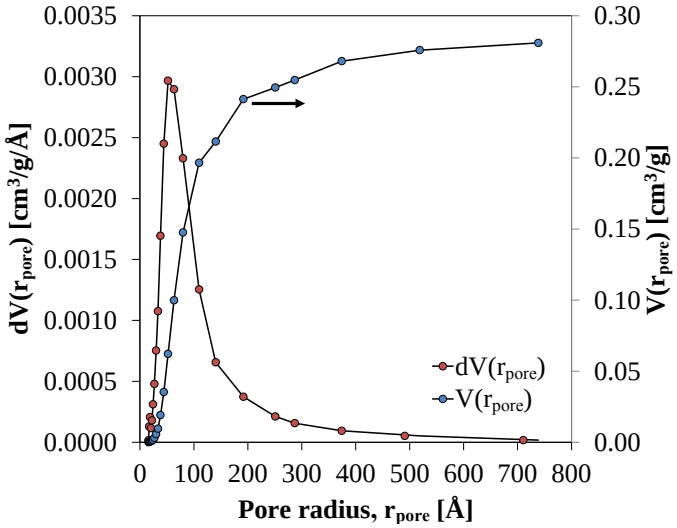

Figure F.2: *Pore size distribution for $MgAl_2O_4$ support, from N_2-physisorption and the BJH model with pore volume, V, and pore radius, r_{pore}.*

G | Mass Balance in the POC Setup

Most of the experiments conducted were subject to deviation in the carbon mass balance which was mainly caused by failure to condense light oxygenates or evaporation of such before analysis of the collected liquid product in terms of mass, density, and composition (by GC-FID/MS).

The online GC-TCD analysis detected N_2, H_2, CO, CO_2, and C_1-C_3 hydrocarbons. Therefore, the possibility for closing the carbon balance relied on full condensation and GC-FID/MS quantification of any other species, such as oxygenates or C_{4+} hydrocarbons. However, since the mass balance deviation was correlated with incomplete condensation of light oxygenates, the calculations of conversion (based on feed and effluent flow of model compounds with high boiling points, i.e. ethylene glycol, cyclohexanol, and phenol) and yields of C_{1-3} gasses (measured by GC-TCD), are reliable.

The impact of non-condensed species was indicated by the difference in mass balance closure at approximately 100 % conversion of ethylene glycol at 400 °C using 4 g of low and higher loading catalysts (see chapter 4), for which a $\sim$ 90 % mass balance closure could be obtained with the more active catalysts, which also produced a total gas yield of $\sim$ 90 % (see table 4.2). The less active catalysts had a total gas yield of $\sim$ 20 % and a poor mass balance closure of $\sim$ 60-70 %.

Figure G.1 compares the mass balances on the basis of ethylene glycol, cyclohexanol, and phenol during the first 100 h on stream of the experiments presented in chapter 6. As it can be seen, the phenol and cyclohexanol mass balances close well with >90 %, indicating that efficient condensation and collection of liquid compounds with high boiling points was possible. The mass balances for ethylene glycol, on the other hand closed to 73 % and were similar for the experiments run with pure ethylene glycol and with phenol in ethylene glycol. Taking into account the good closure of the phenol carbon balance (in an experiment with a poorly closed ethylene glycol balance), this clearly shows that it was ethylene glycol derived compounds, which were not accounted for in the product analysis.

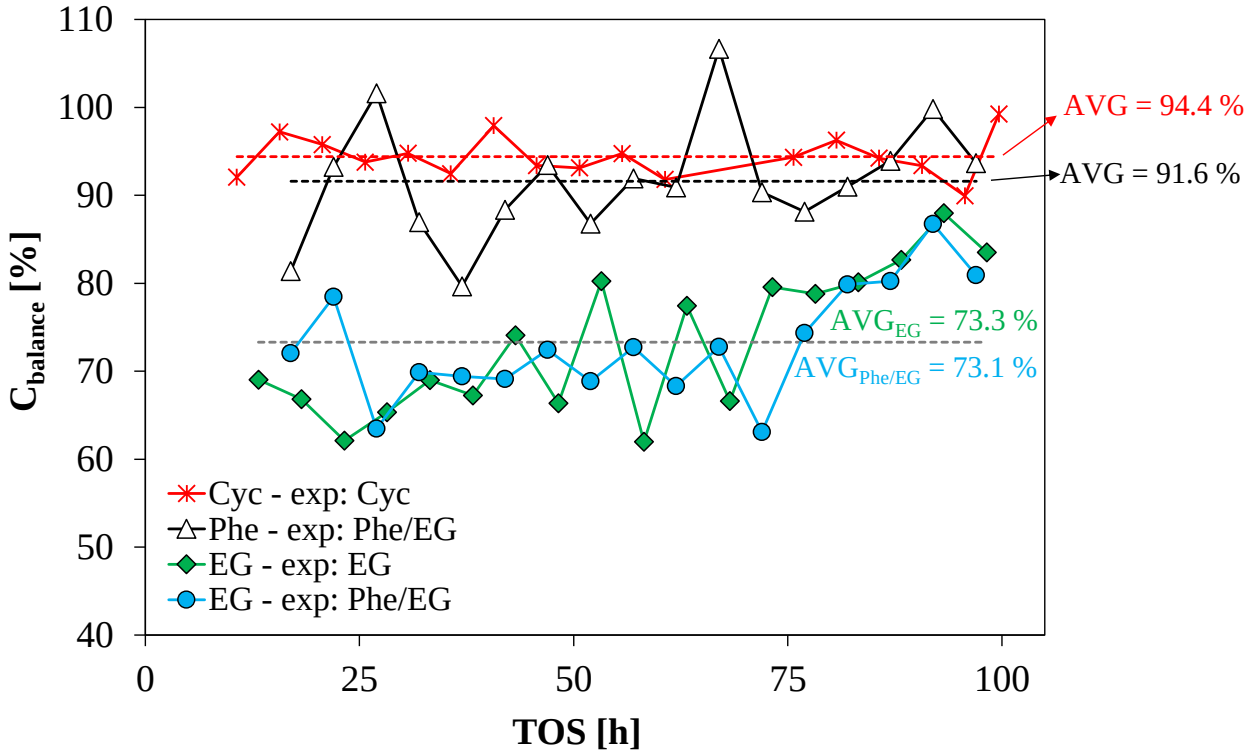

Figure G.1: *Carbon mass balance closure on the basis of ethylene glycol, phenol, and cyclohexanol for the first 100 h on stream of experiments presented in chapter 6 using 0.5 g NiMo#2 (see table 3.3). Operating conditions: 400-450 °C, 550 ppm H_2S, 27 bar H_2, and 40 barg (balance N_2). Experiment EG had an ethylene glycol feed of 2.5 mmol/min. Experiment Cyc had a cyclohexanol feed of 1.5 mmol/min. Experiment Phe/EG had a feed of 0.4 mmol/min phenol and 2.2 mmol/min ethylene glycol. The carbon balance for phenol (experiment: Phe/EG) was based on the yield of unconverted phenol, benzofuran, 2-ethylphenol, and 3-methylphenol (disregarding the C_{1-2} alkyl groups; these were included in the ethylene glycol mass balance, which also contained the remaining liquid products detected and all gas products.*

Some modifications were made during the experimental work to improve the carbon mass balance by improving the condensation and collection of the liquid reactor effluent:

- The holes in the lids of the manifold sample bottles, through which the liquid product was collected via 1/8" tubes, were not sealed in the NiMo and CoMo experiments presented in chapter 4. Since the bottles were stored in a ventilated cabinet, accelerated evaporation could have removed liquid product from the sample bottles. As this was realized, the holes were sealed with parafilm. Parafilm sealing was applied in all following experiments.
- The reactor effluent and separator tube, S1, were not cooled in any of the experiments presented in chapter 4 or in the NiMo experiment presented in chapter 5 (in this chapter, cooling of S1 was however provided for the Mo, CoMo, and Ni tests). Cooling with water was applied in all subsequent experiments. In the 90 h on stream CoMo test presented in chapter 5, insignificant cooling was provided via plastic tubes, but in all subsequent experiments, cooling down to 10-15 °C was provided via copper tubing.

The vapor pressures of relevant oxygenates and hydrocarbons calculated from the Antoine equation at different temperatures are listed in table G.1. The ambient temperature in the pilot hall was typically

25-30 °C, but temperatures up to 35 °C were measured during warm days. There was no internal temperature measurement in the separator tube, so the gas stream passing through it could potentially have been higher than the 10-15 °C measured externally when cooling was applied. Moreover, there was no cooling the the valve manifold or lab cupboards, where the sample bottles were stored upon analysis. In a typical experiment, the ethylene glycol feed was 2.4 mmol/min, the total feed was ∼ 70 mmol/min at 40 barg, and 15-30 % of the feed carbon flow could not be accounted for in the outlet. This corresponds to a missing carbon flow of 0.7-1.4 mmol/min. Assuming all of this carbon was present as acetaldehyde, it would correspond to a flow of 0.35-0.7 mmol/min acetaldehyde and 0.2-0.4 bar, which is below the equilibrium vapor pressure of acetaldehyde at 15 °C and thus would not be condensed in S1. This example illustrates how the presence on non-condensed oxygenates could contribute significantly to the deviation in the carbon balance. The equilibrium vapor pressures of especially acetone, methanol, ethanol, and C_{4-6} hydrocarbons are also significant and indicate a potential impact on the carbon mass balance from these species.

Table G.1: *Boiling points and equilibrium vapor pressures in bar calculated from the Antoine equation using Antoine parameters from [305]. Feed source which was correlated with detection of each compound has been noted. none = not detected.*

Compound	$\mathbf{T_b}$	**Temperature [°C]**		
(feed source)	**[°C]**	**15**	**30**	**50**
Oxygenates				
Acetaldehyde (EG)	21	0.82	1.43	2.72
Acetone (EG)	56	0.19	0.38	0.81
Methanol (EG)	65	0.10	0.22	0.55
Ethanol (EG)	78	0.04	0.10	0.29
1-propanol (EG)	97	0.01	0.04	0.12
1-butanol (EG)	117	<0.01	0.01	0.05
Cyclohexanol (Cyc)	160	<0.001	<0.001	<0.01
Phenol (Phe)	182	<0.001	<0.001	<0.01
Ethylene glycol (EG)	197	<0.001	<0.001	<0.001
Hydrocarbons				
n-butane (EG)	∼0	1.76	2.81	4.93
n-pentane (none)	36	0.46	0.82	1.58
n-hexane (EG)	69	0.13	0.25	0.54
Benzene (none)	80	0.08	0.16	0.36
Cyclohexane (Cyc)	81	0.08	0.16	0.36
Cyclohexene (Cyc)	83	0.07	0.15	0.33

All of the compounds listed in table G.1 were detected in the liquid product from several experiments with varying feedstock, except for benzene, butane, pentane, and hexane. Benzene was not detected, even though it was expected in the liquid product formed during the conversion of phenol in ethylene glycol (see chapter 6). Pentane was never detected, but butane and C_{6+} hydrocarbons were detected on two occasions. In two activity tests using ethylene glycol as model compound (NiMo#1 and Mo#1 as catalyst), an additional gas analysis was performed for a shorter period of time using a Thermo Fisher 1300 Trace GC equipped with three sample loops for efficient analysis of H_2, N_2, CO_2, and C_{1-6+} hydrocarbons. The GC had an FID detector and two TCD detectors, and the following columns: Restek 5 m x 0.53 mm x 3 μm Rtx-1 (C_{6+} hydrocarbons and oxygenates), Restek 25 m x 0.53 mm

Alox/Na_2SO_4 (C_{1-5} hydrocarbons), Hayesep N, XL-sulfur, and Molsieve 5A micro-packed columns (permanent gasses), and Hayesep N and Shincarbon-ST columns (H_2). Using this GC, C_4 and $C_{6+/ox}$ were measured at concentrations of $\leq$0.02 % C_4 (sum of n-butane, trans-2-butene, 1-butene, and iso-butylene) and $\leq$0.02 % $C_{6+/ox}$ (C_{6+} hydrocarbons and/or C_{1+} oxygenates). At a typical gas flow of $\sim$ 70 mmol/min and a feed of 2.4 mmol/min ethylene glycol, these concentrations correspond to 1.2 and 1.8 % of the carbon feed (assuming the latter was present as C_6 hydrocarbons). Hence, it was concluded that the formation of C_{4+} hydrocarbons contributed with $<$5 %-point of the deviation carbon balance.

In the following, the different efforts towards understanding the impacts of the carbon mass balance have been reviewed. Overall, the following setup modifications should be considered in order to improve the carbon mass balance and the liquid collection in general:

- Improved cooling of entire liquid product collection section to ensure a stable temperature, also on warm days.
- Online GC analysis of C_{4+} hydrocarbons and light oxygenates to minimize the need for extensive product cooling and difficult handling of cold samples.
- Automated pressure reduction in the liquid product collection section to minimize flow fluctuations and the risk of plugging of the manually controlled backpressure valve (V10, see figure 3.1).

G.1 Reliability of Liquid Feed and Liquid Product Flow

The reliability of the liquid feed flow and the collected condensed liquid product flow was confirmed in an empty reactor test at conditions relevant to the conducted activity tests, see figure G.2.

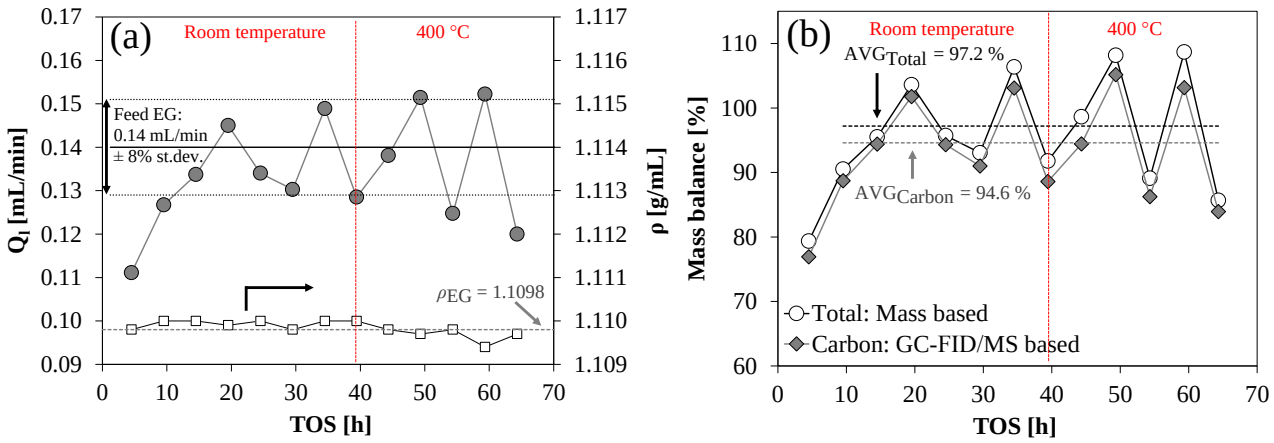

Figure G.2: *Results from an empty reactor test (no cooling of S1) with a feed of 0.14 mL/min ethylene glycol and 500 NmL/min N_2 at a pressure of 40 barg and up to 400 °C. (a) Liquid flow, Q_l, and density, ρ (at 25 °C), of collected liquid product (compared with average feed flow). (b) Carbon mass balance (based on sample mass, density, and GC-FID/MS measurements) and total mass balance based on inlet and outlet liquid mass flows.*

As it can be seen from figure G.2, the first sample collected at a TOS of 5 h was influenced by the initial delay in the product collection compared to the time at which ethylene glycol was initially added to

the system. This point has thus typically been excluded in the data treatment, but has been included here for illustration of the typical product flow. The flow of ethylene glycol collected in the manifold corresponded to the feed flow, which was 0.14 mL/min on average with some fluctuation as noted in figure G.2a. The density of the collected ethylene glycol confirmed that there was a small variation of this property, within the uncertainty of the density measurement. The resulting mass balance (figure G.2b) was evaluated on the basis of the total mass balance of fed and collected ethylene glycol and on the basis of the carbon mass balance, where the mass, density, and GC-FID/MS analysis of collected samples were used to calculate the carbon content. There was a good mass balance closure at 94.6-97.2 % (disregarding the first sample) for both methods with a slightly better closure obtained for the total mass balance, which indicates a slight underestimation of the concentration of pure ethylene glycol using GC-FID/MS.

G.2 Reliability of GC-FID/MS Quantification

It was verified that the GC-FID/MS analysis sufficiently quantified the carbon content in liquid samples within a deviation of <10 %. This was in spite of several species being present in low concentrations, which could not be quantified due to a poor MS signal or overlapping peaks. The total carbon content determined by GC-FID/MS was compared with the content determined from elemental analysis in selected liquid samples. The GC-FID/MS analysis was performed as described in chapter 3.4.1. The elemental analysis was performed using an Eurovector EA3000 CHNS analyzer. The results shown in table G.2 show a good correlation between the carbon content determined from the two methods.

Table G.2: *Liquid product carbon flow determined by GC-FID/MS and elemental analysis during the conversion of ethylene glycol (2.4 mmol/min) over Mo#1 at 400 °C, 27 bar H_2, 550 ppm H_2S, and a total pressure of 40 barg (balance N_2). For TOS activity, see figure 5.3b. Mass balance closure: 64-72 %, i.e. ∼ 1.5 mmol/min carbon unaccounted for.*

TOS	**F_C [mmol/min]**		**Relative difference**
[h]	**GC-FID/MS**	**CHNS**	**[%]**
65-70	2.40	2.49	3.7
70-75	2.06	1.89[a]	-8.5
75-80	2.30	2.09[a]	-9.1
80-85	2.34	2.32[a]	-0.3

[a] Average of two measurements with standard deviation: 1.1-5.7 %.

G.3 Extended Gas Analysis

G.3.1 Qualitative Analysis

The presence of non-condensed oxygenates and hydrocarbons was verified by an extended gas analysis performed for a single sample collected with a gas bag during the conversion of ethylene glycol over a NiMo catalyst. The oxygenates in the gas sample were present in too low concentration for identification with GC-MS. Instead, the sample was analyzed on an Agilent 7890A GC equipped with a Restek Rt-Q-BOND 30 m x 530 μm x 20 μm capillary column, one FID detector, and two TCD detectors (see figure G.3 for FID signals). Apart from detection of gasses that were already measured with the online GC analysis at the POC, the FID signal indicated the presence of several of the oxygenates from the standard mixture, e.g. acetaldehyde, methanol, ethanol, and C_{3-5} oxygenates and hydrocarbons. The corresponding carbon flow of these compounds based on the effective carbon method with ethylene as reference (see chapter 3.4.1) was 0.25 mmol/min, which is approximately 5 % of the missing carbon at the given TOS. The GC spectrum shown in figure G.3 was however considered uncertain due to several issues:

- The gas sampling was performed downstream of the aerosol filter, which could have trapped some of the oxygenates, potentially also larger molecules such as ethylene glycol and polyethylene glycol.
- The gas bag was analysed 1.5 days after sampling, which could have caused some of the contents to diffuse out.
- No heating of the gas bag was performed upon analysis in order to desorb potentially sticky compounds from the bag wall. Upon analysis, the gas bag was handled outside at <5 °C, which might have caused additional adhesion onto the inner bag wall.

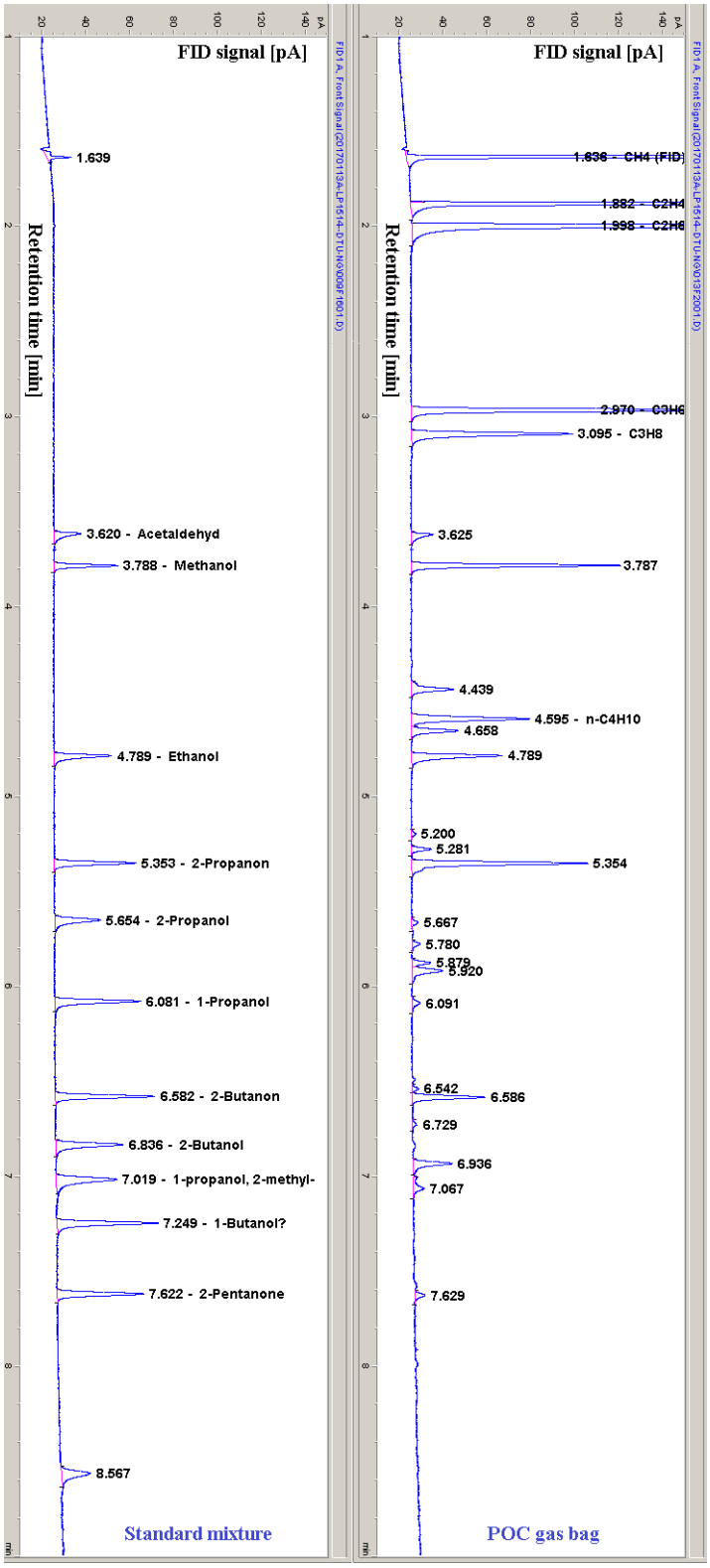

Figure G.3: *GC-FID analysis of a standard oxygenate mixture (acetaldehyde, methanol, ethanol, acetone, isopropanol, 1-propanol, 2-butanone, 2-butanol, 2-methyl-1-propanol, 1-butanol, and 2-pentanone) and of a sample (gas bag) from the conversion of 2.5 mmol/min ethylene glycol at TOS = 29 h over 0.5 g NiMo#1 (see table 3.3) at 400 °C, 27 bar H_2, 550 ppm H_2S, and 40 barg (balance N_2). The carbon balance closure at 28-33 h on stream was 55 %. For TOS activity, see figure 6.11b in chapter 6.*

G.3.2 Quantitative Analysis

A more correct estimate of the contribution from non-condensed oxygenates was performed by analysing gas samples extracted with a syringe upstream of the the aerosol filter on the POC setup followed by immediate analysis on an Agilent 6890 N GC-FID equipped with a 39 m x 0.53 mm HP-PLOT/Q column. This was done during the conversion of pure ethylene glycol over NiMo#2 at 380 °C (see figures 6.3-6.5 in chapter 6 for TOS activity). This Agilent GC measurement (see figure G.4) showed the presence of C_{1-3} hydrocarbons along with methanol, acetone ethanol, and several unknown compounds. Methane, ethane, and ethylene were also detected with the online GC, but the concentration of propane and propylene (<0.01 %) was too low for online detection. Using ethylene as reference in the effective carbon method, the concentrations listed in table G.3 were calculated. As seen, there was some deviation between the online GC measurements and Agilent measurements indicating room for improvement of the gas analysis. Based on the qualitative GC analysis (figure G.3), the unknown compounds were assumed to have a carbon number of 5, which together with a total flow of 70 mmol/min at the given TOS corresponded to a carbon flow of 0.19 mmol/min in the unknowns and 0.086 mmol/min in the appointed oxygenates. The resulting total carbon flow of gas compounds not analyzed by the online GC (0.276 mmol/min) accounted for 55 % of the missing carbon flow at the given TOS.

As shown in table G.2, there was a <10 % deviation in the GC-FID/MS quantification. The quantified liquid carbon flow from the sample bottle at the given TOS (166-171 h) was 4.09 mmol/min, which corresponded to 98.5 % of the total peak area detected by GC-FID/MS. Assuming that the remaining unidentified peaks had a similar response factor as the identified peaks, they were estimated to account for a flow of $(4.09/98.5)\cdot 1.5 = 0.062$ mmol/min carbon. Thus, the total amount of additional gas and liquid carbon in the given experiment was $0.276 + 0.062 = 0.338$ mmol/min, which corresponds to 67 % of the carbon flow originally not accounted for. Taking this additional carbon into account, the carbon balance could be improved from 89.8 % to 96.7 %. It was thus concluded that the formation on undetected species, and mainly non-condensed light oxygenates, caused the often poor closure of the carbon mass balance.

Table G.3: *GC analysis of a sample from the conversion of 2.5 mmol/min ethylene glycol at TOS = 168 h over 0.5 g NiMo#2 at 380 °C, 27 bar H_2, 550 ppm H_2S, and 40 barg (balance N_2). The carbon balance closure at 166-171 h on stream was 89.8 %. For TOS activity, see figures 6.3-6.5 in chapter 6.*

Compound	**Concentration [%]**	
	Online GC-TCD	**Agilent GC-FID**
Methane	0.0374	0.0257
Ethylene[a]	**0.0918**	**0.0918**
Ethane	0.0780	0.0771
Propylene	0	0.0056
Propane	0	0.0019
Methanol	-	0.0755
Acetone	-	0.0029
Ethanol	-	0.0078
Unknown[b]	-	0.0534

[a] Basis for effective carbon method.

[b] Assuming an effective carbon number of 4.

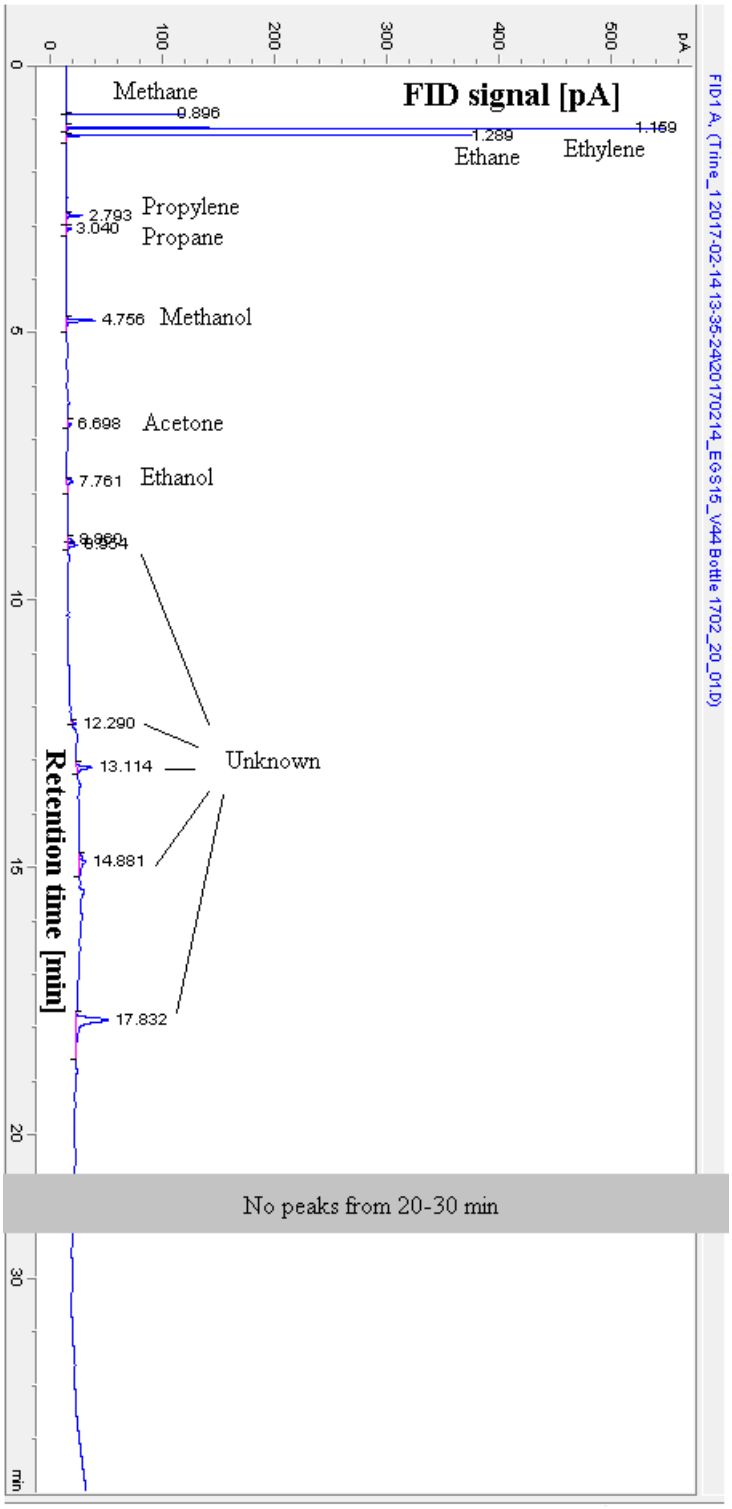

Figure G.4: *GC-FID analysis of a sample (syringe) from the conversion of 2.5 mmol/min ethylene glycol at TOS = 168 h over 0.5 g NiMo#2 (see table 3.3) at 380 °C, 27 bar H_2, 550 ppm H_2S, and 40 barg (balance N_2). The carbon balance closure at 166-171 h on stream was 89.8 %. For TOS activity, see figures 6.3-6.5 in chapter 6.*

H | Appendices for Chapter 5

H.1 Results from Catalytic Activity Tests

The TOS activity in terms of individual gas product yields and total gas carbon yield for the experiments presented in figure 5.3 and figure 5.4 are given below in figure H.1. TOS activity in terms of gas yields, conversion, and temperature for repeated activity tests is shown in figure H.2. The carbon deposited in spent catalysts has been plotted as a function of the TOS in figure H.3 (see table 5.1 for spent catalyst composition).

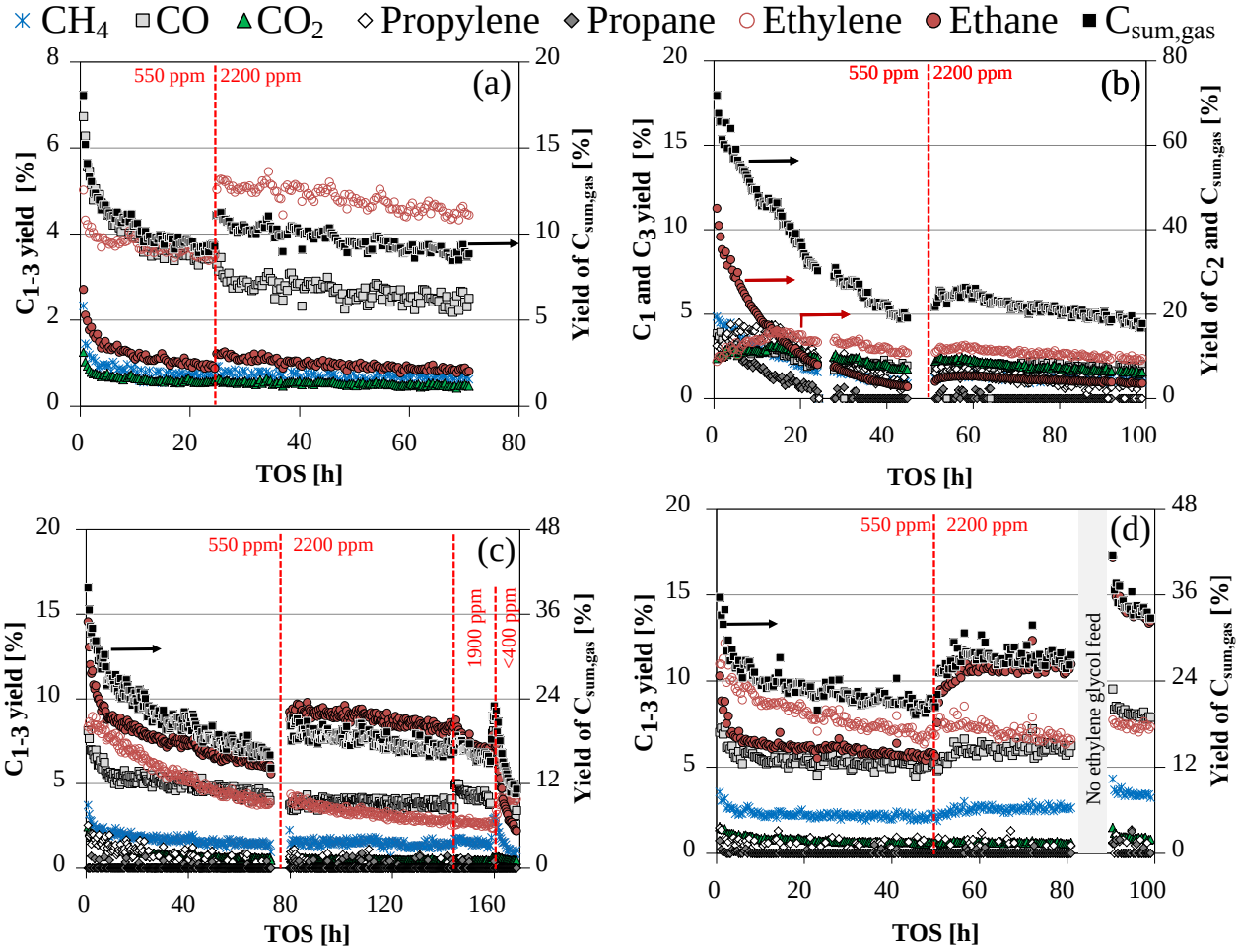

Figure H.1: *Carbon based yields for ethylene glycol conversion at 400 °C, 27 bar H_2, 550-2200 ppm H_2S (noted in figures), 40 barg total (balance N_2), and 3-3.5 mol% ethylene glycol in the feed (a) Ni#1 (1.5 g), (b) Mo#1 (1.5 g), (c) NiMo#1 (0.5 g), and (d) CoMo#1 (0.5 g).*

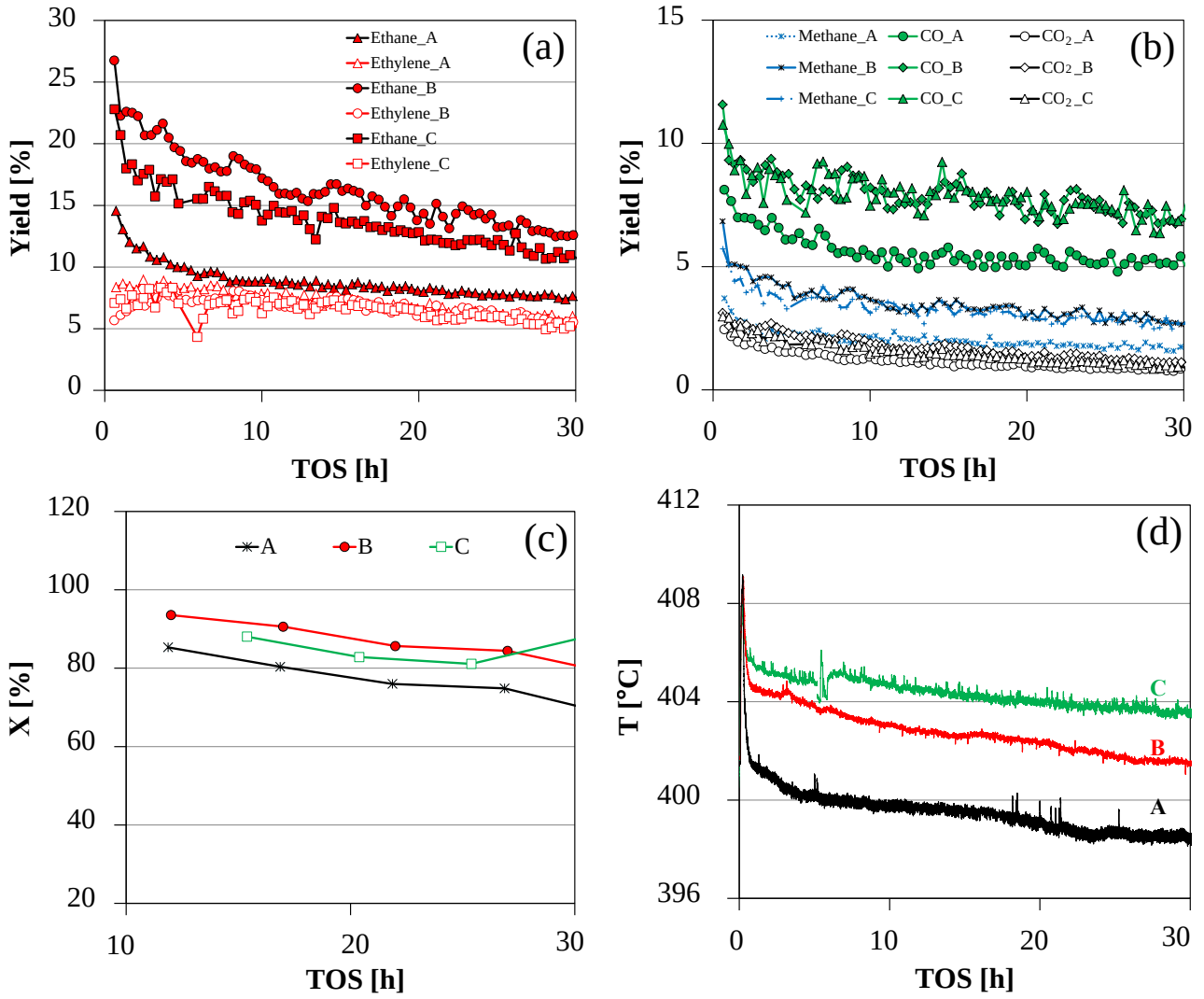

Figure H.2: *Results from three reproduced experiments (A, B, C) with NiMo#1 (0.5 g) for ethylene glycol conversion at 400 °C, 27 bar H_2, 550 ppm H_2S, 40 barg total (balance N_2), and 3-3.5 mol% ethylene glycol in the feed. (a) Ethane and ethylene yield, (b) C_1 yields, (c) conversion, and (d) reaction temperature.*

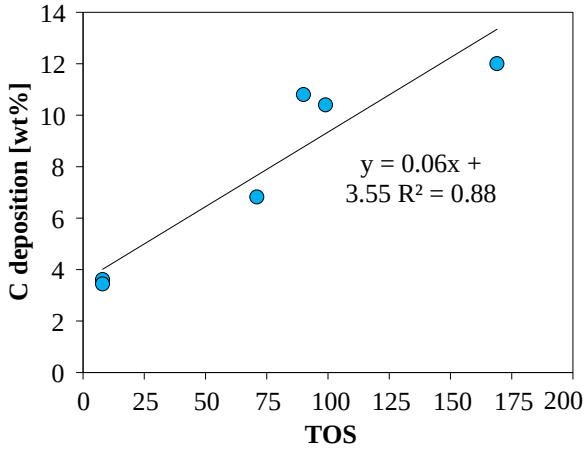

Figure H.3: *Carbon deposition on spent catalysts tested for ethylene glycol conversion at 400 °C, 27 bar H_2, 550-2200 ppm H_2S, 40 barg total (balance N_2), and 3-3.5 mol% ethylene glycol in the feed a function of TOS.*

H.2 Raman Curve Fitting

Curve fitting of the Raman spectra was performed with WiRE 4.2 (Renishaw) using Voigt profiles with the results shown in figure H.4 and table H.1.

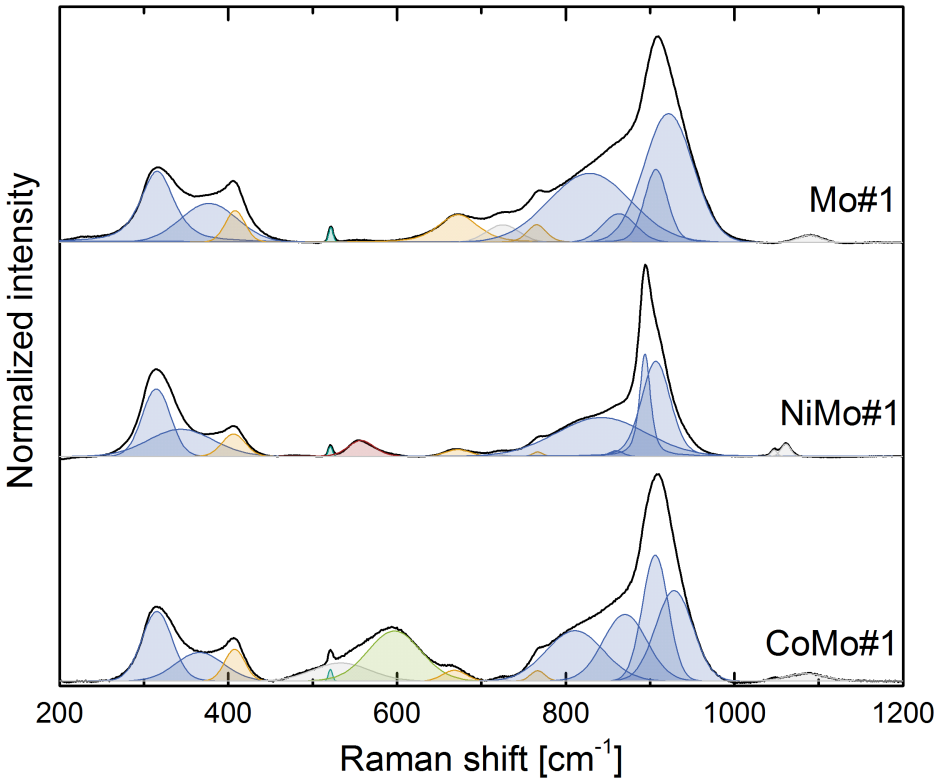

Figure H.4: *Curve fitting results for baseline-corrected Raman spectra of Mo#1, NiMo#1, and CoMo#1 oxide catalyst precursors. The Raman bands were assigned to monomolybdate tetrahedra (blue), $MgAl_2O_4$ support (orange), supported NiO (red), supported CoO (green) and Si impurities (turquoise).*

Table H.1: *List of curve fitting parameters for the curve fitting results presented in figure H.4.*

Catalyst	Curve	Centre	Area	FWHM	Fraction lorentzian
Mo#1	1	316.2	15474.9	47.452	0.694
	2	377.5	10968.8	79.101	0.000
	3	408.6	3314.3	27.678	0.178
	4	522.1	331.5	6.238	0.000
	5	672.8	6780.8	55.869	0.577
	6	725.8	2867.5	45.967	0.000
	7	766.2	1962.8	26.714	0.449
	8	828.9	27970.5	113.839	0.000
	9	863.7	4829.3	47.081	0.018
	10	907.5	9147.3	32.164	0.272
	11	922.5	31268.0	68.288	0.000
	12	1089.5	796.7	30.983	0.000
NiMo#1	1	315.1	11328.4	39.453	0.000
	2	344.2	10389.4	89.916	0.000
	3	406.8	3092.9	32.330	0.008
	4	521.5	235.8	5.610	0.000
	5	558.0	2650.3	36.379	0.214
	6	672.7	993.9	34.371	0.000
	7	717.9	222.1	23.830	0.000
	8	767.5	264.4	14.113	0.000
	9	842.7	20765.8	125.445	0.000
	10	860.3	460.3	19.097	0.000
	11	894.4	8729.9	15.457	0.706
	12	907.4	17975.6	40.438	0.273
	13	1047.6	227.4	8.400	0.000
	14	1061.5	698.9	13.253	0.000
CoMo#1	1	315.5	3208.0	42.446	0.062
	2	366.0	2036.4	66.958	0.000
	3	407.6	955.7	28.302	0.000
	4	521.0	70.0	5.661	0.000
	5	533.5	1539.6	79.946	0.000
	6	597.0	3965.5	73.694	0.032
	7	668.0	371.5	32.408	0.000
	8	723.2	37.1	13.789	0.001
	9	766.8	227.2	20.082	0.086
	10	811.0	4286.0	79.895	0.000
	11	870.3	4335.8	61.118	0.000
	12	906.3	4862.5	36.235	0.000
	13	928.6	4997.1	51.859	0.000
	14	1084.4	431.6	53.885	0.000

H.3 TEM analysis

A NiMo sample was sulfided in the POC setup, and subsequently characterized by elemental analysis (see table H.2) and TEM. As opposed to the freshly sulfided CoMo catalyst presented in table 5.1, this NiMo catalyst was not exposed to increasing temperature and pressure after the sulfidation. This resulted in a higher content of sulfur and carbon indicating that DMDS residues were left in the pores of the catalyst after sulfidation. Fe was detected in a low concentration, indicating that small amounts steel wool could be present in the analyzed catalyst sample. There was a slight decrease in the molar Ni/Mo ratio compared to the oxide phase precursor (see table 3.3), but the ratio remained approximately constant at 0.3.

Table H.2: *Composition and properties of sulfided NiMo#2.*

Mo [wt%]	**Ni [wt%]**	**Ni/Mo [molar]**	**Si [wt%]**	**Fe [wt%]**	**S [wt%]**	**C [wt%]**	**S/Mo [molar]**
3.00	0.49	0.27	<0.02	0.12	4.81	6.30	4.80

TEM revealed highly dispersed particles as it can be seen from the micrograph in figure H.6 and the particle size distribution in figure H.5. The average slab length was 4.3±2.8 nm with a mean stacking of 1.24. 84 % of the particles had a stacking of 1, and 95 % of the particles had a stacking of ≤2. Only 1.6 % of the particles had a stacking of ≥4, and a maximum stacking of 6 was observed. The observed slab length and stacking are in agreement with values obtained in literature for similar catalysts; i.e. MoS_2/Al_2O_3 with an approximate monolayer, or sub monolayer, Mo loading [106, 111, 124].

The XANES and EXAFS results from the *in-situ* sulfidation revealed that average Mo-Mo coordination number at 3.16 Å was <1, which corresponds to nanoparticles smaller than 2 nm. These particles were too small to detect with TEM at the applied resolution.

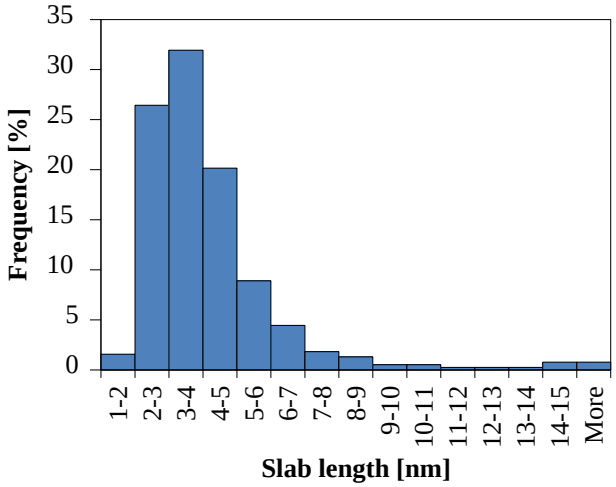

Figure H.5: *Particle size distribution (MoS_2 slab length) for sulfided NiMo#2 (table H.2). Based on 382 particles distributed in 47 TEM images.*

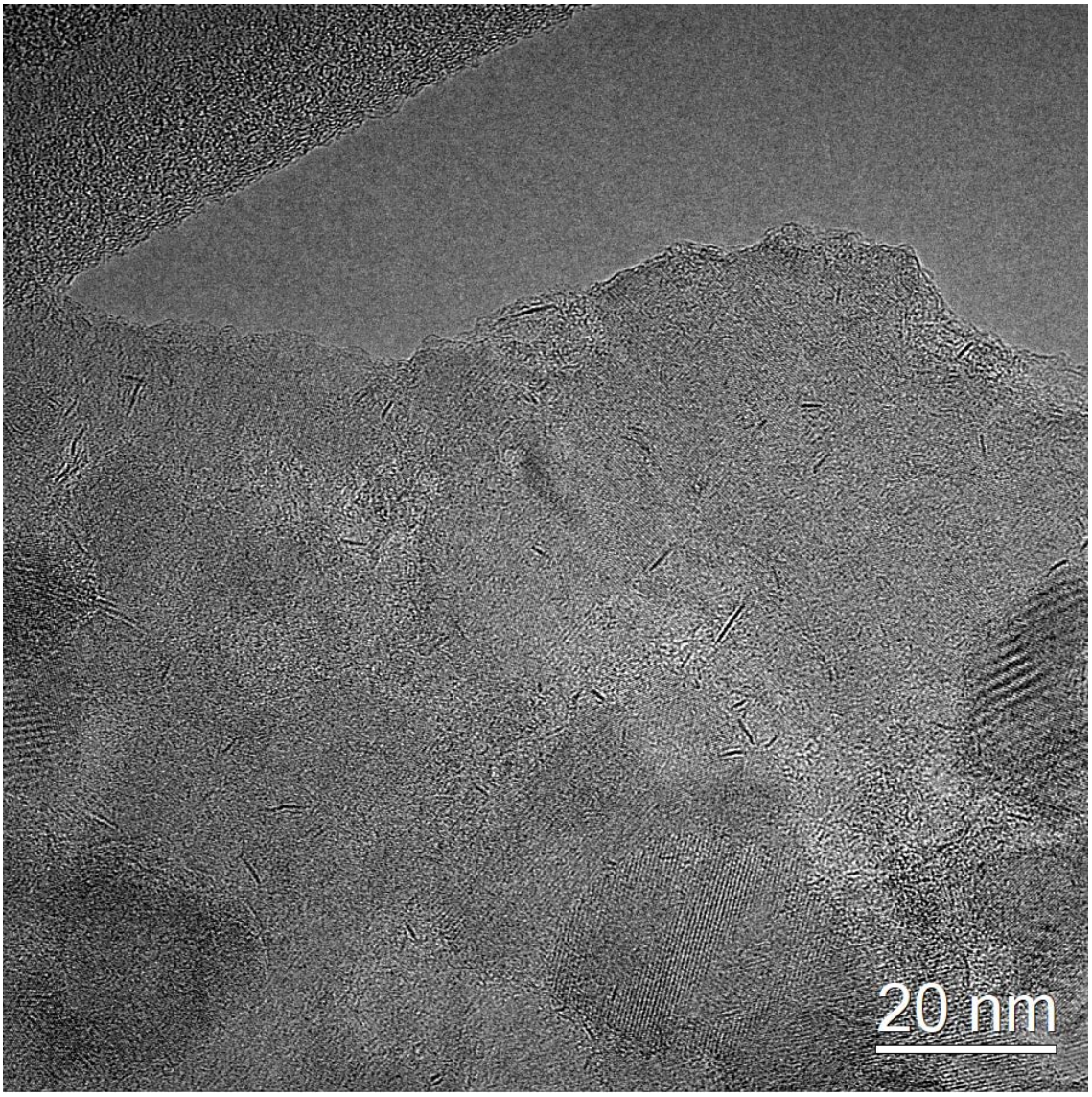

Figure H.6: *TEM image used for particle size distribution (MoS_2 slab length and stacking) for sulfided NiMo#2 (table H.2).*

H.4 EXAFS Fitting Results

XANES spectra from the NiMo#1 and CoMo#1 catalysts are shown in figure H.7. Fourier transformed EXAFS spectra for all samples are shown in figures H.8-H.10.

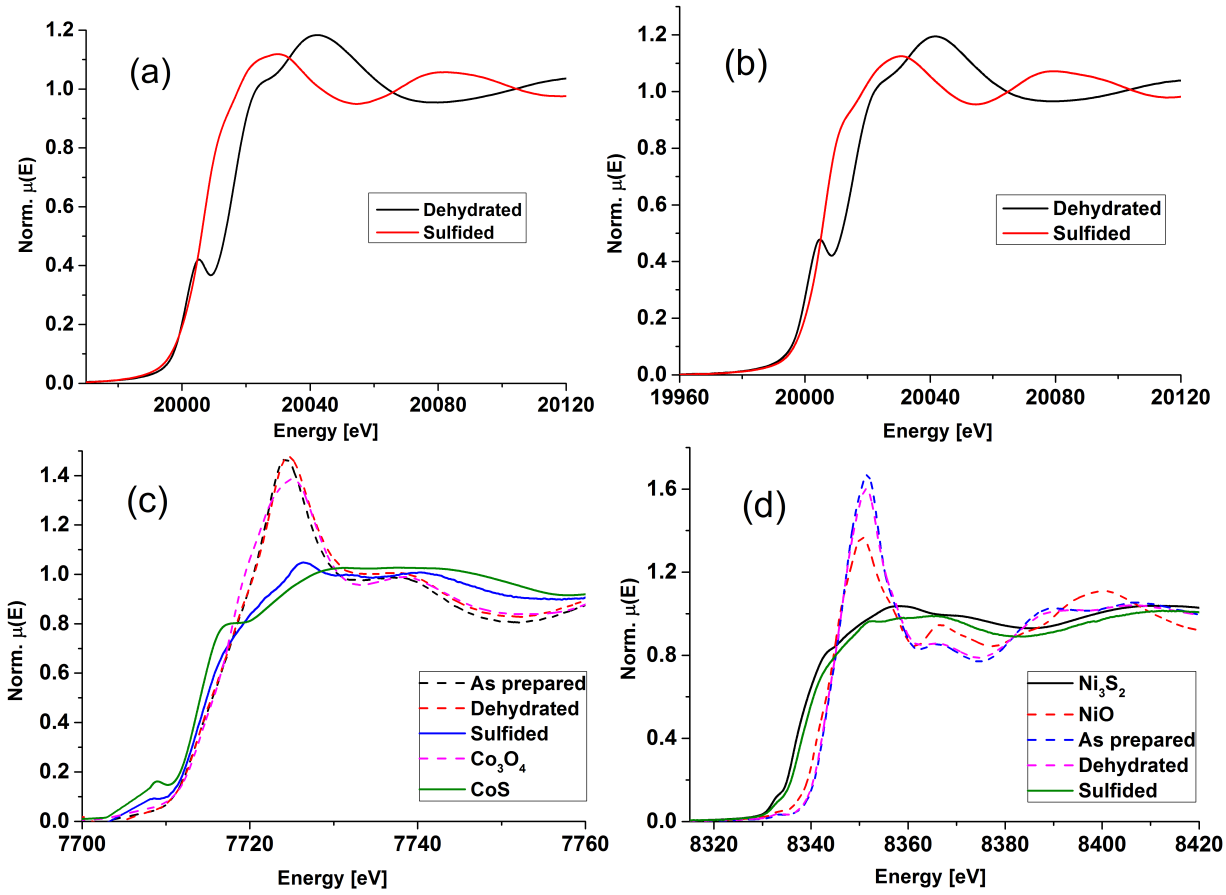

Figure H.7: *XANES spectra of the dehydrated and sulfided catalysts at the Mo K-edge of (a) CoMo#1, (b) NiMo#1, (c) at the Co K-edge of dehydrated and sulfided CoMo#1, and (d) at the Ni K-edge for dehydrated and sulfided NiMo#1. Spectra of reference compounds and as prepared (calcined) samples have been included in (c-d).*

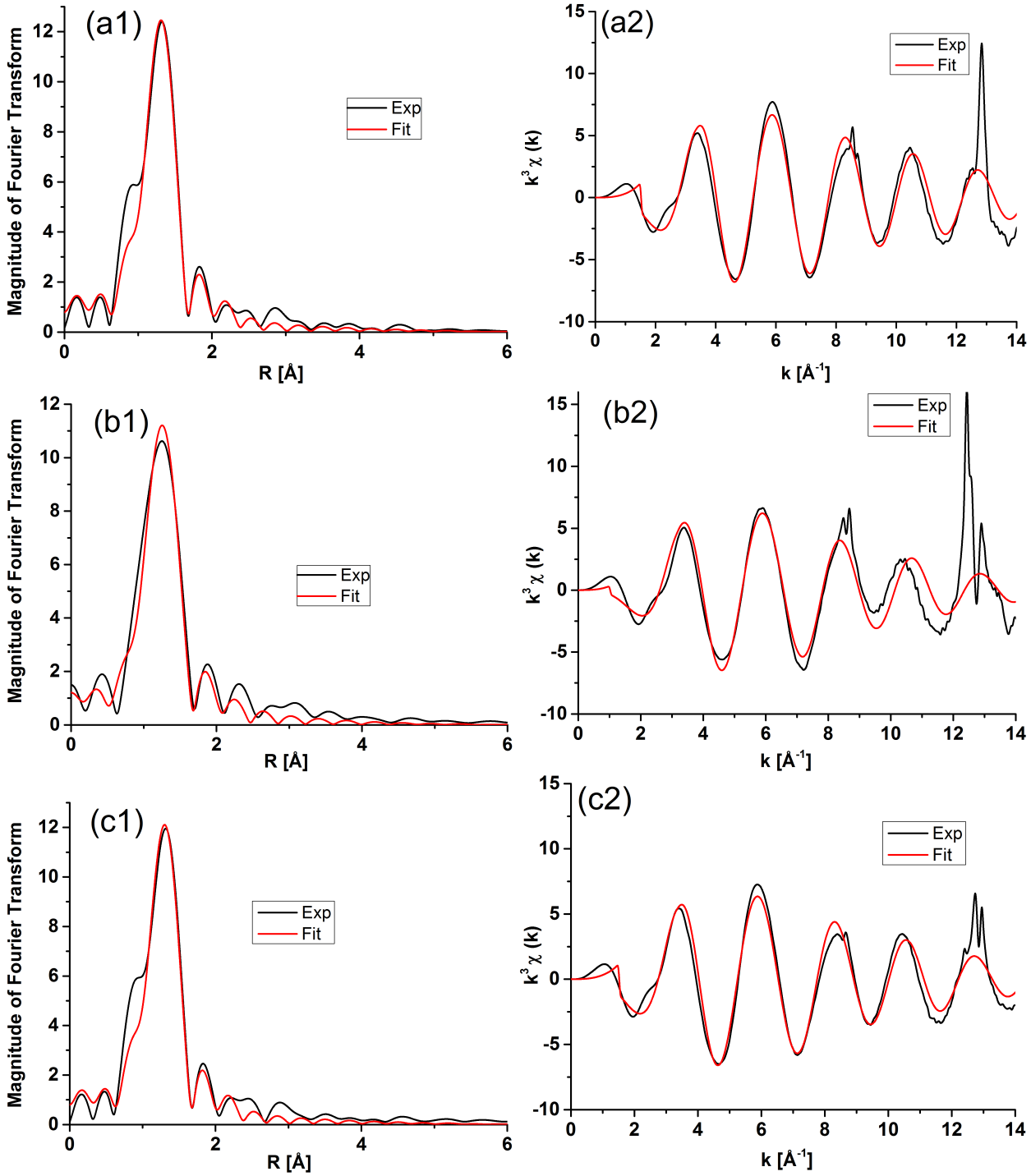

Figure H.8: *EXAFS fitting curves at the Mo K-edge in R-space and k-space with experimental (black) and theoretical fitted (red) curves for (a) dehydrated Mo#1, (b) dehydrated NiMo#1, and (c) dehydrated CoMo#1.*

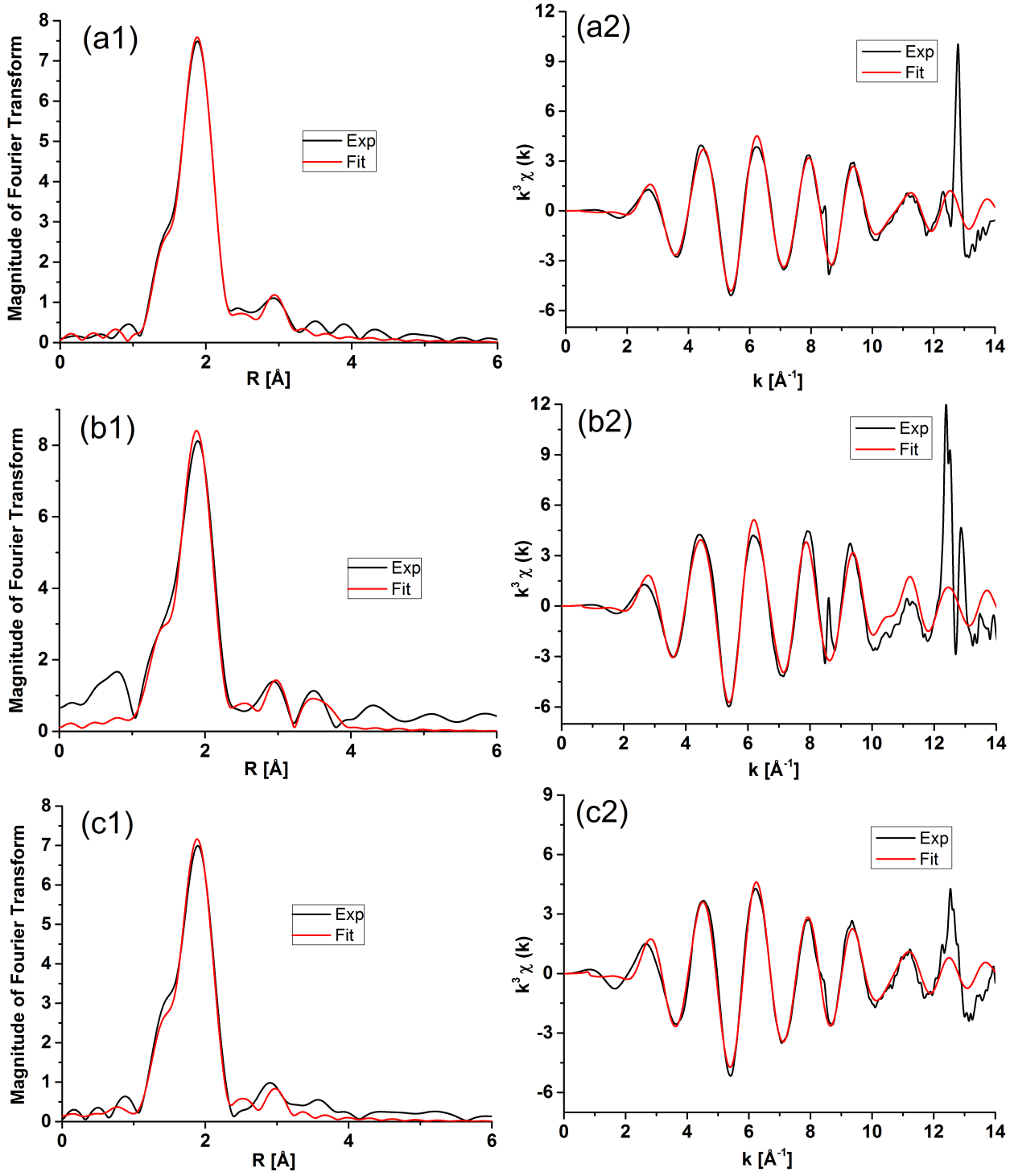

Figure H.9: *EXAFS fitting curves at the Mo K-edge in R-space and k-space with experimental (black) and theoretical fitted (red) curves for (a) sulfided Mo#1, (b) sulfided NiMo#1, and (c) sulfided CoMo#1.*

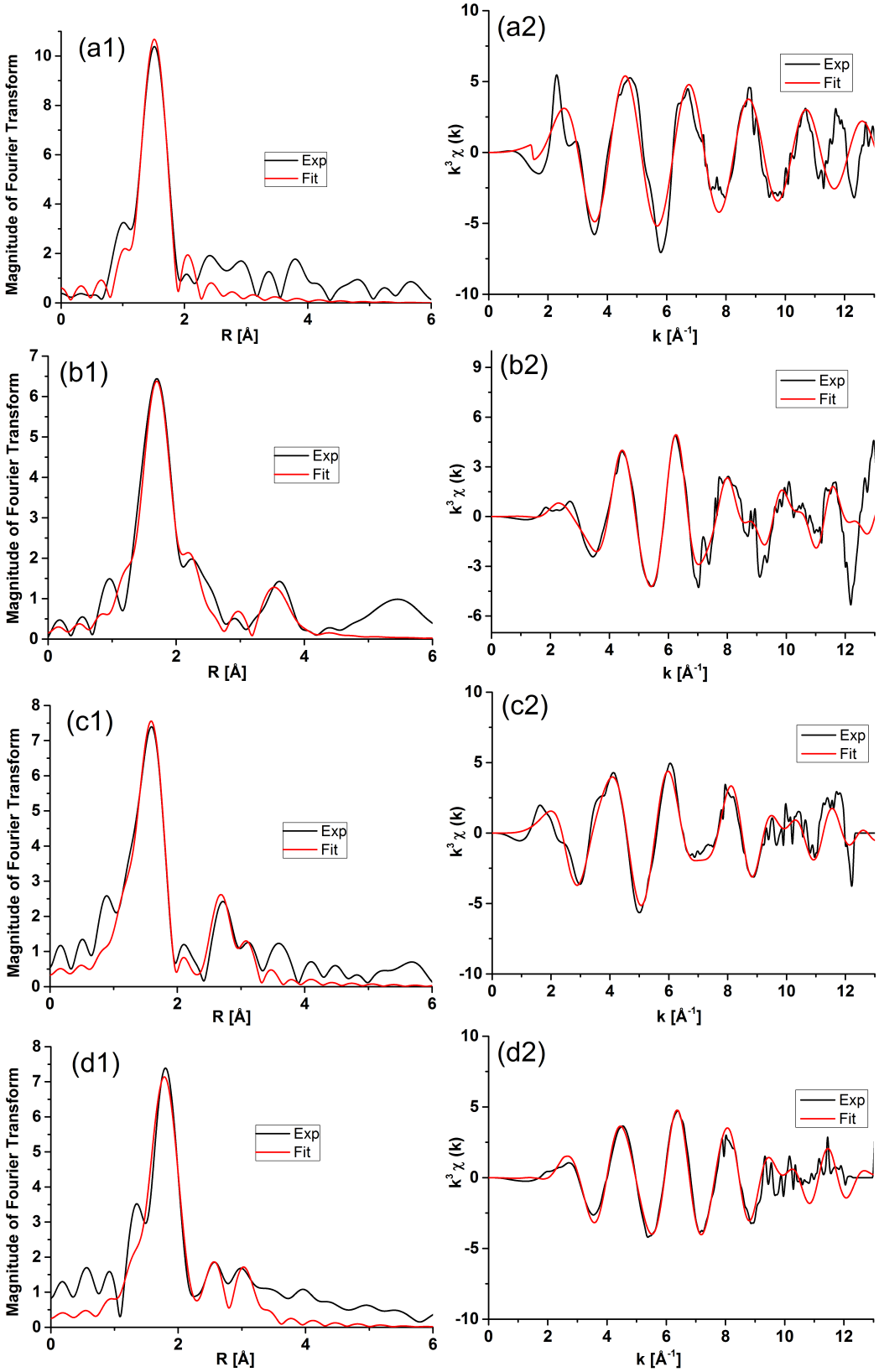

Figure H.10: *EXAFS fitting curves in R-space and k-space with experimental (black) and theoretical fitted (red) curves at the Co K-edge for (a) dehydrated and (b) sulfided CoMo#1, and at the Ni K-edge for (c) dehydrated and (d) sulfided NiMo#1.*

The cluster model used for modelling of XANES spectra (see figure 5.11) is shown in figure H.11.

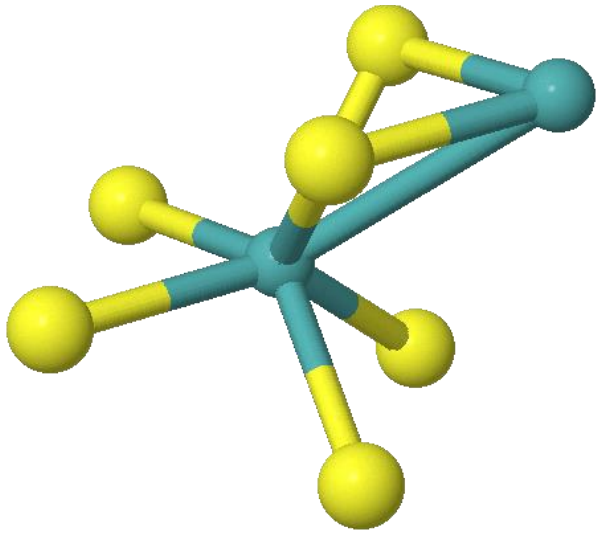

Figure H.11: *MoS_2 cluster modelled by Jmol (FEFF9). Blue = Mo, yellow = S.*

I | Kinetic Models

I.1 Ethylene Glycol Conversion

Ethylene glycol conversion was assumed to follow a consecutive dehydration hydrogenation reaction scheme (see figure 6.7 in chapter 6). Due to the lack of proper quantification of ethenol, acetaldehyde, and ethanol, these compounds were lumped together with ethylene glycol (EG) in a $C_{2,ox}$ term. Thus, the following reactions have been included in the kinetic model:

$$C_{2,ox} + H_2 \xrightarrow{k_1} C_2H_4 + 2H_2O \tag{I.1}$$

$$C_2H_4 + H_2 \xrightarrow{k_2} C_2H_6 \tag{I.2}$$

The rate of reaction for each reaction, r_i in mmol/g/min, is expressed with the rate constant, k_i in L/g/min, and concentrations, C_i in mmol/L, assuming that they are first order in $C_{2,ox}$ and ethylene (ETY), and that hydrogen is present in excess, so that it can be included in the lumped rate constant, k_i':

$$r_1 = k_1 C_{C_{2,ox}}^n C_{H_2}^m = k_1' C_{C_{2,ox}} \tag{I.3}$$

$$r_2 = k_2 C_{ETY}^o C_{H_2}^p = k_2' C_{ETY} \tag{I.4}$$

n, m, o, and p are reaction orders. The concentration of compound i is determined from the molar flow rate, F_i in mmol/min, of the compound and the total volumetric flow rate, v in L/min:

$$C_i = \frac{F_i}{v} \tag{I.5}$$

Due to the large flow of feed gasses with $F_g = 69$ mmol/min (here g denotes N_2, H_2, and H_2S), and a comparatively small oxygenate feed of <3 mmol/min, v was assumed to be constant, since any change in the gas volume due to reaction was negligible (see section I.3.1). v was determined as the total feed flow (gas+oxygenates) in L/min at the applied conditions (temperature and pressure) based on the ideal gas law. For all experiments listed in table 6.2, this flow was 0.099-0.100 L/min on average with a standard deviation of 2.9-4.1 %.

The packed bed reactor model can be used to set up molar flow balances for $C_{2,ox}$, ethylene, and ethane based on reactions I.1 and I.2 and the respective rate expressions in equations I.3 and I.4:

$$\frac{dF_{C_{2,ox}}}{dW} = -r_1 = -k_1' C_{C_{2,ox}} \tag{I.6}$$

$$\frac{dF_{ETY}}{dW} = r_1 - r_2 = k_1' C_{C_{2,ox}} - k_2' C_{ETY} \tag{I.7}$$

$$\frac{dF_{\mathrm{ETA}}}{dW} = r_2 = k_2' C_{\mathrm{ETY}} \tag{I.8}$$

W is the catalyst mass, and the concentrations can be expressed by equation I.5. The rate constants were parameterized according to equation I.9 in order to decouple the activation energy and the pre-exponential factor:

$$k = k_{\mathrm{ref}} \cdot exp\left(\frac{-E_a}{R}\left(\frac{1}{T} - \frac{1}{T_{\mathrm{ref}}}\right)\right) \tag{I.9}$$

k_{ref} is a reference rate constant at the temperature T_{ref} in K. E_a is the activation energy in kJ/mol and R is the gas constant equal to $8.315{\cdot}10^{-3}$kJ/mol.

By using the inlet molar flows of ethylene glycol (typically around 2.2-2.5 mmol/min), ethylene (zero), and ethane (zero) as initial conditions, the system of differential equations I.6-I.8 was solved in Matlab using ode45 by integration throughout the catalyst bed. Matlab's non-linear solver lsqnonlin was used to fit k_{ref} and E_a for the two reactions with the objective function for minimization, f_{obj}, being the absolute difference between the experimentally measured and the modelled outlet flows of ethylene and ethane:

$$error_{\mathrm{ETA}} = |F_{\mathrm{ETA,out,exp}} - F_{\mathrm{ETA,out,model}}|_u \tag{I.10}$$

$$error_{\mathrm{ETY}} = |F_{\mathrm{ETY,out,exp}} - F_{\mathrm{ETY,out,model}}|_u \tag{I.11}$$

$$f_{obj} = error_{\mathrm{ETA}} + error_{\mathrm{ETY}} \tag{I.12}$$

Here, u denotes each set of experimental data points used in the fitting. The modelled outlet molar flows were evaluated at W equal to the catalyst mass applied, i.e. at the outlet of the catalyst bed. The quality of the model fit was then evaluated by parity plots and the mean square error (MSE) for ethane and ethylene, respectively:

$$MSE_{\mathrm{ETA}} = \frac{1}{M}\sum_{u=1}^{M}\left(F_{\mathrm{ETA,out,exp}} - F_{\mathrm{ETA,out,model}}\right)^2 \tag{I.13}$$

$$MSE_{\mathrm{ETY}} = \frac{1}{M}\sum_{u=1}^{M}\left(F_{\mathrm{ETY,out,exp}} - F_{\mathrm{ETY,out,model}}\right)^2 \tag{I.14}$$

Here, M denotes the number of experimental data points used for the model solution and fitting. The conversion in reaction I.1 and I.2 was calculated with the fitted parameters by solving the system of differential equations I.6-I.8 and comparing the resulting outlet flows of ethylene and ethane to the feed flow of ethylene glycol, $F_{\mathrm{EG},0}$:

$$X_1 = \left.\frac{F_{\mathrm{ETY}} + F_{\mathrm{ETA}}}{F_{\mathrm{EG},0}}\right|_{W=0.5\mathrm{g}} \tag{I.15}$$

$$X_2 = \left.\frac{F_{\mathrm{ETA}}}{F_{\mathrm{EG},0}}\right|_{W=0.5\mathrm{g}} \tag{I.16}$$

Only steady state data were used in the modeling, and two sets of data points were used per steady state. The final 5 h at each steady state were used to generate two average sets of data points covering

2.5 h (T, v, $F_{\mathrm{EG},0}$, $F_{\mathrm{ETY,out,exp}}$, $F_{\mathrm{ETA,out,exp}}$). The standard deviation for steady state data was 1.1-8.8 % for the outlet flows of ethane and ethylene, < 0.25 % for $F_{\mathrm{EG},0}$, and insignificant for T and v. Parity plots for the resulting parameter fits are shown in figures I.1-I.5.

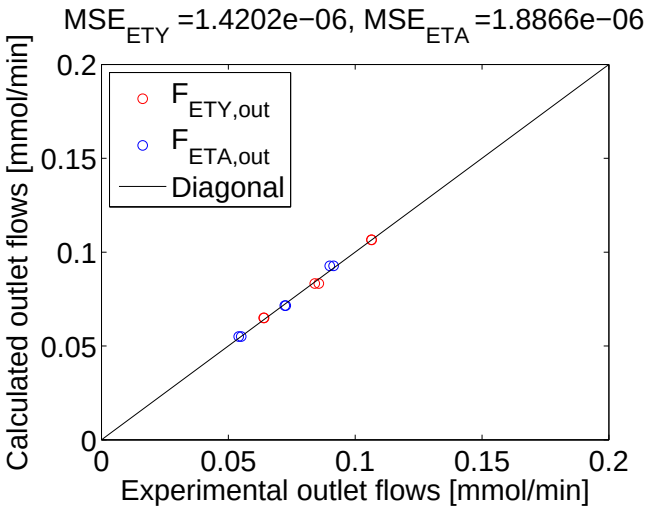

Figure I.1: *Parity plot for EG model fit for steady states in experiment EG (chapter 6).*

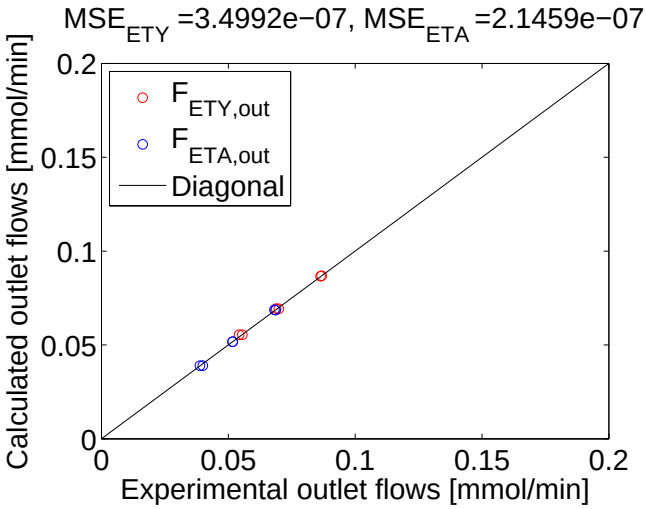

Figure I.2: *Parity plot for EG model fit for steady states in experiment Phe/EG (chapter 6).*

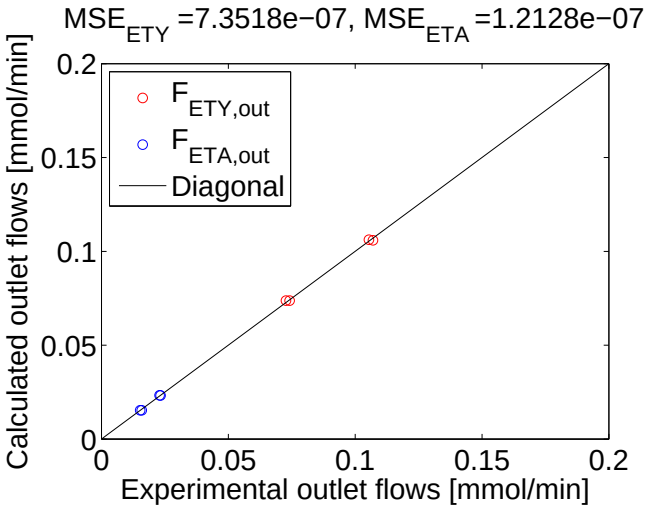

Figure I.3: *Parity plot for EG model fit for steady states in experiment Phe/EG-RegenA (chapter 6).*

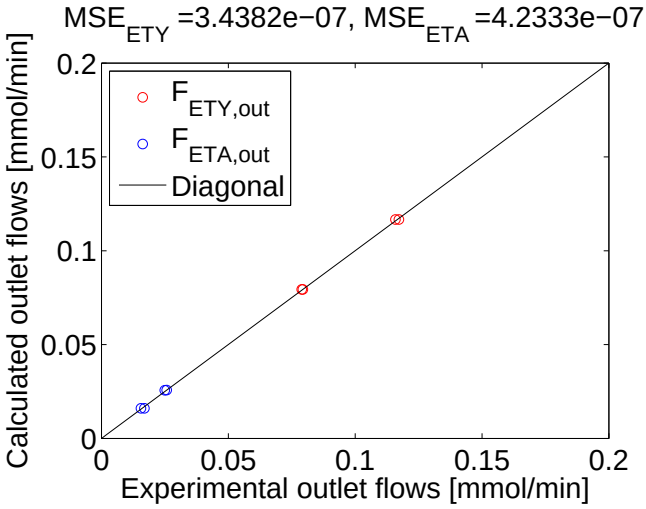

Figure I.4: *Parity plot for EG model fit for steady states in experiment Phe/EG-RegenB (chapter 6).*

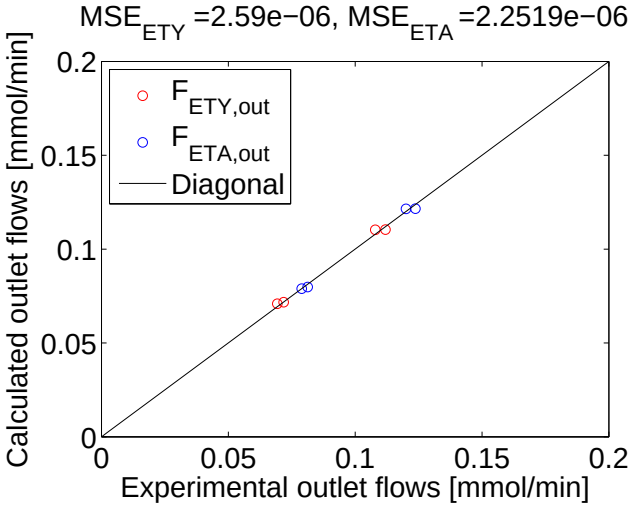

Figure I.5: *Parity plot for EG model fit for steady states in experiment Cyc/EG (chapter 6).*

I.2 Cyclohexanol Conversion

Similar to the procedure for ethylene glycol, a kinetic model was developed for the conversion of cyclohexanol based on the reaction scheme presented in figure 6.10. The reactions considered are:

$$C_6H_{11}OH \rightarrow C_6H_{10} + H_2O \tag{I.17}$$

$$C_6H_{10} + H_2 \rightarrow C_6H_{12} \tag{I.18}$$

With the immediate similarity to the reactions considered for ethylene glycol (see above), the rate constants for reaction 1 and 2 above were calculated in the exact same way as for ethylene glycol with the only difference being that the rate constant for reaction 1 is not a lumped rate constant (no consumption of H_2). In the equations for ethylene glycol above, ethylene can be substituted with cyclohexene (CEN), and ethane can be substituted with cyclohexane (CAN) and solved to get k_1 and k_2' for cyclohexanol conversion. The parity plots for the fitted kinetic model parameters are shown in figures I.6 and I.7.

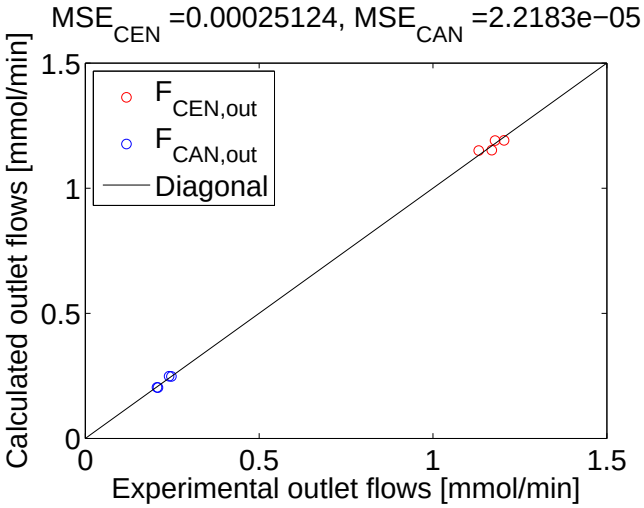

Figure I.6: *Parity plot for cyclohexanol model fit for steady states in experiment Cyc (chapter 6).*

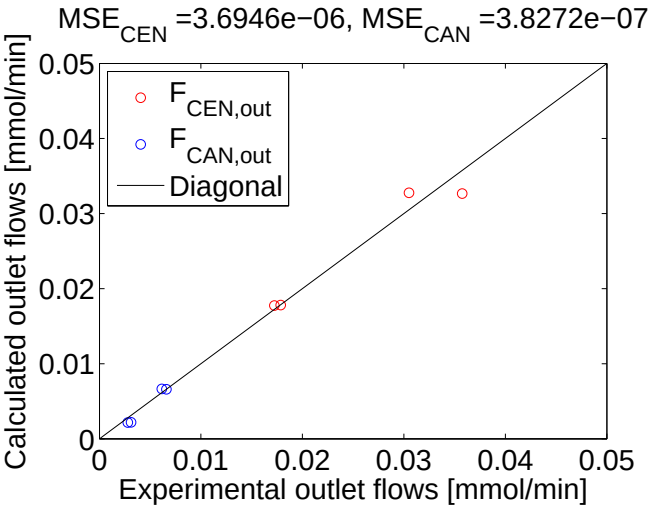

Figure I.7: *Parity plot for cyclohexanol model fit for steady states in experiment Cyc/EG (chapter 6).*

I.2.1 Note on By-product Formation

The formation of cyclohexanone and 1,4-dioxaspiro[4.5]decane was observed when cyclohexanol was converted in the presence of ethylene glycol, i.e. oxidation of cyclohexanol occurred. Cyclohexanone could be formed together with cyclohexane by oxidation of cyclohexanol with cyclohexene according to the reaction:

$$C_6H_{10} + C_6H_{11}OH \rightarrow C_6H_{12} + C_6H_{10}O \tag{I.19}$$

from which 1,4-dioxaspiro[4.5]decane could be formed as an acetal by reaction with ethylene glycol:

$$C_6H_{10}O + C_2H_4(OH)_2 \rightarrow C_6H_{10}(C_2H_4O_2) + H_2O \tag{I.20}$$

However, if only reactions I.19 and I.20 occurred, the measured concentration of cyclohexane in the outlet would be expected to be at least as large as the summed concentration of cyclohexanone and 1,4-dioxaspiro[4.5]decane. This was far from the case (see figure 6.9). Instead, cyclohexanone may have formed through the oxidation of cyclohexanol with ethylene glycol and its products, for example by reactions I.21 or I.22:

$$C_6H_{11}OH + C_2H_4(OH)_2 \rightarrow C_6H_{10}O + C_2H_4 + 2H_2O \tag{I.21}$$

$$C_6H_{11}OH + C_2H_4 \rightarrow C_6H_{10}O + C_2H_6 \tag{I.22}$$

Both I.21 or I.22 would add complexity to the kinetic model, since the conversion of ethylene glycol would be correlated with the formation of cyclohexanone from cyclohexanol. At the same time, there is no immediate influence on the formation of cyclohexene and cyclohexane (target HDO products) from I.21 or I.22, so the formation of cyclohexanone and 1,4-dioxaspiro[4.5]decane have been omitted from the kinetic model.

I.3 Evaluation of Assumptions for Kinetic Models

I.3.1 Excess Hydrogen and Constant Volumetric Flow Rate

The reaction temperature was above the boiling points for all oxygenate reactants during the entire TOS (see table I.1). The oxygenates were assumed to evaporate immediately when entering the reactor. The reaction temperature was in some cases higher than the critical temperature of the oxygenates. The feed composition for each experiment used in the kinetic analysis is listed in table I.2. The partial pressure of each oxygenate reactant (before and after reaction) was low enough to avoid condensation in the reaction zone.

Table I.1: *Boiling points, T_b, and critical temperatures, T_c [305].*

	EG	**Phe**	**Cyc**	**H_2O**
T_b [°C]	197	182	160	100
T_c [°C]	372-517	420	372	374

Table I.2: *Feed compositions at 41 bar total pressure. Average values.*

Experiment	EG [mol%]	Cyc [mol%]	Phe [mol%]	H_2 [mol%]	H_2S [ppm]	N_2 [mol%]
EG	3.4	0	0	65.2	550	31.3
Phe/EG	3.1	0	0.55	65.0	550	31.2
Cyc/EG	3.0	0.54	0	65.1	550	31.3
Cyc	0	2.1	0	66.1	560	31.8

The outlet molar flow rate of hydrogen, water, and deoxygenated hydrocarbons at full HDO depends on whether the hydrocarbons are hydrogenated or not. In both cases, full HDO produces two mol of water per mol of ethylene glycol reacted, one mol water per mol cyclohexanol, and one mol water per mol phenol. Without hydrogenation, one mol H_2 is spent per mol ethylene glycol (giving ethylene+2H_2O), one mol H_2 is spent per mol phenol (giving benzene+H_2O), and no H_2 is spent on cyclohexanol, which is dehydrated to cyclohexene, CEN, (+H_2O). With full hydrogenation, two mol H_2 is spent per mol ethylene glycol (giving ethane+2H_2O), four mol H_2 is spent per mol phenol (giving cyclohexane, CAN, +H_2O), and one mol H_2 is spent on cyclohexanol (giving CAN+H_2O).

The product composition in terms of mol and partial pressures on a 100 mol feed basis (with the composition given in table I.2) has been calculated for full HDO with and without full hydrogenation with the results shown in table I.3. As it can be seen, H_2 is present in great excess, and the the change in the total molar flow as a result of full HDO is less than 5 % with the largest change obtained when no hydrogenation occurs.

Table I.3: *Product composition at full HDO per 100 mol feed with the feed composition given in table I.2 at 41 bar total pressure. Results including full hydrogenation are listed in parenthesis in the cases, where these results differ from the results without hydrogenation.*

Compound/ Experiment	ETY (ETA)	CEN (CAN)	Benzene (CAN)	H_2	H_2S $\cdot 10^2$	N_2	H_2O	Sum
Composition [mol]								
EG	3.4	0	0	61.8 (58.4)	5.5	31.3	6.8	103 (100)
Phe/EG	3.1	0	0.55	61.4 (56.6)	5.5	31.2	6.8	103 (98)
Cyc/EG	3.0	0.54	0	62.1 (58.6)	5.5	31.3	6.5	104 (100)
Cyc	0	2.1	0	66.1 (64.0)	5.5	31.8	2.1	102 (100)
Normalized composition [mol%]								
EG	3.3 (3.4)	0	0	59.8 (58.4)	5.3 (5.5)	30.3 (31.3)	6.6 (6.8)	100
Phe/EG	3.0 (3.1)	0	0.53 (0.56)	59.6 (57.6)	5.3 (5.6)	30.3 (31.8)	6.6 (6.9)	100
Cyc/EG	2.9 (3.0)	0.52 (0.54)	0	60.0 (58.6)	5.3 (5.5)	30.2 (31.3)	6.3 (6.5)	100
Cyc	0	2.1	0	64.7 (64.0)	5.4 (5.5)	31.1 (31.8)	2.1	100
Partial pressures [bar]								
EG	1.3 (1.4)	0	0	24.5 (24.0)	2.2 (2.3)	12.4 (12.8)	2.7 (2.8)	41
Phe/EG	1.2 (1.3)	0	0.22 (0.23)	24.4 (23.6)	2.2 (2.3)	12.4 (13.0)	2.7 (2.8)	41
Cyc/EG	1.2 (1.2)	0.21 (0.22)	0	24.6 (24.0)	2.2 (2.3)	12.4 (12.8)	2.6 (2.7)	41
Cyc	0	0.84 (0.86)	0	26.5 (26.2)	2.2 (2.3)	12.8 (13.0)	0.8 (0.9)	41

Notable cracking also occurred during activity tests (forming CO, CO_2, and CH_4). Cracking of ethylene glycol could produce CH_4 ($C_2H_4(OH)_2 + 3H_2 \rightarrow 2CH_4 + 2H_2O$), CO ($C_2H_4(OH)_2 \rightarrow 2CO + 3H_2$),

and CO_2 ($CO + H_2O \rightarrow CO_2 + H_2$). Formation of CO would affect the volumetric flow rate, as five mol gas are produced per mol ethylene glycol reacted. For the experiment with pure ethylene glycol, full cracking of ethylene glycol into CO and H_2 would result in 114 mol gas per 100 mol feed. This is a larger change compared to the result obtained for HDO (see above), but considering that the yield of CO was <14 % in the pure ethylene glycol experiment, it is fair to assume that the volumetric flow rate through the catalyst bed was constant and equal to the inlet molar flow rate.

I.3.2 Plug Flow

The packed bed reactor model assumes plug flow through the packed catalyst bed. The modified Reynolds number, Re_p, is calculated from the gas density, ρ, the linear gas velocity, U, the particle diameter, d_p, and the dynamic viscosity, η [306]:

$$Re_p = \frac{\rho U d_p}{\eta} \tag{I.23}$$

At 380-450 °C and 41 bar, the average viscosity of hydrogen and nitrogen was estimated to 14 and 32 μPa·s, respectively [307]. The density of hydrogen and nitrogen was estimated to 1.1 kg/m^3 and 20 kg/m^3, respectively [307]. With an approximate feed composition of 65 % H_2 and 35 % N_2, the resulting viscosity and density becomes 20 μPa·s and 7.7 kg/m^3, respectively. With an average gas velocity of 0.1 L/min, and an inner reactor diameter of 8 mm, U becomes 3.3 cm/s, and Re_p becomes 3.8-7.6 with a particle diameter of 300-600 μm. The flow is laminar for Re_p <1 and turbulent for Re_p >1000 [306], meaning that the flow is in the transition region, but far from being fully turbulent.

I.3.3 Constant Pressure Across Packed Bed

Kozeny's equation [306] can be used for estimation of the pressure drop across the catalyst bed, with p_f/l being the pressure drop in Pa per m and ϕ being the catalyst void fraction:

$$\frac{p_f}{l} = 180\frac{U\eta(1-\phi)^2}{\phi^3 d_p^2} \tag{I.24}$$

With a void fraction of 0.59, the pressure drop was 0.03-0.11 mbar per cm bed. With a total bed length of <2 cm in the experiments used for kinetic modelling and a total pressure of 41 bar, the pressure across the catalyst bed could be assumed constant.

I.3.4 Isothermal Conditions

During non-steady state operation, the reaction temperature was seen to depend on the catalyst activity. The temperature typically increased rapidly, when the oxygenate feed was applied, and then decreased as deactivation occurred (see figure 6.1). For steady state operation at 380-400 °C, it was however possible to obtain a steady temperature (measured in the pressure shell thermopocket outside the reactor).

The adiabatic temperature rise at 100 % HDO including hydrogenation at 380-450 °C has been calculated from [294]:

$$T - T_0 = \frac{-\Delta H X}{\sum_i^n \Theta_i C_{p,i}} \tag{I.25}$$

ΔH is the reaction enthalpy, X is the conversion, $C_{p,i}$ is the heat capacity, and Θ_i is the feed flow ratio $F_{i,feed}/F_{A,feed}$, where A is the compound used as basis for the calculations and i denotes all compounds. $T - T_0$ is the adiabatic temperature rise, i.e. the difference in temperature before, T_0, and after, T, reaction. Equation I.25 provides a worst-case estimate, since the reactor was in fact not operated adiabatically.

From the results shown in table I.4, it can be seen that especially ethylene glycol HDO could have contributed significantly to a temperature increase during reaction. The yield of ethane was however not 100 %, rather <40 %, and endothermic reactions counteracted the temperature increase. The influence of endothermic reactions was observed from the measurement of a temperature profile during the cyclohexanol/ethylene glycol experiment (see figure D.1 in Appendix D).

Table I.4: *Thermodynamic properties and adiabatic temperature rise (equation I.25) at full conversion (X=1) in the experiments used for kinetic analysis on the basis of the different oxygenate reactants.*

Property	**Compound**						$\sum_i^n \Theta_i C_{p,i}$	$T - T_0$
/experiment	**EG**	**Cyc**	**Phe**	**H_2**	**H_2S**	**N_2**	**[J/(mol·K)]**	**[°C]**
ΔH_{HDO} [kJ/mol][a]	-190	-84	-290	-	-	-		
$C_{p,i}$ [J/(mol·K)][b]	134.8	275.0	195.2	29.4	40.5	30.7		
$\Theta_i C_{p,i}$ (EG basis) [J/(mol·K)]								**EG HDO**
EG	134.8	0	0	564.3	0.7	282.4	982.2	193.4
Phe/EG	134.8	0	34.6	617.0	0.7	308.8	1096.0	173.4
Cyc/EG	134.8	49.5	0.0	638.6	0.7	320.1	1143.7	166.1
$\Theta_i C_{p,i}$ (Phe basis) [J/(mol·K)]								**Phe HDO**
Phe/EG	759.8	0	195.2	3477.7	4.1	1740.5	6177.2	46.9
$\Theta_i C_{p,i}$ (Cyc basis) [J/(mol·K)]								**Cyc HDO**
Cyc/EG	748.9	275.0	0	3547.5	4.1	1778.4	6354.0	13.2
Cyc	0	275.0	0	926.2	1.1	464.6	1666.9	50.4

[a] Calculated with HSC Chemistry, average from 380-450 °C (variation <3 kJ/mol).

[b] From [305], average from 380-450 °C (variation <2 J/(mol·K) for H_2, H_2S, and N_2, and 10-20 J/(mol·K) for ethylene glycol, phenol, and cyclohexanol.

It has not been possible to perform the experiments at perfect isothermal conditions, but a fairly stable temperature was obtained after the accelerated deactivation performed at 420-450 °C.

I.4 Evaluation of Mass Transfer Restrictions

It was estimated that the experiments were not subject to mass transfer limitations, except for the case of conversion of pure cyclohexanol. The assessment was performed for 400 °C.

I.4.1 External Mass Transfer

The Mears' criterion [294] for external diffusion was used to determine if external mass transfer restrictions were negligible. In that was the case, the system should comply with the following criterion, which is valid for a first order reaction:

$$\frac{r_A \rho_b r_p}{k_c C_{A,b}} < 0.15 \tag{I.26}$$

r_A is the observed rate of reaction for compound A (ethylene glycol or cyclohexanol), ρ_b is the bulk density of the catalyst bed (600 kg/m^3), r_p is the catalyst particle radius (150-300 μm), k_c is the mass transfer coefficient, and $C_{A,b}$ is the bulk concentration of compound A ($\leq$25 mol/m^3 ethylene glycol and $\leq$15 mol/m^3 cyclohexanol).

The mass transfer coefficient was estimated from the correlation given by Thoenes and Kramers [294]:

$$Sh' = Re'^{1/2} Sc^{1/3} \Rightarrow \left(\frac{k_c d_p}{D_{AB}} \left(\frac{\phi}{1-\phi}\right) \frac{1}{\gamma}\right) = \left(\frac{U d_p \rho}{\eta(1-\phi)\gamma}\right)^{1/2} \left(\frac{\eta}{\rho D_{AB}}\right)^{1/3} \tag{I.27}$$

Sc is the Schmidt number, and Sh' and Re' are the modified Sherwood and Reynolds numbers, respectively. d_p is the particle diameter, U is the linear gas velocity determined earlier (0.3 m/s) and γ is the shape factor, which is 16, when assuming spherical particles. ρ is the fluid density and η is the viscosity, both determined earlier (7.7 kg/m^3 and 20μPa·s). ϕ is the void fraction of the catalyst bed (0.59), determined as 1 -(ρ_b/ρ_c), where ρ_c is density of the catalyst particles (1460 kg/m^3). D_{AB} is the diffusion coefficient of compound A in medium B, which in this case is the gas mixture mainly consisting of hydrogen (and nitrogen). D_{AB} can be estimated from the Fuller and Giddings correlation [308] with the unit of cm^2/s:

$$D_{AB} = \frac{0.00143 T^{1.75}}{P M_{AB}^{1/2} \left((\sum_v)_A^{1/3} + (\sum_v)_B^{1/3}\right)^2} \tag{I.28}$$

T is the temperature in K (673.15 K), P is the pressure in bar (41 bar), and $\sum_v$ is the summed diffusion volumes from the atoms in species A and B, respectively. These can be calculated to 6.1 for H_2, 18.5 for N_2, 57.9 for ethylene glycol, and 129.2 for cyclohexanol [308]. M_{AB} is calculated from the molar masses, M_w, in the following way:

$$M_{AB} = 2\left(\frac{1}{M_{w,A}} + \frac{1}{M_{w,B}}\right)^{-1} \tag{I.29}$$

D_{AB} could thus be determined to the values below. Note that the diffusion through nitrogen is more restricted than through hydrogen.

$$D_{EG,H_2} = 4.83 \cdot 10^{-6} \text{ m/s}$$
$$D_{EG,N_2} = 1.18 \cdot 10^{-6} \text{ m/s}$$
$$D_{Cyc,H_2} = 3.29 \cdot 10^{-6} \text{ m/s}$$
$$D_{Cyc,N_2} = 0.79 \cdot 10^{-6} \text{ m/s}$$

The remainder of this example is based on ethylene glycol in hydrogen. The mass transfer coefficient was calculated from equation I.27 giving k_c = 7.88·10^{-2} m/s. The faster the reaction, the higher the risk of mass transfer limitations, so r_A was calculated for the fastest reaction (ethylene glycol hydrogenation) at 100 % conversion in the initial dehydration/hydrogenation step using the largest rate constant determined (see table 6.4):

$$r_2 = k_2' C_{EG,feed}(X_1 - X_2) = 336 \cdot 10^{-3}\,\text{L/min/g} \cdot 25 \cdot 10^{-3}\,\text{mol/L} \cdot (1-0) \\ = 8.4 \cdot 10^{-3}\,\text{mol/g/min} = 0.14\,\text{mol/kg/s} \tag{I.30}$$

Using the feed concentration of ethylene glycol as the bulk concentration, the Mears' criterion (equation I.26) becomes 0.01 (or 0.03 for nitrogen instead of hydrogen), and external mass transfer limitations could be excluded. Similarly for cyclohexanol with a dehydration rate constant of $\geq$524·10^{-3} L/min/g, the Mears' criterion was calculated to a value of 0.03 in hydrogen (or 0.07 in nitrogen), indicating that external mass transfer was negligible.

I.4.2 Internal Mass Transfer

The risk of internal mass transfer limitations was assessed using the Weisz-Prater criterion [294], where internal mass transfer can be neglected if $C_{WP} \ll 1$ is satisfied:

$$C_{WP} = \frac{r_A \rho_c r_p^2}{D_e C_{A,s}} \tag{I.31}$$

$C_{A,s}$ is the concentration of reactant A at the catalyst surface assumed equal to the bulk since external mass transfer limitation could be neglected. D_e is the effective diffusion determined by D_{AB}, the Knudsen diffusivity, D_K, as well as the tortuosity, τ, catalyst porosity, ϕ_c, and constriction factor, σ (estimated to 3.0, 0.40, and 0.8, respectively [294,309]):

$$D_e = \frac{\phi_c \sigma}{\tau} \frac{1}{\frac{1}{D_K} + \frac{1}{D_{AB}}} \tag{I.32}$$

The Knudsen diffusion can be determined from [309]:

$$D_K = 9700 r_{pore} \left(\frac{T}{M_w} \right)^{1/2} \tag{I.33}$$

Here, D_K is determined in cm^2/s from the pore radius, r_{pore} (104 Å) in cm, the temperature, T in K, and the molar mass, M_w in g/mol. For ethylene glycol, D_K was determined to 3.33·10^{-2} cm^2/s. For cyclohexanol, it was 2.62·10^{-2} cm^2/s. This results in an effective diffusivity in hydrogen of 2.10·10^{-7} m^2/s for ethylene glycol and 1.56·10^{-7} m^2/s for cyclohexanol. C_{WP} can then be calculated to 3.0 for ethylene glycol and 7.4 for cyclohexanol with the corresponding values in nitrogen being 7.9 and 17.7, respectively. This suggests, that there could be some internal mass transfer limitations in the experiments, especially for the very fast cyclohexanol dehydration, which occurred at 100 % conversion of the pure feed. A further investigation of this could be performed experimentally by reducing the catalyst particle size used in the experiments.

I.4.3 Effectiveness Factor

The effectiveness factor, η_{eff}, can be used to assess the severity of the internal mass transfer limitation. The effectiveness factor can be expressed by the Thiele modulus, Φ, for a first order reaction over a spherical catalyst particle [294], where k denotes the mass based reaction rate constant:

$$\eta_{\text{eff}} = \frac{3}{\Phi^2}(\Phi coth(\Phi) - 1) \tag{I.34}$$

$$\Phi = \frac{r_p}{3}\left(\frac{k\rho_c}{D_e}\right)^{1/2} \tag{I.35}$$

The resulting effectiveness factor as a function of particle size is shown in figure I.8. As it can be seen, the effectiveness factor is ≥0.94 for the two reactions in the applied particle size range, except for cyclohexanol dehydration in nitrogen, where it is ≥0.89. Thus, the kinetic results presented in chapter 6 are assumed to give a fair representation of the intrinsic reactivity. In the case of pure cyclohexanol dehydration, however, there was approximately 100 % conversion during the entire activity test independent of temperature. To be sure that mass transfer limitations did not restrict this experiment, it should be repeated at lower conversion to observe a temperature dependent activity.

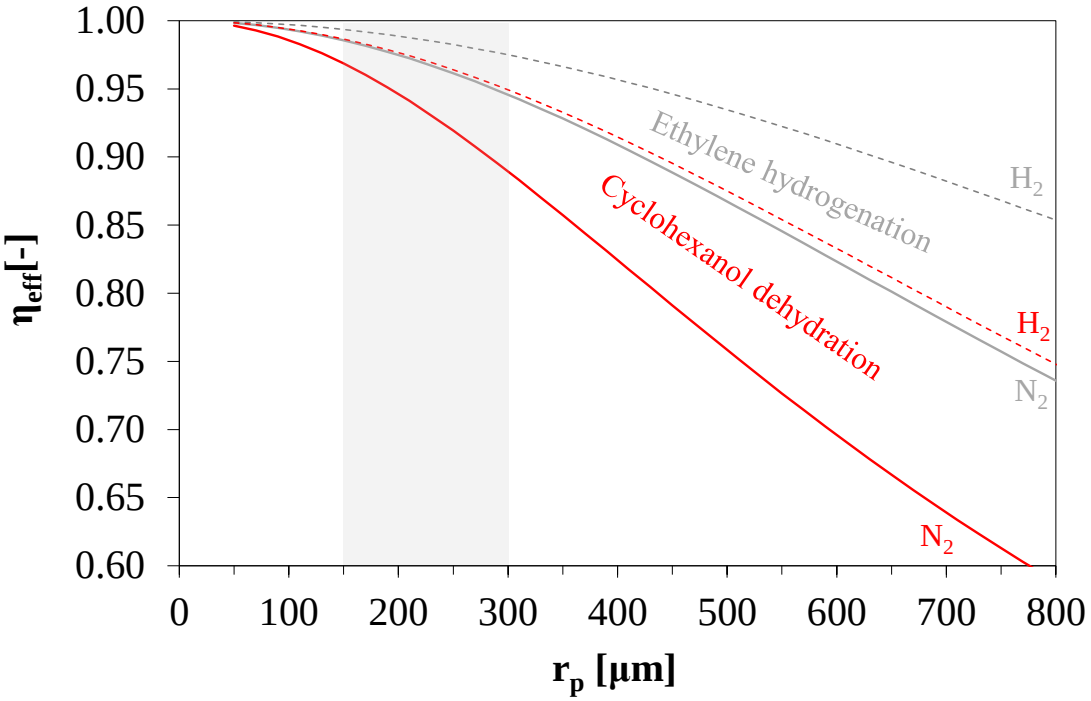

Figure I.8: *Effectiveness factor determined for the fastest reaction in the conversion of ethylene glycol (experiment: EG) and cyclohexanol (experiment: Cyc) over NiMo#2 (see table 3.3) as a function of catalyst particle radius. Based on diffusion in hydrogen and nitrogen. The actual particle radius applied (150-300 µm) is highlighted. For experimental details, see chapter 6, and table 6.2 (feed composition), and tables 6.4-6.5 (kinetic analysis results).*

I.5 Equilibrium Composition during Phenol HDO

The equilibrium composition of phenol, cyclohexanol, and benzene was calculated to investigate the thermodynamics of phenol conversion in an experiment with a phenol in ethylene glycol feed. The experimental feed composition (excluding ethylene glycol and H_2S) was used in the calculations, while water, cyclohexane, and benzene were included as products. The resulting temperature dependent composition is given in figure I.9. Full conversion of phenol was obtained in the calculations in the selected temperature range.

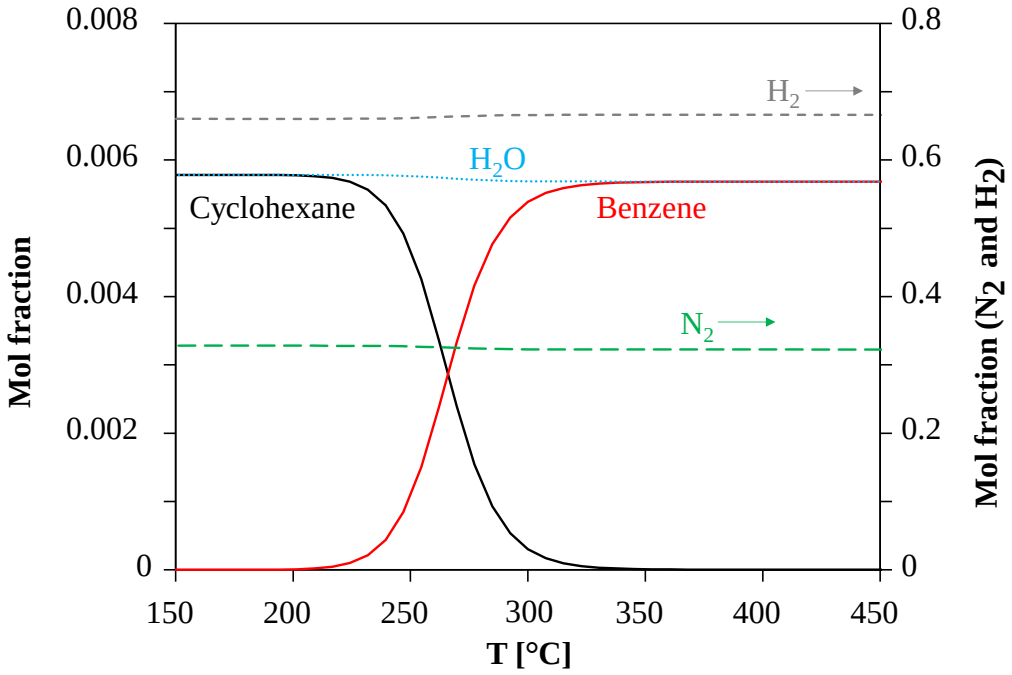

Figure I.9: *Equilibrium composition during phenol HDO at operating conditions relevant to the experiment Phe/EG (feed: 65 kmol H_2, 31.2 kmol N_2, 0.55 kmol phenol, 0 kmol cyclohexane, 0 kmol benzene, 0 kmol H_2O). Calculated with HSC Chemistry.*

J | Catalyst Reactivation by Oxidation and Resulfidation

The following reactions were assumed for the oxidation of deposited carbon and sulfur in MoS_2:

$$C(s) + 0.5O_2(g) \rightarrow CO(g) \tag{J.1}$$

$$C(s) + O_2(g) \rightarrow CO_2(g) \tag{J.2}$$

$$S(s) + O_2(g) \rightarrow SO_2(g) \tag{J.3}$$

The molar flow of N_2 in the in- and outlet was constant and determined by the mass flow controllers. The inlet flow of O_2 was also determined by the mass flow controllers. The inlet molar flow of CO and SO_2 was zero, and the outlet flows were determined by reactions J.1 and J.3. Since technical air (21 % O_2 in N_2) was used to generate the 7.6 % O_2 in N_2 feed, the feed consequently contained 140 ppm ppm CO_2 (seen as the baseline in figure 6.15). In the calculations, the feed flow of CO_2 was assumed to be zero, and the baseline level of CO_2 was simply subtracted after the calculation of the product CO_2 flow. The outlet flow of O_2 was determined from the stoichiometry in reactions J.1-J.3:

$$F_{O_2,out} = F_{O_2,in} - F_{CO_2,out} - 0.5F_{CO,out} - F_{SO_2,out} \tag{J.4}$$

The total gas flow out of the reactor (equation J.5) can be simplified to equation J.6 by insertion of J.4:

$$F_{total,out} = F_{N_2} + F_{O_2,out} + F_{CO_2,out} + F_{CO,out} + F_{SO_2,out} \tag{J.5}$$

$$F_{total,out} = F_{N_2} + F_{O_2,in} + 0.5F_{CO,out} \tag{J.6}$$

Since the flow of CO is determined by its concentration and the total molar flow (equation J.7), equation J.6 can be simplified to equation J.8:

$$F_{CO,out} = y_{CO,out} \cdot F_{total,out} \tag{J.7}$$

$$F_{total,out} = \frac{F_{O_2,in} + F_{N_2}}{1 - 0.5 \cdot y_{CO,out}} \tag{J.8}$$

The molar flow of each of the oxidation products (CO, CO_2, and SO_2) was then calculated based on the measured concentrations and calculated total flow. The flows of CO and CO_2 were then integrated

(using the trapezoidal rule) in the time range shown in figure 6.15 to get the molar amount of CO_x released (including subtraction of the CO_2 baseline), which was 7.65 mmol, corresponding to 91.9 mg carbon. As 0.5 g of fresh catalyst was used in this experiment, it corresponds to a carbon deposition of 15.5 wt% on basis of the oxide precursor. In order to compare with the carbon deposition on the remaining catalysts tested, however, it is necessary to consider the transformation of the oxide precursor into the active sulfide phase.

The composition of the catalyst was 3.33 wt% Mo and 0.66 wt% Ni, which was assumed to be present as MoO_3 and NiO (see table 3.3). Using the molar masses in table J.1, the molar amount of MoO_3 and NiO present per 100 g of catalyst precursor can be calculated (34.7 mmol Mo and 11.2 mmol Ni per 100 g catalyst), and based on this, the mass change resulting from the transformation into Ni-MoS_2 can be estimated (see table J.2).

Table J.1: *Selected molar masses in g/mol. [310]*

Mo	Ni	O	S
95.94	58.69	16.00	32.07

Table J.2: *Presence of MoO_3, NiO, and Ni-MoS_2 in oxide and sulfide catalyst phases of NiMo#2 catalyst (see table 3.3). Based on stoichiometry per 100 g catalyst precursor with 34.7 mmol Mo and 11.2 mmol Ni in the oxide form.*

Amount	NiO	MoO_3	Ni (in Ni-MoS_2)	MoS_2	Sum
Present in oxide precursor					
[mmol]	11.2	34.7	0	0	45.9
[g]	0.83	4.99	0	0	5.82
Present in sulfided sample					
[mmol]	0	0	11.2	34.7	45.9
[g]	0	0	0.65	5.55	6.20

During the sulfidation of 100 g oxide precursor of NiMo#2, 5.82 g is "lost", and 6.20 g is "gained" in the formation of the sulfide phase corresponding to a total gain of 0.38 g per 100 g precursor, which is practically negligible, but taken into account here. The resulting mass of the 0.5 g (500.2 mg) catalyst precursor loaded in the Phe/EG experiment is estimated to:

$$m_{cat,sulfided} = m_{cat,fresh} \cdot \frac{100\text{g} + 0.38\text{g}}{100\text{g}} = 0.5002\text{g} \cdot 1.0038 = 0.5021\text{g} \tag{J.9}$$

The carbon deposition thus corresponds to:

$$\text{C}_{\text{wt\%}} = \frac{m_\text{C}}{m_\text{C} + m_{cat}} = \frac{91.9\text{mg}}{(502.1 + 91.9)\text{mg}} \cdot 100\% = 15.4\text{wt\%} \tag{J.10}$$

The carbon amount includes any carbon deposited on the inner and outer surface of the reactor tube as well as on the inner surface of the pressure shell. With a fair assumption of this area being equal to the area of the outer surface of the reactor tube times three, this area is equal to:

$$SA_{reactor} = 3 \cdot L \cdot 2 \cdot \pi \cdot r_{reactor} = 6 \cdot 0.90\text{m} \cdot \pi \cdot 0.005\text{m} = 0.085\text{m}^2 \tag{J.11}$$

where L is the reactor length and $r_{reactor}$ is the outer reactor radius. The surface area of the loaded catalyst precursor was (see table 3.3) 38.5 m^2. The potentially coked reactor surface area thus constituted <0.5 % of the total coked surface area (on oxide precursor basis), and the influence on the calculated coke deposition of 15.4 wt% was assumed negligible.

Department of Chemical and Biochemical Engineering - CHEC
Technical University of Denmark
Søltofts Plads, Building 229
2800 Kgs. Lyngby
Denmark
Phone: +45 45 25 28 00
Web: www.kt.dtu.dk